Efficiency calculations for the Time Projection Chambers in the BRAHMS experiment at the RHIC accelerator

Truls Martin Larsen
University of Oslo
January 16, 2003

Thesis presented for the Cand. Scient. degree (Master of Science).

Preface

The work on this thesis started very nice, relaxed and easy. I did not know it would be the hardest work I have encountered so far in my life[1]. Thanks to those who have helped me with encouragement and comments.

Oslo, January 16, 2003
Truls M. Larsen

---

[1] I have been competing in cross country skiing from the age of 10 until I reached my 23. birthday. Training 2 passes a day (a total of 3-5 hours a day) being normal for the last 4-5 years of that period, though I never reached the international level. So I thought I would be prepared for hard work ...

Contents

List of Figures

List of Tables

Chapter 1

Introduction

The Relativistic Heavy Ion Collider (RHIC) is situated at Brookhaven National Laboratory (BNL) on Long Island outside New York, USA. This collider has been built with the purpose of studying the thermalized form of deconfined matter, also called Quark Gluon Plasma (QGP). To be able to do this, one has to identify signatures from the QGP. This involves identifying charged hadrons that are created in the collisions. The BRAHMS (*B*road *R*ange *H*adron *M*agnetic *S*pectrometer) experiment is able to do this using two movable spectrometers. This enables BRAHMS to identify charged hadrons over a large region of phase space.

This identification of particles is essential to understand the physics that lies underneath these ultra relativistic collisions. Particle spectra and yields from all parts of the reaction zone are two very interesting measurements that BRAHMS will perform. The yields and shapes of particle spectra are sensitive to the dynamical evolution of the fireball[1], created in the collision and are important in understanding the production mechanism of the particles. This may help us to differentiate between different theoretical descriptions of the system.

To get the correct particle spectra and yields in a collision, you need to correct the measurements with the efficiency of the spectrometers and the software. This thesis is devoted to the studies of the tracking efficiency of the Time Projection Chambers of the BRAHMS experiment, see chapter 6. A software framework for the efficiency analysis has been written, employing the well known method of embedding simulated tracks into real events. The efficiency is studied as a function of track and event properties for the geometric acceptance and for the combined detection/reconstruction efficiency of spectrometer hardware and software. The effects of physical processes, like decay, absorption and multiple scattering, must also be included.

The thesis is built in the following way: Chapter 2 defines some of the quan-

---

[1] See chapter 2 for a description of the participant spectator model.

tities that are used in the text, and shows how they are derived. In chapter 3 the BRAHMS experiment is presented. Then there is a short presentation of the GEANT simulation tool which is used throughout the efficiency analysis and the software that has been developed and used. This is in chapter 4 on page 20. In chapter 5 the BRAHVO and BADTRIP software programs are explained, with updates introduced to them. Chapter 6 is devoted to the description of time projection chamber in general and specifically those in the BRAHMS experiment.

The general procedure for reconstruction of a collision is described in chapter7 as an introduction to how the efficiency analysis was done, which is found in chapter8.

Finally, in chapter 9, the results of the analysis is presented. The efficiencies are calculated for all the TPCs and the ability to detect tracks. In chapter 10 is a small investigation of the two track resolution. And finally there is a conclusion.

The results presented points to many unresolved questions. The momentum determination for high momentum particles and the probability for producing ghost tracks are among the unresolved issues. There also remains work to implement other detectors, in the BRAHMS experiment, into the efficiency analysis, e.g. the time-of-flight detectors.

Chapter 2

An ultra-relativistic collision

The RHIC accelerator at Brookhaven National Laboratory is a collider. It collides particles at speeds that approach the speed of light. At this speed and energy a relativistic description of the kinematics in the collision is needed. Figure 2.1 shows what a collision at RHIC might look like.

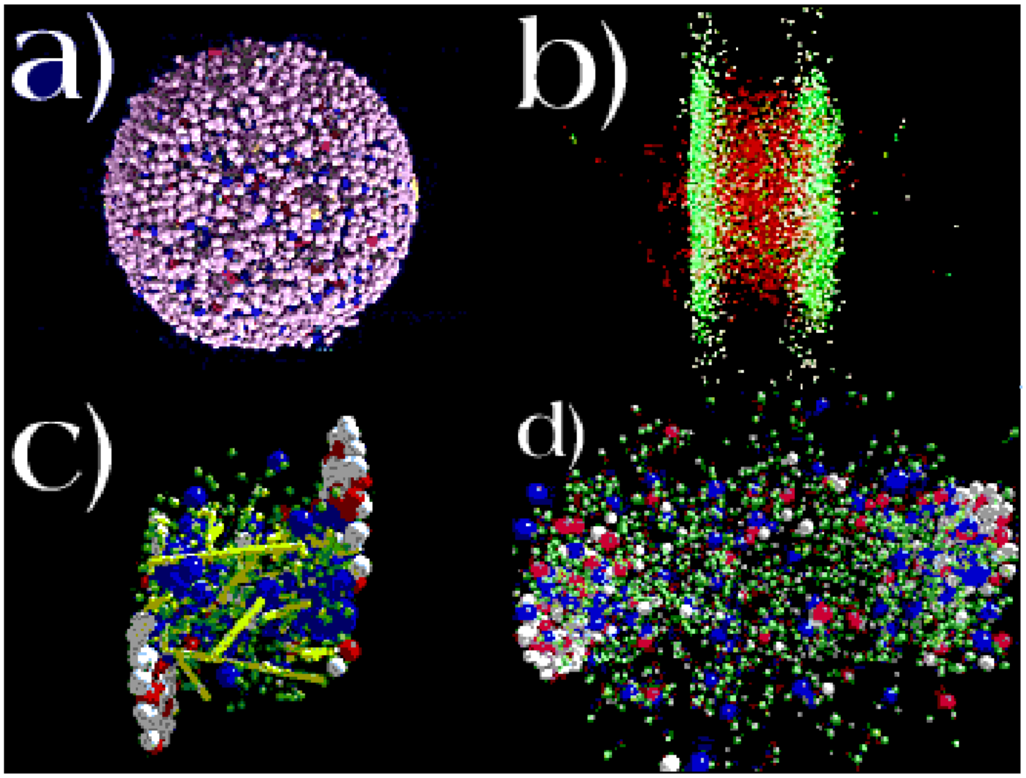

Figure 2.1: a) is an illustration of a Gold nucleus. It's radius is $\sim 6.7\,fm$. b) is a central Gold-Gold collision. c) is a semi-peripheral collision. d) shortly after the collision has occurred.

In the following sections some of the quantities and models that are used to describe the physics at relativistic energies, are presented.

2.1 The participant spectator model

In order to describe a collision between two particles one needs to define some quantitative properties related to the collision. The first thing essential to all collisions is the available energy in the center of mass system, $\sqrt{s_{NN}}$[1]. It is defined as:

$$\sqrt{s_{NN}} = E_1 + E_2 \tag{2.1}$$

where E_n is the total energy of the n'th particle in the collision, measured in the laboratory system.

The first thing one can examine is the geometrical properties, which depend on the centrality of the collision. The centrality of a collision is represented by the impact parameter b, illustrated in figure 2.2.

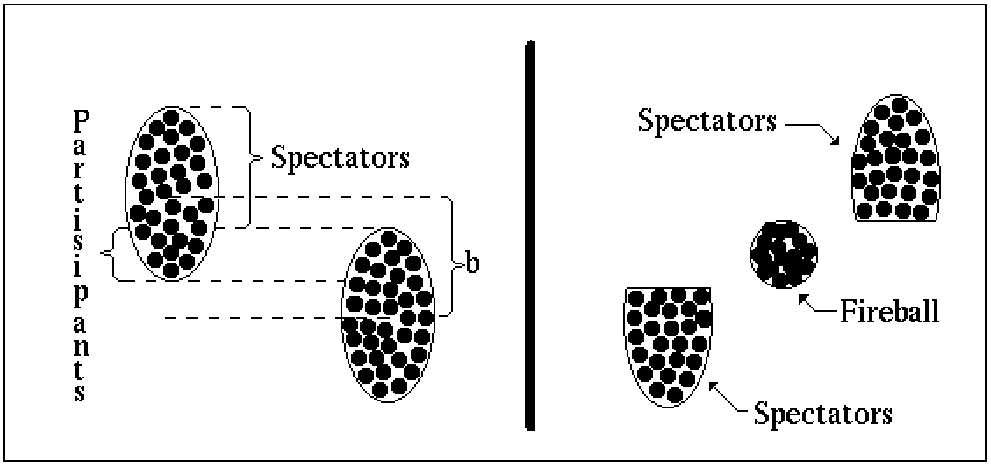

Figure 2.2: The impact parameter b, spectators, participants and fireball. The impact parameter b is defined as the perpendicular distance taken at infinity between the parallel trajectories of the centra of the colliding particles.

The impact parameter in a "classical" collision, which is also valid for relativistic energies to a very good approximation, can have any values between 0 and $R_1 + R_2$, where R_1 is the radius of one of the particles and R_2 is the radius of the other. When $b = R_1 + R_2$, the colliding particles would just miss each other. The most central collisions occurs when $b = 0$.

---

[1] s is one of the Lorentz invariant Mandelstam variables.

The *participant-spectator* model is a commonly used model in all experiments which collide nuclei, illustrated in figure 2.2 on the page before. The nucleons in the colliding nuclei are divided into two groups: *participants*, which will form the *fireball*, and the *spectators* (see figure 2.2 on the preceding page). The fireball is created from the overlapping regions of the two particles, the participants. All the energy from the participants will then be contained inside the fireball. Energy densities inside the fireball can reach those of the very early universe, $10^{-6}\,s$ after the big bang.

This model can be used in both central and peripheral collisions, as well as in symmetric and asymmetric collisions. For ultra-peripheral collisions, i.e. $b > R_1 + R_2$, only the Coulomb forces will act between the collision partners. This case of "collisions" causes Coulomb excitations and electromagnetic dissociation. In this case all the nucleons, in the nuclei, are spectators.

2.2 Some relativistic quantities

The fireball will expand as time evolves and therefore the energy density will drop. During this expansion it will emit particles in all directions. Figure 2.1d is an illustration of this. Since RHIC is operating under relativistic conditions it is convenient to use a quantity called *rapidity* (y). Rapidity is a dimensionless quantity, which is related to an emitted particle's velocity parallel to the beam line. The reason for it's usefulness is it's very simple properties under Lorenz transformation along the beam line. It is just an additive quantity between two systems S and S' with relative rapidity $y_{S'}$. The particle's rapidity, y, in S is $y = y' + y_{S'}$, where the y' is the rapidity of a particle relative to S' and $y_{S'}$ the rapidity of S' relative to S. The definition of rapidity is as follows:

$$y = \tanh^{-1}\left(\frac{v_L}{c}\right) \tag{2.2}$$

where v_L is the emitted particle's speed along the beam line, and c is the speed of light. The rapidity is normally given relative to the beam line, i.e. the speed of the particle along the beam line. The energy of this particle is:

$$\begin{aligned} E^2 &= (p_T^2 + p_L^2)c^2 + m^2c^4 && (2.3) \\ E &= \gamma m c^2 && (2.4) \\ \gamma &= \frac{1}{\sqrt{1-\left(\frac{v}{c}\right)^2}} && (2.5) \end{aligned}$$

where m is the particle's rest mass and v the total velocity, and $\vec{p}_T + \vec{p}_L = \vec{p}$. The subscripts means transverse and longitudinal, respectively. $p_T = p \cdot \sin\theta$

and $p_L = p \cdot \cos\theta$. θ is the angle between the beam line (Z-axis) and $\vec{p}$, with 0 along the positive direction of Z. $\theta \in [0, \pi]$.

The hyperbolic functions are defined like this:

$$\cosh y = e^y + e^{-y} \tag{2.6}$$
$$\sinh y = e^y - e^{-y} \tag{2.7}$$

and are related by:

$$\tanh y = \frac{\sinh y}{\cosh y}, \quad \cosh^2 y - \sinh^2 y = 1 \tag{2.8}$$

If we define the transverse mass m_T, the energy (equation (2.3)) may be written in a new way:

$$m_T^2 c^4 = p_T^2 c^2 + m^2 c^4 \tag{2.9}$$
$$E^2 = m_T^2 c^4 + p_L^2 c^2 \tag{2.10}$$

Equation (2.2) may be rewritten:

$$\tanh y = \frac{v_L}{c} = \frac{\gamma m v_L}{\gamma m c^2} = \frac{p_L c}{E} \tag{2.11}$$

Combining equations (2.6), (2.10) and (2.11), the energy and the longitudinal momentum becomes pure functions of rapidity:

$$E = \sqrt{E^2 \tanh^2 y + m_T^2 c^4} = m_T c^2 \cosh y \tag{2.12}$$
$$p_L c = \sqrt{E^2 - m_T^2 c^4} = \sqrt{m_T^2 c^4 (\cosh^2 y - 1)} = m_T c^2 \sinh y \tag{2.13}$$

If we combine equation (2.12), (2.13) and the definitions of hyperbolic functions (equation (2.6) and (2.7)), some mathematical manipulation of the symbols yields:

$$E + p_L = m_T c^2 (e^y + e^{-y} + e^y - e^{-y}) = 2 m_T c^2 e^y \tag{2.14}$$
$$E - p_L = m_T c^2 (e^y + e^{-y} - e^y + e^{-y}) = 2 m_T c^2 e^{-y} \tag{2.15}$$
$$\frac{E + p_L}{E - p_L} = e^{2y} \tag{2.16}$$
$$\Rightarrow y = \frac{1}{2} ln \frac{E + p_L c}{E - p_L c} \tag{2.17}$$

Two approximations may be done to equation (2.17). When the momentum is much higher than the particle's mass, $pc \gg mc^2$, the energy can approximately be given by $E \approx pc$. This is the case for the beam in the RHIC accelerator. When this approximation is done, the rapidity becomes equal to *pseudorapidity*, (η):

$$\eta = \frac{1}{2} ln \frac{p + p_L}{p - p_L} \tag{2.18}$$

$$\eta = \frac{1}{2} ln \frac{1 + \cos\theta}{1 - \cos\theta} \tag{2.19}$$

$$\eta = \tanh^{-1}(\cos\theta) \tag{2.20}$$

As seen from the above equations the pseudorapidity is a purely geometrical quantity, which can be measured directly. Experimental rapidity determination requires the particle to be identified, *PID*. y is related to the longitudinal momentum, p_L, which has its largest contribution from the source's longitudinal movement. p_T has contribution from the thermal motion and the expansion of the fireball. Equation (2.17), (2.18) and (2.20) will be used later in the text.

2.3 Collision scenarios

What actually happens to the participants in these collisions? Very generally the longitudinal energy (the beam energy) is converted into transverse energy. The transverse energy is used for particle production and their transverse momentum. There are different models that try to describe what happens to the participants. The most extreme cases are outlined by J. D. Bjorken in [1] and by L. D. Landau [2]. J. D. Bjorken assumes that the participants are totally transparent to each other, while Landau assumes full stopping of the participants.

Comparing antimatter and matter (e.g. $\bar{p}/p$ ratios), one is able to tell something about the stopping in the collisions. Full stopping means that all the initial nucleons are transported from beam rapidity to mid rapidity ($y \approx 0$). No stopping, full transparency, should result in a baryon free mid rapidity, since the fireball will have 0 net baryon density.

2.3.1 The Landau picture

The Landau picture [2] of the collision is approximately realized at not so high energies. Full stopping is approximately valid when the center of mass energy lies in the $\sqrt{s_{NN}} \approx 5 - 10\, GeV$ region. This picture results in a collision where all the baryons in the colliding nuclei become part of a fireball at rest in the center of mass system. The resulting hadron gas or quark gluon plasma will therefore have a low anti baryon to baryon ratios in the emitted particles, since there is a high content of original quarks compared to the quark anti-quark pair production. A rapidity spectra from such a collision will indicate a single source. It is expected that heavy neutron stars may contain this type of matter inside its center.

2.3.2 The Bjorken picture

J. D. Bjorken [1] assumes that at sufficiently high energy[2] the colliding nuclei will be transparent to each other. Instead the colliding particles fragment. The net quark number from the original particles are mostly carried by the fragments. The fragments will be a little decelerated in the collision, so they will be found with rapidities close to the colliding nuclei's rapidity. These highly compressed states of matter have chemical conditions similar to those fireballs created from "full stopping" collisions. When the colliding particles starts to move away from each other they leave behind what has popularly been called an *excited vacuum*, in the center of mass coordinate system. This vacuum has zero density of all conserved quantum numbers. It is rapidly filled with with gluons and quark antiquark pairs from the Fermi sea. These conditions are expected to have existed 10^{-6} seconds after the Big Bang. It is this vacuum and the fragments that emits particles in all directions. A rapidity spectra would reveal a longitudinally extended source, with chemical composition varying with y. Hadrons created in the collision at low rapidity will mostly be created in particle - anti-particle pairs. The particle's momentum will come from thermal and collective expansion in this low rapidity region. The ratio between anti-baryons and baryons will therefore be ~ 1 at central rapidity. At higher rapidities this number will drop because it will have contribution from fragments from the collision partners. These particles usually have high momentum, where both the thermal expansion and mainly the longitudinal movement of the source contribute.

The central rapidity will have a "central plateau" of produced particles from the baryon poor region. An approximate plateau, with an approximate boost invariant chemical conditions, can be seen in a conference proceeding, by Djamel Ouerdane on rapidity dependence of charged particle yields in the BRAHMS experiment, in figure 2.3, see [3]. Figure 2.4 compares net-proton production at different center of mass energies, see [4]. This plateau has been predicted since J. D. Bjorken published his article in 1982.

There does not seem to be a sharp transition between full stopping and full transparency, but a gradual increase in the transparency as the available energy

---

[2] At the energies achieved at RHIC, $\sqrt{s_{NN}} = 200\,GeV$, complete transparency is still not seen, only to a good degree. One expects that full transparency will be reached when the Large Hadron Collider (LHC) is build. There the center of mass energies will be as high as $\sqrt{s_{NN}} = 6300\,GeV$.

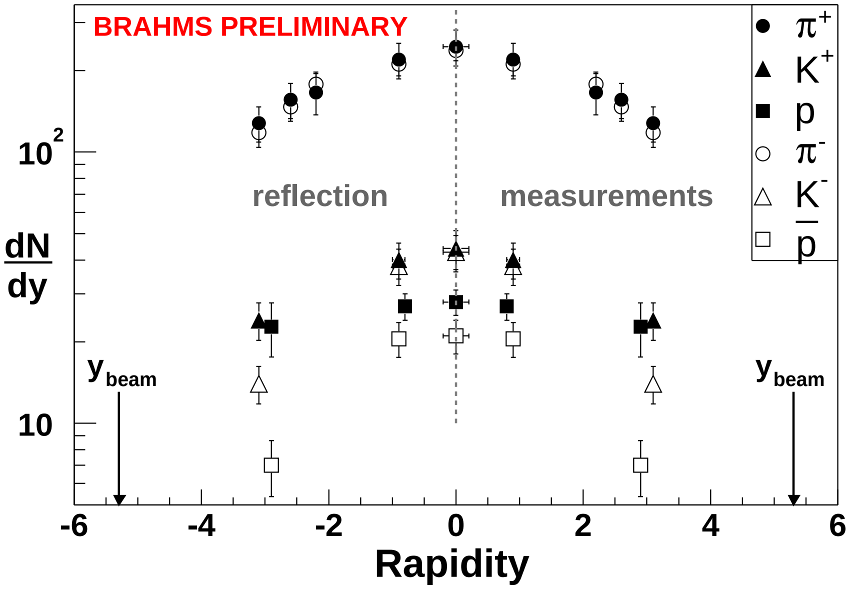

Figure 2.3: Particle yields plotted as a function of rapidity. The figure taken from [3].

in the collision increases. At SPS energies the stopping is clearly incomplete. Results published by the *BRAHMS* experiment shows that the anti-proton to proton ratio, at $\sqrt{s_{NN}} = 200\,GeV$, is still below 1, see figure 2.3.

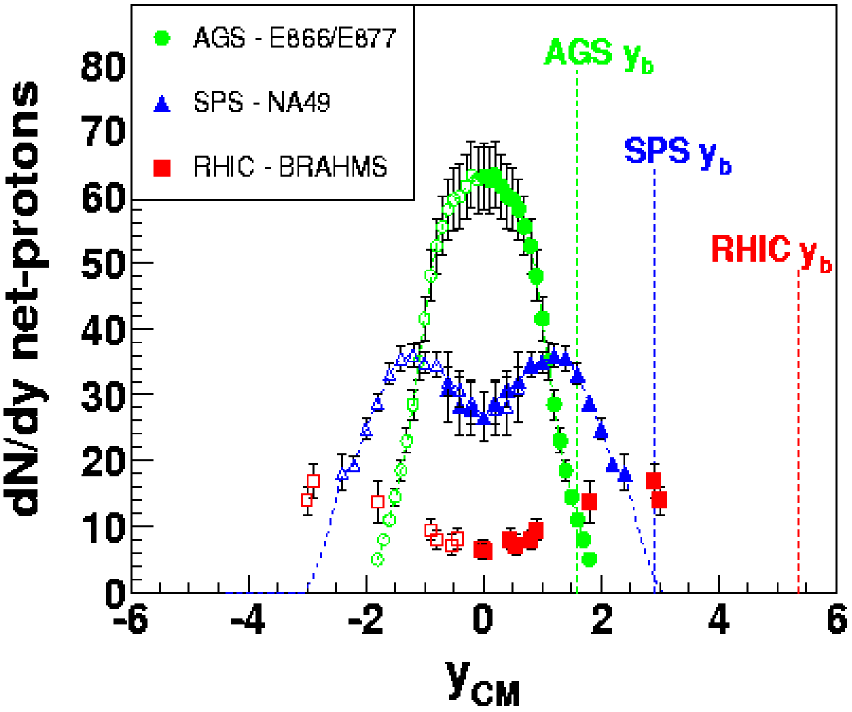

Figure 2.4: Net-proton yields plotted as a function of rapidity, compared with results from the AGS and SPS. The figure taken from [4].

Chapter 3

The RHIC and BRAHMS

The BRAHMS experiment is one of the four experiments in the RHIC ring. The beam line has 6 intersection regions. Four of these contain an experimental setup. The BRAHMS experiment is situated in the 2 o'clock area of the RHIC accelerator. The other experiments PHOBOS, PHENIX and STAR occupy three of the other areas. See figure 3.1 on the following page.

3.1 The RHIC accelerator facility

During the first two years of running, the RHIC has been colliding gold (Au) ions and protons. But RHIC has been designed to use every nuclear species from protons (p) up to Au. The spring and summer of year 2000 and the summer and autumn of year 2001 RHIC was dedicated to Au-Au collisions. The first year the center of mass energy was for most of the run 130 $AGeV$, but during the second the accelerator was run at maximum energy, 200 $AGeV$. Christmas year 2001 and the first month of 2002 were dedicated to polarized protons. This data will provide knowledge on the possibility to extrapolate from 2 participants in a collision to (the theoretical maximum of) 394 ($2 \cdot 197$) in a $b = 0$ central Au-Au collisions. The $0-5\%$ most central collisions have $< N_{part} > \sim 350$. Comparison between $p - p$ and Au-Au collisions will help to isolate nuclear effects.

Before the ions enter the RHIC ring, they go through a series of pre-acceleration stages. See [5]. For Au (and other heavy ions) it starts at the Tandem Van der Graaf. They pass through a stripping foil, and typically exit this machine with a charge of +12e and an energy of 1 $AMeV$. Then they go through another stripping machine and get a charge of +32e. They enter the Booster synchrotron where they are accelerated to 95 $AMeV$. Yet another stripping follows, removing another 35 electrons. At this stage they enter the old Alternating Gradient Synchrotron (AGS) ring. Here they are accelerated to 10.8 $AMeV$. They are then removed from the AGS and stripped of the last to electrons, giving them a charge of +79e. Finally injection into the RHIC ring

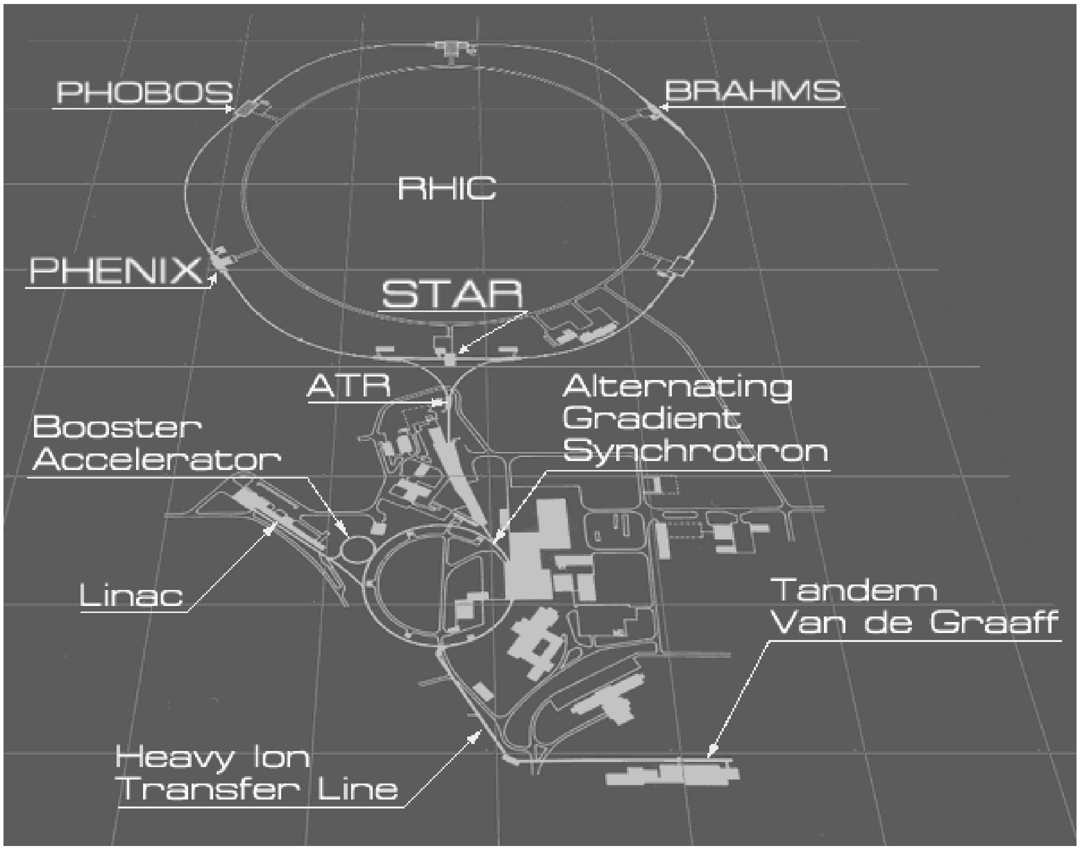

Figure 3.1: The RHIC accelerator with the four experiments, PHOBOS, PHENIX, STAR and BRAHMS.

accelerates them to an energy of $100\,AMeV$. This gives us a center of mass energy in the collisions of $\sqrt{s_{NN}} = 200\,AGeV$.

In the RHIC ring the particles go around in bunches. It has been designed to take as many as 120 bunches at a time, but so far no more than 60 has been used. They tried with 120 bunches during autumn 2001, but encountered too many problems at that stage. The two beams (called yellow and blue) are synchronized so the bunches collide in the four Interaction Regions (IR). There are actually six IRs but only four of them are instrumented.

The reaction rate for a collider can be written as:

$$R_{reactions} = L \cdot \sigma_{int} = \frac{f\,n_1 n_2\,\sigma_{int}}{4\pi\sigma_x\sigma_y} \tag{3.1}$$

The luminosity L of the beam is then defined as $L = f\,n_1 n_2/(4\pi\sigma_x\sigma_y)$. The two beam bunches contain n_1 and n_2 particles, which collide with frequency f. σ_x and σ_y are the widths of Gaussian characterizations of the bunch profiles in

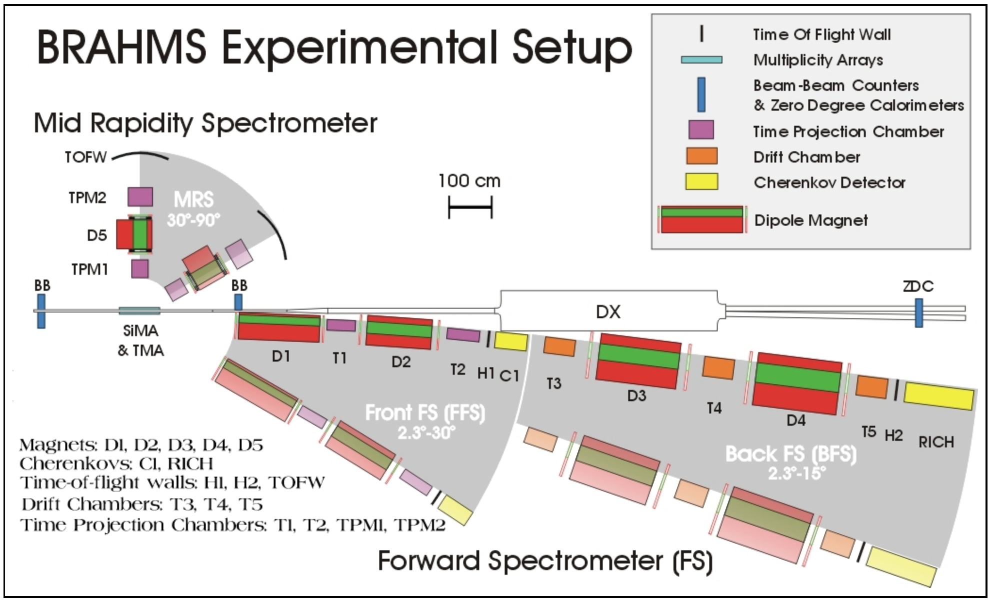

Figure 3.2: Experimental overview over the BRAHMS experiment.

the horizontal (plane of the collider ring) and the vertical direction, respectively. σ_{int} is the nuclear interaction cross section. For Au-Au collisions the inelastic interaction cross section can be calculated to be $\sim 6.8\,b^1$.

RHIC's design luminosity is

$$L_{Design}^{Au-Au} \approx 2 \cdot 10^{26} \frac{1}{cm^2 s} \tag{3.2}$$

This means that during Au-Au collisions the experiments will have a minimum bias collision rate of

$$R_{reaction} \approx 7\,b \cdot 2 \cdot 10^{30} \frac{1}{m^2 s} = 1400 Hz \tag{3.3}$$

During RHIC's second run the BRAHMS experiment had at times rates of this order. Some of the other experiments achieved full design luminosity.

3.2 Experimental layout

The experimental layout of the BRAHMS experiment is shown in figure 3.2.

BRAHMS is an experiment similar to one of the earlier experiments at the AGS. The main purpose of the detector is to measure particles at high rapidities. To achieve this, BRAHMS was designed in three major components, 2

---

[1] The calculation is done using the Glauber model with a Woods-Saxon density distribution, with Au nuclear radius $R = 6.65 \pm 0.3\,fm$, diffuseness $a = 0.54 \pm 0.01\,fm$, and nucleon-nucleon cross section $\sigma_{nn} = 40 \pm 5\,mb$. As has been done in [6, 7].

movable spectrometer arms and a set of global detectors. The first spectrometer covers mid-rapidity while the other covers forward rapidities. They just overlap at 30°, in order to make consistency checks between the measurements made with the two arms. The tracking in the spectrometers is done using tracking chambers. There are series of tracking chambers in each arm, 2 in the mid rapidity and 5 in the forward rapidity arm, separated by dipole magnets. The tracking chambers are either *T*ime *P*rojection *C*hambers[2] (TPC) or *D*rift *C*hambers (DC). This setup provides the particle trajectory and momentum. *T*ime *o*f *F*light (TOF) walls and Čherenkov detectors are placed after (or in the middle of) the tracking, providing the *P*article *ID*entification.

The global detectors in BRAHMS measure the general characteristics of the collision. They provide the triggering of an event, the interaction point position (*vertex*[3]) and the centrality.

The following sections contain a rough description of the different detectors. For a more thoroughly description of the BRAHMS experiment see the nuclear instrumentation paper, [8].

3.2.1 The global detectors

The global detectors are used to select events with certain properties, e.g. collisions (events) within a certain interaction point range or centrality range. The following list is the Global detectors. The pseudorapidities are all calculated from a nominal vertex:

- **ZDC left and right** are the Zero Degree Calorimeters. They are situated $\pm 18\,m$ from nominal vertex. They detect neutral particles (mostly spectator neutrons) that continue in a straight line from the interaction point. All four experiments have these. They are mostly used by the *main control* for beam diagnostics. But they also provide a rough vertex determination from the left-right time difference (see fig 7.1 on page 43), and a minimum bias[4] trigger[5]. It can also nicely measure the centrality.

- **BB left and right** each consists of sets of tubes made of Čherenkov radiating material connected to photo multiplier tubes. They are situated $\pm 2.25\,m$ from nominal vertex. They give the main collision trigger, and provide the start time[6] trigger of an event. The Beam Beam counters are

---

[2] See chapter 6 on page 29 for a more detailed description on TPC technology.

[3] A description of the vertex determination is in section 7.2 on page 42

[4] A minimum bias trigger should not reject any nuclear events, but accept all regardless of the centrality of the collision.

[5] Triggers serve two functions: to initiate readout of the detectors and provide a start time for the TDC (*T*ime to *d*igital *C*onverter) signals. In BRAHMS there are 8 triggers, see table 7.1 on page 43 for a short description.

[6] This also includes when the electronics from all detectors are supposed to be read out.

our main device for determining the vertex, with a precision of $\sim 0.65\,cm$. The energy deposited in the BB tubes is roughly proportional to the number of particles produced in the collision, which is a measure of the collision centrality. In pseudorapidity they cover: $3.0 \leq \eta \leq 4.5$.

- **TMA (Tiles) and SiMA (Silicon)** measure the multiplicity (centrality) of the collisions (MA standing for *M*ultiplicity Array). These two detector are segmented hexagonal barrels around the beam line. The energy deposited in a detector segment is on average proportional to the number of charged particles that passed through it. The total energy deposited in the MA, for a fixed vertex position, is proportional to the total number of particles produced, which is a measure of the collision centrality. Their pseudorapidity coverage is $|\eta| \leq 2.0$ and $|\eta| \leq 2.2$ for TMA and SiMA, respectively.

3.2.2 The forward arm

The *F*orward *S*pectrometer (FS) arm consists of a series of detectors. It covers a very small solid angle: $0.8\,msr$. The first section of the FS is the *F*ront *F*orward *S*pectrometer (FFS). The elements D1, T1, D2, T2, H1 and C1 are mounted on a movable arm, going from 2.3° to 30° in θ. See section 8.1 on page 59 for details of the geometry in BRAHMS. The remaining elements, T3, D3, T4, D4, T5, H2 and RICH, are mounted on a separate platform, the *B*ack *F*orward *S*pectrometer (BFS). It covers the angles $2.3° < \theta < 15°$. It is this part of the BRAHMS Detector system that is unique, because of the ability to measure particles at high rapidities. The FS cover pseudorapidity from 3.9 to 1.3 for the FFS and 1.7 for the BFS. Below is a short description of the magnets and detectors:

- **D1** is a dipole magnet. It enables measuring particles at angles as low as 2.3°. Since it's so close to the beam pipe, it needs to be very narrow. Therefore a *Septum*[7] design was chosen for it. A *Septum* magnet has a very narrow design. This is important since the magnet can be as close as 2.3° from the beam line, which corresponds to $23\,cm$ from the center of the magnet. The *septum* design is not only narrow, but have a sufficiently low outside magnetic field not to disturb the beam. The beam will experience $3\,G$ when the center field is at D1's maximum magnetic field, $12.6\,kG$[8]. Using the vertex position and a track in T1, assuming it is a primary track, the momentum can be determined for that track.

---

[7] The iron in the magnet has a cross section which is "C" shaped. The open side is facing the beam line. This open side is covered by a $0.95\,cm$ thick "septum plate" made of the same iron as the magnet iron.

[8] Usage of full field at 3° has been tried, but has not been successful. So far it has caused to much disturbance of the beam.

- **T1** is the first tracking detector in the Front Forward Spectrometer (FFS). It is a TPC. This TPC is designed to deal with particle densities of up to 0.2 $particles/cm^2$.

- **D2** is the second magnet. It has a conventional design, just like D3-5. This magnet enables us to determine the momentum of the particles that fly through T1, D2 and T2.

- **T2** This TPC is the second tracking detector in the FFS. It is a bit bigger than T1, and the chamber is divided into two sections (see table 6.1 on page 30 and section 6.2 on page 32).

- **H1, also called TOF1,** is the first *T*ime *O*f *F*light hodoscope. It measures the time the particle uses from the vertex. The BB counters provide the start time, through a trigger, and a signal in one of the slats in the TOF provides the stop time for the particle. It consists of 40 plastic scintilator slats with a fast photo multiplier at each end. It is situated $8.6\,m$ from nominal vertex and has a time resolution of $\sim 75ps$[9].

- **C1** is a threshold Čherenkov detector. A Čherenkov detector consists of a transparent material with refractive index >1. When a charged particle flies through the detector with a speed higher than the speed of light in the transparent material, it will cause the medium to be polarized. The excitation energy will reappear as coherent radiation. This radiation is then picked up by *P*hoto *M*ultiplier *T*ubes (PMT). The threshold Čherenkov detector checks whether the particle's velocity is above the threshold value for emitting Čherenkov light. See the book "Particle Physics" [9] p.64-67, for a short description on Čherenkov detectors.

- **T3** is the first of the DCs. This is the first detector on the BFS platform, and it is a tracking detector. It does not manage as high particle densities that we have in e.g. T1, but was considered to be efficient enough this far from the vertex when they were designed. A more detailed description of all the BRAHMS DCs can be found in [8].

- **D3** is the third dipole magnet. D3 has a conventional magnet design. Combining the tracks in T3 and T4 through D3 determines the momentum of the particle.

- **T4** is the second DC. Together with T3 and D3, and/or with D4 and T5 it can measure the high momentum particles emitted at high rapidities.

---

[9] Nominal value. Resolution achieved so far is more like $\sim 80ps$, but is at the moment of writing being improved towards $\sim 75ps$.

- **D4** is yet another dipole magnet. Together with T4, T5 and the RICH it enables momentum determination and particle identification determination from 4 GeV/c to ~25 GeV/c. It has a conventional design.
- **T5** is the third DC.
- **H2 also called TOF2** is the last Time of flight hodoscope, positioned $18.8\,m$ from nominal vertex. It is similar to H1 but with just 32 slats. The time resolution is $\sim 75ps$.
- **RICH** is a Ring Imaging Čherenkov detector. The difference from C1 is that this Ring Imaging Čherenkov detector utilizes that the radiation is emitted in a cone about the particle trajectory. A spherical mirror reflects the Čherenkov light onto a ring in the focal plane which is equipped with PMT's. The particle's velocity can be calculated from the ring radius, see section 7.6 on page 53. It is operated with C_4F_{10} gas as radiator. The resolution of the RICH is $\Delta r/r \approx 2\%$.

3.2.3 The mid rapidity arm

The *M*id *R*apidity *S*pectrometer (MRS) covers a solid angle of $6.5\,msr$, significantly more than the FS. It consists of 3 detectors and one magnet. They are mounted on a platform that is movable from 95° to 30° in θ. That is $-0.1 < \eta < 1.3$ in pseudorapidity (assuming a nominal vertex). The MRS uses the same technology and analysis techniques as the FS, to ensure consistent measurements for the entire rapidity range. This coverage of the midrapidity region allows comparison with the other detectors at RHIC. This way we are also able to check if the experiments are consistent. Here is a short description of the elements:

- **TPM1** is the first detector in the MRS. It is a TPC. This detector can also be used for vertex determination for central collisions. See section 7.3 on page 46.
- **D5** is the second magnet. It enables us to determine the momentum of the particles that fly through T1, D1 and T2. The magnet has a maximum field of $13.5\,kG$.
- **TPM2** This TPC is the second tracking detector.
- **TOFW** is the biggest one of the TOFs. It has 83 plastic scintilator slats, and is placed $4.3\,m$ from nominal vertex.

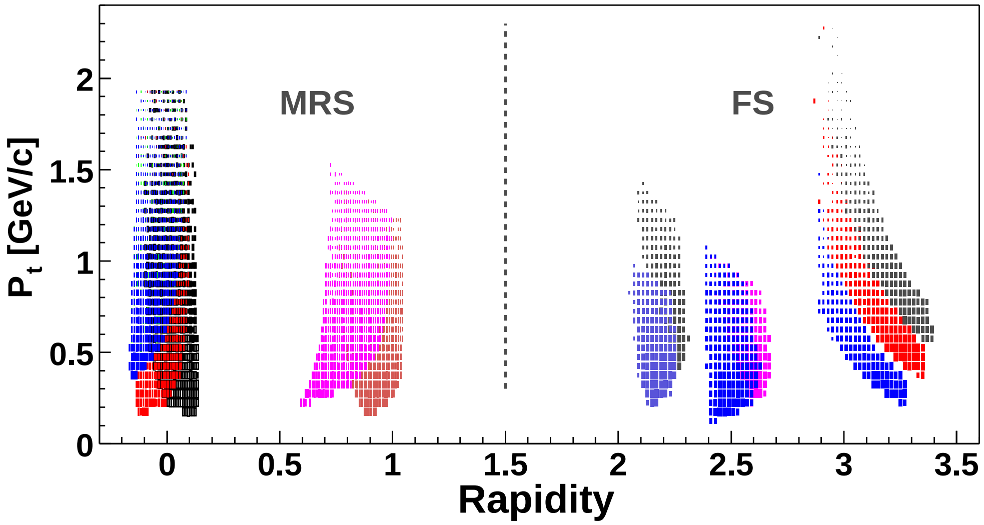

Figure 3.3: Acceptance regions for pions used in the Quark Matter proceedings by Djamel Ouerdane in [3].

3.3 What can BRAHMS measure?

Because of the movable spectrometer arms, the BRAHMS experiment covers a much bigger rapidity window than the other experiments at RHIC. The beam rapidity is 5.37 when RHIC runs Au at full energy, then BRAHMS can go from $y \approx 0$ to $y \approx 4$. BRAHMS' first goal is to measure rapidity density distributions ($\frac{dN}{dy}$) and spectra ($E\frac{d^3N}{dp^3}$) for pions ($\pi^{\pm}$), kaons ($K^{\pm}$), protons (p) and anti-protons ($\bar{p}$). This is measured for a selection of rapidities throughout the available range, by varying the angular and magnetic setting. Figure 3.3 illustrates the large acceptance for pions in the BRAHMS experiment. The figure only shows a selection of settings.

Yields and spectra at different rapidities gives information on the reaction dynamics. In particular, by looking at the net proton rapidity distribution, see figure3.4 and [10], the stopping in the collision can be studied. Thermal and chemical conditions can also be studied extensively in all parts of the reaction zone from the nearly net baryon free midrapidity region to th baryon rich fragmentation zones, $y \gtrsim 3$.

The most unique and important part of the BRAHMS experimental program is doing physics at high rapidities using the forward spectrometer, FS. The high p_T particles can give information from the early stages of the reaction dominated by hard partonic collisions. New physics from this region has just been published by BRAHMS in [11], showing particle ratios above 2 in rapidity. This illustrates what kind of physics BRAHMS is able to measure.

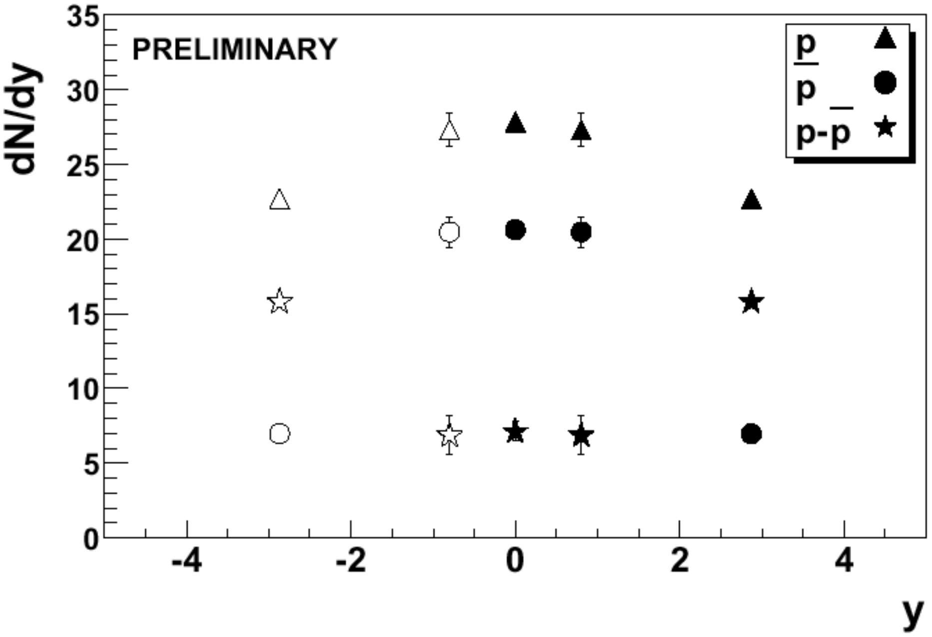

Figure 3.4: Net-proton yields plotted as a function of rapidity. The figure is taken from [10].

Chapter 4

Software in BRAHMS

All the analysis in the BRAHMS experiment is done using software programs. The amount of data that is produced during many months of running is several hundred gigabytes. The only way to deal with this amount of data is by using fast programs on fast computers. The base for the programs made in the BRAHMS collaboration, are three packages. These three packages are called *GEANT*, *ROOT* and *BRAT*. Geant is written in Fortran an the other two are written in the programming language C++.

4.1 The BRAG simulation tool

GEANT 3.21 is part of the CERNLIB package freely available from CERN, [12]. It is a tool used by most of the heavy ion and particle physics community. It simulates the interactions of elementary and composite particles with matter. It is possible to program an experimental setup into GEANT. BRAHMS has done this to match the entire physical setup of the experiment as closely as possible, with respect to geometry and materials on a sufficiently detailed level. This software is now called BRAG. BRAG simulates all the interactions with the surrounding matter, the magnetic fields, decay in flight and the processes in the sensitive volume of particle detectors being hit by a given particle with a given momentum.

The input to GEANT is either a vertex with a momentum vector of a specific particle, or the output from an event generator. Event generators provide details on all produced particles from a collision, simulated according to the model on which the event generator is based. The given particles are then propagated through the description of the experimental setup. The simulated output is stored as hit positions and associated energy deposits in the sensitive parts of the detectors. The rest of the simulation and analysis, up to spectra of identified particles, is part of the BRAT package, e.g. signal transport in the detector, digitization at readout, clustering, tracking and finally particle identification.

To make simulated data as realistic as possible, “slow simulation” (See e.g. [13]) is used to mimic the detectors’ response. This is further described in section 6.3 on page 33.

This output can in turn be fed to the analysis tools, also used on raw data, by experimenters, to produce model dependent predictions of the number of particles we expect to reconstruct in a detector per collision. This enables corrections on raw data which may or may not be model dependent. Single GEANT tracks can, digitized or not, be used to find the geometric acceptance of the detectors and digitized simulated tracks can be used for calculating detector/software efficiency. These are model independent.

This procedure is often our only way of correcting experimental data for background from secondary particles or the effect of nearby dense material like magnets or detector stands. The combination of GEANT and the event generators is therefore a tool both for designing experiments, testing analysis software, understanding the output of detectors during real data taking, correcting for various sorts of background, inefficiencies and other losses.

BRAG (known before in BRAHMS as GBRAHMS) has been in use since the design stage of the BRAHMS experiment [14] and is still our main tool for calculating our acceptance and the important parts of background contamination in our data. It does not describe all the background, e.g. from collisions between the beam and gas which may be present inside the “vacuum” inside the beam pipe. BRAG is used throughout this thesis, but without the information from event generators. Only one particle at a time, with a given production vertex and a given momentum vector is used. This gives an excellent control over what goes through the detectors. BRAHMS needs reconstruction efficiency for single tracks with specific properties. When particle type and momentum vector is known the efficiency can be calculated as a function of particle and event properties, as presented in chapter9. Geant provides a very nice tool for the efficiency analysis (chapter 8 on page 58) in the BRAHMS experiment.

4.2 ROOT

ROOT is developed at CERN and is freely distributed over the world wide web (see [15]). It is a package that is maintained by Rene Brun and Fons Rademakers, but there are many people that have contributed. Root has all the basic features for doing data analysis. It handles everything from writing and reading data objects from files, storing data in accessible ways, displaying data in all all sort of ways and all other basic functionality for an analysis framework.

Root has become the accepted replacement for the older package PAW. PAW was written in FORTRAN, and is still in use in pre-ROOT experiments. This package is therefore still maintained so the older experiments don’t have to rewrite their programs. But all new experiments now use ROOT. Root is also much more than PAW. It has a lot of features that are not really necessary for physical data analysis, e.g. a Graphical User Interface (GUI)[1]. Among other ambitious projects are interacting with LaTeX, for well typeset outputs, parallel processing, interacting with database packages like MySQL[2] [16], drawing Feynman diagrams, allowing threads[3] and other useful features. Even though it has a very huge library of classes, it is very stable software. There is extensive information on the ROOT package on their web pages [15], with all the source code available. There is comprehensive class documentation and information on how to download and install ROOT on almost any platform. The updates on the package is also announced these web pages.

Since ROOT is such a stable "platform", BRAHMS has used it as the foundation for their own specialized package, BRAT. BRAT utilizes all the general features of ROOT and at the same time fulfills the specific needs of the BRAHMS experiment.

4.3 BRAT

*B*rahms *R*econstruction and *A*nalysis *T*oolkit (BRAT) has become a large package (not as huge as ROOT though). It is a package that is still constantly under development. Many people in the collaboration (appendix D on page 159) are involved in the development. This means that from time to time it is not as stable as it should be. But during the last two years it has improved enormously. To be able to run BRAT these days you need more than ROOT. You also need a third package, MySQL, which is freely distributed on the World Wide Web [16]. To obtain a version of BRAT you need to have an account on the BNL network. BRAT can then be be obtained from the *C*oncurrent *V*ersion *S*ystem (CVS) by doing a checkout of the "BRAHMS_CVS/brat" directory. How BRAT is compiled and how it works is also described in "The hitchicker guide to BRAT", available from [17].

4.3.1 The classes

There are, at the time of writing 305 classes in BRAT. These classes cover everything from reading and writing files in BRAHMS specific format, to reconstructing particles in a collision. They are divided into five categories[4]:

---

[1] The BRAHVO and BADTRIP (see chapter 5 on page 25) software both uses the GUI extensively, making the shift procedures much easier. The chance of loosing data during running is also reduced since these applications beeps and blinks when something is wrong.

[2] MySQL has now been introduced in the *B*rahms *R*econstruction and *A*nalysis *T*oolkit (BRAT) package for consistent use of parameters during data analysis (see section 4.3).

[3] Threads are used in the BADTRIP program which is described in section 5 on page 25).

[4] These are thoroughly explained in the BRAT GUIDE which you get from [17]

- **Data classes** contain data structures of various complexity. This is everything from raw data to combinations of spectrometer tracks with *P*article *Id*entification (PID) information.
- **Utility classes** are classes that are useful for doing geometry and mathematics calculations and various other supporting functionality.
- **Managers** ensures consistent use of parameters in the analysis, like run information, calibrations and detector/spectrometer geometry.
- **Modules** do all the actual work. They handle input and output of data classes and analysis of raw and processed data.
- **Packages** doesn't do much themselves. They group related modules together making analysis easier and less error prone.

Last of all but not least there is a special program in BRAT, called *bratmain*. This is a small program utilizing BrMainModule, which is a module container. In essence it is a module pipeline. One can create a script where one just adds modules to BrMainModule. Then you do a call on bratmain and give the script as the first parameter. These are then interpreted by your script. Input and output files, along with various other optional parameters, are set on the script command line. Then BrMainModule sets the added modules to work in a standardized way. *Bratmain* makes writing programs for data analysis more easy, more standardized and portable than before. Hopefully it will enable the experiment to produce results for publications faster.

Outside of BRAT there is also applications that people have written that does more specific things. These are found in *brahms_ app* which is also located in the CVS repository. An example is the classes for acceptance calculations.

The latest addition to the BRAHMS CVS is a directory called *bdst* (*B*rahms *D*ata *S*ummary *T*ree). It contains ROOT tree based classes, see [15], that enables a compact storage of data that has gone through the first steps of the analysis. The last stage of the analysis, producing the physics results, utilizes the easy access of this data.

4.3.2 BrTpcAddSeqModule and BEAT

My contribution to BRAT has been *BrTpcAddSeqModule*. This class adds *TPC sequences*[5] together. The class was needed to enable efficiency calculations using the "embedding" method. Embedding is adding simulated tracks to raw data events on the TPC sequence level.

---

[5] Chapter 6 on page 29 contains a short explanation of TPCs and the output from them.

In addition to *BrTpcAddSeqModule* four new classes was needed. These I called *BrEffGeantModule*, *BrTrackMatcherModule*, *BrEffRecoModule* and *BrEffHistModule*. They are not a part of BRAT and were all compiled into a library, which was then loaded and utilized by a bratmain script called *B*rahms *E*fficiency *A*nalysis *T*ool (BEAT). This software is available from *brahms_ app*. These classes was needed to work on multiple data sets, to handle multiple analysis pipelines, while *bratmain* is only designed to handle one. In the analysis there are three sets of *TPC sequences* for each TPC in each event. The standard BRAT software can not keep these three sets of TPC sequences apart, but the beat library can. BEAT performs full track reconstruction on all the three sets. Then these are compared in the *BrEffHistModule*, and the efficiency is calculated. For a more detailed description on the BEAT software see section 8.4 on page 64.

Beat also includes a graphical user interface for making running of the program as easy as possible (see appendix B on page 152 for explanations of how to run beat with or without the GUI).

Chapter 5

BRAHMS high voltage software

BRAHMS is a complex experiment with 18 different detectors. These detectors are specifically designed for our purpose and are connected to mainframes which deliver the power they need to operate. To be able to control these detectors, and the mainframes they are connected to, software had to be written. The detectors that require a high voltage power supply (mainframes) when in operational mode also need online surveillance. The following detectors and their power supplies are under surveillance: all the TPCs, all the DCs and the Silicon multiplicity array. It is the TPCs and the DCs that mostly require to be monitored. The way these detectors are built may cause them to be reset from time to time. This must be done when they “trip”. These detectors are sensitive to accumulated space charges. When the particle flux is high, which may occur during unstable beam, charges are accumulated in the detectors which may causing them to “trip”. The trip causes the voltage value to drop to near zero.

5.1 BRAHVO

The *BRA*hms *H*igh *VO*ltage (BRAHVO) monitoring and control program was written by Claus Ekman, available in the BRAHMS CVS respository under he *oncs/* directory. See [18] for instructions on how to run BRAHVO. It controls all the high voltage channels in the BRAHMS detector. Since the RHIC is a collider, the beam is dumped and reinjected at irregular time intervals[1]. This means that the high voltage may need to be taken down and up again many times during a shift. BRAHVO's *G*raphical *U*ser *I*nterface (GUI) is excellent for making this task user friendly.

When I encountered it the first time, BRAHVO had some unsatisfying features. Something like 10-20 buttons had to pressed to turn the voltages down.

---

[1] Reinjection of the beam has so far had its ups and downs. The main control still needs more experience with the accelerator to make it work optimally.

A bit of waiting between each button was also necessary. So what I did was to make new buttons and a new class that did all of this automatically, illustrated in figure 5.1 on the next page.

The bottom window in figure 5.1 is the GUI that pops up when the "Tpc & Dc On" or "Tpc & Dc Off" button is pressed. The window is an instance of a class I called *TpcDcPopUpWidget*. By inserting the voltage values for the anodes in the white text fields, you can change as many detectors you want to in one go. The application also "remembers" what you typed last time it was used, to avoid typing errors. The "Which detectors are Off" button checks all the detector and puts a check mark on those who are off. The application uses all the features that were already implemented in BRAHVO, e.g. reading status of mainframes, reading voltages from the detectors, turning them on/off and changing the voltage.

5.2 BADTRIP

There was also another feature that was missing in BRAHVO. It was not able to check the high voltage by itself on a regular basis. Sometimes the detectors trip[2], and the only way to see if it is tripped is to read off the voltage value. This had to be done manually before the *B*rahms *A*ctive *D*etect *TRIP* (BADTRIP) program was introduced. BADTRIP must be started by the person on shift when there is beam, which is broadcasted by the *main control* to a TV in the BRAHMS counting house, and checks that none of the high voltages has tripped. When the beam is lost/dumped the person on shift must stop BADTRIP. If some high voltage trips it starts to beep, alerting the person on shift. A message will also pop up in the message area telling the person on shift what has happened. This way the high voltage channel can be reset, and the person on shift can check that everything goes back to normal, or if any extraordinary steps must be taken. Loss of beam time is avoided this way. The program is built upon the BRAHVO framework. Two new classes was also introduced to make the program work, "TripWidget" and "TripSettingWidget". BADTRIP also features a small application for choosing which detectors to monitor, and set the voltage value that specifies a trip. This is done in the class "TripSettingWidget". Figure 5.2 on page 28 contains a picture of th BADTRIP GUI. The buttons are mostly self explanatory. The biggest one on the right shows the state of BADTRIP, i.e. whether it is running, stopped or has detected a trip.

When the program is started it starts a thread in the computer. A thread is used in programs that does not need much CPU from the computer. Most of

---

[2] When the high voltage on a detector trips, the voltage suddenly drops to near zero. Both the detector and the mainframe are checked. BADTRIP reports the status of the detector and the mainframe. This actually happens from time to time.

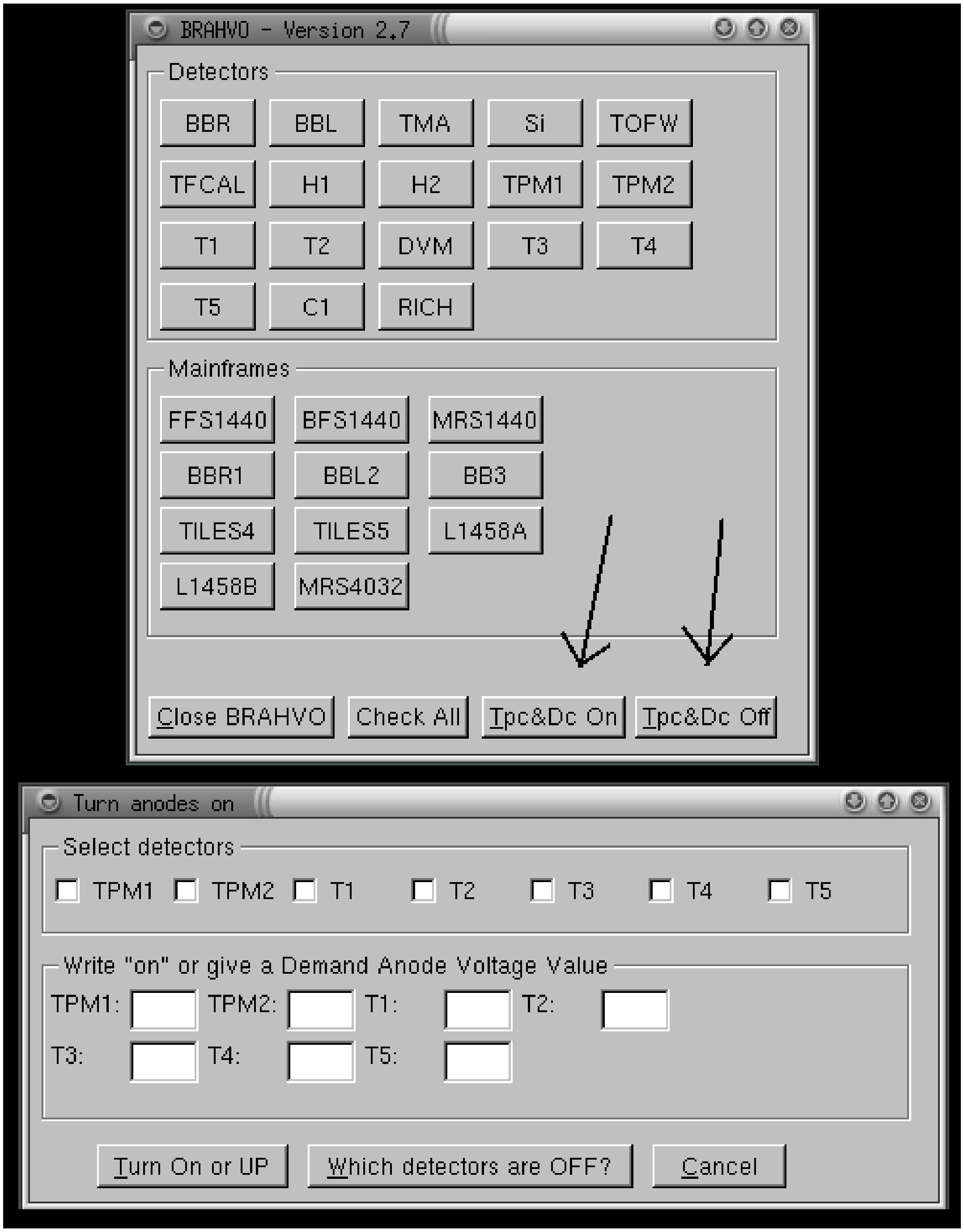

Figure 5.1: This is an illustration of the BRAHVO GUI. The lower part of the figure contains the window that pops up when one of the buttons, pointed to by the arrows, are pressed.

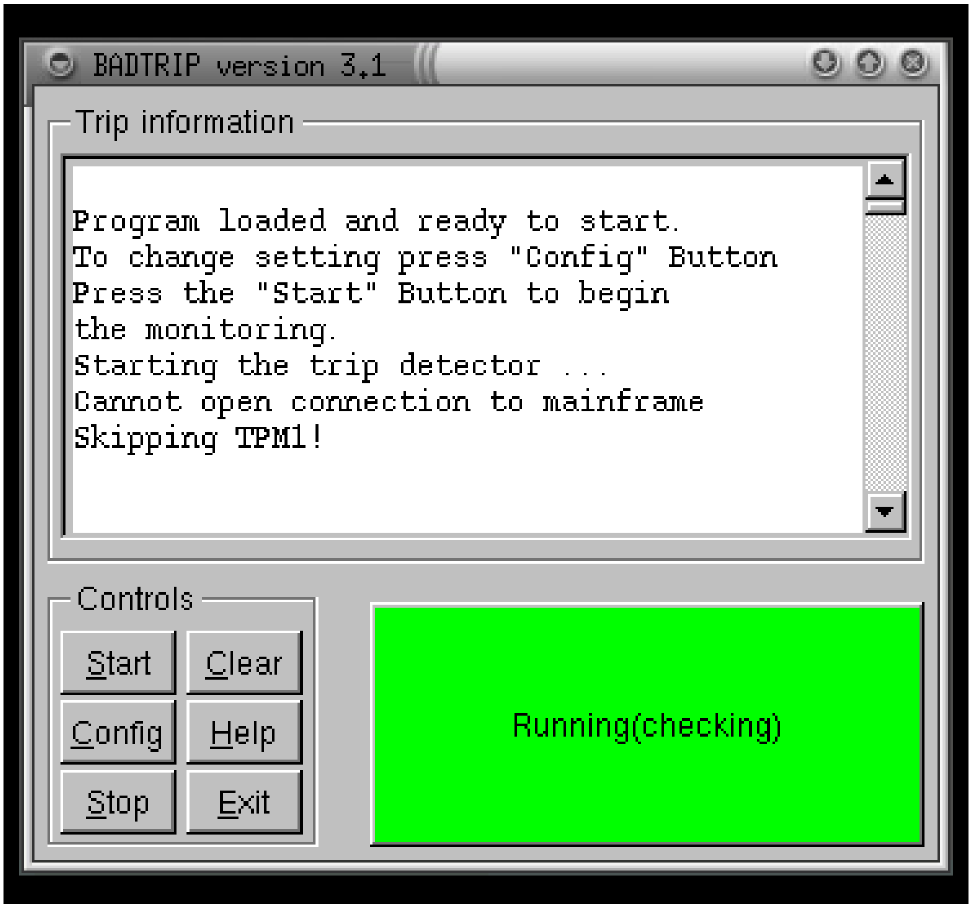

```
Program loaded and ready to start.
To change setting press "Config" Button
Press the "Start" Button to begin
the monitoring.
Starting the trip detector ...
Cannot open connection to mainframe
Skipping TPM1!
```

Figure 5.2: This is an illustration of the BADTRIP GUI.

the time this thread just sleeps i.e. does nothing and requires no CPU. If the program had not been implemented as a thread it would have eaten up all the computers CPU as long as it was running, since it would then be an eternal loop. At even time intervals it checks the voltage values of all the detectors you have chosen to be monitored. If everything is OK, all values are above some specified value, the thread goes back to sleep. This way other programs can run on the computer. That would have been impossible without threads. The threads in the program are made by the ROOT class TThread. This is not a straight forward class to use, and the best way to figure out how it works is to consult [19]. The actual control of the thread is through the BADTRIP GUI. A thread is created every time the monitoring is started, and deleted every time it is stopped. All the software is available from the the BRAHMS CVS repository, under *oncs/brahvo*.

Chapter 6

Time Projection Chambers

Most of the work involved in the analysis presented in this thesis is centered around the four TPCs in the BRAHMS experiment. The basic ideas behind all TPC detectors is presented in the following sections. None of the four TPCs in the BRAHMS experiment are equal. Table 6.1 on the next page contains their specifications. In order to understand a TPC as well as possible it is also necessary to be able to simulate processes inside it and output from it. This chapter also contains explanations on how this is done. Proper simulations involves a huge amount of work to understand he response of the TPC, which has been done on the BRAHMS TPCs by Jens Ivar Jørdre, who checked the TPC response using cosmic rays, in [20] and by Trine S. Tveter, who compared experimental and simulated Au-Au data.

6.1 Basic TPC technology

The time projection chamber is a detector designed to give a high position resolution and to give accurate three dimensional trajectories of particles flying through them. It is also possible to measure ionization energy loss per unit path length, dE/dx, which is a method for *P*article *ID*entification (PID). Bethe-Bloch's energy loss formula looks like this:

$$-\frac{dE}{dx} = 4\pi N_A r_e^2 m_e c^2 z^2 \frac{Z}{A}\left(\frac{1}{2}\ln\frac{2m_e c^2\beta^2\gamma^2 T_{max}}{I^2} - \beta^2 - \frac{\delta}{2}\right) \tag{6.1}$$

The function is from was used/derived by Bethe, Bloch and others, has gotten the name "Bethe-Bloch's energy loss formula". The equation assumes that the particle's mass, m, is much larger than the electron mass, m_e, $m >> m_e$. This formula should be valid for muons and heavier particles. N_A is Avogadro's number, r_e is the classical electron radius, m_e is the electron mass, z is the passing particle's charge (dimensionless number, $\pm 1\ \pm 2 \ldots$), Z is the

Name	Width (cm)	Height (cm)	Depth (cm)	Padrows	Pads/row
TPM1	37.44	20.00	36.60	12	96
TPM2	67.68	19.80	50.00	20	144
T1	33.60	19.80	56.00	14	96
T2	39.60	19.80	75.50	$2 \cdot 8$	112

Table 6.1: The main geometric parameters of the BRAHMS TPCs. The given size is the inner, active volume.

atomic number of the medium, A is the atomic mass of the medium in g/mol, T_{max} is the maximum kinetic energy which can be imparted to a free electron in a single collision, I is the mean ionization energy of the medium and δ is the density effect correction to the ionization energy.

They now represent the key detector in many experiments, like STAR (standing for "Solenoidal Tracker At RHIC") and ALICE (standing for "A Large Ion Collider Experiment" at CERN LHC). These detectors are huge TPC barrels, covering 2π azimuthally around the collision point (low η).

The basic TPC design begins with a box filled with a gas that is easily ionized by charged particles passing through, but that is chemically inert. Mixtures of Ar and CO_2 or Ne and CH_4 are common choices. Inside the box is a homogeneous electric field, so that when electrons are liberated from the gas by the passing particles, they drift in this field to a specified side of the box that is covered by readout pads and strung with anode wires (the *padplane*). See illustration in figure 6.1 on the following page. The liberated electrons all drift to the anode wires, inducing a charged signal. A mirror charge is also induced on the pad plane, distributed over the nearest pads. This is illustrated in figure 6.2 on page 32

TPCs are operated at electric fields such that the field gradients close to the anode wires accelerate the electrons enough to trigger electromagnetic avalanches. This amplifies the original electron cloud in a way proportional to the originally liberated charge, allowing for a precise measurement of the energy loss dE/dx of the passing particle.

The anode and field wires in figure 6.1 on the following page maintain the electric field. In many applications there is a magnetic field parallel to the electric field. This makes all the trajectories in the TPC curved. From the curvature and the strength of the field one can calculate the momentum of the particle. The magnetic field also keeps the liberated atomic electrons with low momentum spiraling around these lines as they drift towards the pad plane. The electrons are then hindered from drifting in the transverse directions. Long drift distances can then be used without loss of position resolution. This kind of B-fields are used in the large TPCs in the STAR and ALICE detectors. Since the TPCs in BRAHMS are very small, such an external magnetic field is not

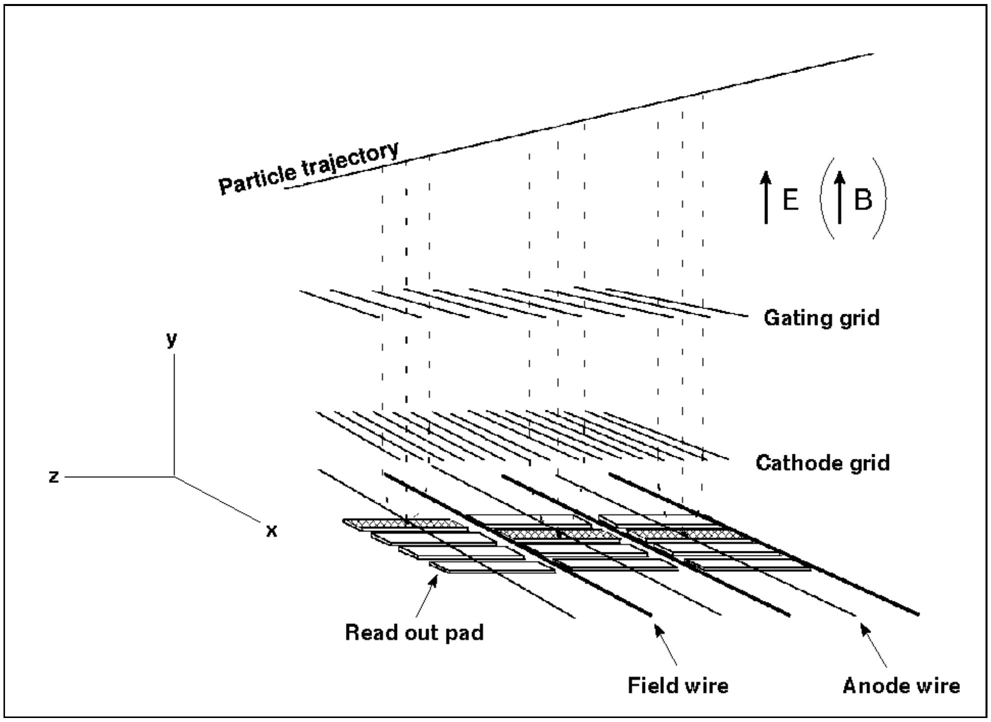

Figure 6.1: Schematic illustration of a TPC. Electrons are liberated when charged particles go through the gas. They drift in an electric field towards a plane of readout pads. (Figure borrowed from [21])

used. No magnetic field results in linear tracks in the TPC.

The speed of the electrons in the gas parallel to the electric field, is called *drift velocity*. It is usually in the order of $cm/\mu s$. Knowing the drift velocity and the drift time, one can calculate how far from the pad plane the electrons were liberated (the Y coordinate[1]).

The pads in the TPC provides all the data. They are read out repeatedly at specified times (time bins) after a trigger has been satisfied in a collision. The induced charge on a pad is converted to an ADC (*A*nalog to *D*igital *C*onverter) value for a specific time bin. A sequence of ADC values from a pad, i.e. consecutive time bins, is called a *TPC sequence*. These sequences are then processed in an analysis to obtain clusters. Neighboring pads with sequences of ADC values that overlap in time are combined into groups of TPC sequences. Electron clouds from primary ionization over one padrow produces such clusters. The weighted average of the cluster is then found to produce the hit coordinates. The drift time, needed to find the y coordinate, is found from the average time bin of the cluster. The two last coordinates (z and x) are given from the average position of the charge distribution in the pad rows, x from the the average

---

[1] Section 8.1 on page 59 specifies the coordinate systems in BRAHMS.

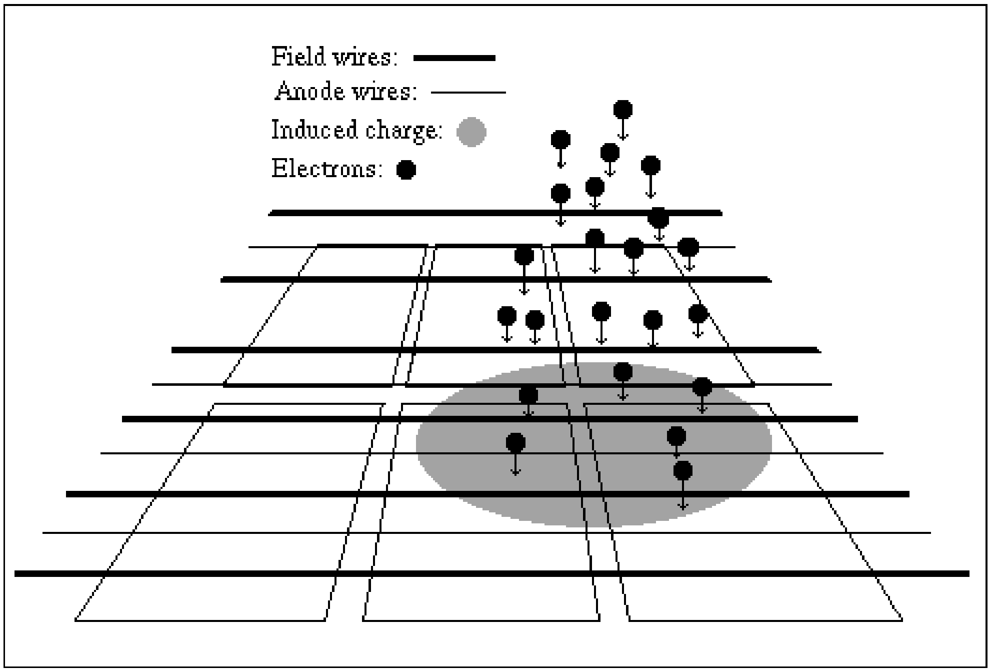

Figure 6.2: The electrons drift towards the wires and an induced charge is deposited on the closest pads, gray ring.

position in the pad direction and z from the padrow position.

6.2 The BRAHMS TPC design

The BRAHMS detector includes four TPCs, named T1, T2, TPM1 and TPM2 (see figure 3.2 on page 13 for an illustration of their sizes and positions). They are all of a basic box design with a single pad plane positioned in the ceiling. The TPC boxes are made of plexiglas, and the entrance and exit windows are $25\,\mu m$ mylar foils. They are all positioned outside any external magnetic fields, so they will measure straight tracks.

The sizes of the BRAHMS TPCs and their number of pad rows and pads per row are given in table 6.1 on page 30. They all flow a 90/10 % mixture of Ar/CO_2, and have drift distances of roughly $20cm$. The drift voltage is $229\,V/cm$. The anode wire sitting at $-5000\,V$, according to [8]. The drift velocity is $\sim 1.5cm/\mu s$ for all the TPCs, but it is a bit varying from run to run from still unknown reasons. A lot of work has been put into this, and a temporary solution has been made. This is a database with time dependent average drift velocities for all our data. The drift velocities are also not quite homogeneous over the TPC volume. This results in slight distortions of measured tracks. It is possible to correct for this distortion row by row and maybe even pad by pad, but more work on this problem will then be needed.

All of the TPCs have been designed to give a two track resolution[2] of less than $1\,cm$, to cope with track densities up to $0.2\,particles/cm^2$. The pads in all TPCs are $3\,mm$ wide, and just below $3\,cm$ long except for TPM2 where they are $2.4\,cm$. This is because that TPC will see the highest crossing angle of tracks and thus needs a better resolution also in direction away from the vertex.

6.3 Simulating the TPC response

There are two steps that need to be done when hits in a TPC is to be digitized properly. First a good simulation of the processes in the TPC must be established. This involves the transport of the liberated electrons in the TPC volume and the processes occurring at the readout plane. Then the time dependent charge distribution on the readout plane must be converted to the raw data format. A number of parameters associated with these two steps must be determined to make the simulated hits look like real hits.

6.3.1 The digitization

The efficiency analysis presented in chapter 9 is calculated by embedding simulated tracks into real collision data (events). But before this can be done the energy deposits dE/dx and position in the detector volume, which is computed by BRAG, must be translated to ADC values. First the ionization of the gas in the TPC, caused by the particle flying through it, must be estimated, and the transport of these liberated electrons in the TPC gas must be described. The electrons, reaching the anode wire, must then be translated into a response of the readout plane. This process is called the *digitization*. To digitize the hit properly a number of functions must be combined. This kind of digitization is called “slow simulation”.

The small charge could of liberated electrons from a short track segment, from a passing particle, starts to drift towards the padplane. The original charge cloud spreads out due to diffusion. This is a continuous process as the cloud traverses the drift length. The diffusion is due to collisions with other electrons. The knockout/reabsorption of the electrons is approximate balanced in the drift volume. So the number of electrons in the cloud stays approximately constant throughout the drift distance. The amplification of the electron cloud happens close to the anode wires, a chain reaction of knockouts that increases the number of electrons in the cloud. Once electrons hit an anode wire, a mirror charge is induced on the pads below it. The diffusion of the electron cloud is a continuous process. D_T is the diffusion velocity in the transverse direction, D_L is the diffusion velocity in the longitudinal direction and y_0 is

---

[2] See Chapter 10 on page 130 for a further discussion of two track resolution.

the distance from the position where the first liberated electron to the readout plane. The smearing of the charge cloud over one padrow, in the transverse and longitudinal direction, due to diffusion and additional effective smearing due to the track angle, can then be written as:

$$\sigma_T'^2 = D_T^2 \cdot y_0 + \frac{l^2 \cdot \tan^2 \beta}{12} \tag{6.2}$$

$$\sigma_L'^2 = D_L^2 \cdot y_0 + \frac{l^2 \cdot \tan^2 \lambda}{12} \tag{6.3}$$

where $\sigma_T'2$ and $\sigma_L'2$ is the width of the charge cloud in transverse and longitudinal direction when the charge cloud reaches th padplane, respectively. l is the pad length, β is the angle between the track projection in the pad plane and the pad direction and λ is the angle between the track and the pad plane.

The Pad Response Function (PRF) describes how a hit from a space point (x_0, y_0, z_0) is distributed over the pads in the readout plane of the TPC. The PRF function, $f_{PRF}(x_p, x_0)$, describes the distribution of the mirror charge on the padplane produced by a point charge on the anode wire. The mirror charge is a gaussian distribution over the nearest pads, equation (6.4). To get the total response to a charge cloud, an integral must be taken over all the individual electrons in the charge cloud. Translated into the BRAHMS coordinate system, [13] estimated the total to response of the charge cloud to look like this:

$$f_{PRF}(x_p, x_0) = \frac{e^{-\frac{(x_0 - x_p)}{2\sigma_{PRF}^2}}}{\sqrt{2\pi} \cdot \sigma_{PRF}} \tag{6.4}$$

$$\sigma_T^2 = \sigma_{PRF}^2 + \sigma_T'^2 \tag{6.5}$$

$$F(x_p, x_0) = \int_{-\infty}^{\infty} \frac{e^{-\frac{(x' - x_p)^2}{2\sigma_{PRF}^2}}}{\sqrt{2\pi} \cdot \sigma_{PRF}} \frac{e^{-\frac{(x_0 - x')^2}{2\sigma_T'^2}}}{\sqrt{2\pi} \cdot \sigma_T'} \, dx' = \frac{e^{-\frac{(x_0 - x_p)^2}{2(\sigma_{PRF}^2 + \sigma_T'^2(y_0))}}}{\sqrt{2\pi(\sigma_{PRF}^2 + \sigma_T'^2)}} \tag{6.6}$$

where σ_{PRF}, the pad response function constant, is the width of the charge distribution on the pad if there is a point charge on the anode wire. The subscript p's indicate the pad. σ_T is the effective width of the cluster in the transverse direction. This function determines the charge distributed over adjacent pads in a pad row, that is in the x (transverse) direction.

The remaining direction to shape the signal is in the drift (time) direction. The response to a δ function in time, arriving at time t_0, is called the shaper response function, equivalent to a drifting point charge:

$$g(t, t_0, \tau) = \phi(t, t_0) \cdot \left(\frac{t - t_0}{\tau} \right)^2 e^{-\frac{t - t_0}{\tau}} \tag{6.7}$$

where the τ is the characteristic time from the readout electronics and $\phi(t)$ is a step function. Setting $t' = t$ provides a lower limit for the step function. Folding this function with the shape of the charge cloud after the longitudinal diffusion yields:

$$T(t, t_y) = \int_{-\infty}^{\infty} g(t - t', \tau) \cdot \frac{e^{-\frac{(t'-t_y)^2}{2{\sigma'_L}^2}}}{\sqrt{2\pi}{\sigma'_L}^2} dt' \tag{6.8}$$

where t' is the arrival time of the charge cloud element to the readout plane, $t_y \equiv \frac{y_0}{v_d}$, and v_d is the drift velocity of the electrons in the gas. The resulting shape of the cluster in the time direction is a non-gaussian shape. The width, σ_L, of the cluster in the time direction, can be written as:

$$\sigma_L^2 = \sigma_0^2 + {\sigma'_L}^2 \tag{6.9}$$

where σ_0 is approximately proportional to τ.

A simple absorption function, which try to mimic that dE/dx falls with increasing diffusion length, due to electron absorption in the gas, is also used:

$$n_e = n_0 e^{-k \cdot y_0} \tag{6.10}$$

where n_e is the number of electrons. Noise is also usually added to the hit through the shaper function. The noise is usually frequency independent. BRAHMS uses a random, gaussian distributed noise. The default width is 2 ADC unit.

Combining all these functions we get the signal on a pad, from a primary ionization at (x_0, y_0, z_0):

$$S(x_p, z_p, t) = ADCgain \cdot n_e \cdot F(x_p, x_0) \cdot T(t, t_y) + Noise \tag{6.11}$$

The $ADCgain$ is a factor related to the amplification of the charge cloud at the anode wire. $S(x_p, z_p, t)$ is then the ADC value on the pad, at position x_p, at timebin t and z_p is the position of the row.

The contribution to the residuals, i.e. how far from the track line the centroid of the hit is, from multiple scattering is taken care of by GEANT. Statistical fluctuations in the charge cloud, which also contribute to the residuals, is taken care of by adding random gaussian distributed numbers to x_0 and t_y. All these features have been implemented into the BRAT class *BrDigitizeTPC*. The widths, δ_T and δ_L, of the gaussian distribution of the transverse and longitudinal residuals are described by:

$$\delta_T^2 = \delta_{T,0}^2 + \frac{D_T^2 \cdot s_{drift}}{l \cdot N_{tot}} + \frac{l^2 \cdot \tan^2 \beta}{12 \cdot N_{eff,pad}} \tag{6.12}$$

$$\delta_L^2 = \delta_{L,0}^2 + \frac{D_L^2 \cdot s_{drift}}{l \cdot N_{tot}} + \frac{l^2 \cdot \tan^2 \lambda}{12 \cdot N_{eff,pad}} \tag{6.13}$$

where N_{tot} is the number of primary electrons collected over the padrow ($N_{tot} = n_e$, and $N_{eff,pad}$ is the effective average number of primary electrons collected per pad in the cluster.

To make the digitization work properly the following parameters must be set: σ_{PRF}, D_T, τ, D_L, k, n_0 (or N_{tot}, since they are uniquely related to each other), $N_{eff,pad}$ and $ADCgain$. Since $N_{eff,pad} \propto N_{tot}$, only $N_{eff,pad}/N_{tot}$ has to be determined. In the calculations in chapter 9 these parameters were set as shown in appendix A on page 150.

6.3.2 Extracting the digitization constants

Approximately realistic values of the digitization parameters for simulated BRAG TPC hits have been determined by digitizing central Hijing Au-Au events data, with a realistic particle mixture and energy distribution, and comparing histograms of appropriate quantities for simulated and real data.

A selection of the compared quantities are shown in Figure 6.3 — 6.8, where the experimental data are depicted in gray (red), the simulated ones in in black (blue).

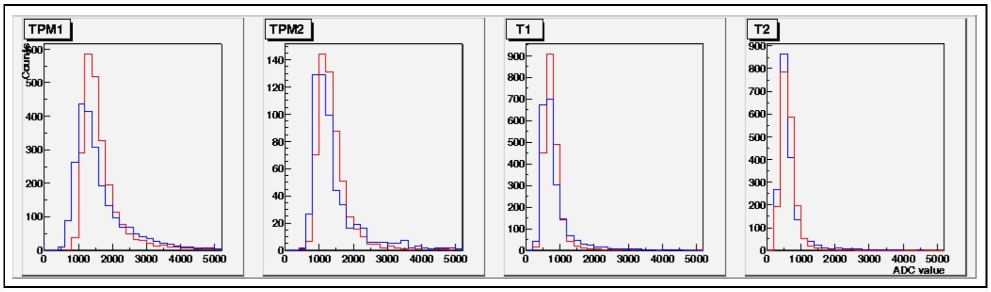

Figure 6.3: Distribution of ADC sum per cluster averaged over each track. A truncated average is used (70% of the clusters with the lowest ADC sums). Used to tune the $ADCgain$.

For TPM1, a vertex cut was imposed to exclude secondary tracks, in particular δ-electrons with low charge and high average residual, which are not well described by BRAG and which perturb the distributions for hadrons.

In order to extract a correct reconstruction efficiency for simulated tracks embedded in real events, it is important that the conversion factor between deposited energy and ADC value is the same for simulated and real data. A too low conversion factor will give weak embedded tracks drowning in the background at high occupancy, while a too high factor will produce prominent clusters resulting in a too high reconstruction efficiency. The important digitization parameters, which must be tuned in combination, in this connection are:

- **ADC gain**, which is dependent on e.g. the anode voltage, that controls the cascade multiplication at the anode wires. May have to be tuned run by run in some cases. This has not been further investigated here.
- **Electrons liberated per unit of deposited energy**, which is a property of the gas and not likely to vary much under normal circumstances.

The ADC gain has been tuned by comparing distributions of cluster integrated ADC values (figure 6.3 and 6.4) averaged over each track. For each track, the 30 % of clusters with highest ADC sum have been excluded from the averaging to reduce the Landau tail and get a more well-defined distribution. The cluster ADC sum is proportional to path length per row, and average ADC sums for tracks with different slopes have been normalized to the same path length.

The variation in ADC sum as a function of the track y position, which includes the effect of electron absorption, given in equation (6.10), is shown in figure 6.4.

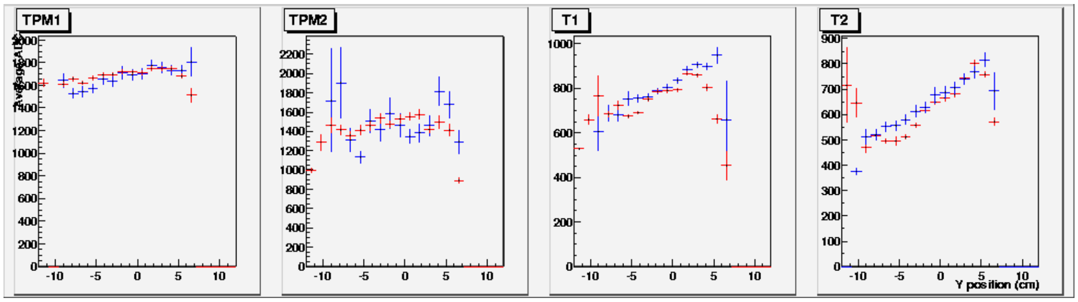

Figure 6.4: ADC sum per cluster as a function of track y_0 position. y_0 is found from the track's intersection with the TPC midplane, so y_0=<y_0>. It is a truncated average over over each track. Used to tune the absorption coefficient k, and the $ADCgain$.

Cluster shapes and widths are also important for the occupancy dependency of the tracking efficiency, in particular efficiency loss due to overlapping, i.e. non-resolvable clusters from closely spaced tracks. Important parameters are:

- **The width** σ_{PRF} of the pad response function.

- **The width** τ of the time shaper response function.
- **Transverse diffusion velocity** D_T.
- **Longitudinal diffusion velocity** D_L.

Instead of a Gaussian, the shaper response function is given by equation (6.7), where the parameter actually tuned is a factor c scaling τ, $\tau = c \cdot t_{shaping}$, where $t_{shaping}$ is a constant shaping time equal to 180 ns.

Cluster widths σ_L, equation (6.9), and σ_T, equation (6.5), in the pad and time direction are shown in figure 6.5 and 6.6, respectively. Oscillations in σ_L and σ_T as function of y_0 are seen for the FFS TPCs. It is not yet well understood, but the average behavior is well reproduced by the simulation.

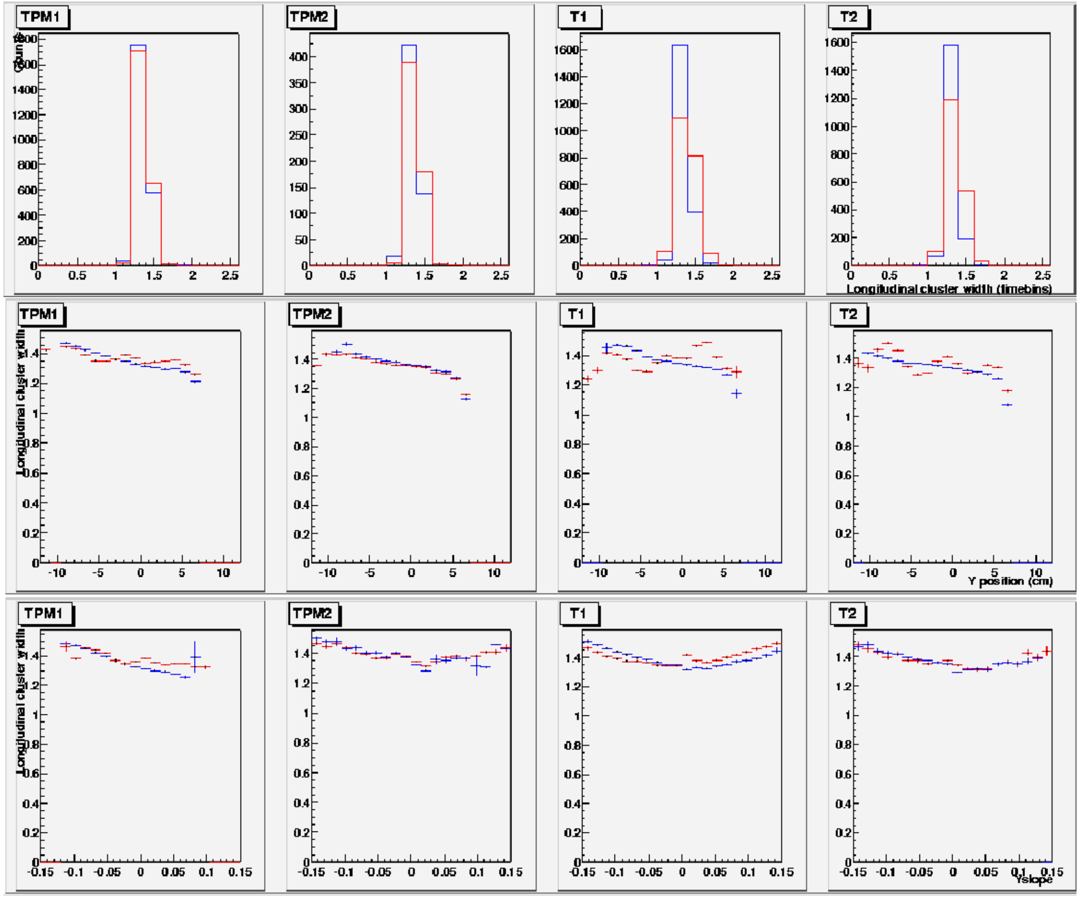

Figure 6.5: Distributions of longitudinal cluster widths per hit, σ_L, in timebin units, and of track average $<\sigma_L>$ as function of y_0 position and the slope in the y direction, $\tan\lambda$. This figure is used for tuning of the τ and D_L in equation (6.9).

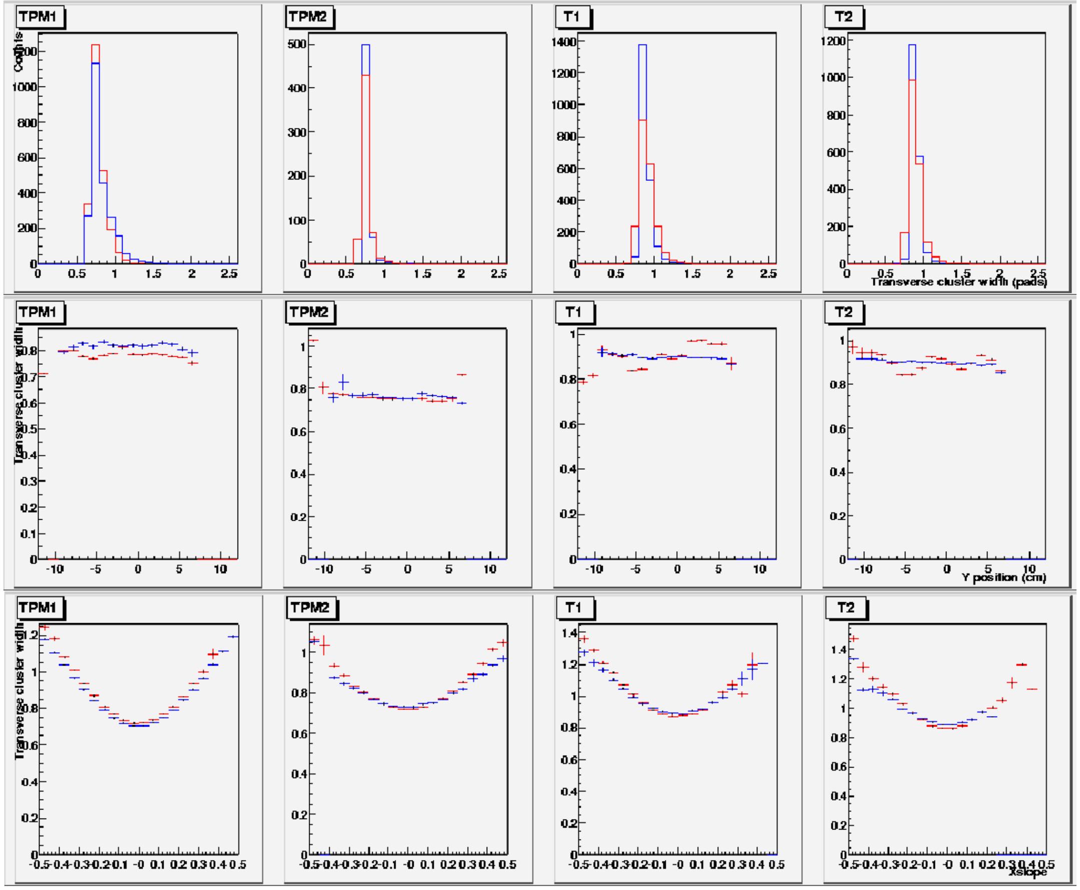

Figure 6.6: Distributions of transverse cluster widths, σ_T, in number pad units, and of $<\sigma_T>$ as function of y_0 and the slope in the x direction, $\tan\beta$. This figure is used for tuning of the σ_{PRF} and D_T in equation (6.5).

The residuals, distances between hits and fitted tracks, in transverse direction, equation (6.12), and longitudinal directions, equation (6.13), are shown in figure 6.8 and 6.7, respectively.

Besides multiple scattering, statistical fluctuations due to a finite number of electrons in the shower are a major source of deviations from a straight line. In the digitization this statistical effect is simulated by shifting the hits in x and y with two random numbers drawn from Gaussian distributions with widths equal to δ_T and δ_L, respectively.

The value of $N_{tot}/N_{eff,pad}$ have been empirically found to be of the order 5 - 10, from figure 6.7 and 6.8.

The constants $\delta_{T,0}$, $\delta_{L,0}$ are not explicitly included in the digitization algorithm. A major contribution to these quantities, multiple scattering of the ionizing particle, is automatically taken care of by BRAG. The δ_T distribu-

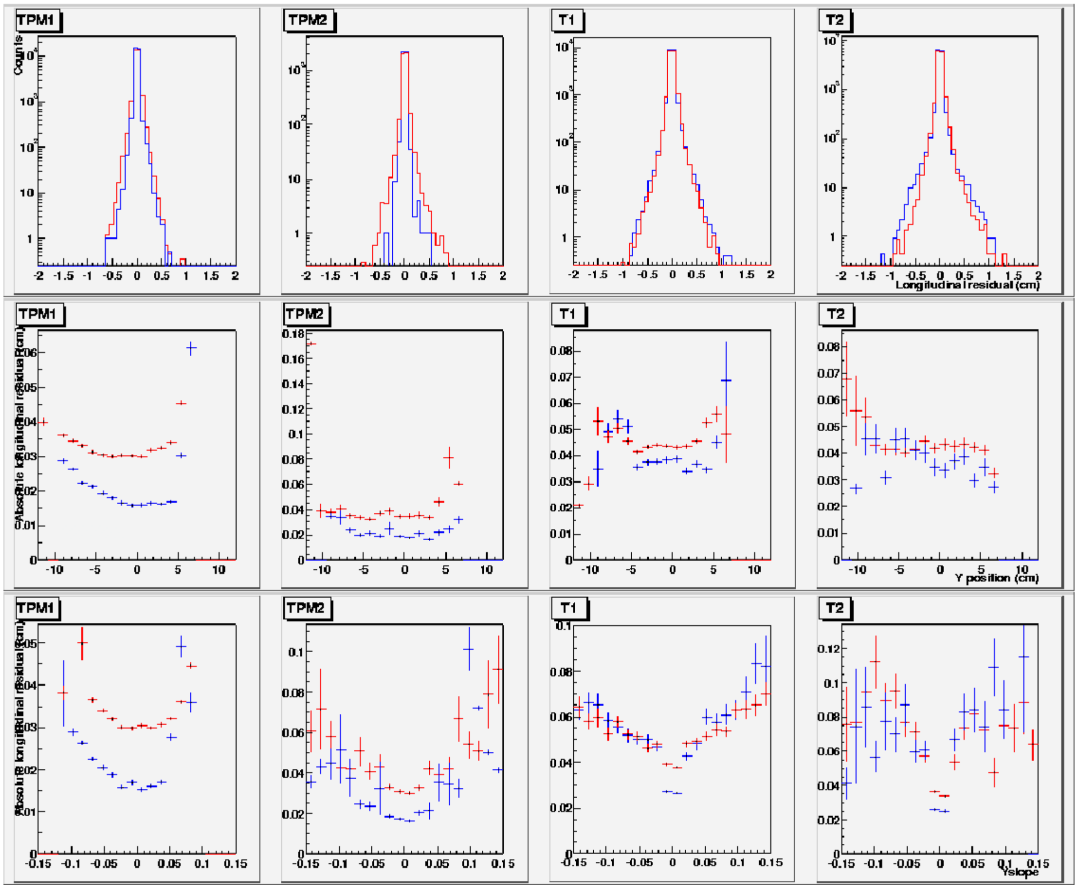

Figure 6.7: Distributions of longitudinal residuals, δ_L in timebin units, and of $<\delta_L>$ as function of y_0 and slope in y direction, $\tan\lambda$. This figure is used for tuning of (D_L), N_{eff}, $\frac{N_{tot}}{N_{eff,pad}}$ and noise in equation (6.13).

tion and dependences are reasonably well reproduced by the digitization. On the other hand, it turns out to be difficult to reproduce the experimental δ_L values, which are systematically larger than the simulated ones, especially for TPM1 and TPM2 in the MRS. Inhomogeneities in drift velocities within the TPC are most likely to be responsible for the increased longitudinal residuals. An attempt has been made to correct for these row by row, using a first-order polynomial:

$$y_{corr} = y_{raw} + (\Delta y_i + a_{y,i} \cdot y_{raw}) \tag{6.14}$$

where Δy_i and ay_i are different for each padrow. But even after this correction the experimental δ_L overshoot the simulated ones, maybe due to non-linear effects in drift velocity. Variations are also known to be present across padrows.

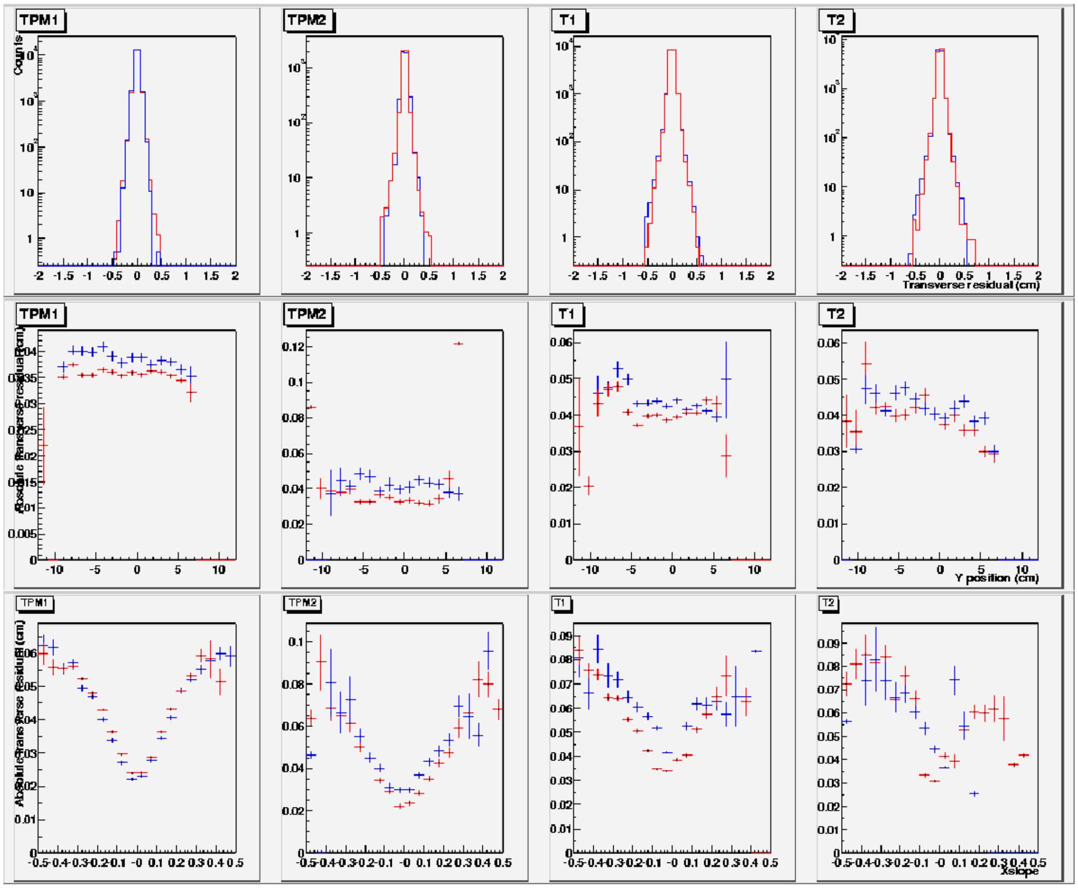

Figure 6.8: Distributions of transverse residuals, δ_T in number of pads units, and of $<\delta_T>$ as function of y_0 and $\tan\beta$. This figure is used for tuning of (D_T), N_{eff}, $\frac{N_{tot}}{N_{eff,pad}}$ and noise in equation (6.12).

This problem is believed to be of minor importance to the efficiency estimates, and further corrections have not been attempted.

The tuning of the parameters were done by hand, using a complex try-and-fail procedure. There is undoubtedly more than one set of "adequate parameters" which reproduce the properties of the experimental data equally well, since each measured quantity depends on several parameters simultaneously. Several forms of distortion is not taken into account. Nevertheless the found parameter values describe the cluster shapes, residuals and ADC sums well enough to give a realistic estimate of the tracking efficiency. All the parameters are given in appendix A on page 150.

Chapter 7

Event Reconstruction

The huge amount of digital data that is recorded when the BRAHMS experiment is running, has to be processed by the software in BRAT to extract physics results. The first step in the reconstruction chain is to look at the trigger that initiated the detector readout. The different triggers trigger on different global event characteristics. Next the vertex position must be found. Then the centrality is determined, and finally all the particles that flew through the detectors are reconstructed and identified.

7.1 The triggers

The triggers provide a way of determining if there was a collision. If any of them are satisfied all the electronics in the experiment is read out, and the data stored in an event. All events are characterized by the trigger that started the event. In BRAHMS there are 8 different triggers that may have started the event. The triggers are described in table 7.1 on the next page. Trigger 1 through 6 are the physics triggers. The BBs triggers bias towards more central events, since they detect produced particles from the fireball, while the ZDCs is a minimum bias trigger that detects the spectators in a collision.

7.2 The Vertex

When one performs high energy experiments it is important to find out where the collision occurs. In a stationary target experiment the interaction point (vertex) is restricted to be inside the target, but when it comes to colliders like RHIC it becomes more difficult. The beams in the RHIC collider consist of bunches of particles. To get a collision in the interaction regions, the beams must be synchronized so two bunches pass an IR at the same time. Since the bunches are pretty long, the vertex will not stay at the same position, it will fluctuate back and forth along the beam line over a range of $\pm 1\,m$. The first thing that is important to the experiment is therefore to determine the vertex. In the BRAHMS experiment there are three ways to do this: timing signals from the *B*eam *B*eam counters (BB) and/or the *Z*ero *D*egree *C*alorimeters (ZDC) and clusters or tracks from TPM1. The last method requires that the clustering and tracking is done first.

The two first possibilities, BBCs and ZDCs, work in the same way, see figure 7.1. The timing signals from each side of the interaction point (e.g. at times T_L from BBL and T_R from BBR) are compared. The vertex position is determined as follows when the timing signals have been calibrated:

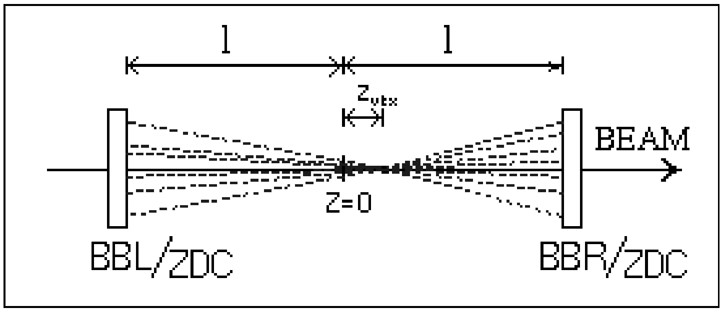

Figure 7.1: Signals going from vertex to the BB counters (or ZDCs). The vertex is determined from the time difference in the signals.

Trigger	Description
1	At least two *P*hoto *M*ultiplier (PM) tubes in each BB counter firing within a 4 ns time gate, which corresponds to a 2.4 meter Z vertex window.
2	Reserved for TPC testing.
3	Reserved for TPC testing.
4	Both ZDCs firing within 14 ns time gate, which corresponds to a 8.5 meter Z vertex window.
5	At least three big PM tubes in each BB counter firing within a 14 ns time gate.
6	Two fixed big PM tubes in each BB counter firing within 14 ns time gate. The signals from tube 37 and 41 in the left BB counter, and tube 31 and 33 in the right BB counter have been carefully timed to make this trigger.
7	Reserved for pulser tests.
8	1 Hz Synchronization trigger.

Table 7.1: The triggers in the BRAHMS experiment.

$$T_L = \frac{l}{c} + \frac{Z_{vtx}}{c} - T_{coll} \tag{7.1}$$

$$T_R = \frac{l}{c} - \frac{Z_{vtx}}{c} - T_{coll} \tag{7.2}$$

$$Z_{vtx} = \left(\frac{T_L - T_R}{2}\right) \cdot c \tag{7.3}$$

We assume that the velocity of the particles are approximately the speed of light[1], c. T_{coll} is unknown, but fortunately is cancels. Z_{vtx} is the position of the vertex, and the distance between the BB counters (or ZDCs) is $2 \cdot l$.

Using the clusters or tracks in TPM1 to find the vertex, provides the most accurate determination. By projecting the tracks back to the beam pipe, and finding out where they intersect, you find the vertex. This provides the highest vertex resolution, but it is restricted to events that contain at least two tracks in TPM1, and need more tracks to be reliable. See section 7.4 on page 47 for a description of the tracking algorithm and [21] for a thorough explanation on how the vertex is found. There is also another way to get the vertex from TPM1. This method utilizes all the hits in the TPC. It draws a line from all possible pairs of hits and projects them back to the beam plane. All the Z coordinates of the crossing points with the beam plane is histogrammed and fitted to a gaussian function, and the mean is calculated. This is also thoroughly explained in [21]. Both of these methods are very inefficient in peripheral events, because of the low occupancy in TPM1, but works very well for high multiplicity events.

The track vertex is also used to calibrate the BBCs and the ZDCs. Only events with a good TPM1 vertex is used. By comparing the average difference in vertex position found from the BBCs/ZDCs and TPM1, the offset in the BBCs/ZDCs vs the TPM1 is used to find the calibration offsets. When the offset is found for a particular run, all events in that run can get an accurate vertex using the BBCs/ZDCs. The vertex resolution for the BB counters is $0.65\,cm$, for TPM1 it is $\sim 2\,mm$ and for the ZDCs it is $\sim 4\,cm$.

The vertex distribution found from these four different methods, done on the same sample of events, can be found in figure 7.2 on the following page. The difference between the distributions are mostly due to their different vertex range efficiency. The distribution of the ZDC vertex is slightly broader than the BB and Track vertex. The difference between the BB vertex and the ZDC vertex may be related to the resolution. The cluster vertex is very broad and has very long tails. The reason for this is that the method fails if the vertex is far from the nominal vertex. The trails are incorrect values. Main peak is

---

[1] The Beam travels with a velocity of 99.995% of the speed of light, and the remaining neutrons are those which the ZDC measure. The BBCs are hit by the participants from the fragmentation zones. Since the BBCs consist of Čherenkov radiating material, only particles with velocity close to c are detected.

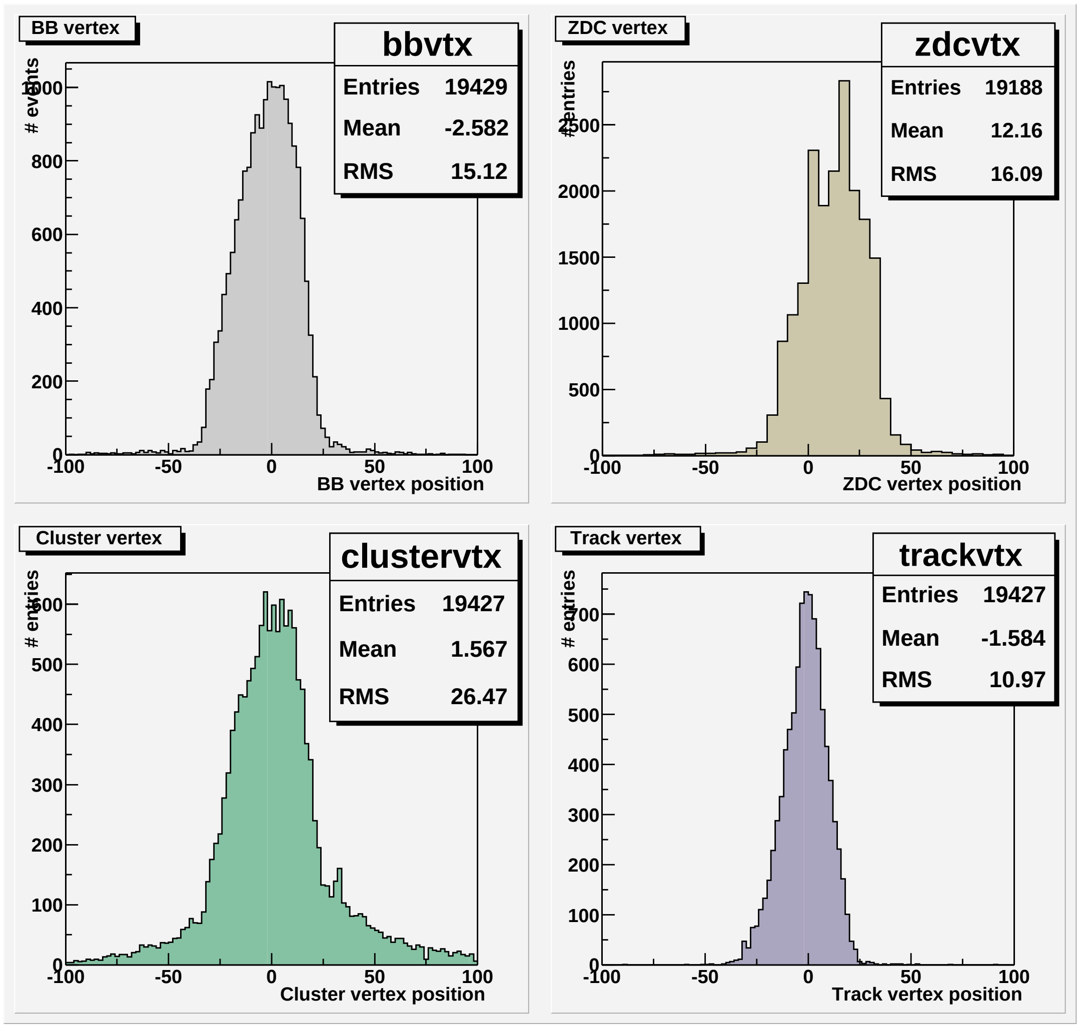

Figure 7.2: Vertex distribution found using the BB counters on the top left panel, ZDCs on the top right, clusters on the bottom left and track on the bottom right. The data $200AGeV$ Au-Au collisions taken during the autumn of 2001.

dominated by good values, very similar in shape to the BB vertex distributions. The track vertex requires at least three tracks to make a vertex position. These are, as mentioned, mostly high multiplisity events. The track vertex distribution is very narrow mostly because it is efficient over a smaller vertex range than the cluster vertex. Events with less than three tracks were not analyzed in figure 7.2.

It is the BBC vertex that is commonly used in the analysis. Even though an accuracy of $0.65\,cm$ is poorer than the TPM1 track vertex, it is also efficiency for semi peripheral events. It is sufficiently good to sort out secondary tracks.

All tracks must be projected back to the beam line and if they don't point close to the BB vertex, they are considered secondaries. All primary tracks point back to the vertex.

7.3 Centrality of the collision

A very important global property of a collision is its centrality, as has been discussed in chapter 2 on page 3. In Au-Au nuclear collisions the impact parameter b for nuclear interactions can range[2] from $0 \rightarrow 2R \sim 14fm$. The summed energy deposits, dE/dx, in the multiplicity barrel is used to measure the particle centrality. $<dE/dx>$ per unit path length for a realistic particle composition must first be found from simulations. The dE/dx of each segment of the multiplicity barrel can then be converted to a number of charged particles, using the knowledge of the vertex position, which is related to the path length to the segment. The acceptance of the multiplicity barrel, and thereby the number of particles measured at given centrality, is vertex dependent.

To measure the centrality a minimum bias event sample is needed. Such a sample is found i figure 7.3 on the next page. This is obtained from the minimum bias ZDC coincidence trigger (see section 8.3 on page 63). The event sample contains nuclear collisions from "head on" to those just "touching" each other. This sample is difficult to measure and is easily contaminated from very peripheral collisions with only Coloumb interactions, resulting in electromagnetic dissociation or junk events like beam - gas interaction. To remove the contamination from non-nuclear events, cuts have to be introduced and the effect of those cuts must be studied in simulations. When it is done the collision centrality can be determined from the measured multiplicity.

There have to be a minimum of 4 particles hitting the multiplicity barrel.

After this sample is collected, it has to be analyzed. First a desired set of centrality bins is selected. Then the lowest "multiplisity" value[3], M_c, for the $c\%$ most central events must be determined. This value must satisfy the following equation:

$$c = \frac{\int_{M_c}^{M_{max}} \frac{dN}{dM} \cdot dM}{\int_{0}^{M_{max}} \frac{dN}{dM} \cdot dM} \tag{7.4}$$

The integral in the numerator is the top $c\%$ of the multiplicity distribution, and the denominator is the entire multiplicity distribution. Each event's vertex z

---

[2] The radius of a nucleus is $R = R_0 \cdot A^{\frac{1}{3}}$. Where the constant $R_0 \sim 1.2fm$ and A is the number of nucleons in the nucleus. For gold $A = 197 \Rightarrow R = 7fm$.

[3] This may be a calibrated multiplisity or it can just be the total energy signal, where the energy deposit in each segment of the multiplisity barrel in corrected for the vertex dependent path length of primary tracks.

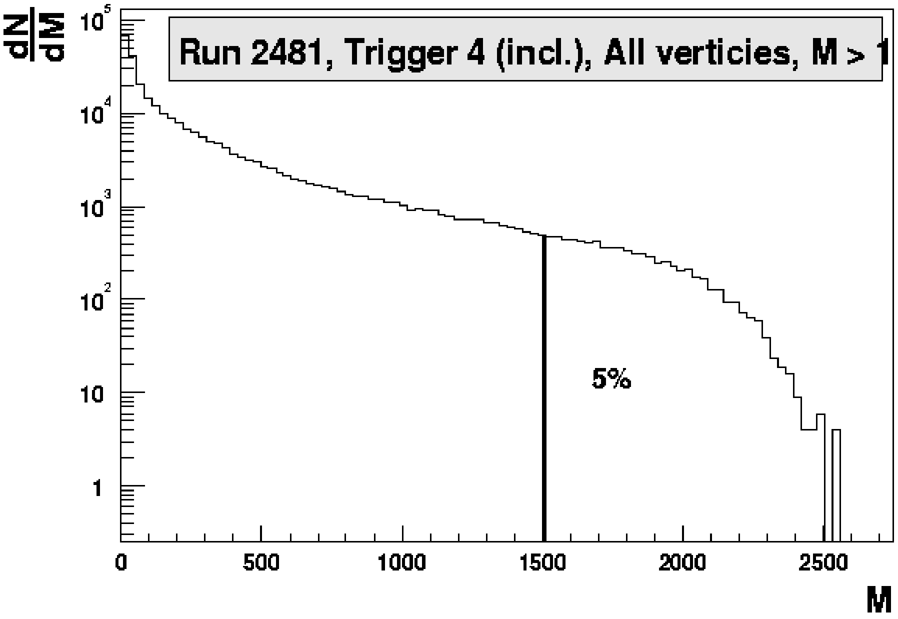

Figure 7.3: This is a minimum bias sample from the TMA. It is collected using trigger 4. The figure is taken from [22].

coordinate, must also be determined, since the M_c value is strongly dependent on the vertex position. The (z, M_c) pairs are then plotted and fitted with a n^{th} degree polynomial, which gives the cut functions $f_c(z)$.

To determine an event's centrality bin, from its multiplicity value M, the lowest c for the $f_c(z)$ function is picked, keeping $f_c(z) < M$. The event's centrality bin is then the chosen c. Figure 7.4 on the next page shows a minimum bias sample that has been analyzed and divided into different centrality bins. For an explanation and comparison of different centrality methods, see [23].

Using the event generator HIJING it is possible to relate this relative centrality to the impact parameter b. This is shown in table 7.2 on page 49. Only approximate ranges for each centrality bin is shown. It should be noted that this comparison is highly model dependent.

7.4 Local tracking in the TPC

The track reconstruction is done in a number of steps. The first step is to find the hits in the TPC. In BRAT the class *BrTpcHitPackage* does this in the following way. Fist some cleanup among the TPC sequences is done, e.g. removing early timebins, where oscillations are present. Then it reads through all the TPC sequences, and constructs islands of TPC sequences from adjoining pads, overlapping in time, the clusters. Then it takes all the TPC sequences,

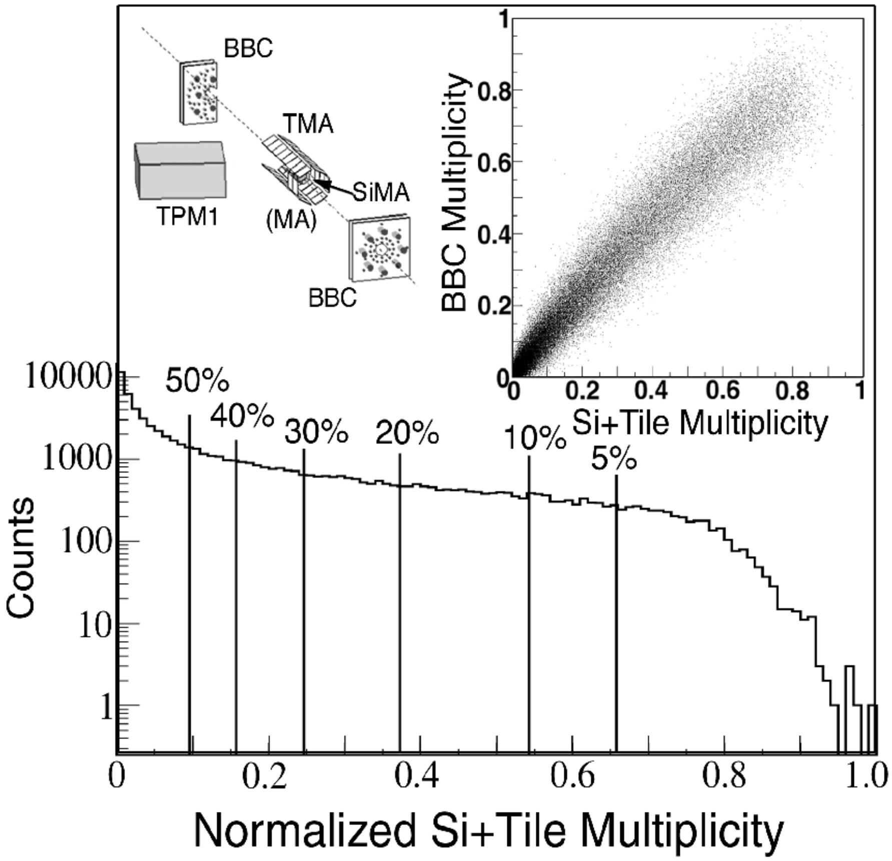

Figure 7.4: Centrality found using the TMA and SiMA. Also shown is the good correlation with BB counters. A schematic of the detectors is in the upper right corner. The figure is taken from [24].

belonging to a cluster, from a pad row and finds the weighted average and the width in the pad vs time plane. Figure 7.5 on page 50 show what clusters look like. The average is the centroid of the cluster of TPC sequences. Clusters with widths above a certain settable value, default is $1.6\,cm$, are further analyzed to see if they originate from *multi hit clusters*. Both the time width and the pad width are compared to this value. If these wide clusters have more than one maximum, they are divided into two (or more) clusters along the valley between the peaks. This is called *deconvolution*.

From the clusters hits are constructed and are given three coordinates, X, Y and Z, from the TPC geometry and the time position relations ship in the drift direction. Other quantities are also set: uncertainty in X, Y, Z, the width of the cluster, the ADC sum and a status (noise hit, single hit, multi hit (wide enough to be deconvoluted but only having one peak), single hit deconvoluted or multi hit deconvoluted). These hits are given to a package in brat, called

Centrality %	$\sim b$ range
0 - 10	0 - 5
10 - 20	5 - 7
20 - 30	7 - 8.5
30 - 40	8.5 - 10
40 - 50	10 - 11

Table 7.2: Centrality bins with their corresponding approximate impact parameters. The table is from [23].

BrTpcTrackPackage[4]. This package does the reconstruction of trajectories of local TPC tracks from the hits.

The algorithm works in the following way. It selects one of the hits in the first pad row and constructs a track seed. Then it searches for hits in the next pad row within a search window, called the search width. An illustration of how it might find a track is found in figure 7.6 on page 51. If a hit is found in the next pad row, the track seed parameters are updated, making a new linear fit to the current set of hits. The procedure is then repeated. If more than one hit is found within the search window, the searching is branched into two track seeds, and the procedure of alternating refits and hit searches is repeated for both seeds. If it does not find a hit within the next pad rows, the algorithm stops further search for that particular track seed. There is a settable number of how many padrows are allowed to be without hits, default is 3. When all the hits have been processed, hits belonging to a track seed, propagating through the entire TPC, have straight lines fitted to them, if there are enough hits. The track seed has now become a track candidate. This may be a particles trajectory. After that, some cleanup is done. Some track candidates might share some hits. If they share more than a settable number of hits, default is 3, the one with the best straight line fit (lowest χ^2) is kept, and the other ones are discarded. This final cleaning up of presumably unphysical track candidates is popularly called the *ghostbusting*.

7.5 Determining the momentum

After the local linear tracks segments are obtained, they must be combined through the magnets, to obtain the spectrometer tracks. This will give a momentum to all charged spectrometer tracks.

First the tracks have to be matched through the magnet. This is done in the following way. Two tracks, one from the front TPC (TPM1 or T1) and

---

[4] *BrTpcTrackPackage* also contain an instance of *BrTpcHitPackage*. The methods in this package is called before the methods in *BrTpcTrackPackage*.

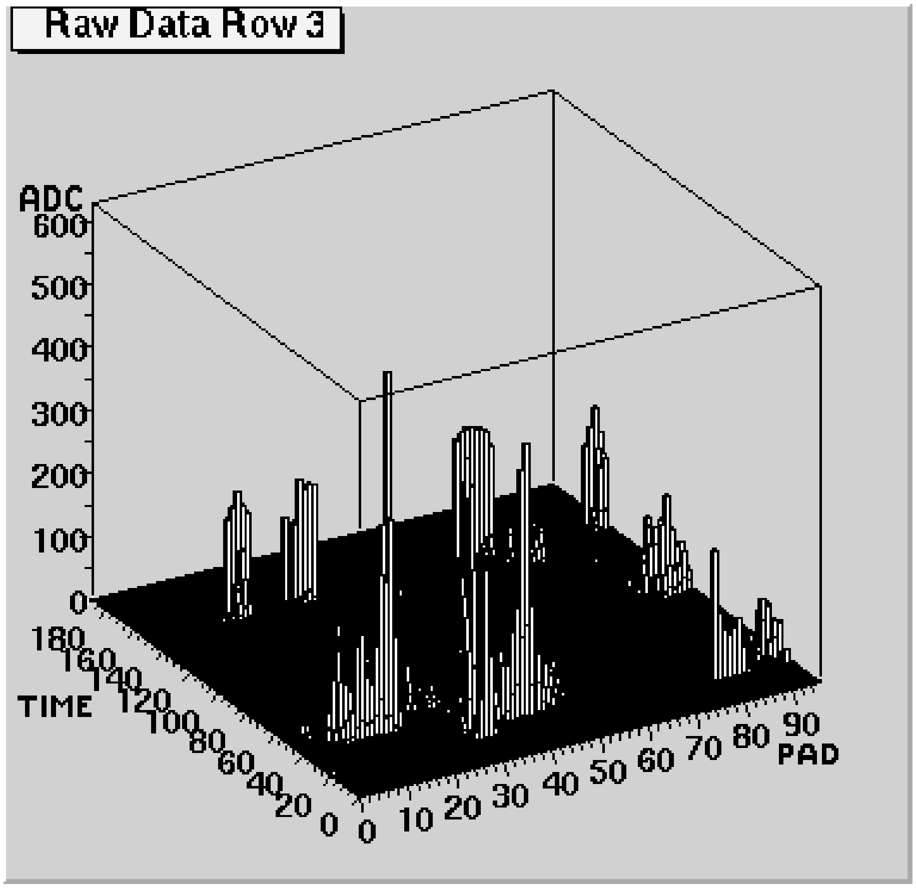

Figure 7.5: An illustration of how raw data clusters might look like in TPM1. All of the peaks in the figure are clusters. Some of the smaller ones might be noise and some might originate from particles flying through the TPC, ionizing the gas.

one from the back TPC (TPM2 or T2), are extrapolated into the middle of the magnet, where they must have the same y position. The two tracks must have the same inclination/slope (α_y or $\tan\lambda$) in the non-bending plane. Also the angles formed by the front and the back track with the line connecting the entrance and exit points in the magnet, must be the same. This is the angle b in figure 7.7 on page 53.

Distribution of these differences for reconstructed tracks should ideally be narrow and centered on zero. In practice there are offsets and widths in these distributions, which vary run by run for each magnet. The distributions of $d\alpha_y$, dy and $dAng$ are fitted with a gaussian. Centroid and σs are tabulated and available for all runs in ASCII files. These files contains the centroid position and the allowed deviation from the centroid of the distribution.

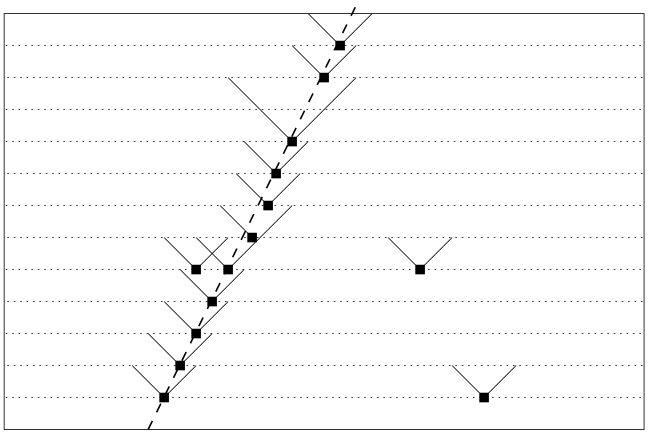

Figure 7.6: Starting in front of a TPC, the algorithm searches for hits within a specified window in the next pad rows. If enough hits are found through the detector, a local track is made from the hits. Figure borrowed from [21].

The quantities important for the matching are:

- $d\alpha_y$ — which is the allowed difference in $\tan \alpha_y$, where $\alpha_y (= \lambda)$ is the angle the track and the horizontal plane.
- dy — which is the difference between the two extrapolated tracks' y coordinates at the midplane of the magnet.
- $dAng$ — which is the difference in angle b, for front and back track, in figure 7.7 on page 53.

If these criteria are fulfilled and the connecting helical segment stays within fiducial cuts within the magnet gap, the tracks are matched. Poorly matched tracks and matched tracks that share the front or back track, selecting the poorest match, are then removed in the ghost busting.

When two good matching tracks are found the momentum can be found in the following way for a charged particle. The Lorenz force, F, is given by:

$$\vec{F} = q\vec{v} \times \vec{B} \tag{7.5}$$

where q is the particle's charge, $\vec{v}$ its velocity and $\vec{B}$ is the magnetic field. Equation (7.5) can be written with absolute values[5] if v is taken as the velocity

---

[5] The magnet gaps in the BRAHMS experiment are very narrow in the y direction so the $\vec{B}$-field can be taken to be vertical everywhere, so that the horizontal component of $\vec{v}$ is always perpendicular to $\vec{B}$. The three dimensional $\vec{p}$ is corrected for p_y component at the end.

perpendicular part to $\vec{B}$. If we ignore effects like the fact that charged particles will radiate if accelerated and thereby loose momentum, which has a negligible effect in the small BRAHMS magnets, the momentum can be calculated from the centripetal force:

$$F = \gamma m \frac{v^2}{r} \tag{7.6}$$

where γ is given in equation (2.5), m is the mass of a particle traveling at velocity v and r is the radius of the curvature of the trajectory. By combining equation (7.5), (7.6) and $p = \gamma m v$, the horizontal component of p becomes:

$$p = RqB \tag{7.7}$$

Since three of the quantities in equation (7.7) are always known, or easily found, it is easy to calculate the momentum. $\vec{B}$ is measured, q is assumed to be $\pm e$ and the radius is found by a geometrical calculation. The radius R is obtained the following way from angles μ_1 and μ_2 between the tracks and the magnet length axis at the corresponding entry and exit points, the magnetic field B and the length of the field G_{len}, using the effective edge approximation (see figure 7.7 on the next page):

$$\begin{aligned}
\sin\frac{\mu_2 - \mu_1}{2} &= \frac{d}{2R} \Rightarrow R = \frac{d}{2 \cdot \sin\frac{\mu_2 - \mu_1}{2}} \qquad (7.8)\\
\cos\frac{\mu_2 + \mu_1}{2} &= \frac{G_{len}}{d} \Rightarrow d = \frac{G_{len}}{\cos\frac{\mu_2 + \mu_1}{2}} \qquad (7.9)\\
R &= \frac{G_{len}}{2 \cdot \sin\frac{\mu_2 - \mu_1}{2} \cdot \cos\frac{\mu_2 + \mu_1}{2}} \qquad (7.10)
\end{aligned}$$

The symbols are all found in figure 7.7 on the following page. The momentum can now be found after some mathematical manipulation of the symbols in equation (7.10):

$$p = \frac{qBG_{len}}{\sin\mu_2 - \sin\mu_1} \tag{7.11}$$

This formula assumes that $\vec{G}_{len}$ is perpendicular to $\vec{B}$[6], and that the $\vec{B}$-field is homogeneous all along the length of the magnet. Equation (7.11) is used in

---

[6] This is an effective edge approximation of the magnetic field. The $\vec{B}$-field must be homogeneous over the magnet cross section at arbitrary local z-coordinate, i.e. can not vary with (x, y) at fixed z, but it can vary with $z \Rightarrow z(l)$. BG_{len} must the be replaced by $\int_{l_1}^{l_2} B(l)dl$.

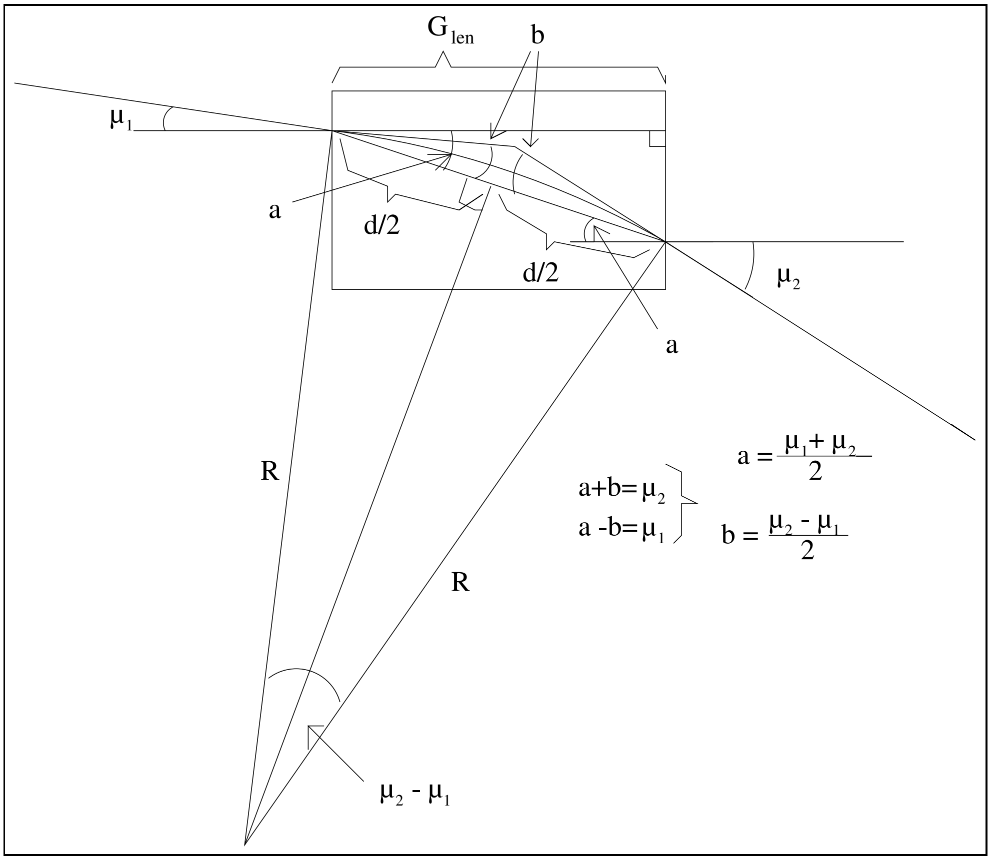

Figure 7.7: Illustration on how to obtain the radius from the angle of the incoming trajectory and the angle of the outgoing trajectory. a is the angle between the line connecting the entrance and exit point and the magnet length direction. b is the angle between the track lines and the line connecting the entrance and exit point. Matching tracks have the same b. μ_1 and μ_2 are the incoming track and outgoing track angle relative to the magnet length direction, respectively. R is the radius of the arc inside the magnet. l is the length of the magnet.

BRAT to determine the momentum component in the bending plane Finally the p_y component is added to get the three dimensional momentum vector, $\vec{p}$.

Finally primary tracks are selected by imposing a two dimensional cut on the tracks closest distance to the vertex.

7.6 Particle Identification

Once the trajectory and the momentum of the particle is found the *P*article *ID*entification (PID) has to be established, using hits from a PID detector corresponding to a track. The time of flight hodoscopes determines the speed of the particle in a very simple manner, by measuring the time the particles used from the vertex to the TOF wall.

$$v = \frac{L}{t_{TOF}} \tag{7.12}$$

where t_{TOF} is the time used and L is the length of the path from the vertex to the TOF detector. The particle's mass is then determined like this, using equation (2.4):

$$\begin{aligned} \beta &= \frac{v}{c} && (7.13) \\ mc^2 &= \sqrt{E^2 - p^2c^2} = \frac{p \cdot c}{\beta \cdot \gamma} = pc \cdot \sqrt{\beta^{-2} - 1} && (7.14) \end{aligned}$$

where γ is given in equation (2.5).

Now that the velocity (and mass) and the momentum of the particles surviving the previous cut is determined, particle separation may be done by plotting $1/\beta$ vs p, as is done in figure 7.8 on the next page. The experimental uncertainty in particle mass is found from measured $1/\beta$ and p in the statistical distribution of masses, determined according to equation (7.14), around the nominal particle mass. In figure 7.8a), MRS at 90°, there is four bands on each side. The topmost band is the protons, the next is kaons and the lowest one is the pions. The fourth band is partially mixed with the pions, but can be seen as the little cluster of dots, where $1/\beta = 1$ in the middle of the figure. These particles are electrons. The same goes for figure (b), FFS at 12°, except there are no visible electrons here, only protons, kaons and pions.

Figure (c) and (d) are mass distributions which clearly show the mass peaks of the three particles. In the shaded part in (c), all the pions are subtracted, using information from C1. This part only contains protons and kaons. The C1 threshold Čherenkov detector can veto[7] all the pions from the sample and thus the shaded plot can be made. Plot (d) is made by using the RICH. An illustration of the rings that are created in the detector is found in figure 7.9 on page 56. From the radius of these rings β can be determined and then the particle's mass. The opening angle of the cone of radiated Čherenkov light, when a fast particle passes through a medium, is given by:

$$\cos\theta = \frac{c}{v \cdot n} \tag{7.15}$$

---

[7] In a certain momentum range, determined from the medium's index of refraction only pions produce čherenkov light in C1. Kaons and protons will not produce any light at all.

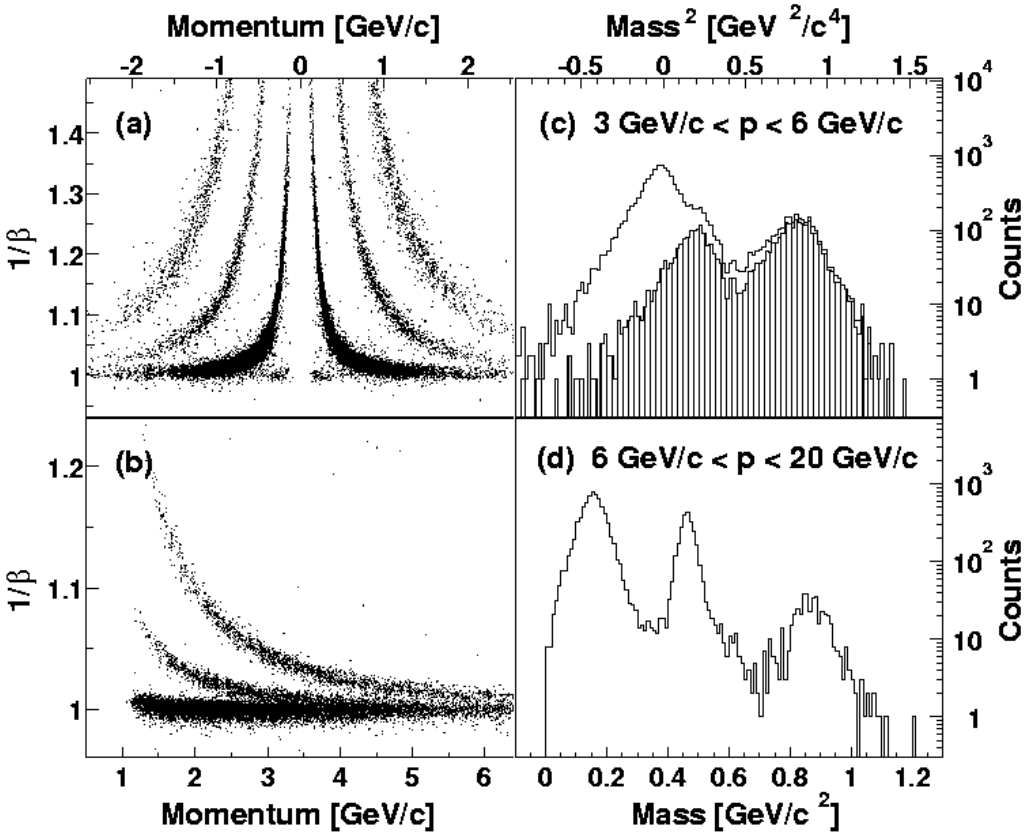

Figure 7.8: Particle identification ability in BRAHMS. Clear separation between pions, kaons and protons. (a) and (b) is $1/\beta$ versus the momentum, (c) and (d) versus mass square and mass, respectively. (a) The MRS is at 90° and both charges are accepted (negative momentum means negative charge). (b) The Measured spectrum from the FS at 12° with the TOF walls. (c) Mass square from the FS, positioned at 12°. The shaded region includes vetoing of pions in C1 (threshold Čherenkov). (d) Mass spectrum in the FS using the RICH (Ring imaging Čherenkov). The figure is taken from [11].

where c is the speed of light in vacuum, v the particles velocity and n is the refractive index of the radiating material. The radiation from one cone is reflected onto a ring in the focal plane of the RICH, which is read out by PMTs. From the reconstructed radius, R, θ can be determined, when the mirror focal length L_{focal} is known (the radius of the spherical mirror is $2L_{flocal}$):

$$\theta = \arctan \frac{R}{L_{focal}} \tag{7.16}$$

Then the velocity of the particle can be found from equation (7.15).

When the momentum has been determined from the tracking detectors and magnets, the mass of the particle may be found using equations (7.15) and $p = mv/\sqrt{1 - v^2/c^2}$:

$$mc^2 = pc \cdot \sqrt{\frac{c^2}{v^2} - 1} = pc \cdot \sqrt{n^2 \cos^2 \theta - 1} \tag{7.17}$$

A plot showing the ring radius as a function of mass is found in figure 7.10 on the next page.

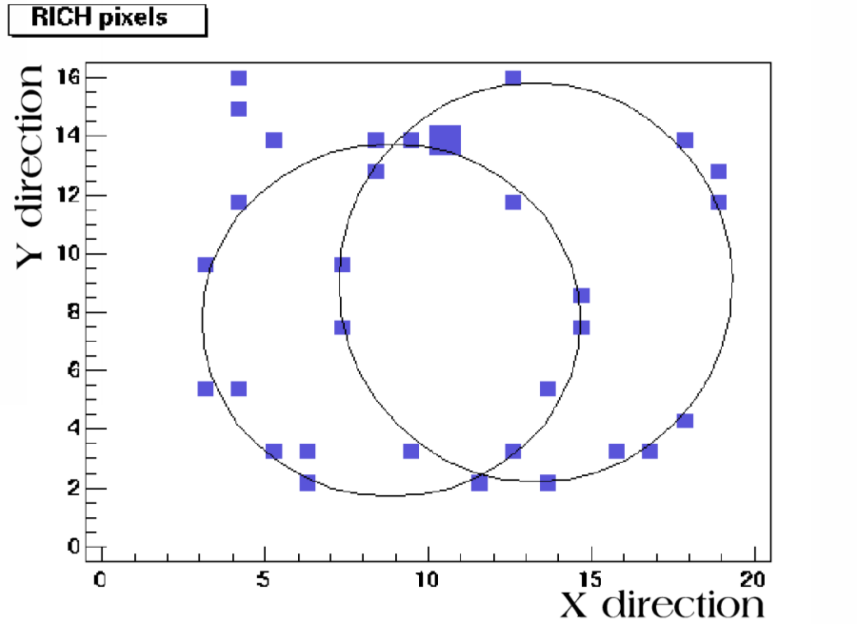

Figure 7.9: The dots, representing pixels with signals, clearly form rings in the RICH. The rings are made by čherenkov radiation from a particle that has traveled through the RICH detector. The axes are the pixel number in the detector. The size of the rings determines the velocity. The figure is from [25].

The PID is limited upwards in momentum due to velocities approaching c. This is seen in figure 7.8a and b as particle bands merging together at high momentum. When the bands merges together it is impossible to separate the particles from one another. Table 7.3 on the following page shows the different PID detector's ability to determine a particles' mass.

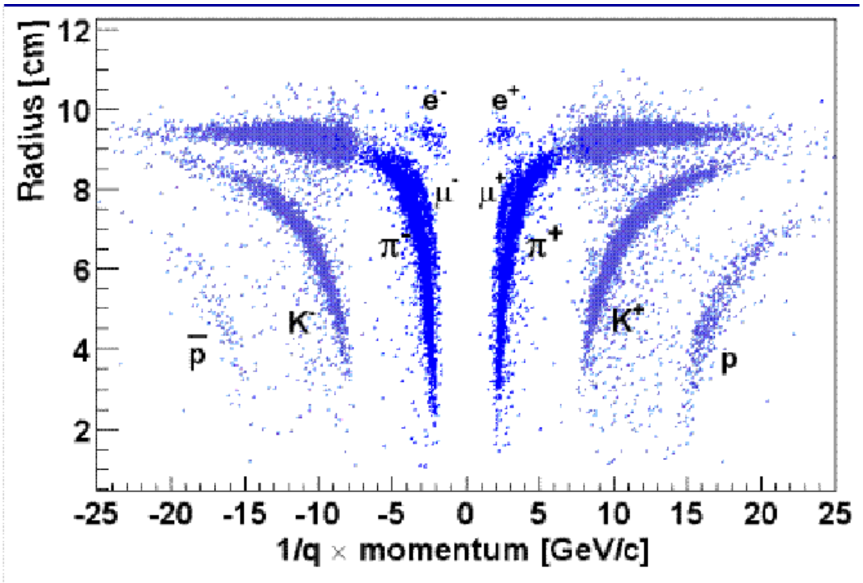

Figure 7.10: RICH ring radius plotted versus momentum. (Negative momentum means negative charge.). Clear separation between p, K and π is seen to really high momenta. μ and e are also present, but merge with π at low momenta. The figure is from [26].

Detector	π/K separation	K/p separation
H1(TOF1)	$\rightarrow 3.3\,GeV/c$	$\rightarrow 5.7\,GeV/c$
C1	veto $3.0 - 10\,GeV/c$	veto $10 - 18\,GeV$
H2(TOF2)	$\rightarrow 5.8\,GeV/c$	$\rightarrow 8.5\,GeV/c$
RICH	$\rightarrow 25\,GeV/c$	$\sim 10 - 35\,GeV/c$
TOFW	$\rightarrow 2.0\,GeV/c$	$\rightarrow 3.5\,GeV/c$

Table 7.3: Particle identification capabilities for the different detectors in BRAHMS. Adequate separations are defined as distances bigger than 3σ between nominal mass and and $1/\beta$ vs p curves. The C1's pion threshold is $3.0\,GeV/c$, kaon threshold at $10\,GeV/c$ and proton threshold at $18\,GeV/c$.

Chapter 8

Efficiency calculations/applications

There are many things that may affect the ability to reconstruct particles that fly through our detectors. First of all there is always a limitation on the detectors. They are designed with a specific position resolution, which may be too poor or be good enough for experimental track densities, but nevertheless sets the upper limit. The efficiency calculations presented in chapter 9 explores this limit. Global properties of an event can reduce the efficiency. High multiplicity events, resulting in high TPC occupancy, as well as vertex positions far away from the nominal vertex, making the tracks cross the pad rows at steep angle giving wide clusters, might reduce the efficiency, at least in TPM1 and TPM2 which may be exposed to tracks with steep angles. They are therefore designed to handle these tracks. Another example is that a time of flight wall will favourize fast light particles over slower, heavier ones, whose signal is lost if they hit the same slat as the faster particle. TPCs favors tracks with high dE/dx, which is dependent on the particle type and its momentum. It may also treat two particles flying very close to one another as one track instead of two. The ability to separate close lying tracks is usually called the "*Two Track Resolution*[1]".

The second constraint is the software. Ideally the software should reconstruct all available information from the detectors. This is something an experiment strives to achieve, but it may require much experience with both the detectors and the software before it is reached. The improvement of the software is an iterative process, which takes time. It is also important to be aware of the risk of implementing information in the raw data that is not really there. This is can easily be done when one attempts to improve the software with cuts and corrections.

Many of these limitations may be corrected for in an efficiency calculation. By knowing the efficiency of the detector, and associated software, all experimental measurements can, to a certain extent, be corrected. Simulations of the

---

[1] Chapter 10 on page 130 discusses "Two Track Resolution".

physical processes taking place when a particle, with known properties, passes through a detector enables the calculation of the efficiency of the detector and analysis software. The simulation must include the particle's interactions with matter and the signal transport in the detector. This is described in section 6.3 on page 33, and is used in the calculations presented in chapter 9.

The BRAHMS experiment decided to do the efficiency analysis by embedding simulated tracks into real events. Realistic occupancy, the amount of noise and malfunctioning parts of the detector are to a large extent automatically incorporated in such an analysis. The embedding of simulated tracks is an excellent way for determining the efficiency of the detectors in the BRAHMS experiment. This gives control over what should be reconstructed from the detector. It involves knowledge on how to digitize simulated tracks, but once that is found to an acceptable precision, the rest of the analysis can be done in a nice understandable way.

There exists other means to obtain the efficiency. One of the methods, which have been tried in BRAHMS, see [27], is to extrapolate a track from one detector through all the others. The other detectors must then be examined to see if the corresponding local track really is there. This method has some limitations. There has to be a track through at least one detector (at least two with a magnet in between if momentum is to be determined). If no detector has a track that may be used as reference the method is useless. Tracks that should be there, according to the extrapolation of the reference track, but are not reconstructed, might be absent for a number of reasons beside inefficiencies in the hardware and software. The particle might for instance have decayed, have scattered or been absorbed. This is easier to overcome in the FS than in the MRS, since the FS also has three DCs after the two TPCs providing more references with momentum determination. T2 could for example be studied using matched tracks from T1 to T3, and then checking if the track is also present in T2. The method has only been partially used in the MRS when the magnetic field has been turn off, to allow linear extrapolation from front/back TPC reference track. This method may give an artificially low efficiency due to the mentioned effects. It is also not possible to look at particles with special properties, i.e. you might not know what particle you are looking at since the momentum and the PID could be unknown. The embedding method excels in this respect, but is fully dependent on the simulation of physical processes in the detector. The outline for this alternative efficiency method, implemented by Pawel Staszel, is found in [27].

8.1 The geometry systems

Before one can specify any quantities related to a collision, one needs to define the coordinate system. In BRAHMS there are two coordinate systems. The

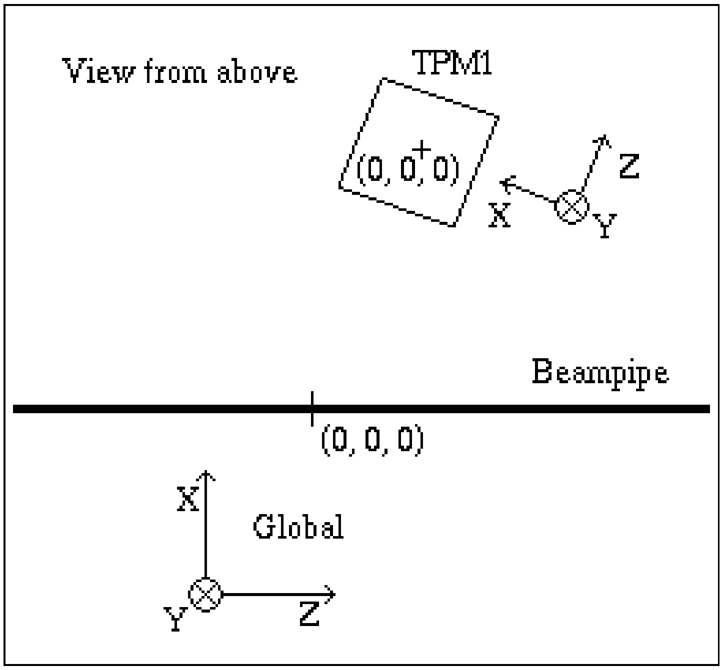

Figure 8.1: The global and the detector specific coordinate systems. The detector specific system is from TPM1.

first one is the global coordinate system. This system is a static one. It has it's z coordinate along the beam pipe, the y coordinate vertically and the x coordinate horizontally towards the MRS, perpendicular to the beam pipe. The nominal vertex $(x, y, z) = (0, 0, 0)$ is inside the beam pipe in the center of the TMA and SiMA barrel. See figure 8.1. In addition to this, there is a local coordinate system that is relative to each detector. The z-axis is defined along a line from nominal vertex through the center of the detector in the MRS, y is vertical and x is horizontal, perpendicular to z. Both of the systems are right handed, and the origo of the detector system is in the geometric center of the detectors. In the FS this is not the whole truth. The detector here are slightly rotated relative to each other. The z-axis is in these cases the symmetry axis of the detector, pointing roughly away from nominal vertex in the direction of the movement of the particle.

See figure 8.1 for an example.

8.2 Selecting angles for BRAG

The calculations is done in the following way. First BRAG is used to generate tracks through the spectrometers. These tracks are of a given particle species, have a given momentum and a given direction. The trajectories are not pre-

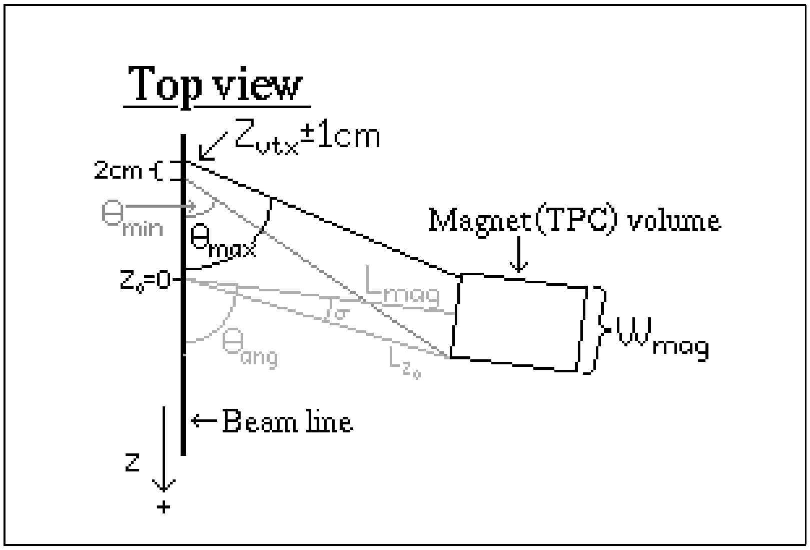

Figure 8.2: The angles that are fed into brag are calculated from the definitions stated in the figure. z_{vtx} is the vertex position, z_0 is nominal vertex, L_{mag} is the distance from z_0 to the geometrical center of the magnet (or TPC) opening, L_{z_0} is the distance from z_0 to the middle of the side of the magnet (or TPC) opening, σ is the angle between L_{mag} and L_{z_0}, θ_{ang} is the magnet (or TPC) angle setting relative to nominal vertex and the particles are thrown with angles between θ_{min} and θ_{max}.

cisely known at the time of "production" but can easily be found by doing a reconstruction with the software. They all come from a given vertex. A set of 20 vertex[2] bins, each $2\,cm$ wide, has been chosen. A brag file is generated for each vertex bin. Within each vertex bin the vertex distribution is flat. Raw data events with vertex between $\pm 20\,cm$ can then be analyzed. Simulated tracks are then to be embedded into raw events with the same production vertex. This is important, since it gives a realistic efficiency. In particular, it includes efficiency loss due to tracks going out close to each other and nearly parallel tracks, see chapter 10. When the efficiency calculation is done for spectrometer tracks the particle is aimed at the magnet opening. When the efficiency of TPM1 is calculated, the opening of the TPC is chosen instead. Figure 8.2 shows how the angles are selected from a given vertex, z_{vtx}.

The reason for aiming at the magnet opening and not the opening of the TPC[3] is a maximized chance of the particle flying through the entire spectrometer. The spectrometers cover very small solid angles: $0.8\,msr$ for FS and $6.5\,msr$ for the MRS (see [8]). From figure 8.2 the angles can be calculated.

---

[2] The acceptance corrections are done with 6 vertex intervals, each $5\,cm$ wide, between $\pm 15\,cm$.

[3] This is only possible for TPM1. T1 has the D1 magnet in front of it.

Name	L_{mag}	W_{mag}	H_{mag}	G_{len}	L_{z_0}	σ (°)
D1	250.1	20.00	8.000	200.0	250.3	2.29
TPM1	76.30	38.40	20.00	36.60	78.67	14.1
D5	151.9	35.00	10.00	76.20	152.9	6.57

Table 8.1: All the number are in cm, except from σ which is in degrees. L_{mag} is the length from nominal vertex to the center front of the magnet, W_{mag} is the width of the magnet, H_{mag} is the height of the magnet, G_{len} is the length of the magnet. See equation (8.3) and (8.4) for L_{z_0} and σ, respectively.

Some geometrical considerations shows that θ_{min} and θ_{max} can be written in the following way:

$$\theta_{min} = \arctan\left(\frac{\sin(\theta_{ang}-\sigma)}{\cos(\theta_{ang}-\sigma)-\frac{z_{max}}{L_{z_0}}}\right) \tag{8.1}$$

$$\theta_{max} = \arctan\left(\frac{\sin(\theta_{ang}+\sigma)}{\cos(\theta_{ang}+\sigma)-\frac{z_{min}}{L_{z_0}}}\right) \tag{8.2}$$

$$L_{z_0}^2 = \left(\frac{W_{mag}}{2}\right)^2 + L_{mag}^2 \tag{8.3}$$

$$\sigma = \arctan\left(\frac{W_{mag}}{2L_{mag}}\right) \tag{8.4}$$

This is applicable for all θ_{ang} and vertex positions. W_{mag}, L_{mag}, σ and L_{z_0} are constants. They are all listed in table 8.1 for the different magnets.

To utilize as many as possible of the brag generated tracks, another condition is implemented. The L_{mag} is lengthened to the back[4] of the magnet or TPC ($L_{mag} \rightarrow L_{mag} + G_{len}$) in the calculation of θ_{min} or θ_{max} in the following cases:

1. **Positively** charged particles in **B-polarity** field, or **negatively** charged particles in **A-polarity** fields:
   — if θ_{min} is less than θ_{ang}: lengthen L_{mag} in calculation of θ_{min}.
2. **Negatively** charged particles in **B-polarity** field, or **positively** charged particles in **A-polarity** fields:
   — if θ_{max} is greater than θ_{ang}: lengthen L_{mag} in calculation of θ_{max}.

In BRAHMS B-polarity bends positively charged particles right and negatively charged particles left, and vice versa in A-polarity fields.

---

[4] The reason for this choice is that the bending of the particle is only a few cm, depending on the particle's momentum and charge, and the strength and polarity of the magnet field. See equation (7.11).

It it is much less probable to get any spectrometer tracks when the vertex is outside of $\pm 20\,cm$ from the nominal vertex. Therefore this has been chosen as the vertex limits for the brag generated particles.

The formula for the angles was implemented to improve the speed of the analysis program. Larger BRAG generated files and longer CPU time would be needed if the aiming was just towards the opening of the TPC or magnet. This kind of aiming is more suitable when acceptance maps are produced, since you need a lot of particles that that fall outside the acceptance to locate the edges of the acceptance regions.

The second angle that need to be inserted into BRAG is the angle ϕ. ϕ lies in the yz plane. Therefore the choice of the angle ϕ can be directly calculated from the geometry:

$$\phi = \arctan\left(\frac{H_{mag}}{2(L_{mag} + G_{len})\sin\theta_{ang}}\right) \tag{8.5}$$

H_{mag} is the height of the magnet (TPM1) opening and G_{len} is the length of the magnet (TPM1) opening. The geometries for D1 and D5 is listed in table 8.1.

The geometry and magnetic fields of all magnets and detectors are read out from the BRAHMS database. These are specific for all runs. The simulation files generated are therefore specific for each geometry and field setting.

8.3 Choosing events

Selection of raw events for embedding has been done based on the global characteristics. The simplest way of doing this is to look at the trigger that started the event. The 8 different triggers in BRAHMS is shown in table 7.1 on page 43. Trigger 1 through 6 are the physics triggers, and they select different centralities. This is shown in figure 8.3 on the next page.

It is also possible to select centrality ranges by looking at the multiplicity. This is typically what is done when only certain centralities are to be studied.

In this efficiency analysis there are two constraints used to accept or reject an event for analysis. The first thing is the trigger. All of the analysis in chapter 9 are done using trigger 6. This is not a minimum bias trigger, which trigger 4 is, but a trigger that only selects the most central events. Trigger 6 provides events that typically have the largest multiplicity of all the triggers, $\sim 25\,\%$ most central events. This gives the highest occupancy in the detectors and will give the lowest efficiency and the best event sample for studying efficiency loss.

The second constraint on the events is the vertex. It has been chosen to be between $\pm 20\,cm$. A larger vertex range could have been chosen, but it is not very likely that there will be many spectrometer tracks from vertices outside

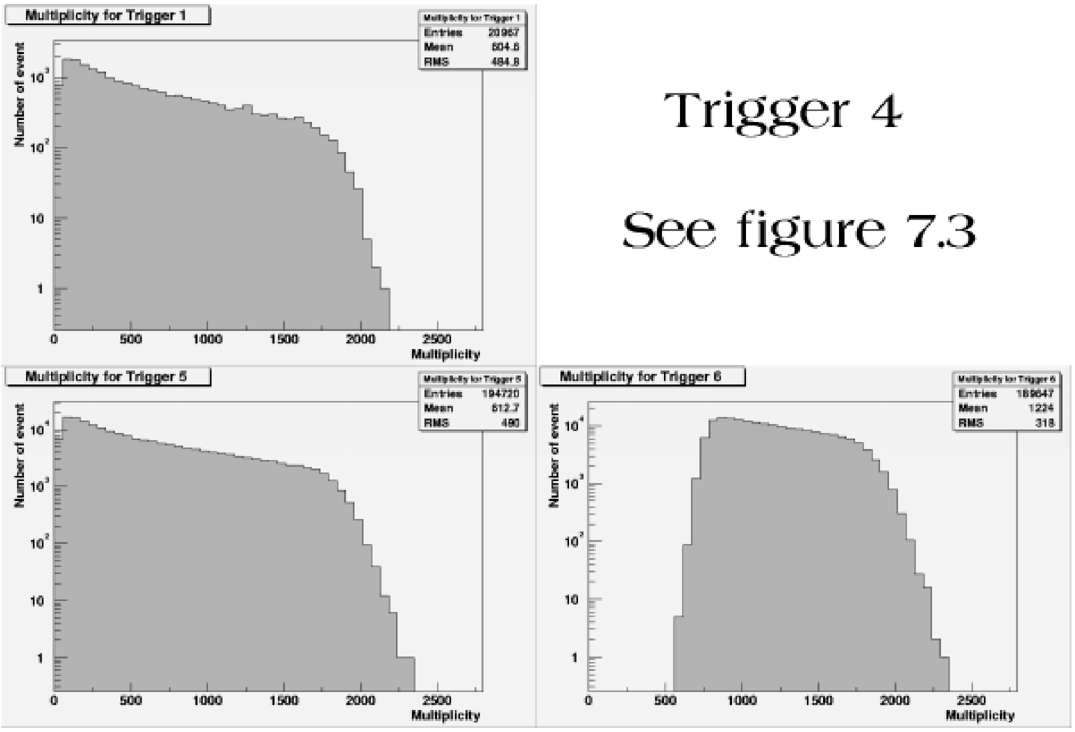

Figure 8.3: Multiplicity distribution for trigger 1, 5 and 6. Notice the scale the y-axis.

this region. The acceptance calculations even have a narrower window, $\pm 15\,cm$. This is what will be used in the future for most of the physics analysis.

8.4 Reconstructing the simulated track

The following subsections explains what the different classes in BEAT do. This is also an explanation of the efficiency analysis chain. The BEAT library consists of *BrEffGeantModule*, *BrTrackMatcherModule*, *BrEffRecoModule* and *BrEffhistModule*. In addition the graphical user interface consists of a class called *BrEffWidget* and compiled program called *BEAT*. The bratmain script BEAT can be run directly or through the graphical user interface.

The efficiency analysis is done by summing over a large number of events, to get high statistics, and the efficiency for the detector/spectrometer for this specific type of particle, is found. This can then be done with as many particle species as desired for a specific spectrometer setting and magnetic field. The momentum can either be a sample of fixed values or it can be a continuous spectrum between desired limits. There is an enormous amount of choices. Adequate choices must be made. This will be discussed in section 8.4.8.

8.4.1 The BEAT bratmain script

The Bratmain program, which reads the script, is explained in section 4.3[5]. The script starts with a deciphering of the parameters given to the script. It then connects to the BRAHMS *D*ata *B*ase (DB). The DB contains all the calibrations and geometries needed in an analysis, and makes sure they are used in a consistent way. The first module in the pipe line reads a raw data event from a file. The next module is a trigger filter. It selects only events with requested triggers. This event is then passed on to a series of modules that performs calibrations of the BB counters, BB data reduction and finally finding the BB counter's vertex. A vertex filter decides if the vertex is in the requested region. When an appropriate vertex is found, *BrEffGeantModule* searches one of the BRAG generated files, corresponding to the raw event vertex (see section 8.2 on page 60), for a reconstructible track. For the definition of a reconstructible simulated track, see section 8.4.2. Then it digitizes it, and does full reconstruction on the digitized simulated track. The *BrTpcAddSeqModule* adds the raw event and digitized simulated track together on the TPC sequences level. This is the so-called "embedding". After the embedding of the digitized TPC sequences, we have the following three events:

- **The raw event** containing raw data from a collision.
- **The digitized event** containing the digitization of the simulated track, the reconstructed local tracks and the matched track.
- **The embedded event** which has all the raw data plus the digitized simulated track embedded in it.

After this step the rest of the track reconstruction of the raw and embedded event is done in the *BrEffRecoModule*. A couple of modules then determines the centrality of the collision, as described in section 7.3 on page 46. And finally *BrEffhistModule* performs the efficiency calculations and the histogramming done. All the reconstructed data is written to an output file, so that further/reanalysis can be done.

8.4.2 BrEffGeantModule

This class is responsible for reading the an appropriate BRAG generated event. The module start by reading the vertex position and determines which vertex bin it belongs to. A BRAG generated event with a particle coming from this vertex bin is then read. Digitization is performed, using the hard coded digitization constants[6]. Then the module reconstructs the track. Four checks can be performed:

---

[5] All of the efficiency software will be made available in the BRAHMS CVS.

[6] The determination of these constants are discussed in section 6.3.2 on page 36.

1. The local detector tracks must be found, when the GEANT hits are passed to BrGeantToTpcTrackCandidate. It checks that there are valid hits in a sufficient number of padrows, and that a straight line can be fitted to them, with an acceptable χ^2. (It is a rather loose cut, to allow for multiple scattering.)

2. The simulated particle must come from the found vertex bin and still has the same track ID number provided by BRAG. (This does not exclude the possibility for multiple scattering.)

3. Matching of the local detector tracks must be possible, using the parameters described in section 7.5 on page 49. This is handled by *BrTrackMatcherModule* (see section 8.4.3).

4. The momentum must be as specified, ±10% to exclude tracks subject to any dramatic interaction with matter.

The two first checks are always done. If the last two (3, 4) are omitted, the efficiency loss due to poor matching in the magnet is also included in the calculations. This loss is probably very sensitive to multiple scattering. Ensuring that also check 3 and 4 are satisfied, i.e. verifying that that the simulated tracks are matchable, will result in a calculated efficiency which only include the combined tracking efficiency in the front and back TPC. If any of the required checks fails, the module must read a new BRAG event, and perform the same checks again. This must be done until the selected checks are all satisfied. Finally the module removes internally needed data from its output.

8.4.3 BrTrackMatcherModule

This module just wraps the BRAT class *BrModuleMatchTrack*[7]. It starts by reading an ASCII file containing the matching parameters[8]. These parameters are found by doing matching of the raw tracks in a specified run. This has been done on almost all of the BRAHMS raw data. These parameters are then passed on to *BrModuleMatchTrack*.

After having received the matching parameters, *BrModuleMatchTrack* is then requested to do the matching of the local detector tracks and calculate the momentum of the trajectory. Then *BrTrackMatcherModule* puts the found matched tracks into an appropriate output table, easily readable for the rest of the analysis chain.

---

[7] See section 7.5 on page 49 for an explanation on how it performs the matching.

[8] These parameters will soon appear in the BRAHMS database, but are still ASCII files scattered around in the collaborators home directories. One single file usually don't contain calibrations for all runs, but with a bit of searching, and copy'n'paste, it is easy to get the needed calibrations for all desired runs.

8.4.4 BrTpcAddSeqModule

The digitized and raw TPC sequences are added together, to make the "embedded" event, in this module, which is a part of the BRAT library. The module works in the following way. The module takes two events as input. One is the raw event and the other is a BRAG simulated, digitized[9] track. The module then takes the two lists of TPC sequences, and starts comparing them, in order to make a third one. It takes the first sequence from the digitized track and copies it. Then it compares if there are any sequences in the raw sequence list from the same pad as the sequence from the digitized track. If there are any, the ADC values are added to the copied sequence from the digitized track in the correct time bin. If the raw sequence contain time bins not present in the digitized sequence, the copied sequence must be expanded. Then the digitized sequence list is searched for more sequences from the same pad. They are added to the copy if found. The copied sequence now contains all the ADC values, in their corresponding time bins, from both the raw and digitized sequence list. This new sequence is then added to a new sequence list. The next sequence in the digitized sequence list is copied and the procedure is repeated. When both of the sequence lists have been exhausted, the new sequence list is returned. This is called the *embedded event*.

8.4.5 BrEffRecoModule

This module performs the last reconstruction. Local tracks are now reconstructed in both the raw data and the "embedded" data. The local tracks are then delivered to *BrTrackMatcherModule* which performs the track matching as described above. Some clean up in the output from the module is done. For efficiency determination, only the total occupancy of the TPC is needed, and this is provided by the number of hits in the TPC, which is stored in the output from the tracking algorithm.

8.4.6 BrEffHistModule

This module performs all the efficiency calculations, and the filling of histograms. The module compares the originally simulated, digitized track with all the tracks in the "embedded" event.

To determine whether or not the correct track is reconstructed, a geometrical overlap between the simulated and found track is calculated. A cylinder is put around the part of the trajectories that is inside the TPC. In this analysis a radius of $\sim r = 0.4\,cm$ was chosen for the cylinders[10]. Then the overlapping

---

[9] See section 6.3 on page 33 for an explanation on how this is done.

[10] This is not the actual radius of the cylinder, only a good approximation. This value is the radius of the circle in the xy-plane.

volume of the two cylinders is calculated and a relative overlap between the two is found. 0 means that they do not overlap at all, and 1 means that they exactly overlap each other. The algorithm distorts the cylinders in order to have a circular intersection between the cylinders and planes at arbitrary z. Then it calculates the overlap numerically.

Let a trajectory be represented like this:

$$x = A \cdot z + a \tag{8.6}$$

$$y = B \cdot z + b \tag{8.7}$$

where x, y and z is our coordinates, and A, a, B and b are constants that define the trajectory. If the trajectories are parallel:

$$(A_1 - A_2)^2 + (B_2 - B_2)^2 = 0 \tag{8.8}$$

the relative overlap between the cylinders will be the relative overlap between two circles, as illustrated in figure 8.4 on the following page. The distance between the trajectories is:

$$D = \sqrt{(a_1 - a_2)^2 + (b_1 - b_2)^2} \equiv d \cdot 2r \tag{8.9}$$

where r is the radius of the cylinders and the d ($d \equiv \frac{D}{2r}$) is the relative distance between two overlapping circles with radius r. If $d > 1$ there is no overlap. The subscripts represents trajectory 1 and 2.

From figure 8.4 on the next page the relative overlap between two identical circles that overlap each other can be calculated. It can be done like this:

$$x = \sqrt{r^2 - \frac{D^2}{4}} \tag{8.10}$$

$$B = r^2 \cdot \frac{\mu}{2} \tag{8.11}$$

$$\cos\frac{\mu}{2} = \frac{D}{2r} \Rightarrow \mu = 2 \cdot \arccos d \tag{8.12}$$

$$A = 2\left(B - \frac{xD}{2}\right) = 2B - D\sqrt{r^2 - \frac{D^2}{4}} \tag{8.13}$$

$$= r^2(\mu - 2d\sqrt{1 - d^2}) \tag{8.14}$$

$$= 2r^2(\arccos d - d\sqrt{1 - d^2}) \tag{8.15}$$

B is the area of a circle sector subtended by the angle μ. To obtain the relative overlap, A is divided by the area of the circle, πr^2, which yields:

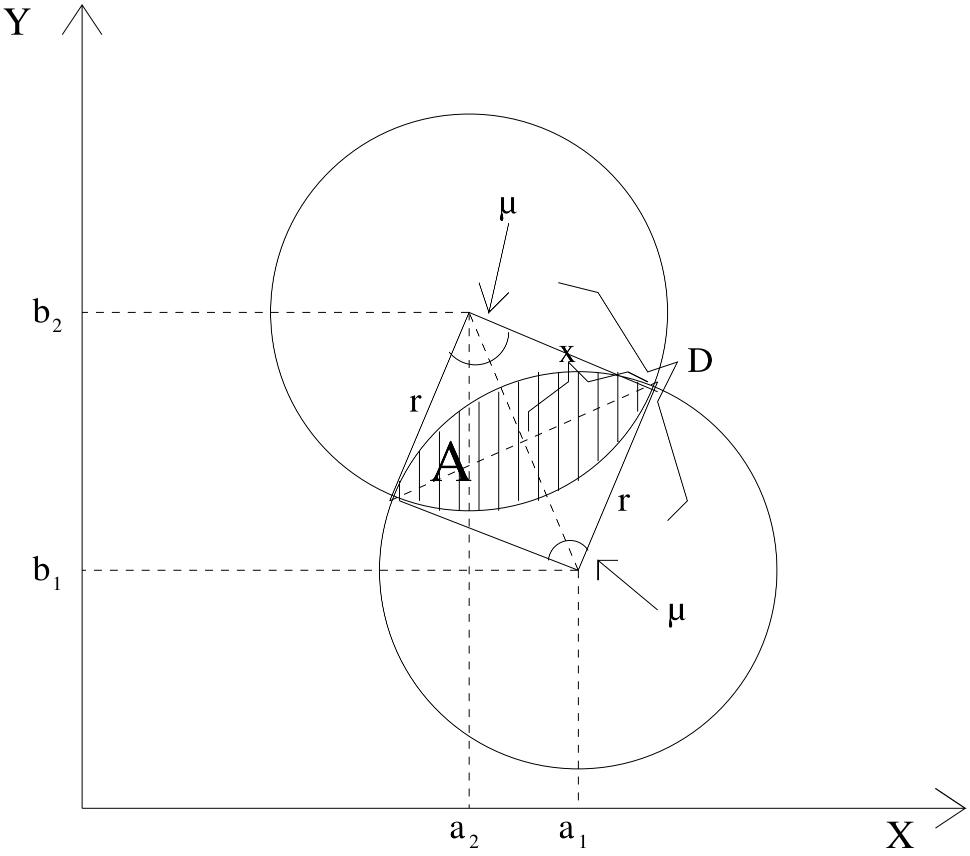

Figure 8.4: Two overlapping circles with radius r, overlapping area A and distance between circle centers D.

$$O_{circ} = \frac{2}{\pi}(\arccos d - d\sqrt{1-d^2}) \tag{8.16}$$

If the tracks are not parallel, an expression for the distance, $D(z)$, between the tracks must be established as a function of the z coordinate:

$$\begin{aligned}
\Delta D_x &= (A_1 - A_2) && (8.17)\\
\Delta D_y &= (B_1 - B_2) && (8.18)\\
\Delta P_x &= (a_1 - a_2) && (8.19)\\
\Delta P_y &= (b_1 - b_2) && (8.20)\\
D^2(z) &= (x_1(z) - x_2(z))^2 + (y_1(z) - y_2(z))^2 &&\\
&= z^2(\Delta D_x^2 + \Delta D_y^2) + 2z(\Delta D_x \Delta P_x + \Delta D_y \Delta P_y) &&\\
&\quad + \Delta P_x^2 + \Delta P_y^2 \equiv d^2(z) \cdot 4r^2 && (8.21)
\end{aligned}$$

The value for $d(z)$ in equation (8.21) is then inserted into equation (8.16). The next step is to find the lower and upper z values for the integration. This region is where the value of $d(z)$ is less than $2r$:

$$\begin{aligned} a &= \Delta D_x^2 + \Delta D_y^2 && (8.22)\\ b &= \Delta D_x \Delta P_x + \Delta D_y \Delta P_y && (8.23)\\ c &= \Delta P_x^2 + \Delta P_y^2 && (8.24)\\ \sqrt{a \cdot z^2 + 2b \cdot z + c} &< 2r && (8.25)\\ -\frac{b}{a} - \frac{\sqrt{b^2 - a(c - 4r^2)}}{a} &< z < -\frac{b}{a} + \frac{\sqrt{b^2 - a(c - 4r^2)}}{a} && (8.26) \end{aligned}$$

Let us call the left hand side of equation (8.26) z_{min} and the right hand side z_{max}. If z_{min} or z_{max} is outside the TPC volume, they must be changed to the z value that marks the front or the back of the TPC. This results in the following integral when equation (8.21) is inserted into equation (8.16), which is the relative overlap, O_{tot}, between the cylinders around the two trajectories:

$$\begin{aligned} d(z) &= \frac{1}{2r}\sqrt{a \cdot z^2 + 2b \cdot z + c} && (8.27)\\ O_{tot} &= \frac{2}{\pi}\int_{z_{min}}^{z_{max}} \left(\arccos d(z) - d(z)\sqrt{1 - d^2(z)}\right) \cdot dz && (8.28) \end{aligned}$$

This integral is readily numerically. A simple way to do it is to take the average relative overlap for 5 values of z between z_{min} and z_{max}, distributing them evenly in this range.

If the relative overlap, equation (8.16), is bigger than 0.6, using a cylinder radius of $0.4\,cm$, the embedded local track is reconstructed. For matched tracks, the relative overlap found in the front TPC is multiplied with the relative overlap in the back TPC. Figure 9.1 on page 79, displaying the distribution of relative overlaps, shows that this definition seems sound. If the overlap is less, the track was not considered to be the same track. The efficiency is then the number of events with reconstructed track found, divided by the total number of events, with a reconstructible track according to *BrEffGeantModule*.

The module then fills histograms containing efficiency versus vertex position, centrality, number of hits in the TPCs, number of tracks, rapidity y and transverse momentum p_T. $dN/dO_{overlap}$ is also histogrammed to determine what the minimum overlap criteria for reconstructed tracks should be, figure 9.1 on page 79. Finally the probability of producing "ghost tracks" and losing tracks is histogrammed. These are tracks found/not found in the embedded event, that were not present/present in raw event.

8.4.7 The BEAT GUI

The beat GUI is just a simple widget that makes the command line for you. There are a lot of parameters that have to be supplied at the command line. The widget makes sure you have entered all that is necessary to perform the efficiency calculation. The class is called *BrEffWidget*, and is started by the program *beat*. An illustration on how the GUI looks like can be found in figure B.1 on page 153.

8.4.8 Choosing particles and momenta

There are mainly three particle types flying through the spectrometers. These are protons (p, $\bar{p}$), kaons ($K^{\pm}$) and pions ($\pi^{\pm}$), which are all stable to semi-stable particles. These are of course of major interest to BRAHMS. Other more exotic particles decay before they reach the end of the spectrometer, so they will not be detected. But their decay products can be detected because they very often are p's, K's or π's. This choice of particle species falls very natural. Since the magnet opening of D1 in the FS is long and narrow, it will accept particles of mostly one type of charge, while the other charge is deflected into the wall of the magnet. Switching the magnet field from A to B will accept the other charge. The calculations have therefore been done using only positively charged particles in B fields. The opening of the D5 magnet in the MRS is much larger (and this spectrometer is symmetric in design). It will accept both charges, but has a slightly favored charge - magnetic field setting. Ratios and yields are usually calculated for the favored setting.

The momenta chosen for these particles are flat distributions taken in the range where the spectrometer is able to reconstruct particles. The momentum range chosen for the particles and spectrometers are listed in table 8.2, and were selected by looking at the reconstructed momentum spectra in their respective runs. The momentum ranges cover the area where the particle spectra have good statistics. This area is most relevant for yields/inverse slopes determination. For high p_T studies, the analysis can be easily be done for a wider momentum range.

8.5 From raw particle numbers to yields

When the raw particle numbers have been found, they are plotted as shown in figure 7.8a. The raw data analysis is done without employing any other cuts than already discussed in this chapter. This is the time to start applying PID cuts. If the experiment was perfect, with infinite precision momentum determination and time-of flight, all the particles would lie on the curve

Angle	Run Nr	Pion E(GeV)	Kaon E(GeV)	Proton E(GeV)
3.0°	5548	3.5 - 10.0	3.5 - 10.0	3.5 - 12.0
4.0°	5508	5.0 - 11.0	5.0 - 11.0	5.0 - 13.0
8.0°	5573	2.0 - 5.0	2.0 - 5.0	2.0 - 7.0
12.0°	5642	2.5 - 7.0	2.5 - 7.0	2.5 - 9.0
12.0°	5677	1.5 - 4.0	1.5 - 4.0	1.5 - 5.0
20.0°	5713	1.0 - 3.0	1.0 - 3.0	1.0 - 4.0
40.0°	5508	0.2 - 1.5	0.2 - 1.5	0.3 - 2.0
40.0°	*5548*	*0.3 - 2.0*	*0.3 - 2.0*	*0.4 - 3.0*
40.0°	*5573*	*0.3 - 2.0*	*0.3 - 2.0*	*0.4 - 3.0*
52.5°	5677	0.2 - 1.5	0.2 - 1.5	0.3 - 2.0
60.0°	5642	0.2 - 1.4	0.2 - 1.4	0.3 - 2.0
90.0°	5713	0.2 - 1.2	0.2 - 1.2	0.3 - 1.7

Table 8.2: Particle energies used in the efficiency calculation. Angles from 20° and below are analysis of the FFS efficiency. Above is the MRS. The emphasized lines are runs not analyzed.

$\frac{1}{\beta} = \sqrt{\frac{m^2c^2}{p^2} + 1}$, which is just a slight modification of equation (7.14). Unfortunately the detectors have finite resolution, so the measured $(1/\beta, p)$ values will have a gaussian distribution around this equation at arbitrary p. Adding and subtracting 3σ, found from the gaussian distribution, to the modified equation (7.14), gives a upper and lower limit of where the particles of a specific type should be. This also limits the particle separation ability upward in p, i.e. π/K separation can be done up to the p value where $1/\beta(p)_{max}$ line for πs crosses $1/\beta(p)_{min}$ line for Ks. All particles between two lines are then determined to be of that specific type. This raw particle yield must then be corrected for acceptance and efficiency.

The tracking efficiency should be should be parametrizedd as a function of the number of hits in the TPC if there is a strong dependence of the efficiency vs the TPC occupancy. Momentum and vertex dependence of the efficiency is also expected, and must be studied. Chapter 9 suggests that occupancy corrections should be done. This correction must be done event by event, since each event will have a different occupancy in the TPC.

Then the efficiency corrected yield must be corrected for acceptance. The acceptance is represented by (p_T, y) matrices for a set of vertex intervals. The efficiency corrected yield can then multiplied with these matrices. This should give the correct particle yield. Some example of these matrices are plotted in figure 8.7 on page 77. The most convenient combination of efficiency and acceptance correction needs some consideration.

Ideally the efficiency should also include the PID. This is not discussed in this thesis. It requires a good digitization algorithm and good digitization parameters for the TOFs, enabling the embedding method in the TOF raw data format. When this is done it can easily be implemented in the framework build for the efficiency analysis. Embedding could also be done on the other tracking and PID detectors, the DCs, C1 and RICH. Dependencies of particel type, momentum nad occupancy is also expected here.

8.5.1 Acceptance corrections

To understand, and correct for, what the detectors are able to measure, the geometric acceptance of the spectrometers must be determined. This is most easily calculated numerically for complex detector setups. Considering one detector in one setting provides an easy analystic example on how to get the theoretical geometric acceptance map as a function of p_T and y.

The transverse momentum can be represented as a function of rapidity for some fixed value of θ, and as another function of rapidity with a a fixed value of the velocity, which is uniquely determined by the energy if the mass is known. A fixed value of θ would correspond to a spectrometer setting and a fixed vertex position, and the velocity would limit the topmost particle identification capability. Consider figure 8.5. First p_T is expressed as a function of θ:

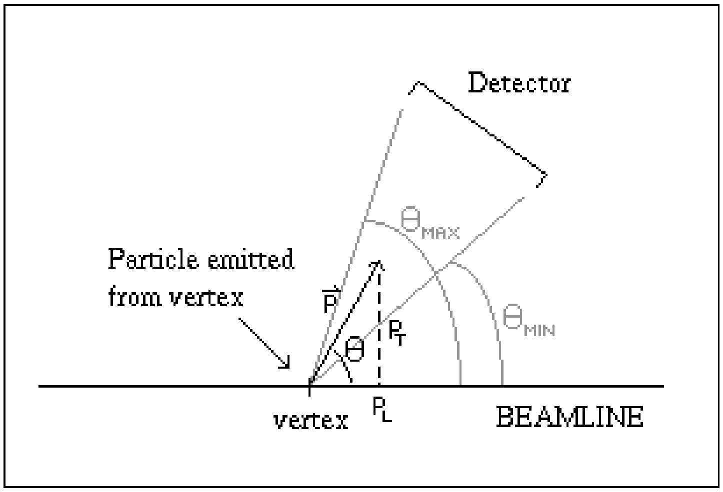

Figure 8.5: A Particle is emitted from vertex with momentum $\overrightarrow{P}$. The window of the detector is between θ_{max} and θ_{min}.

$$\sin\theta = \frac{P_T}{P} \tag{8.29}$$

Combining equation (2.12), (8.29) and the expression of momentum $pc = \sqrt{E^2 - m^2c^4}$, yields:

$$P = c\sqrt{m_T^2 \cosh^2 y - m^2} \tag{8.30}$$

P_T can now be expressed in terms of the mass m, θ and y:

$$\begin{aligned} P_T &= c \cdot \sin\theta \sqrt{m_T^2 \cosh^2 y - m^2} && (8.31) \\ P_T^2 &= c^2\left(\left(\frac{P_T^2}{c^2} + m^2\right)\cosh^2 y \cdot \sin^2\theta - m^2 \sin^2\theta\right) && (8.32) \\ P_T &= mc \cdot \frac{\sin\theta \cdot \sinh y}{\sqrt{1 - \cosh^2 y \cdot \sin^2\theta}} && (8.33) \end{aligned}$$

and If the particles have a constant energy E, some manipulation of equation (2.12) expresses P_T as:

$$P_T = \sqrt{\left(\frac{E}{c \cdot \cosh y}\right)^2 - m^2c^2} \tag{8.34}$$

If equations (8.33) and (8.34) are plotted twice in the same figure, with $\theta = \theta_{max}$, θ_{min} and $E = E_{max}$, E_{min}, it will look like figure 8.6 on page 76. The colored area in the figure is the acceptance of the detector, red for protons and blue for pions. Outside this area it can not measure any particles. The energy E_{max}, E_{min} is determined from the PID capability, and the θ_{max}, θ_{min} is determined from the maximum and minimum momentum determination capability in the magnets. The equations get quite complex with addition of magnets and PID detectors, i.e. θ would be a function of $\vec{p}$. The example shown is purely geometric for one tracking detector with no $\vec{B}$-field.

If more complex detector setup is considered, with e.g. magnets, the calculation gets much more complex, and doing the analysis in a "numerical" way is usually easier. Doing it in a "numerical" way would involve using simulation tools. The reason to do it like this is the complexity of the spectrometers. Both single detectors and spectrometer arms have an acceptance which depends on th angle, the magnetic field settings and the momentum for a given particle. The acceptance might also depend on the vertex position (e.g. the SiMA and TMA). In BRAHMS and many other experiments, finding the acceptance involves GEANT[11]. The essence of what is done is this:

One particle species at a time is thrown in well defined intervals in θ and ϕ. The particle is thrown in a momentum and solid angle interval covering at least the expected acceptance. The spectrometer is set at a fixed angle and with fixed magnetic fields. Throwing the particles from different vertex bins

---

[11] GEANT is introduced in section 4.1 on page 20.

is also necessary. An accepted track is a track which physically goes through the spectrometer and has enough valid hits in each subdetector. Matchability according to section 7.5 on page 49 may or may not be demanded.

The acceptance, A, is then calculated for all (p_T, y) values:

$$A(p_T, y) = \frac{N_{accepted}(p_T, y)}{N_{thrown}(p_T, y)} \tag{8.35}$$

and the corrected yield would be:

$$< Yield >_{acccorr} (p_T, y) = \frac{< Yield >_{raw} (p_T, y)}{A(p_T, y)} \tag{8.36}$$

If the acceptance is plotted as a function of transverse momentum and rapidity a window corresponding to figure 8.6 on the following page would appear. This has been done in BRAHMS by Peter Christiansen. Acceptance classes library and scripts for doing acceptance calculations are located in the BRAHMS CVS under *brahms_ app*. Some of his acceptance plots are shown in figure 8.7 on page 77. The plots are from a single $5\,cm$ vertex bin. When the vertex is varied, the narrow stripe in phase space is shifted a little in y, and a lesser degree in p_T.

Through these histograms the acceptance matrices are obtained. They enable the acceptance correction on the raw particle yield.

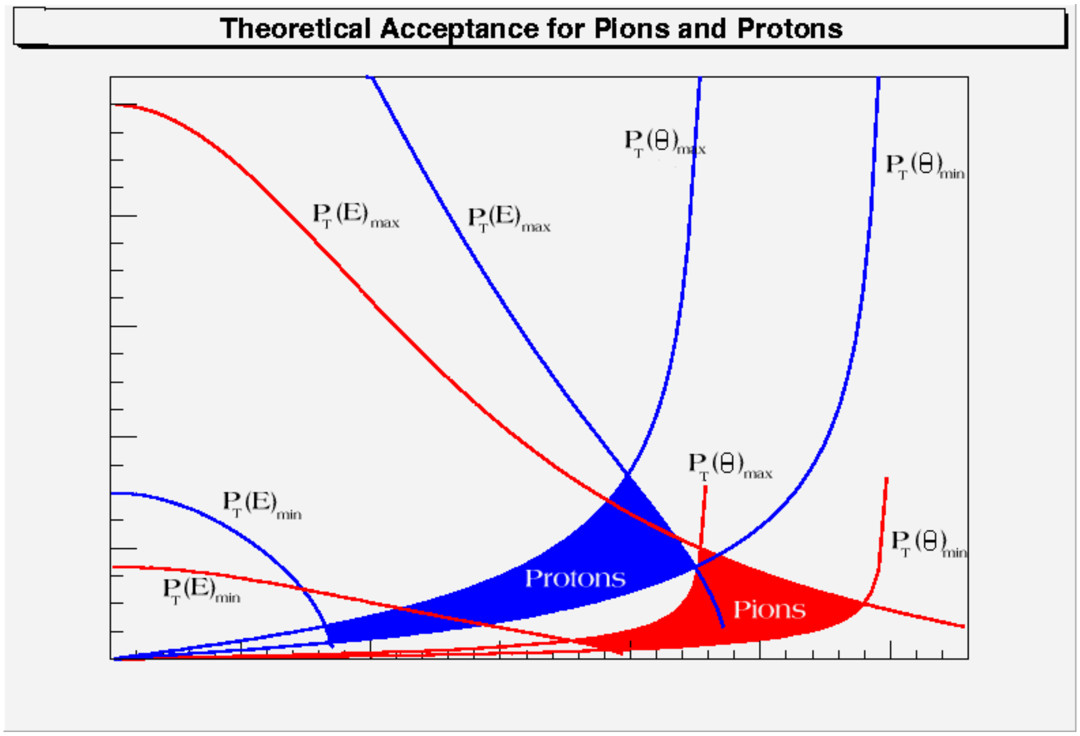

Figure 8.6: Theoretical acceptance plot. $P_{T,\theta_{max}}$ has θ as a constant with maximum value, $P_{T,\theta_{min}}$ has θ as a constant with minimum value for particle to pass the detector. The shaded area is the window where the detector can detect particles. Protons is shown in red and pions in blue.

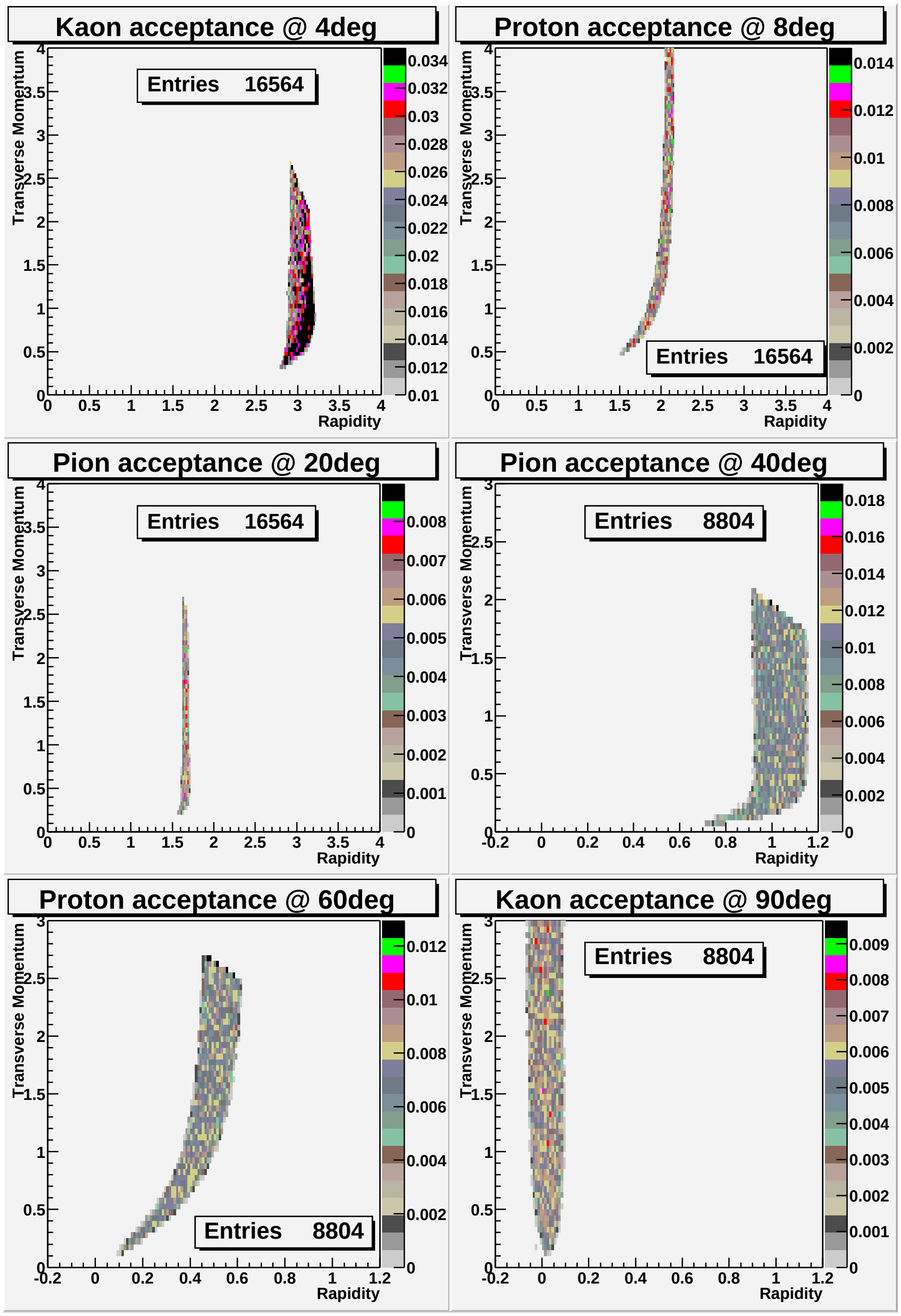

Figure 8.7: The real acceptance for a selection of settings in the FFS and MRS. The particles are thrown from a vertex bin between $-5\,cm$ and $0\,cm$.

Chapter 9

Efficiency results

First of all a clear definition of 100% efficiency is needed. In the analysis presented in this chapter the track reconstruction efficiency is relative to the tracks that physically goes through the spectrometer according to BRAG, has enough valid GEANT hits in both the front and back TPC, has the original PID from BRAG and comes from the primary vertex.

The efficiency for the spectrometers is presented in large matrices, p_T-y diagrams and as functions of centrality, the number of hits in the TPCs and the vertex position. The matrices are similar to the ones obtained for the acceptance of the spectrometers (see [8] for theoretical values). The vertical columns in these matrices are transverse momentum p_T and the horizontal are rapidity, y. There are three sets of matrices, one for each particle analyzed. The sets are divided into different centralities.

The analysis was done on 9 different settings, 4 for the MRS and 5 for the FFS. The settings are listed in table C.1 on page 158. There was a B-field in the magnets in most of the runs, but two runs of the FFS had an A-field. In the B-field π^+, K^+ and protons where used, and in the A-field π^-, K^- and antiprotons. Since the detectors are symmetric in design the assumption is that the efficiency for positive particles in a B-field will be the same for negatives in an A-field[1].

The first thing to look at is the relative overlap between the originally simulated digitized track, and the tracks found in the embedded event. When spectrometer tracks are considered the relative overlap in the front TPC is multiplied with the relative overlap in the back TPC. The criterion for a reconstructed track is a relative overlap bigger than 0.6, for both local and spectrometer tracks. Figure 9.1 on the next page shows the distribution overlaps between the embedded spectrometer track and all the reconstructed spectrometer tracks. Most particles have either a very high overlap or nearly nothing. At 0.6 the overlap drops nearly all the way down to zero, so this seemed a good lower limit

---

[1] This comparison has not been done in this thesis.

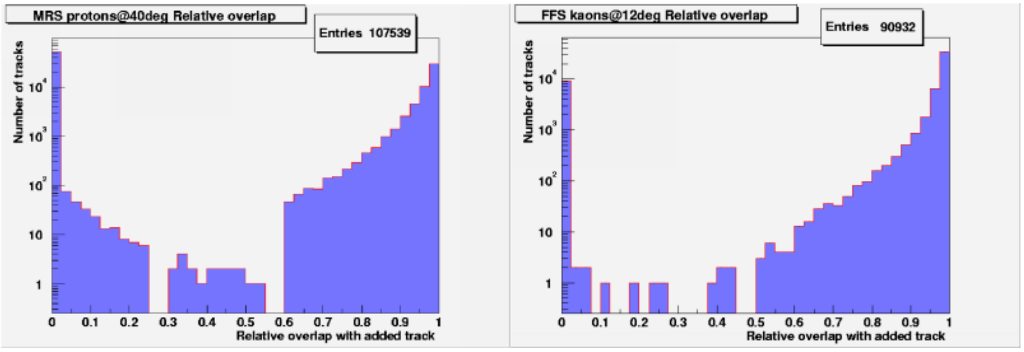

Figure 9.1: Relative overlap for proton and kaon spectrometer tracks at 40° and 12°, respectively. Note the log scale.

for the overlap criterion. Having established this value, the rest of the analysis can be done. The following sections shows the efficiency results using this value.

9.1 MRS efficiency as function of occupancy

In the MRS the first TPC is not behind a magnet. This makes the TPC experience very high occupancy in central events. There are clearly many more hits in this TPC than any other. A total of $\sim$ 1200 hits are normal for central events in the MRS, where most of them ($\sim$ 80%) comes from TPM1. The efficiency vs the number of hits and centrality is shown in figure 9.2 — 9.5. This efficiency is an average over all momenta thrown in this angle. The plots have been fitted with a first degree polynomial. The fit parameters *p0* and *p1* are shown in the histograms, $\varepsilon(H) = p0 + p1 \cdot H$, where H is the total number of hits TPM1 and TPM2. It is seen that increasing average energy deposition for each cluster (increasing mass for this momentum region) gives a better efficiency, i.e. protons are highest while pions are lowest, see table 9.1 on the following page. This is nevertheless small compared to the statistical uncertainties, which would suggest that the efficiency is approximately: $\varepsilon = 0.95 - H \cdot 10^{-4}$. Since there is a large difference between the number of hits in the different settings, the fit range for the polynomial is not the same. This might also suggest that the efficiency vs the number of hits is the same function for a specific particle in all the angle settings. The last row in table 9.1 on the next page shows a weighted average function for each particle. The trend is not the same for the efficiency vs centrality. The same centrality will give different occupancy in different spectrometer settings. Since the analyzed data is only trigger 6[2], the lowest centrality is $\sim$ 25%.

---

[2] See table 7.1 on page 43 for a description of the triggers.

Because of the strong dependence on the occupancy, efficiency corrections should be done using the occupancy.

	Pions	**Kaons**	**Protons**
40°	$0.950 - 9.8 \cdot 10^{-5} \cdot H$	$0.958 - 9.0 \cdot 10^{-5} \cdot H$	$0.976 - 9.5 \cdot 10^{-5} \cdot H$
52.5°	$0.956 - 11 \cdot 11^{-5} \cdot H$	$0.966 - 11 \cdot 10^{-5} \cdot H$	$0.956 - 7 \cdot 10^{-5} \cdot H$
60°	$0.947 - 11 \cdot 10^{-5} \cdot H$	$0.953 - 10 \cdot 10^{-5} \cdot H$	$0.949 - 6.8 \cdot 10^{-5} \cdot H$
90°	$0.945 - 7.4 \cdot 10^{-5} \cdot H$	$0.952 - 7.2 \cdot 10^{-5} \cdot H$	$0.956 - 6.0 \cdot 10^{-5} \cdot H$
W.Av.	$0.948 - 9.6 \cdot 10^{-5} \cdot H$	$0.955 - 9.0 \cdot 10^{-5} \cdot H$	$0.959 - 7.2 \cdot 10^{-5} \cdot H$

Table 9.1: Summary of efficiency vs total number of hits in the MRS. H is the number of hits. The uncertainties in the fit parameters are omitted, see figures 9.2 — 9.5. On average the constant has an statistical uncertainty of 0.004 and the slope $6 \cdot 10^{-6}$ in 40°, constant 0.004 and the slope 10^{-5} in 52.5°, constant 0.003 and the slope $8 \cdot 10^{-6}$ in 60° and constant 0.002 and the slope $7 \cdot 10^{-6}$ in 90°. The last line shows a weighted average function for each particle.

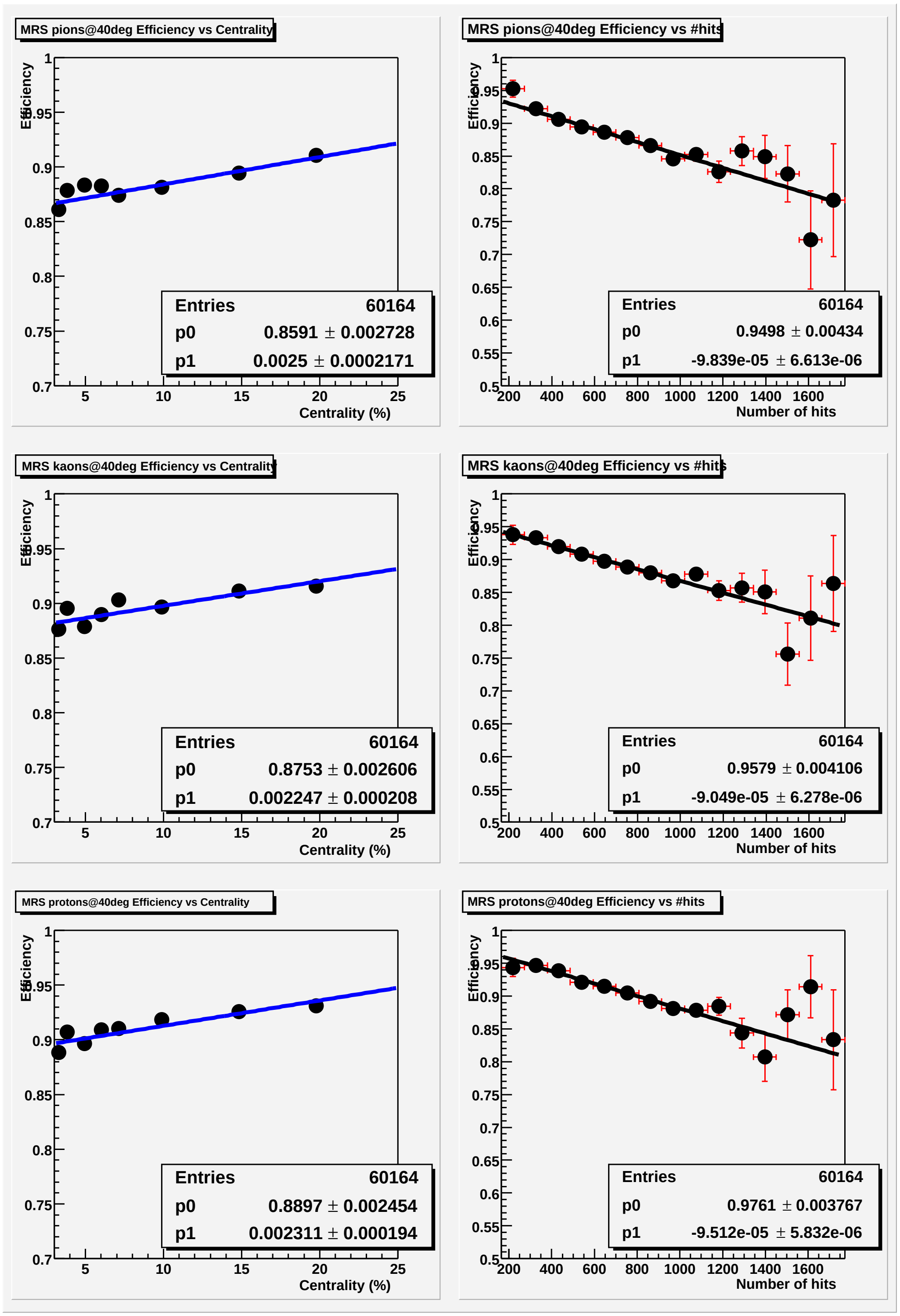

Figure 9.2: Efficiency vs centrality and number of hits at 40°.

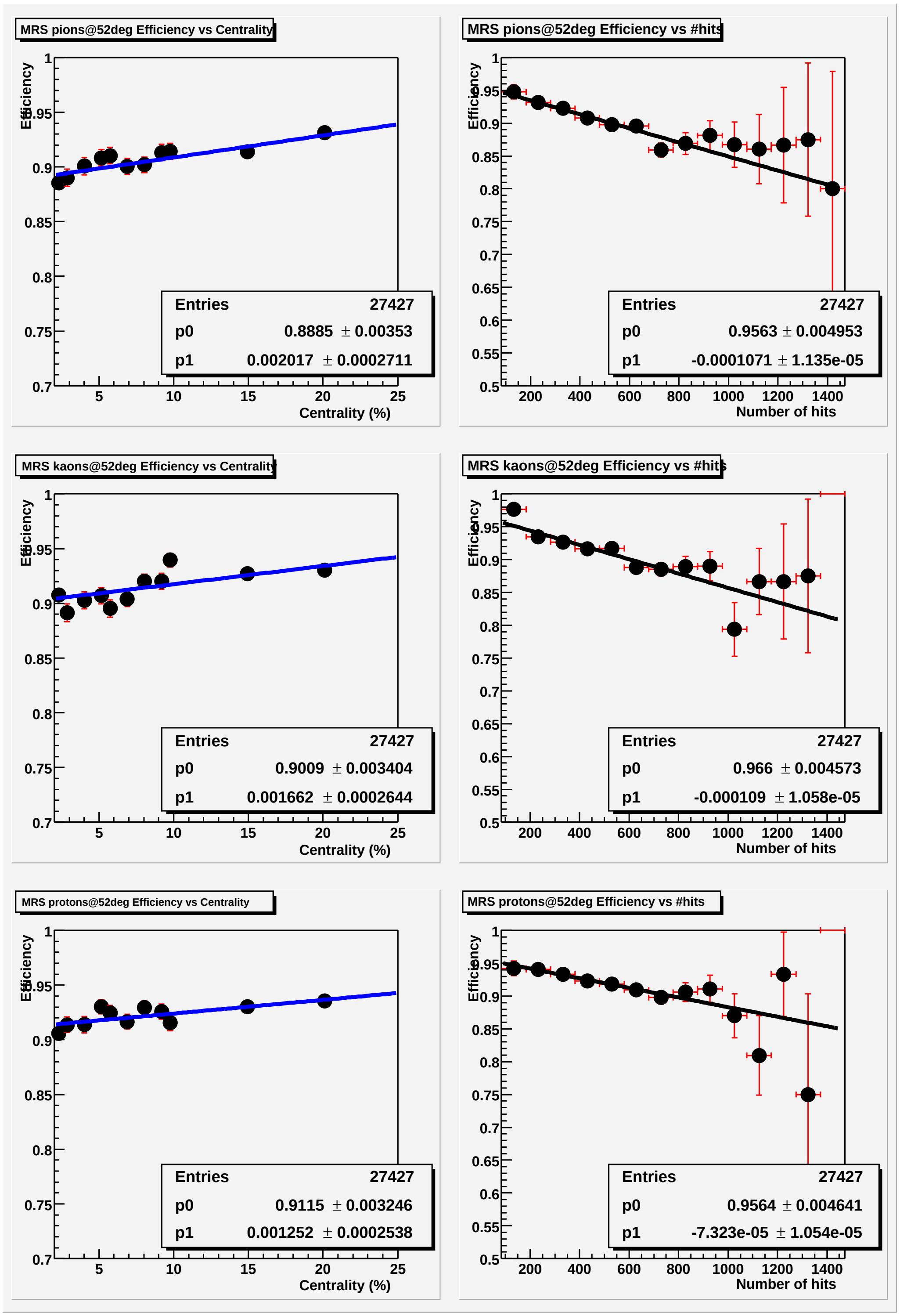

Figure 9.3: Efficiency vs centrality and number of hits at 52.5°.

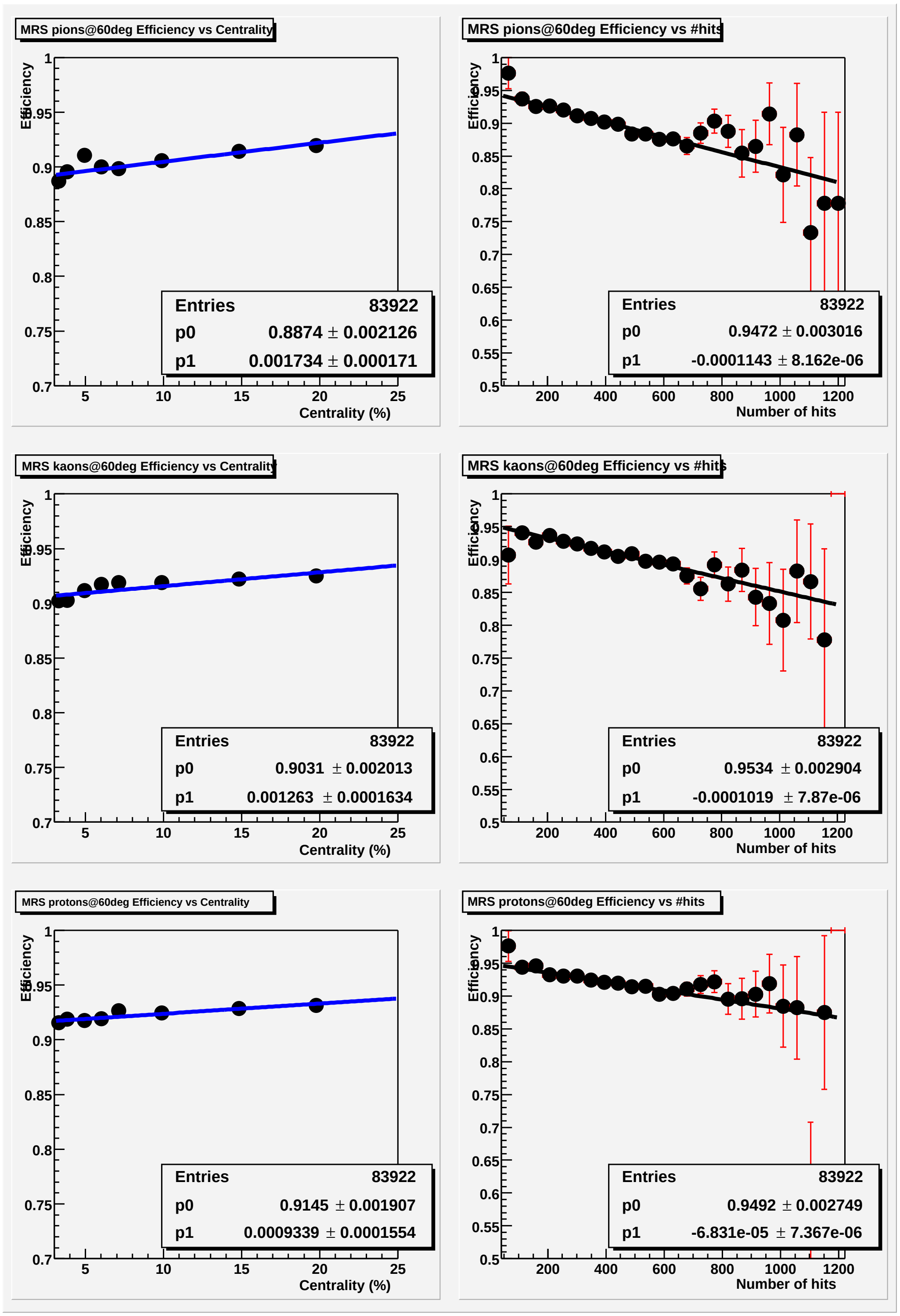

Figure 9.4: Efficiency vs centrality and number of hits at 60°.

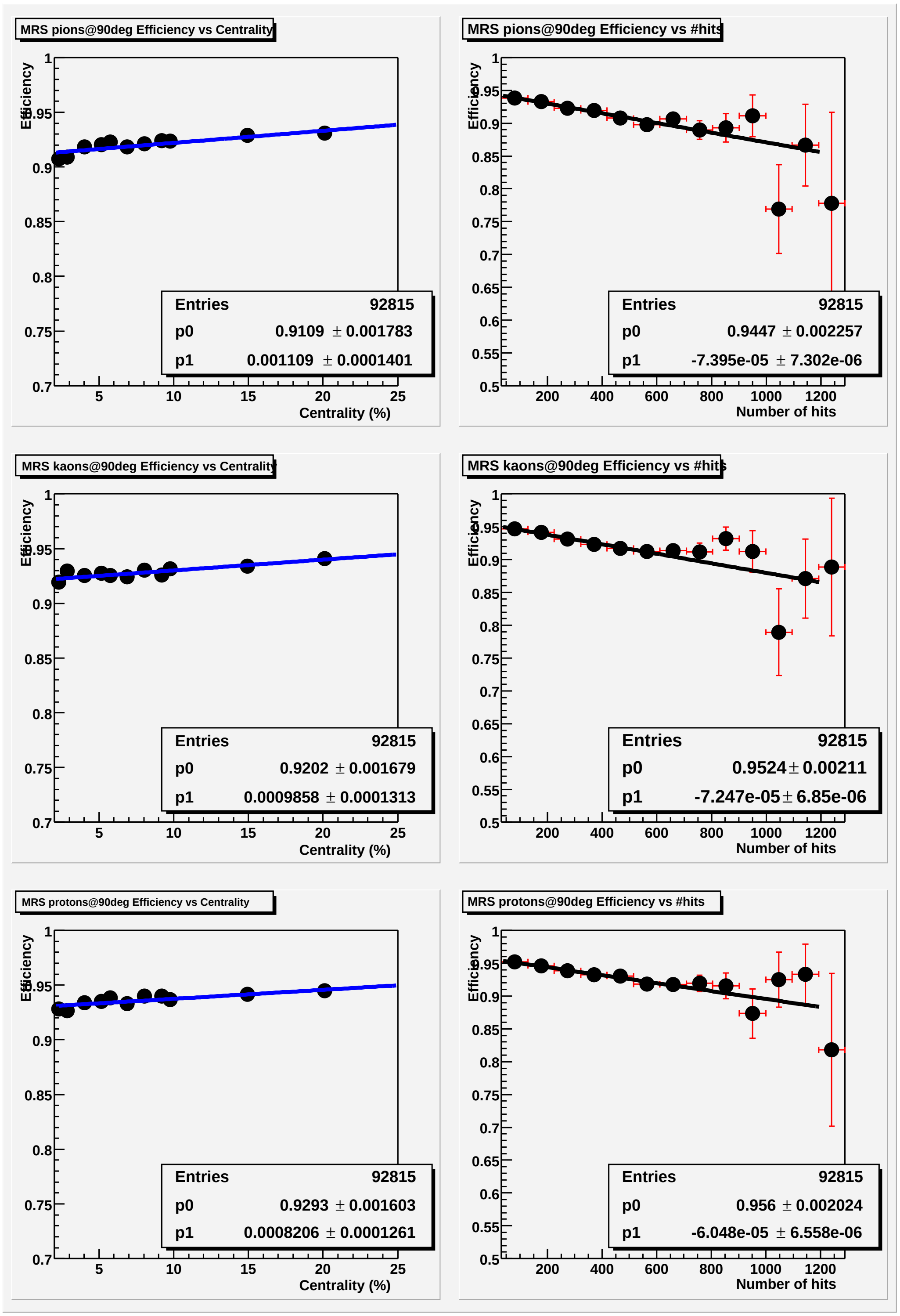

Figure 9.5: Efficiency vs centrality and number of hits at 90°.

	Pions	**Kaons**	**Protons**
3°	$0.965 - 22 \cdot 10^{-5} \cdot H$	$0.974 - 30 \cdot 10^{-5} \cdot H$	$0.965 - 29 \cdot 10^{-5} \cdot H$
4°	$0.975 - 14 \cdot 10^{-5} \cdot H$	$0.972 - 17 \cdot 10^{-5} \cdot H$	$0.980 - 21 \cdot 10^{-5} \cdot H$
8°	$0.963 - 13 \cdot 10^{-5} \cdot H$	$0.968 - 23 \cdot 10^{-5} \cdot H$	$0.963 - 12 \cdot 10^{-5} \cdot H$
12°	$0.977 - 6 \cdot 10^{-5} \cdot H$	$0.973 - 9 \cdot 10^{-5} \cdot H$	$0.980 - 13 \cdot 10^{-5} \cdot H$
20°	$0.961 + 4 \cdot 10^{-5} \cdot H$	$0.962 - 1 \cdot 10^{-5} \cdot H$	$0.968 - 9 \cdot 10^{-5} \cdot H$

Table 9.2: Summary of efficiency vs total number of hits in the FFS. H is the number of hits. The uncertainties in the fit parameters are omitted, see figures 9.7 — 9.11. On average the constant has an statistical uncertainty of 0.0045 and the slope $1.5 \cdot 10^{-5}$ in 3°, constant 0.0025 and the slope $1 \cdot 10^{-5}$ in 4°, constant 0.004 and the slope $4 \cdot 10^{-5}$ in 8°, constant 0.001 and the slope $2 \cdot 10^{-5}$ in 12° and constant 0.0015 and the slope $3.5 \cdot 10^{-5}$ in 20°. The positive sign in the slope parameter for pions at 20° seems to suggest that the efficiency increases with the occupancy. Looking at the uncertainty in the parameter would rather suggest that the efficiency is constant.

	Pions	**Kaons**	**Protons**
3°	$0.935(\pm 3) - 0.013(\pm 1) \cdot T$	$0.921(\pm 3) - 0.013(\pm 1) \cdot T$	$0.920(\pm 3) - 0.025(\pm 1) \cdot T$
4°	$0.967(\pm 2) - 0.012(\pm 1) \cdot T$	$0.963(\pm 2) - 0.016(\pm 1) \cdot T$	$0.963(\pm 2) - 0.015(\pm 1) \cdot T$
8°	$0.974(\pm 3) - 0.018(\pm 3) \cdot T$	$0.975(\pm 4) - 0.023(\pm 3) \cdot T$	$0.970(\pm 4) - 0.014(\pm 3) \cdot T$
12°	$0.986(\pm 2) - 0.012(\pm 2) \cdot T$	$0.987(\pm 2) - 0.017(\pm 2) \cdot T$	$0.993(\pm 2) - 0.019(\pm 2) \cdot T$
20°	$0.971(\pm 3) - 0.010(\pm 3) \cdot T$	$0.971(\pm 3) - 0.011(\pm 3) \cdot T$	$0.980(\pm 3) - 0.017(\pm 3) \cdot T$

Table 9.3: Summary of efficiency vs total number of tracks in the FFS. T is the number of tracks.

9.2 FFS efficiency as function of occupancy

The FFS is really bombarded with high energy particles at small angles. The D1 magnet strongly limits the number of particles getting into the TPCs. The FFS does not have more than about $\sim$ 700 hits for central events at the smallest angles, going down to about $\sim$ 160 at 20°. Figure 9.7 — 9.11 shows the efficiency vs centrality and the total number of hits in the TPC. The results are summarized in table 9.2. This spectrometer behaves pretty much the same as the MRS, discussed in previous section. As the angle decreases the efficiency falls faster and faster with increasing occupancy. This seems a bit strange, since a fixed occupancy is expected to have the same efficiency regardless of where the spectrometer is situated, which is the case for the MRS. The trend in table 9.2 seems significant.

The efficiency vs the number of tracks, should then show the same behavior, since the number of spectrometer tracks should be proportional to the number of hits. Table 9.3 shows that there does not seem to be such a correlation.

The reason for this might be that the number of hits is not proportional to the number of tracks. Figure 9.6 shows the number of hits as a function of the number of tracks. The figure clearly indicates a linear dependence. But there seems to be a trend that the average number of hits pr track gets a little lower when there are many tracks. This might not be statistically significant since the first degree polynomial goes through all the statistical error bars, and has a low χ^2. The reason for the reduced number of hits in high occupancy events might be that when the track density gets high there may be many overlapping hits. If these overlapping hits have clearly separated peaks they will be deconvoluted into two (or more) hits. If they overlap too much they will not be deconvoluted, and there will therefore be less found hits than real hits. This will give an artificial increase in *p1*, in table 9.3 on the page before, as the found occupancy increases.

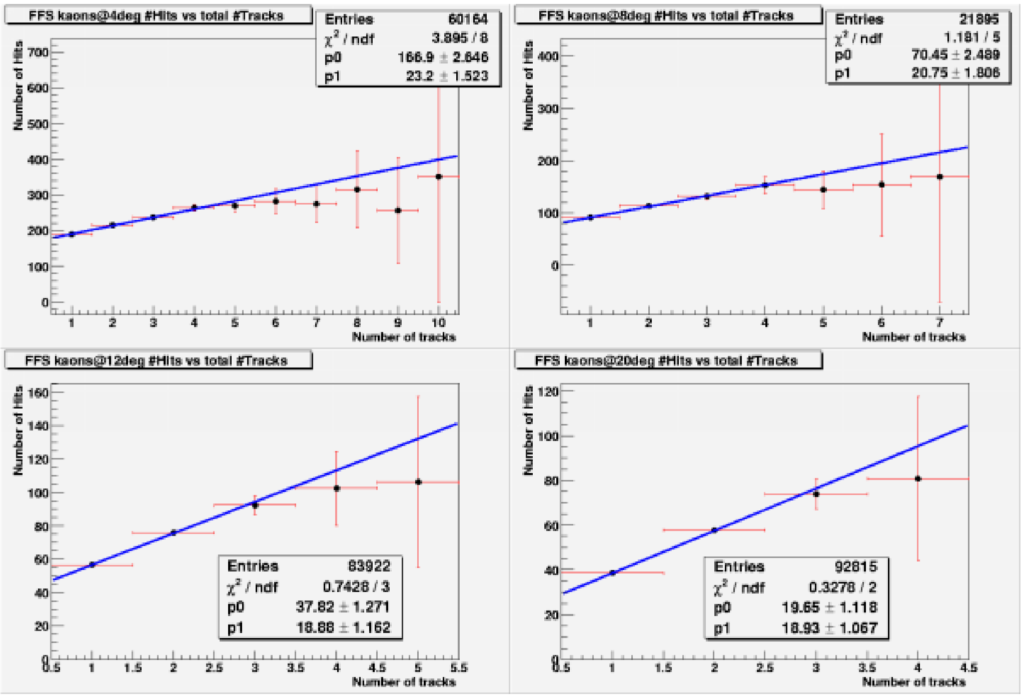

Figure 9.6: The number of hits vs the number of FFS tracks for kaons.

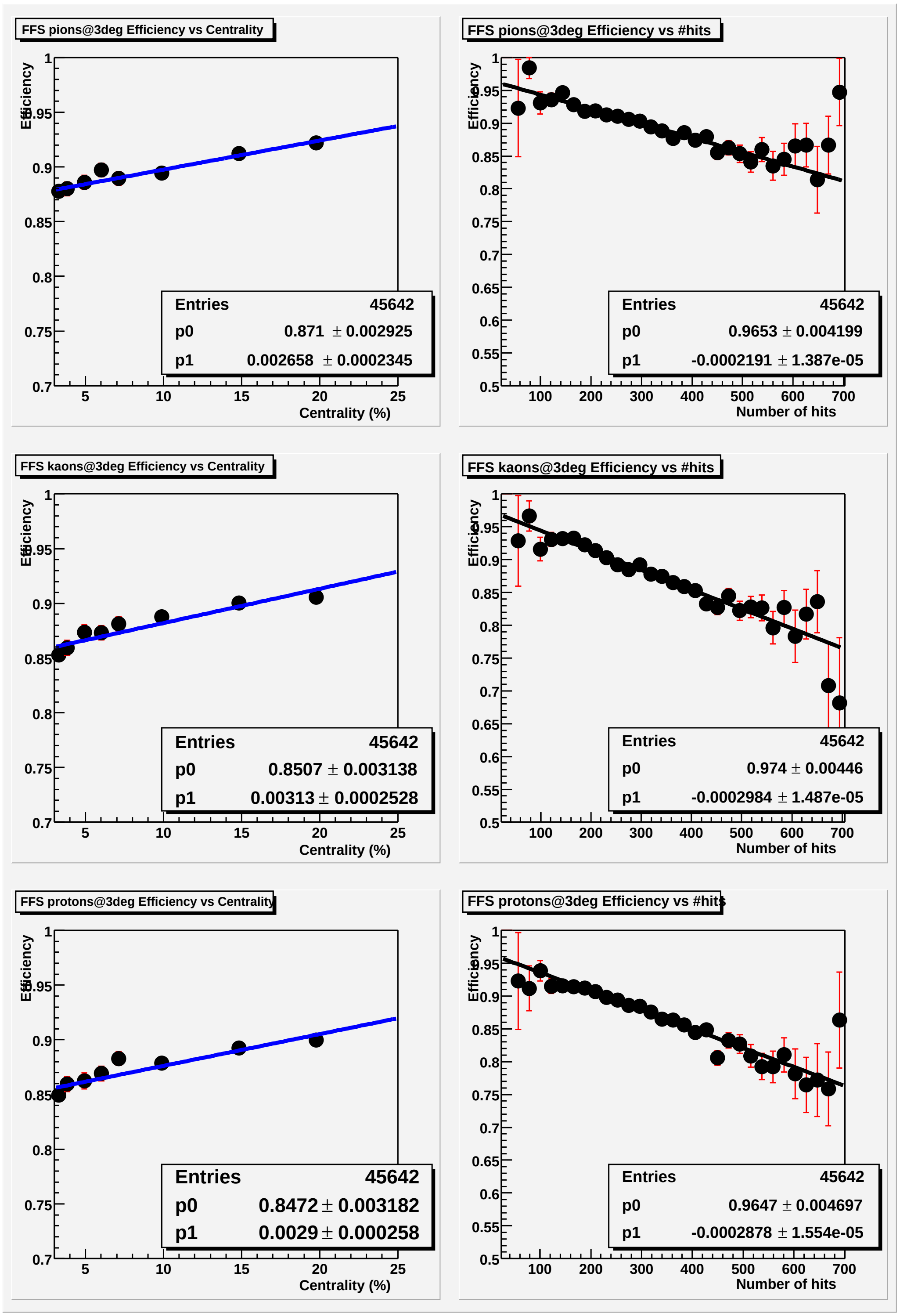

Figure 9.7: Efficiency vs centrality and number of hits at 3°.

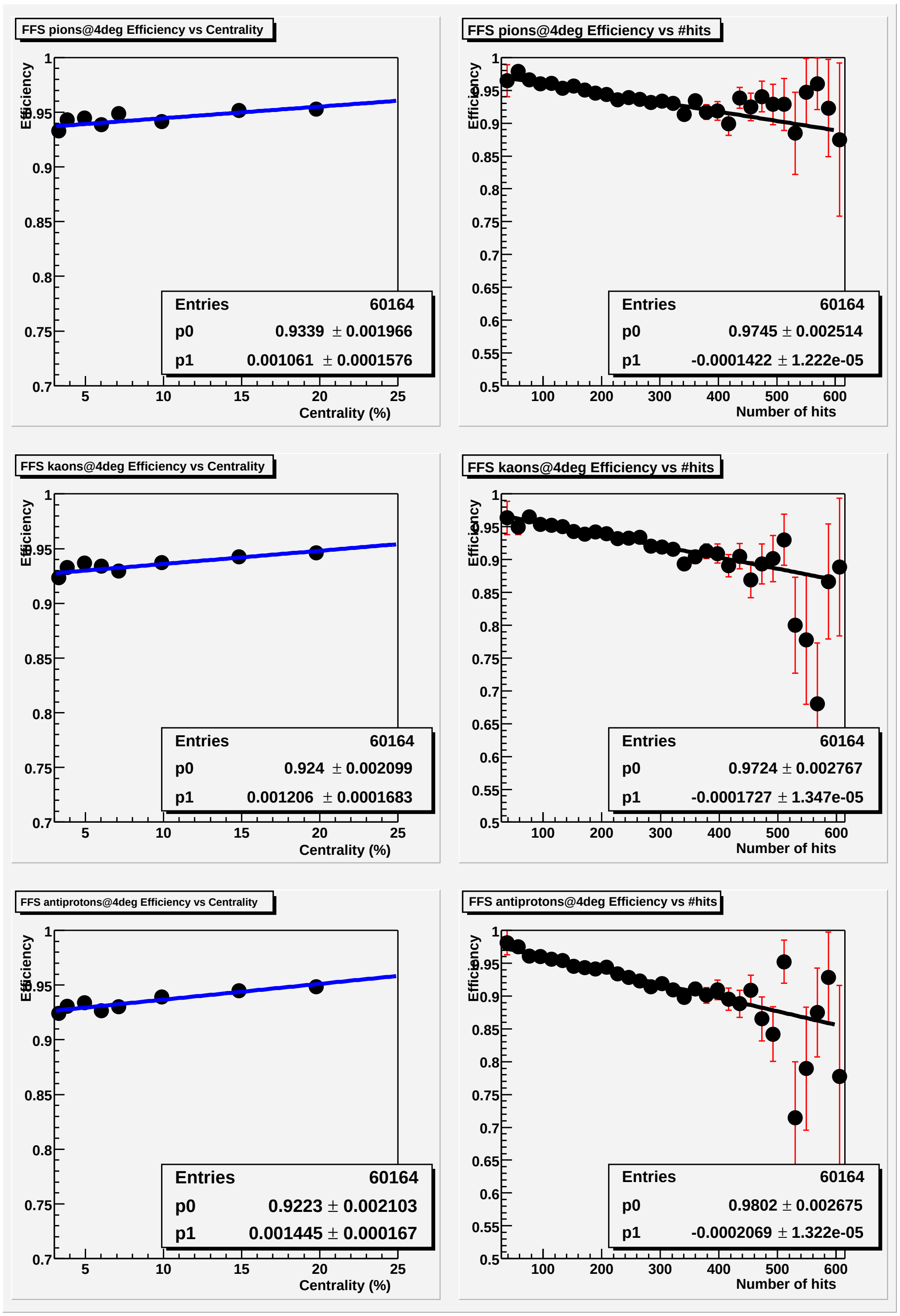

Figure 9.8: Efficiency vs centrality and number of hits at 4°.

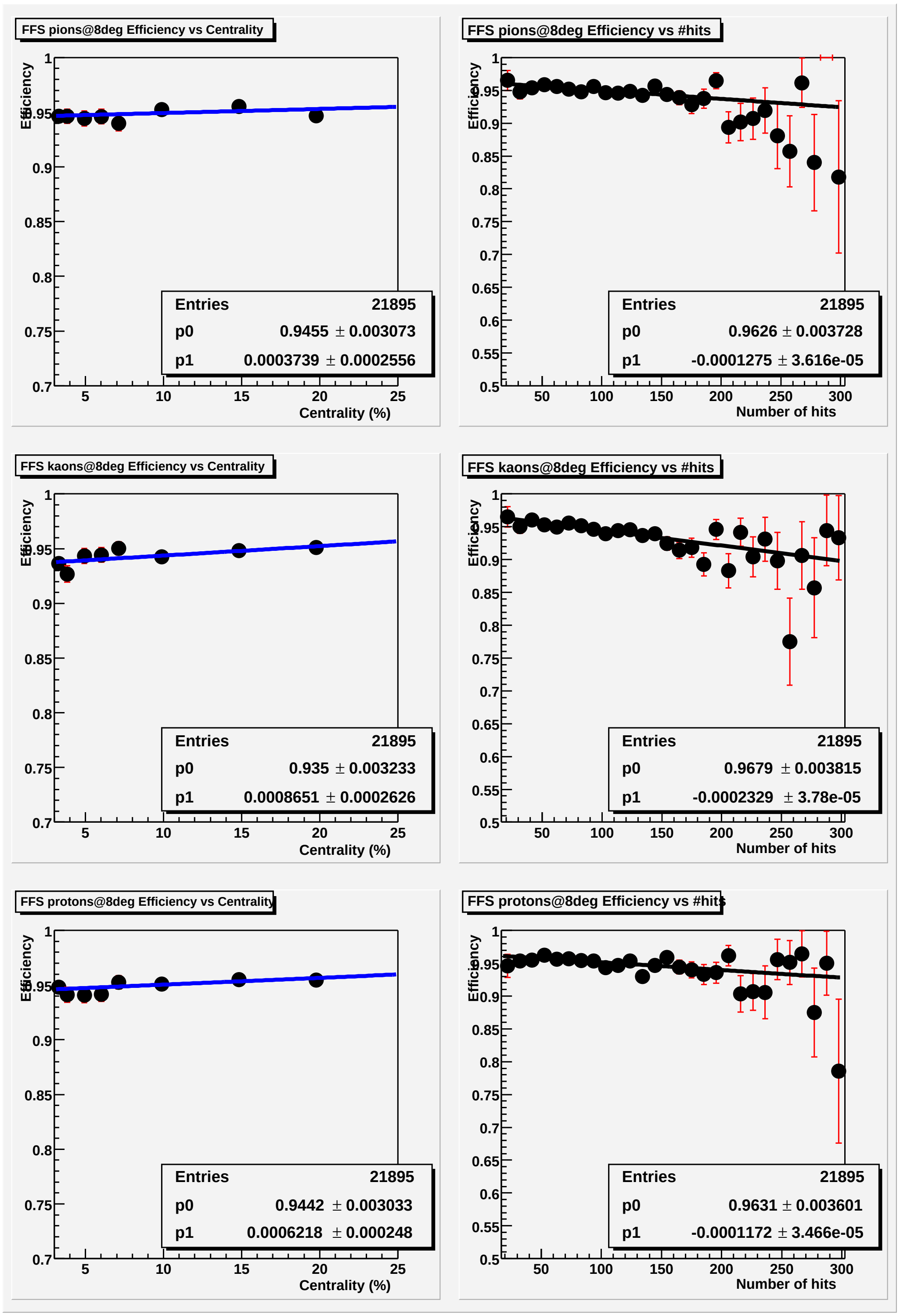

Figure 9.9: Efficiency vs centrality and number of hits at 8°.

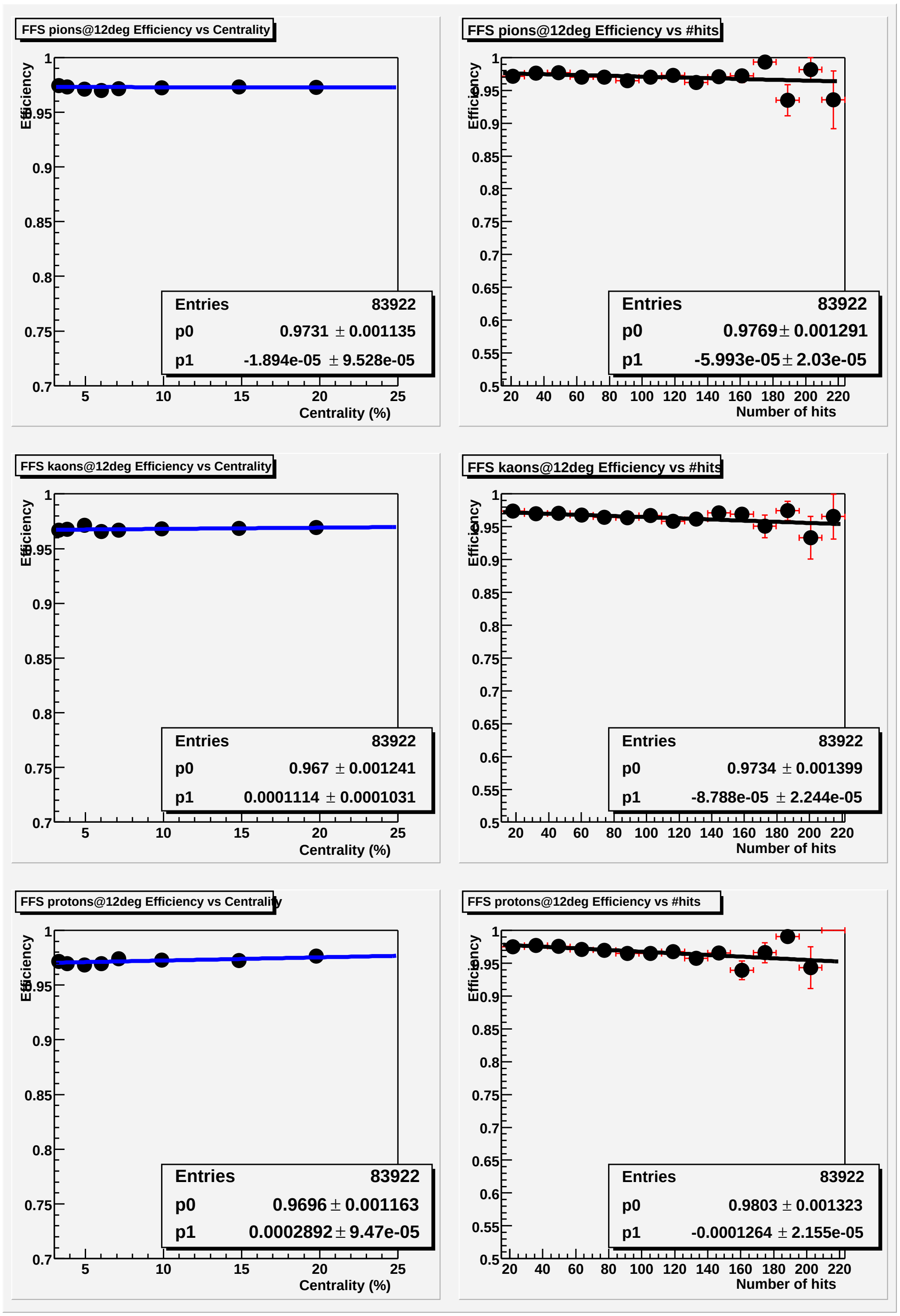

Figure 9.10: Efficiency vs centrality and number of hits at 12°.

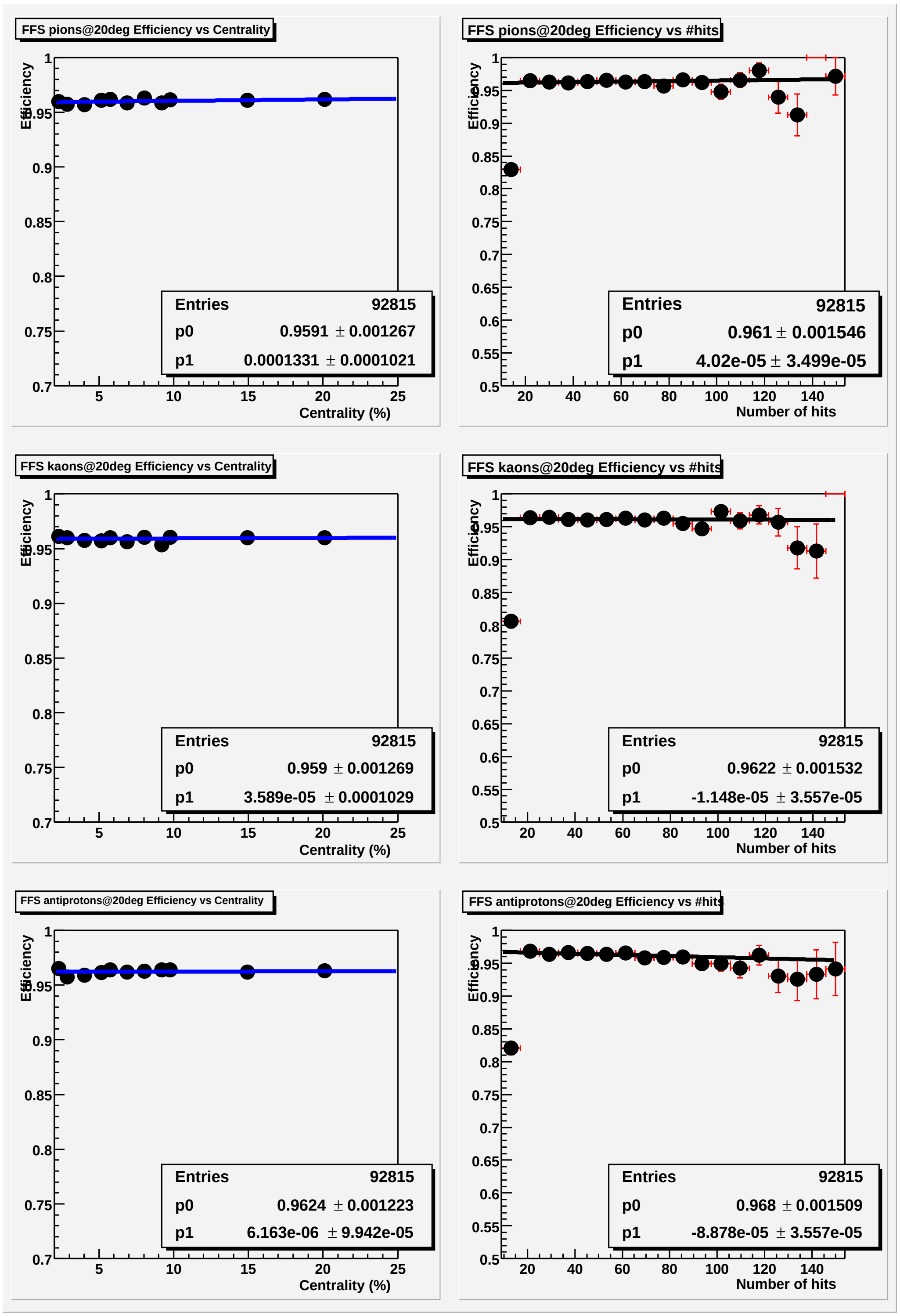

Figure 9.11: Efficiency vs centrality and number of hits at 20°.

9.3 Efficiency vs vertex position

The analysis in this section is averaged over all momenta and centralities. The efficiency shows only a weak dependence on the vertex z position. Figure 9.12 shows a sample of the efficiency vs the vertex position. All the figures were fitted with a first degree polynomial, but could also be fitted with a constant, without changing the χ^2 much. The trend seems to be that in most cases there is a decrease in efficiency as the vertex z value increases. The pions at 60° behaves opposite. The difference in efficiency will be $\sim 1\%$ between $15\,cm$ and $-15\,cm$, which is the values used in published results from BRAHMS.

The efficiency could of course be corrected for this as well, but the systematic uncertainties are much bigger than the observed variation with vertex, see section 9.8 on page 124, and it might therefore not be required.

The seen effects in figure 9.12 might be caused by lower track densities when the z value is negative, since there will be a smaller effective acceptance. The opposite should then happen when z is positive. This effect might be reduced a bit, since η is higher when z is negative than when z is positive for a fixed spectrometer setting. If this is what happens, then the MRS at 90° should show a symmetric efficiency vs the vertex position. This is not the case. In the bottom right part of figure 9.12 the efficiency falls with increasing vertex position.

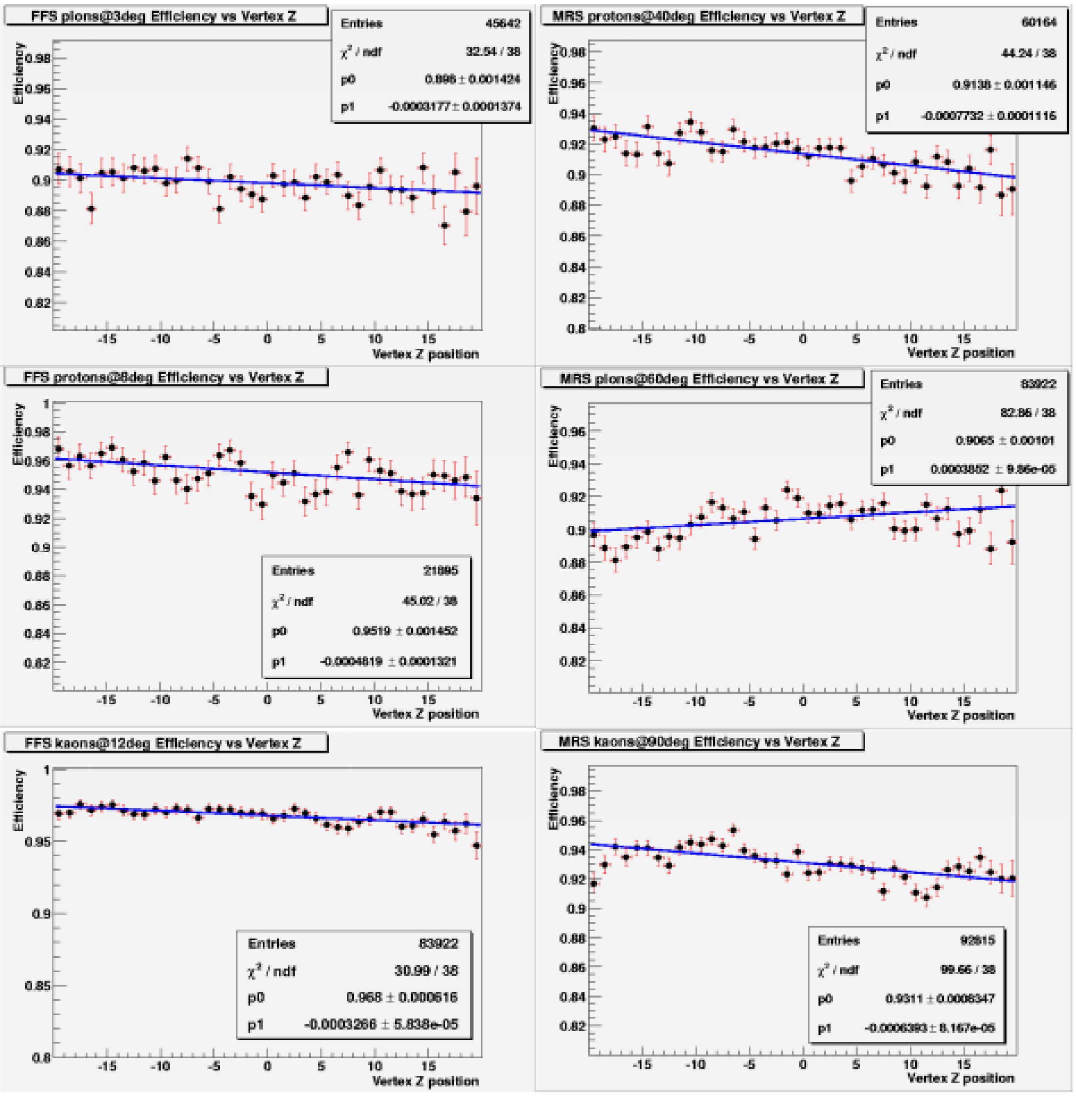

Figure 9.12: Selected plots of the efficiency vs the vertex position.

9.4 The efficiency vs P_T and y

First, lets look at the efficiency vs the momentum. This is shown in figure 9.13. Low momentum particles tends to get bigger residuals than high momentum particles, due to multiple scattering. The χ^2 of these low momentum tracks can get big. This will then lead to a bigger probability for the matching algorithm to fail, hence the efficiency will also drop.

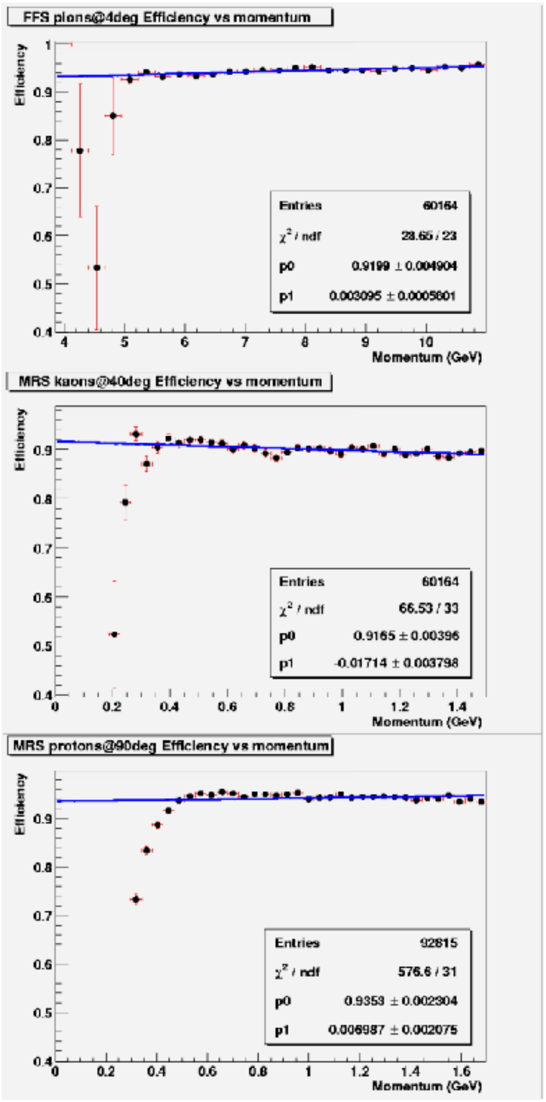

Figure 9.13: Efficiency vs p for pions at 4°, kaons at 40° and protons at 90°. The efficiency falls off, as expected, at low momentum. The momentum is that provided by BRAG.

The momentum value is specified by BRAG, so even if the matching algorithm fails, the momentum of the not reconstructed particle is known. As seen in the figure, the efficiency drops off at low momentum, as expected. A weak additional dependence reflecting the $<\frac{dE}{dx}>$ variation with the momentum may also be present. This effect is small, and the figures could as well have been fitted with a constant as a first degree polynomial.

The efficiency vs rapidity shows the same behavior, dropping down at the edges of the setting's "preferred" rapidity values. They are therefore not shown.

Section 8.5.1 on page 73 shows acceptance plots which are usually plotted against the transverse momentum and the rapidity. Efficiency results have also been represented as (p_T, y) matrices. If these histograms are multiplied together, it is easy to correct for both acceptance and efficiency at the same time.

Figures 9.14 — 9.19 are essentially a summary of the efficiency. The efficiency is shown summed over all centralities and vertices for each particle and for a selection of centrality bins and particles. The centrality histograms have many bins and the statistics is not good enough to make a sufficiently small statistical uncertainty in each $(p_T, y, centrality)$

bin, to be used in an efficiency correction. The average statistical uncertainty is about $\sim 10\%$. For the actual efficiency corrections higher statistics should be obtained. These figures are shown for their illustration purposes.

The first three histograms have better statistics and have an uncertainty of about $\sim 5\%$. The "banana" shaped bands in the figures shows the following settings from left to right, $90°$, $60°$, $52.5°$, $40°$, $20°$, $12°$, $8°$, $4°$ and $3°$. The $52.5°$ setting completely fills the gap between the $60°$ and $40°$ setting. The $12°$ "banana" are actually two runs with different magnetic fields, and is the only place where two runs with different magnetic setting are mixed in this thesis, see table C.1 on page 158. The $4°$ and $3°$ also overlap in phase space. The $4°$ setting sits higher in p_T than the $3°$, because it had a higher magnetic field. Table 9.4 — 9.6 shows a sample of the efficiencies from figure 9.14 — 9.16.

The cloud of particles seen between $8°$ and $4°/3°$, especially in the pions and kaons histograms, needs some explanation. There are even some with higher rapidity in the $3°$ setting. The particles in question have a rapidity between 2.75 and 3.0 and transverse momentum between $0.25\,GeV$ and $1.2\,GeV$. Since these values are those provided by BRAG, and these particles should not be able to go through the spectrometer, something must have happened to them on their way to the spectrometer. Their reconstructed momentum and rapidity may therefore be within the acceptance of the spectrometer. This problem is not understood at the moment of writing and needs further investigation. However, the number of such "anomalous" particles is small enough not to influence the general conclusions from the efficiency analysis.

$P_T(GeV)$	$0.1\,GeV$	$0.3\,GeV$	$0.5\,GeV$	$0.7\,GeV$	$0.9\,GeV$	$1.1\,GeV$	$1.3\,GeV$
$Y = 0.02$	74(±9)	88.0(±3)	91.9(±2)	92.9(±2)	93.2(±2)	93.8(±2)	0.0(±0)
$Y = 0.52$	51(±3)	81.0(±4)	89.4(±3)	91.8(±2)	92.5(±2)	93.4(±2)	92.6(±6)
$Y = 0.72$	69(±3)	84.6(±7)	90.0(±5)	91.2(±5)	92.3(±4)	92.5(±4)	92.5(±4)
$Y = 0.95$	66(±1)	85.9(±3)	89.1(±3)	90.1(±2)	90.3(±3)	87(±1)	0.0(±0)
$Y = 1.69$	0.0(±0)	92.2(±4)	95.6(±1)	96.4(±1)	96.7(±1)	96.6(±2)	0.0(±0)
$Y = 2.20$	83(±15)	94.5(±4)	96.2(±2)	96.7(±1)	97.2(±1)	97.5(±1)	97.8(±1)
$Y = 2.56$	0.0(±0)	93.7(±4)	95.1(±2)	95.4(±3)	87(±12)	0.0(±0)	0.0(±0)
$Y = 3.23$	0.0(±0)	93.8(±4)	94.3(±2)	94.5(±1)	95.2(±2)	96(±4)	0.0(±0)
$Y = 3.42$	87(±1)	89.2(±2)	90.3(±2)	90.7(±5)	50(±35)	0.0(±0)	0.0(±0)

Table 9.4: Efficiency vs p_T and y summed over all centralities and vertices for pions. The rapidity is the average for each "banana". The "banana" is divided into 7 p_T bins. The efficiency for each such bin is shown in the table. Numbers are given in %. Errors are given for the last digits.

P_T	$0.1\,GeV$	$0.3\,GeV$	$0.5\,GeV$	$0.7\,GeV$	$0.9\,GeV$	$1.1\,GeV$	$1.3\,GeV$
$Y = 0.01$	83(±15)	88.2(±4)	93.7(±2)	93.3(±2)	93.3(±2)	93.5(±2)	0.0(±0)
$Y = 0.45$	55(±8)	82.9(±5)	91.6(±3)	92.3(±2)	92.2(±2)	92.5(±2)	92.3(±5)
$Y = 0.64$	62(±6)	91.8(±7)	92.2(±5)	91.0(±5)	92.3(±4)	92.3(±4)	91.8(±4)
$Y = 0.80$	85(±2	91.4(±3)	89.9(±3)	89.8(±2)	89.4(±2)	88(±1)	0.0(±0)
$Y = 1.51$	70(±14)	94.6(±4)	95.7(±1)	96.0(±1)	96.2(±1)	95.7(±2)	0.0(±0)
$Y = 2.06$	0.0(±0)	94.2(±4)	95.9(±2)	96.1(±1)	96.6(±1)	97.0(±1)	97.2(±1)
$Y = 2.27$	0.0(±0)	93.9(±4)	94.4(±2)	94.7(±3)	89(±7)	0.0(±0)	0.0(±0)
$Y = 3.00$	73(±7)	92.5(±5)	93.4(±2)	93.8(±2)	94.2(±2)	90(±4)	0.0(±0)
$Y = 3.01$	85(±1)	88.1(±2)	88.3(±2)	89.0(±5)	71(±11)	0.0(±0)	0.0(±0)

Table 9.5: Efficiency vs p_T and y summed over all centralities and vertices for kaons. The rapidity is the average for each “banana”. The “banana” is divided into 7 p_T bins. The efficiency for each such bin is shown in the table. Numbers are given in %. Errors are given for the last digits.

P_T	$0.1\,GeV$	$0.3\,GeV$	$0.5\,GeV$	$0.7\,GeV$	$0.9\,GeV$	$1.1\,GeV$	$1.3\,GeV$
$Y = 0.01$	0.0(±0)	81.2(±6)	93.5(±2)	95.0(±2)	95.0(±2)	94.4(±2)	94.4(±2)
$Y = 0.39$	0.0(±0)	74.7(±7)	90.4(±3)	93.8(±2)	93.7(±2)	94.1(±2)	93.6(±2)
$Y = 0.55$	0.0(±0)	86.6(±9)	94.5(±4)	93.6(±4)	93.2(±4)	92.3(±5)	92.2(±5)
$Y = 0.68$	79(±8)	92.0(±3)	93.0(±3)	90.8(±3)	91.4(±3)	90.6(±3)	91.0(±3)
$Y = 1.29$	0.0(±0)	94.0(±4)	95.8(±1)	96.6(±1)	96.4(±1)	96.3(±2)	96.7(±2)
$Y = 1.86$	50(±35)	95.5(±4)	96.2(±2)	96.8(±1)	96.9(±1)	97.3(±1)	97.4(±1)
$Y = 1.99$	0.0(±0)	93.5(±5)	95.2(±3)	95.6(±3)	95.0(±3)	95.5(±6)	0.0(±0)
$Y = 2.59$	87(±1)	87.2(±3)	87.7(±3)	88.1(±3)	90.2(±1)	0.0(±0)	0.0(±0)
$Y = 2.70$	0.0(±0)	93.3(±5)	93.4(±2)	93.8(±2)	93.9(±2)	94.1(±4)	92(±7)

Table 9.6: Efficiency vs p_T and y summed over all centralities and vertices for protons. The rapidity is the average for each “banana”. The “banana” is divided into 7 p_T bins. The efficiency for each such bin is shown in the table. Numbers are given in %. Errors are given for the last digits.

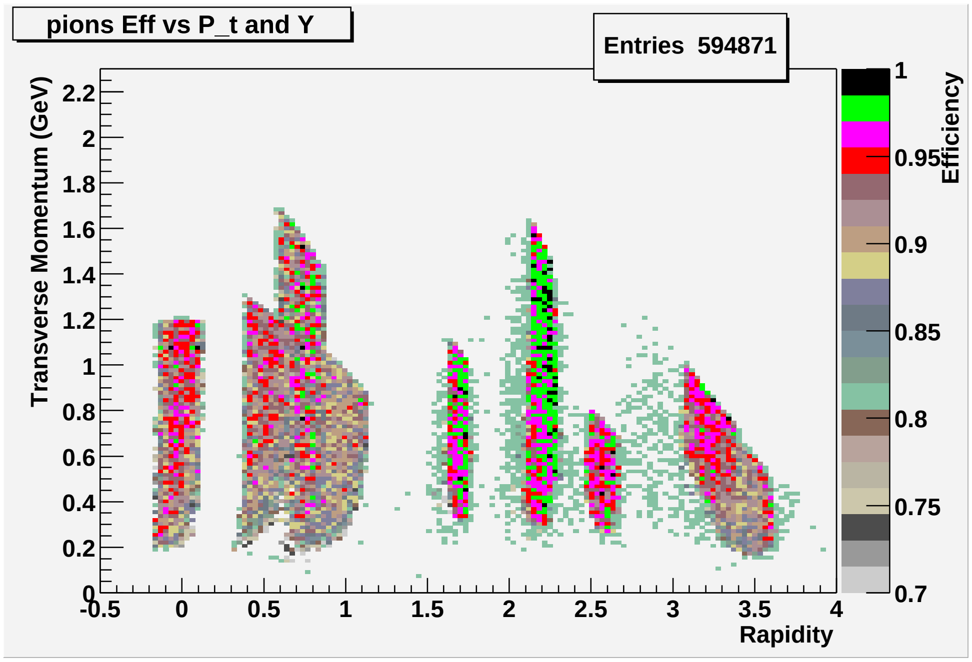

Figure 9.14: Efficiency vs P_T and Y for pions.

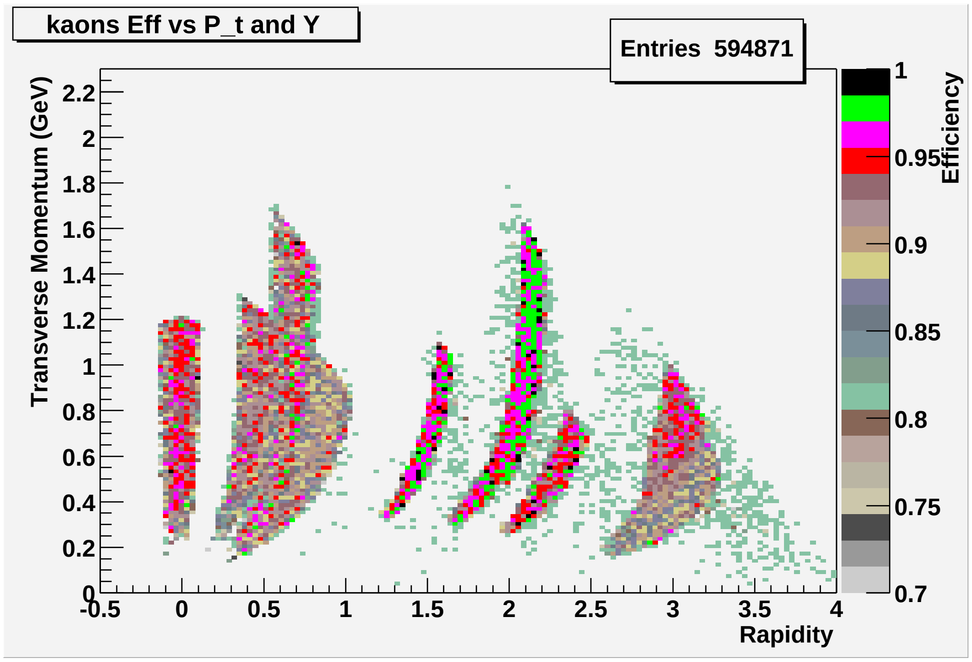

Figure 9.15: Efficiency vs P_T and Y for kaons.

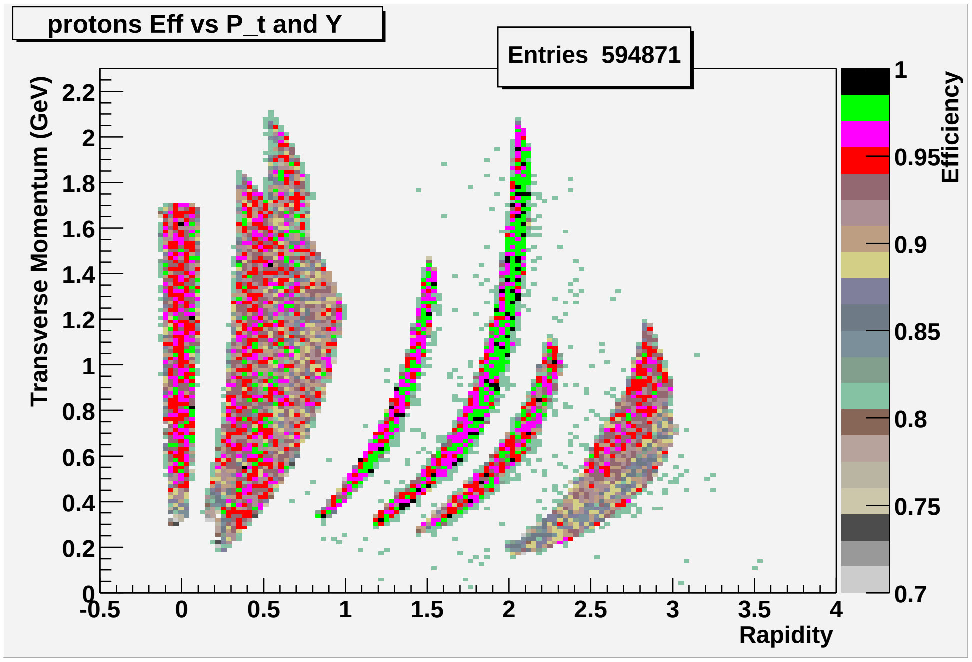

Figure 9.16: Efficiency vs P_T and Y for protons.

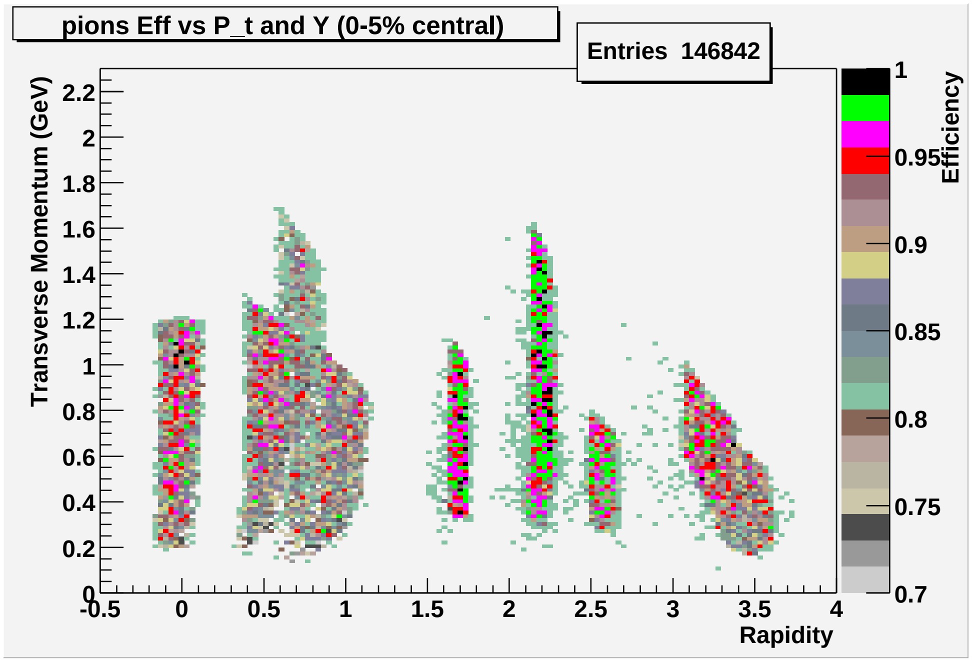

Figure 9.17: Efficiency vs P_T and Y for 5% most central pions.

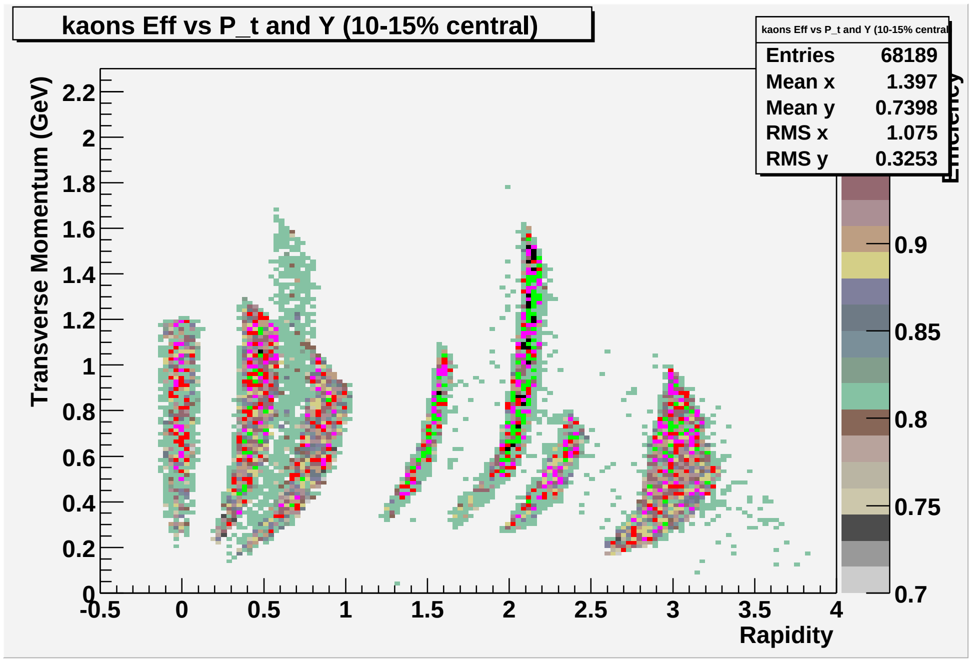

Figure 9.18: Efficiency vs P_T and Y for 15% most central kaons.

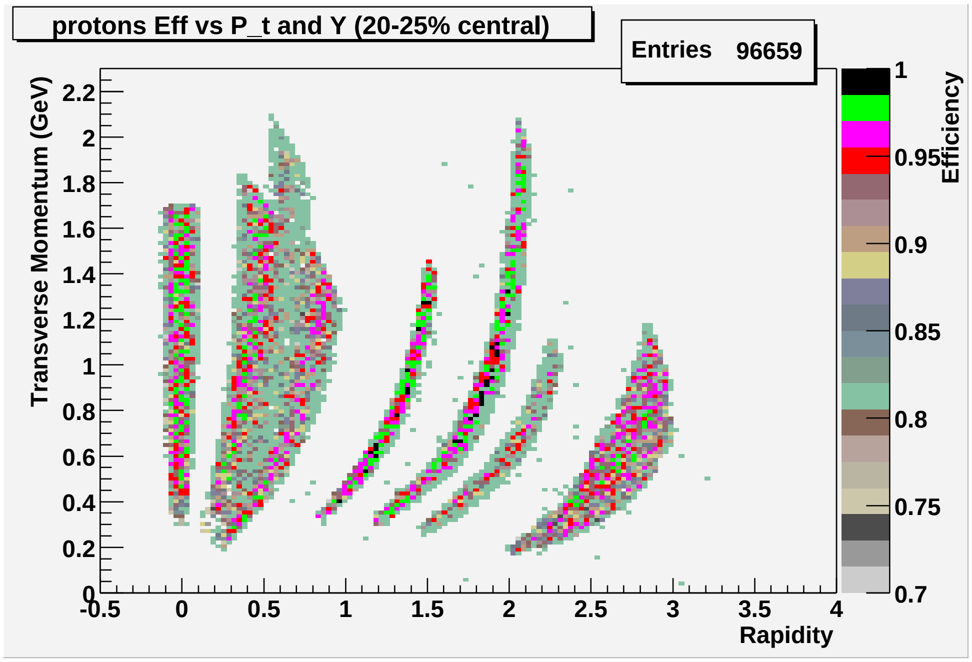

Figure 9.19: Efficiency vs P_T and Y for 25% most central protons.

9.5 The momentum resolution

The momentum resolution of the spectrometers is calculated by comparing the reconstructed momentum from the embedded particle with the BRAG momentum. The relative deviation is given by:

$$\Delta p_{rel} = \frac{p_{BRAG} - p_{reco}}{p_{BRAG}} \tag{9.1}$$

This relative deviation was then plotted and fitted with a gaussian. This was done for all three particles. The result is shown in figure 9.20 — 9.22. They were obtained by summing over all the analyzed data.

Table 9.7 on the following page shows that the heavier particles have a poorer resolution than the lighter ones. This may be explained by a poorer accuracy of the local tracks for heavier particles, i.e. more misalignment between the reconstructed track and where the particle trajectory actually is. The average multiple scattering angle is proportional to $1/\beta^2$ for a singly charged particle. For a fixed momentum there will be a broader distribution in momenta for heavier particles. This is further described in GEANT manual [12] p. 234 and references therein.

Also interesting to notice is that the FFS seems to calculate a momentum that is ~ 0.5% too high on average. In the MRS the momentum offset is an order of magnitude smaller.

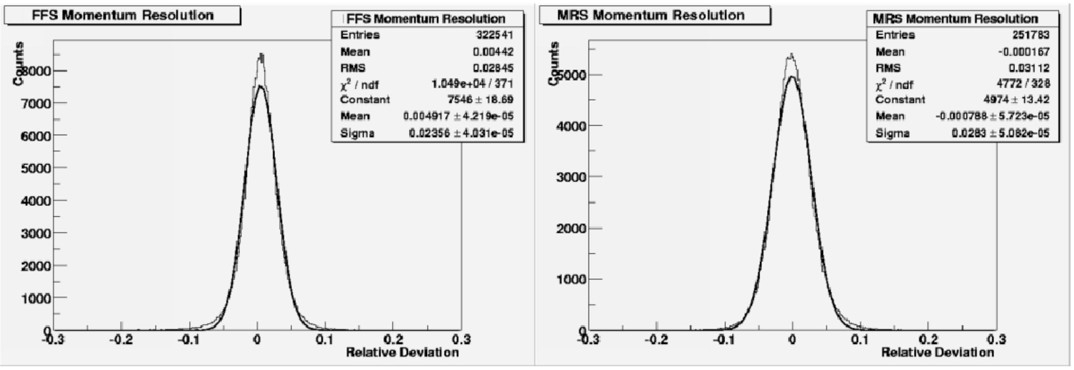

Figure 9.20: Momentum resolution for pions, MRS (left) and FFS (right).

The deviation between the BRAG specified momentum and the reconstructed momentum may also be plotted as a function of the reconstructed momentum. The tails at low and high momentum illustrates the smearing of the flat input momentum distribution. The first degree polynomial dependence seen for the FFS may indicate a small but systematic average shift of the reconstructed momentum. Figure 9.23 on page 102 shows a sample of these histograms. They do

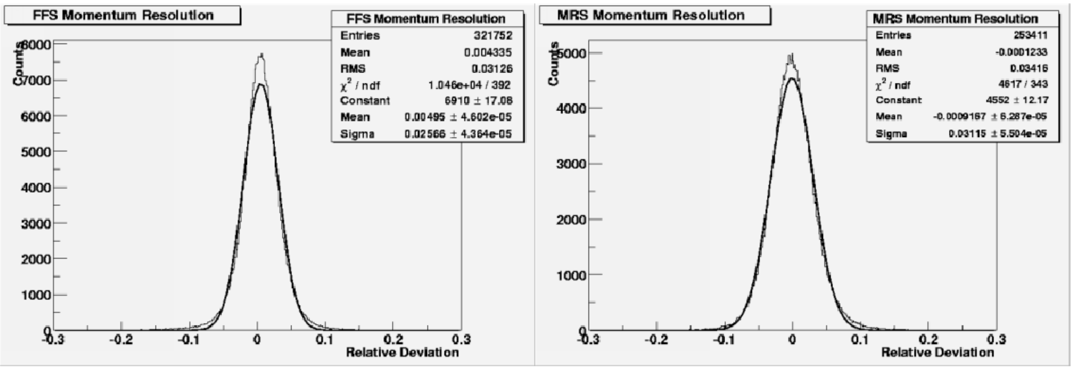

Figure 9.21: Momentum resolution for kaons, MRS (left) and FFS (right).

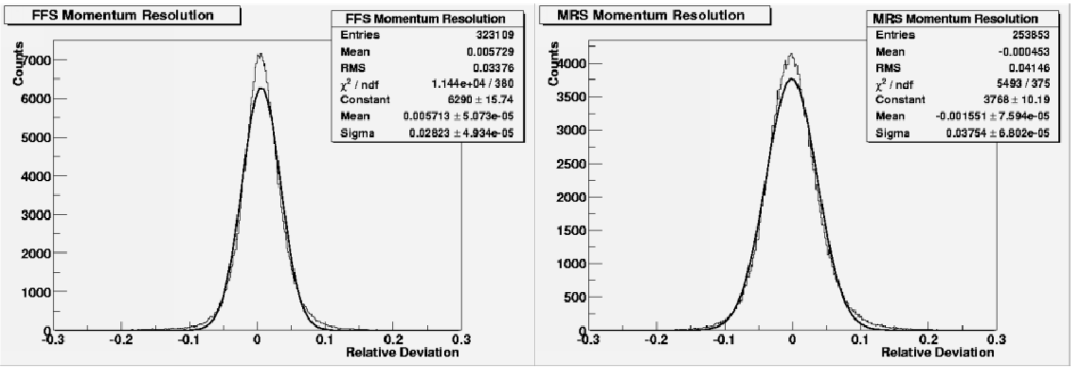

Figure 9.22: Momentum resolution for protons, MRS (left) and FFS (right).

Spectrometer	**Pions**	**Kaons**	**Protons**
FFS σ	±2.36 %	±2.56 %	±2.82 %
FFS 3σ	±7.08 %	±7.68 %	±8.46 %
MRS σ	±2.83 %	±3.12 %	±3.75 %
MRS 3σ	±8.49 %	±9.36 %	±11.25 %

Table 9.7: Momentum resolution from matching tracks through D5 in D2 compared to the given momentum from BRAG, were σ is the standard deviation for a gaussian distribution.

not show a very pretty first degree polynomial dependence, but are nevertheless fitted to one.

The last figure in this section shows 2 dimensional distributions of the relative momentum deviation, specified by equation (9.1), vs the reconstructed momentum.

Momentum smearing and systematic momentum shifts may influence the

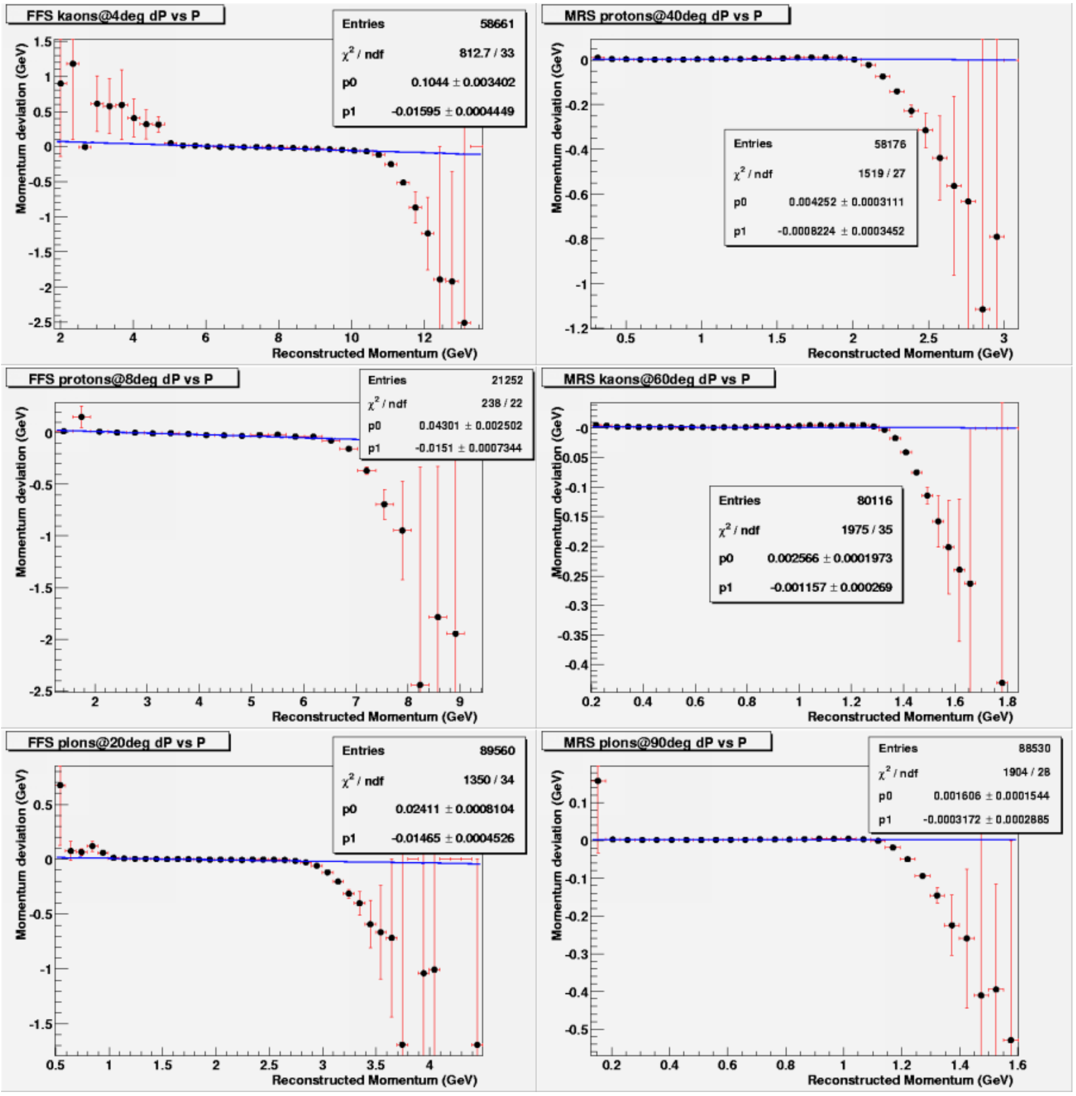

Figure 9.23: Momentum deviation plotted against reconstructed momentum at 4°, 8°, 20°, 40°, 60°, and 90°.

shape and average slope of particle spectra plotted against momentum. It might be necessary to correct for such effects. This problem has not been investigated any further in this thesis.

9.6 Edge effects

Edge effects may occur when a particle flies through the detector close to one of the side walls. This can result from the electric field not being uniform at the edge of the inner volume of the TPC, or that part of the electrons forming

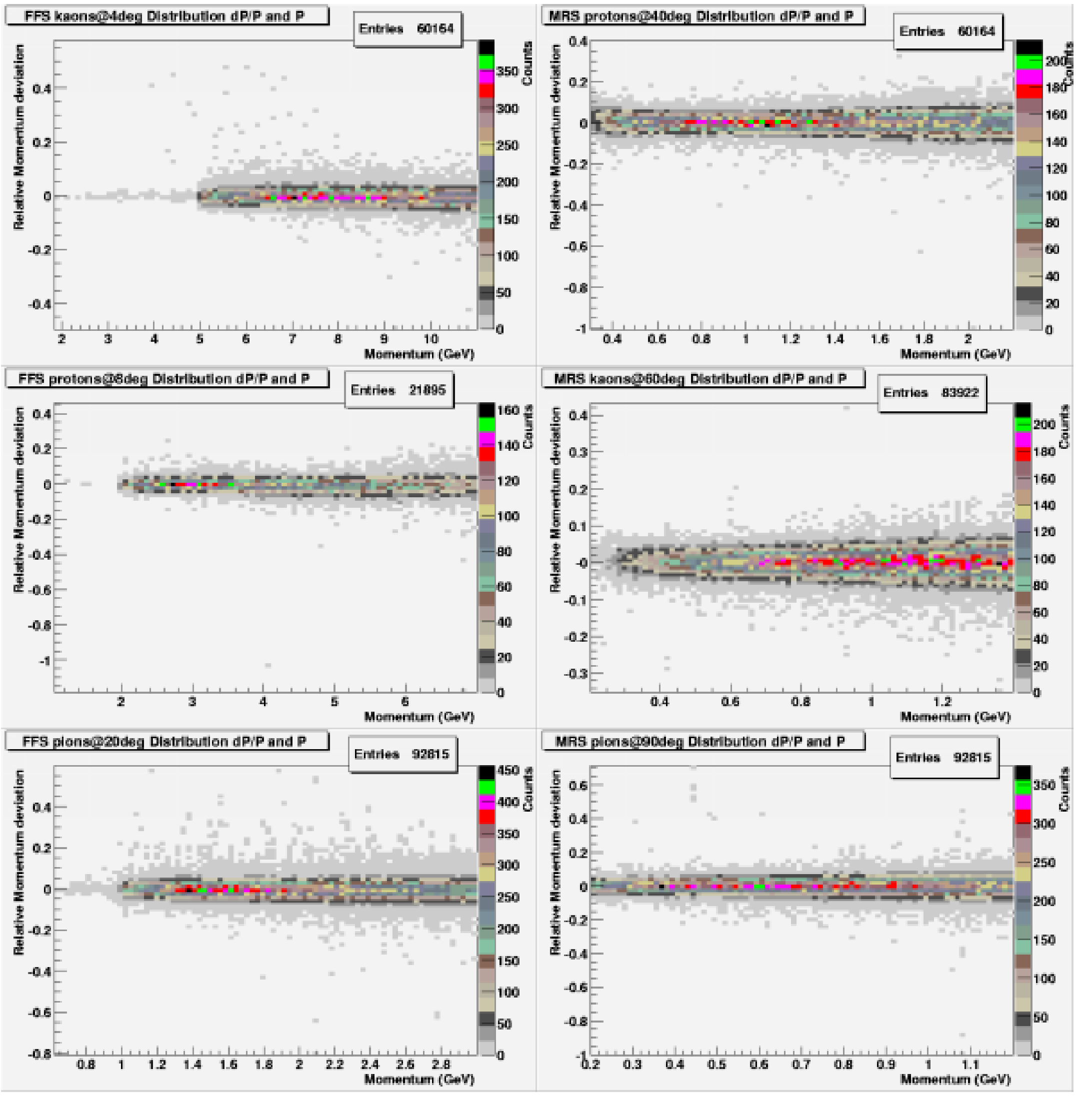

Figure 9.24: Relative Momentum deviation distribution plotted against the momentum provided by BRAG for a sample of the analyzed runs.

the cluster are not hitting any pads, but the wall instead. Noisy clusters at the edge of the TPC have been seen before in the BRAHMS experiment, but the TPCs have had a hardware fix since then.

The embedding method used in this thesis is not the best way to study edge effects. The digitization does not take into account inhomogeneities in the electric field at the edge of the TPC, or any other distortions that may occur at the edges. Dead pads are taken into account in the digitization, but nothing special is done for pads at the edge of the TPC. Regions in the TPC with noise in the raw data will mask the embedded clusters and thereby lower the

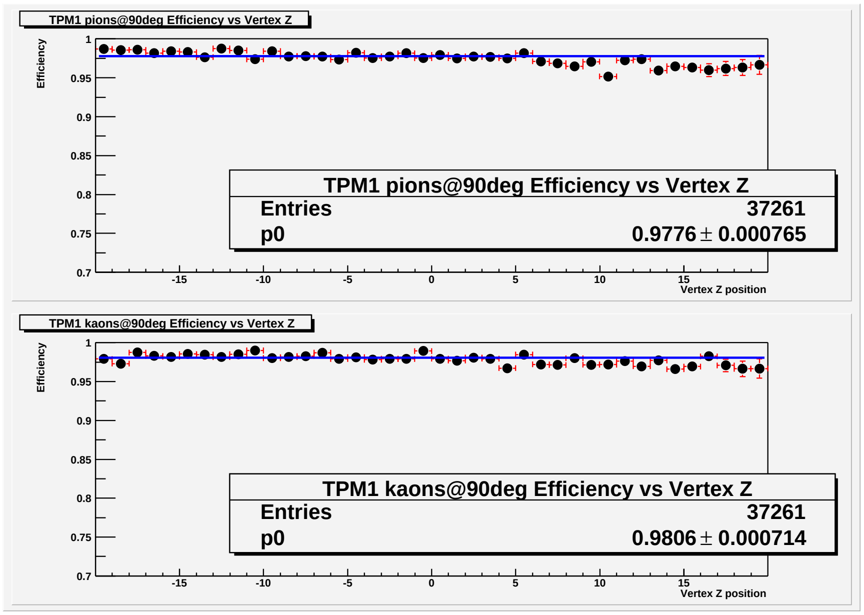

Figure 9.25: TPM1 Efficiency vs vertex position for pions and kaons at 90°.

efficiency. Otherwise the method proposed in [27], briefly discussed in chapter 8, might be more useful in doing an edge efficiency estimate. But the magnet gaps may also be too small. This section only shows results from the embedding method with it's limitations, and is included for completeness.

Studies of edge effects are easiest in the MRS, again because there is no magnet in front of TPM1. At the extreme accepted ends of the vertex position, $\pm 20\,cm$, it should be possible to see if the detectors exhibit any edge effect. Of course not many of the tracks will go along the edge of TPM1, but there should be more of them at these vertex positions than anywhere else. So if the efficiency is lower at the edge of the TPC, e.g. due to noise in the raw data close to the edges, a small decrease should be seen at the edge of the accepted vertex.

Figure 9.25 shows the efficiency vs vertex position for pions and kaons in TPM1. It is not easy to draw any conclusion from the figure, but it looks like there is no significant loss in the efficiency. For reconstructible spectrometer tracks, the tracks will not go very close to the edge. Comparing the width of TPM1 and D5, see table 8.1 on page 62, it is seen that TPM1 is a bit wider than D5. Spectrometer tracks will have a chance to be close to the side of the TPC, but only in the first couple of padrows if it goes through the entire magnet. This is even constrained further by cutting in the vertex position. The efficiency analysis was done with a vertex cut of $\pm 20\,cm$. In results published by BRAHMS, narrower cuts have mostly been used, $\pm 15\,cm$.

There still might be real edge effects, since the simulation of particles will

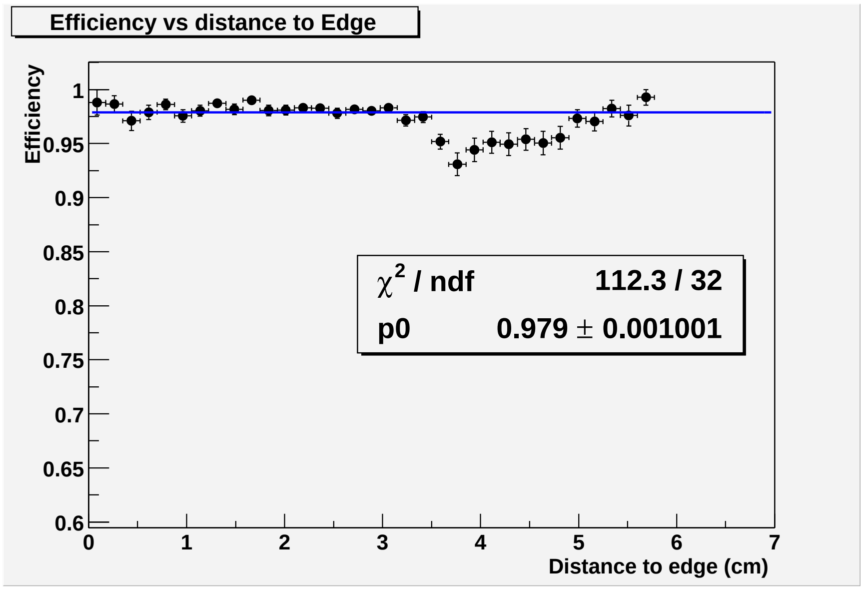

Figure 9.26: Efficiency vs the average x distance to the closest of the two side walls for pions in TPM1 at 90°. The figure came from an analysis of $\sim$ 100000 trigger 6 events, only accepting vertices between $[-20\,cm,\,-11\,cm]$ and$[11\,cm,\,20\,cm]$.

make hits on an equal footing throughout the TPC volume. The digitization does not either do anything specific with hits close to the edges of the TPC. It is therefore impossible to exclude actual edge effects from this simulation analysis.

To establish if any edge effects are detectable with the embedding method, an analysis only on TPM1 was done. Only events with vertex position between $\pm[20, 11]\,cm$ was chosen. The simulated tracks had an angle θ between 87° and 93°, and were emitted in vertex bins of $2\,cm$. The result was plotted as Efficiency vs the average distance the track had to the side wall and is shown in figure 9.26.

There is one interesting feature in figure 9.26. At $\sim 3.7\,cm$ from the edge of the TPC there is a small valley in the efficiency. This may be correlated with where the track efficiency starts to drop in the data.

Figure 9.27 on page 107 shows the average density of tracks pr event, reconstructed from raw data, in the entry, center and exit plane of TPM1. The average distance to the edge is most easily seen in the center plane along the x axis. The x axis boundaries are the side walls of the TPC. On the left side there seems to be no tracks that have an average distance to the edge of the TPC less than $\sim 4\,cm$, which is right at the small bump in figure 9.26. The center plane track density is not symmetric, suggesting that the TPC pads may behave differently on the left and right side of the TPC. The edge effects have not been investigated any further.

A $\sim 2.5\,cm$ blank area in the y direction, close to the top of the TPC, is caused by the TPC preprocessor, which discards the earliest timebins. These TPC sequences are discarded due to oscillations. The effect is that the information close to the padplane is not analyzed. The padplane is positioned in the ceiling and this gives the observed effect.

It is probably not feasible to detect edge effects using FFS tracks. Estimates from the efficiency analysis showed that none of the embedded spectrometer tracks were less than $7\,cm$, in the average x direction, from the edge of the TPCs.

9.7 Ghost tracks and lost tracks

Ghost tracks are tracks that are reconstructed after the embedding, which were not found in the raw event before the embedding. These tracks are not believed to be from physical particles that fly through the spectrometer. The opposite is losing tracks. This means that there are less reconstructed tracks after the embedding than reconstructed in the raw event. This gives an opportunity to investigate the stability and reliability of the tracking algorithm.

The embedding imposes a perturbation of an event. If this perturbation leads to many ghost tracks or lost tracks, it may indicate that tracking instabilities can be important sources of systematic uncertainties in yields and spectra.

When considering spectrometer tracks, there might be several reasons for the production of a ghost track:

- Wrong combination of **true** front and back local track.
- Combination of **true** front/back local track with **ghost** back/front local track.
- Combination of **2 local ghost tracks**.

Figure 9.30 — 9.33 show a selection of the probability for ghost and lost tracks in the MRS and FFS. These figures are all obtained by just counting the extra or lost spectrometer tracks. This will include all the possibilities listed above. The probabilities were only calculated on events where the embedded track was reconstructed. It is possible to do this also on most events where the embedded track is not reconstructed, but then the overlap for each track in the embedded event must be checked with each track in the raw event. But even with this method, there still might be some events where the question would be unresolved, because the calculated overlap might not always be above 0.6

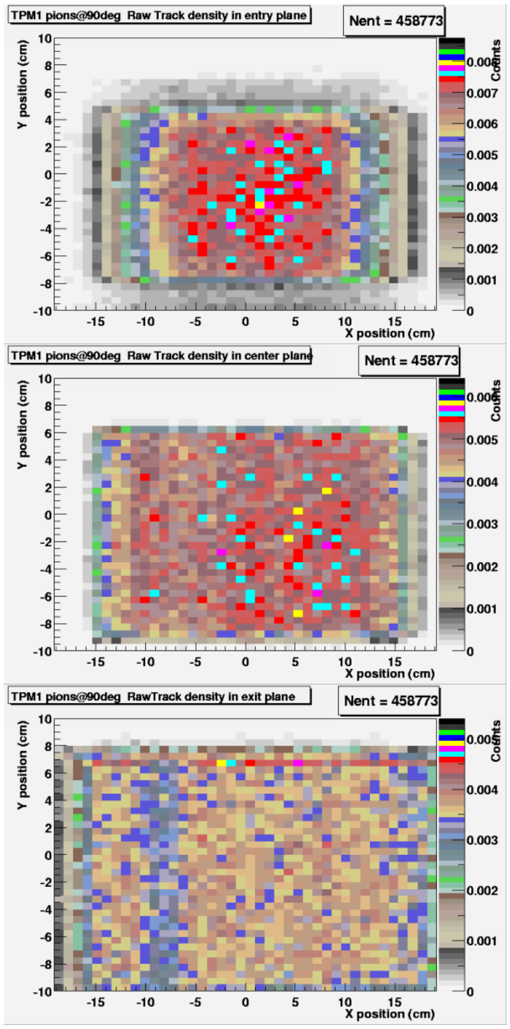

Figure 9.27: Track density in TPM1 from experimental data. Edges are clearly seen in the figure, suggesting that edge effects are present. The figure shows the cross section of the inner active volume, at entry, center and exit plane. The center plane is the average distance the track has to the edge of the TPC. The color is average number of tracks pr event. The edges of the plot are the edges of the TPC.

even though it is the same raw track in the raw and embedded event being compared. This will probably only happen in very few cases. No comparison track by track, in an events where the embedded track was not reconstructed, has been done in this thesis.

The right number of ghost/lost tracks may be different than that obtained by counting. Consider this extreme case: If X tracks are found in the embedded event and $X+1$ are found in the raw event, there might actually be $X+1$ lost tracks and X ghost tracks. This is an extreme case, but more probable cases, e.g. losing 1 track and producing 1 ghost, which yields the right number of tracks, can occur much more often. This has not been done in this thesis, and should be further investigated.

The figures show a selection of the extreme cases of the runs that have been analyzed, 90° and 40° for the MRS and 20° and 3° for the FFS. As seen in the figures, there are large differences in the probabilities.

All the probabilities are stated in table 9.12 — 9.16. There is clearly a much higher probability for producing ghost tracks than losing tracks. This sounds reasonable, since the embedding of a track introduces more hits in the TPC, and thereby more possibilities for spurious combinations.

Worth noticing is that the FFS at 3° has a 8% probability of producing at least one ghost track for all particle species. The probability for ghost tracks shows a strong dependence on the angle, which probably means that increasing occupancy increases the ghost track probabilities. This can be seen in figure 9.28 on the following page, where the ghost track probability is plotted against the collision centrality for pions. There is a approximate linear dependence on the centrality, which points to a combinatorial source. The other particles exhibited the same trend.

There does not seem to be any dependence on the particles species for the ghost track probabilities, but maybe a slight one for losing tracks. When embedding tracks with high dE/dx, smaller cluster in the raw event may drown, resulting in a raw track that is no longer reconstructible. Different particles have different dE/dx for the same momentum. A slight dependence would have seemed reasonable.

The ghost tracks were further analyzed to see if they have any features different from the other tracks. This was done by comparing all the tracks in the embedded event, except the embedded track itself, with the tracks in the raw event. It was only done on events where the embedded track was reconstructed and which contained at least one ghost track, determined by counting. Not all of the "ghost" events could be resolved. Unfortunately comparing each track in the embedded event with the tracks in the raw event did not always yield the same number as the counting of tracks. Some yielded more ghosts and others less. These events could not be analyzed, since they could consist of distorted raw tracks, no longer having a relative overlap with itself above 0.6. They constituted $\sim$ 10% of the events containing ghosts. This points to the possibility that the actual probability of having ghost tracks and losing tracks might be even higher than determined by just counting.

In table 9.8 — 9.10 the local track composition of the matched ghost tracks is shown. Local ghost tracks are completely dominating the source of spectrometer ghost tracks, but there is a clear difference between the MRS and the FFS. While there are very few ghosts that are composed of a ghost front and a ghost back track in the MRS, this is the case for $\sim \frac{1}{3}$ of the spectrometer ghost tracks

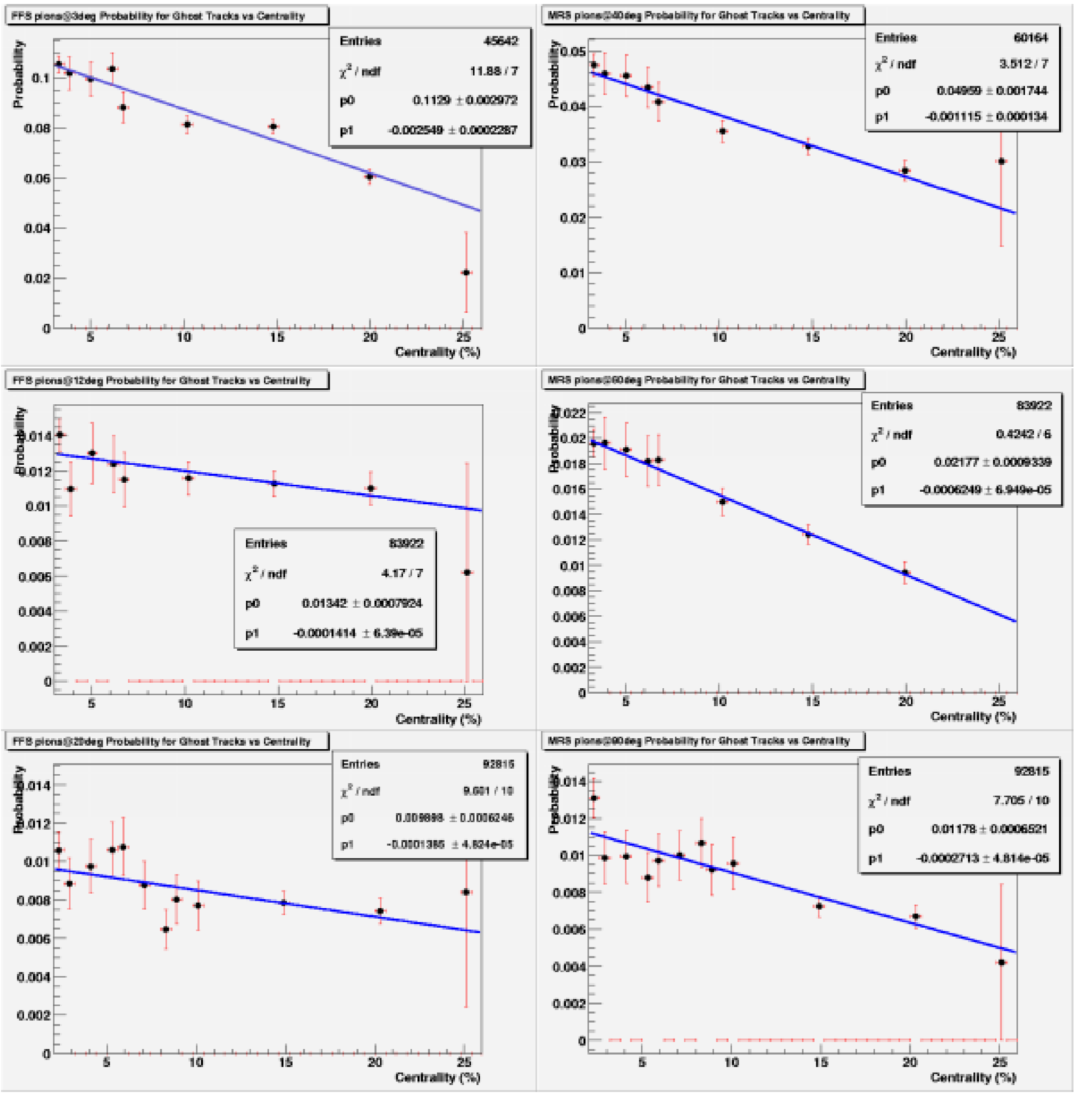

Figure 9.28: The probability of producing at least one ghost track for each centrality, from embedding pions.

in the FFS. Except for the 52.5° setting, there is a very low probability that the ghost tracks consists of a true front and a true back track. The MRS in most cases matches a true local track with a local ghost track.

Combinations of a true front and a true back track gives informations on the stability of the track matching. There are few occurrences of this, the 52.5° setting being an exception.

The momentum distributions of these ghost tracks is shown in figure 9.29 on page 113 as triangles. Comparing these reconstructed momenta and the ones in table 8.2 on page 72 shows that the ghost tracks lie within the same momentum range as the raw particles. Figure 9.29 on page 113 also shows the momentum distribution of the embedded particles, as squares, and the raw particles, as circles. The embedded particles have nearly a box shape, which they were thrown with, while the raw particles and the ghosts have a near exponential shape. The ghost tracks are therefore not easily distinguishable from the real tracks.

The distributions of the matching parameters[3] for the ghost tracks, are not in the same range as the raw tracks. The statistics are a bit poor, so no plots are shown, but the distributions seemed to be at least 3 times as wide as the raw tracks matching parameter distributions. Often they had a flat/box distribution instead of a gaussian shape. It would also be interesting to study the χ^2 distribution of the local ghost tracks.

The ghost track distributions shows in some cases a hint of a none exponential shape at high momentum. The shapes are consistent with the one expected from combinations of one local track with another with random direction in the bending plane.

The charge of the ghost tracks should also examined, to see if they have the same sign as the "preferred" value for the magnetic field.

Any further investigation has not been done in this thesis.

Ghost tracks, originating from local ghosts in TPM2 or T2, should disappear automatically from the particle spectra when they are compared with hits in the TOF walls. Combinations of a true local track in TPM2 or T2 might lead to contamination of the identified particle spectra. The TOF walls are not yet incorporated in the efficiency analysis and this possible removal or reduction of the number of ghost tracks have therefore not been tested.

The source of the high ghost track probabilities should be further investigated, since it could have an impact on yields and spectra.

---

[3] See section 7.5 on page 49 for a discussion of the matching parameters.

	θ	T.F.&T.B.	G.F.&T.B.	T.F.&G.B.	G.F.&G.B.
FFS	3°	1.9(±0.2)%	38.7(±0.9)%	48.8(±1.0)%	10.6(±0.5)%
FFS	4°	1.0(±0.2)%	31.3(±1.0)%	44.5(±1.2)%	23.2(±0.8)%
FFS	8°	1.7(±0.6)%	27.0(±2.2)%	34.4(±2.5)%	36.9(±2.6)%
FFS	12°	0.3(±0.2)%	20.9(±1.3)%	25.0(±1.5)%	53.8(±2.1)%
FFS	12°	1.1(±0.5)%	19.5(±2.1)%	33.1(±2.8)%	46.2(±3.3)%
FFS	20°	0.6(±0.3)%	12.9(±1.2)%	21.1(±1.6)%	65.4(±2.8)%
MRS	40°	3.1(±0.3)%	34.9(±1.1)%	60.8(±1.5)%	1.2(±0.2)%
MRS	52°	15.2(±2.0)%	20.6(±2.3)%	62.9(±4.0)%	1.3(±0.6)%
MRS	60°	2.7(±0.4)%	23.7(±1.3)%	72.9(±2.2)%	0.7(±0.2)%
MRS	90°	4.9(±0.7)%	29.1(±1.7)%	64.9(±2.6)%	1.1(±0.3)%

Table 9.8: The ghost tracks, from embedding pions, are composed of true local front TPC track (*T.F.*), local ghost front TPC track (*G.F.*), true local back TPC track (*T.B.*) or local ghost back TPC track (*G.B.*). The top occurrence of the 12° setting is run 5642, and the one below is run 5677. The numbers in parenthesis is the statistical uncertainty.

	θ	T.F.&T.B.	G.F.&T.B.	T.F.&G.B.	G.F.&G.B.
FFS	3°	2.2(±0.2)%	38.3(±0.9)%	48.5(±1.0)%	10.9(±0.5)%
FFS	4°	0.9(±0.2)%	32.6(±1.0)%	43.3(±1.2)%	23.2(±0.8)%
FFS	8°	1.7(±0.6)%	21.1(±2.0)%	35.6(±2.6)%	41.5(±2.8)%
FFS	12°	0.5(±0.2)%	20.7(±1.4)%	27.3(±1.6)%	51.5(±2.2)%
FFS	12°	0.5(±0.3)%	27.1(±2.6)%	35.7(±3.0)%	36.7(±3.0)%
FFS	20°	0.2(±0.2)%	11.6(±1.2)%	19.6(±1.6)%	68.6(±2.9)%
MRS	40°	3.6(±0.4)%	36.0(±1.2)%	59.1(±1.5)%	1.2(±0.2)%
MRS	52°	12.2(±1.7)%	17.1(±2.1)%	70.0(±4.2)%	0.7(±0.4)%
MRS	60°	4.3(±0.6)%	23.5(±1.3)%	71.8(±2.2)%	0.5(±0.2)%
MRS	90°	4.8(±0.7)%	28.1(±1.7)%	65.8(±2.6)%	1.4(±0.4)%

Table 9.9: The ghost tracks, from embedding kaons, are composed of true local front TPC track (*T.F.*), local ghost front TPC track (*G.F.*), true local back TPC track (*T.B.*) or local ghost back TPC track (G.B.). The top occurrence of the 12° setting is run 5642, and the one below is run 5677. The numbers in parenthesis is the statistical uncertainty.

	θ	T.F.&T.B.	G.F.&T.B.	T.F.&G.B.	G.F.&G.B.
FFS	3°	2.5(±0.2)%	38.6(±0.9)%	48.8(±1.0)%	10.0(±0.5)%
FFS	4°	0.9(±0.2)%	32.5(±1.0)%	47.2(±1.2)%	19.4(±0.8)%
FFS	8°	2.2(±0.7)%	29.9(±2.4)%	38.7(±2.8)%	29.3(±2.4)%
FFS	12°	0.5(±0.2)%	22.9(±1.5)%	29.3(±1.7)%	47.4(±2.2)%
FFS	12°	0.5(±0.4)%	24.6(±2.5)%	37.8(±3.1)%	37.0(±3.1)%
FFS	20°	0.5(±0.3)%	13.6(±1.4)%	23.6(±1.8)%	62.3(±2.9)%
MRS	40°	3.8(±0.4)%	34.7(±1.1)%	60.2(±1.5)%	1.3(±0.2)%
MRS	52°	14.1(±1.9)%	19.5(±2.3)%	64.9(±4.2)%	1.6(±0.7)%
MRS	60°	3.2(±0.5)%	25.0(±1.3)%	70.7(±2.1)%	1.1(±0.3)%
MRS	90°	4.7(±0.7)%	29.7(±1.7)%	64.8(±2.5)%	0.8(±0.3)%

Table 9.10: The ghost tracks, from embedding protons, are composed of true local front TPC track (*T.F.*), local ghost front TPC track (*G.F.*), true local back TPC track (*T.B.*) or local ghost back TPC track (*G.B.*). The top occurrence of the 12° setting is run 5642, and the one below is run 5677. The numbers in parenthesis is the statistical uncertainty.

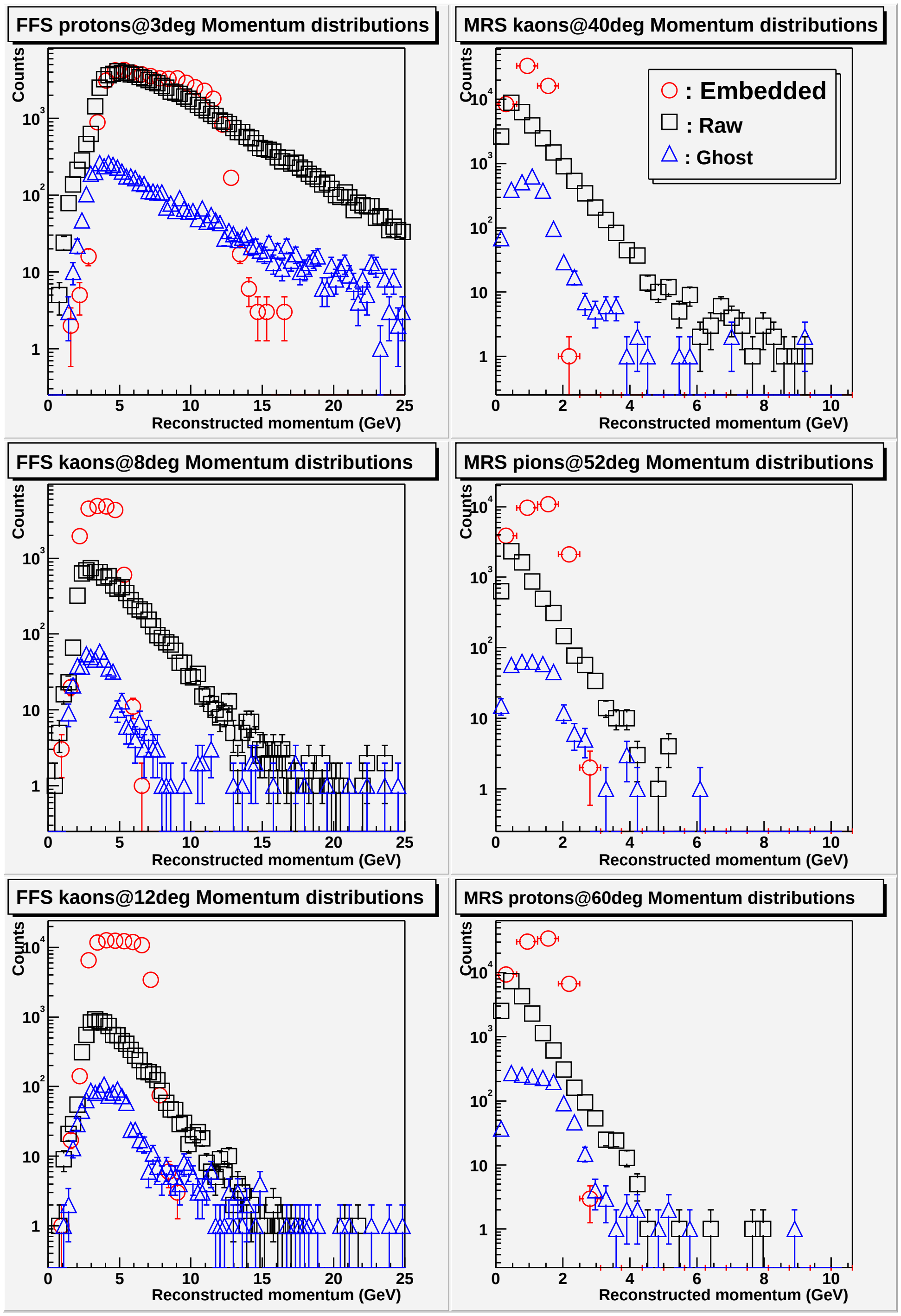

Figure 9.29: Ghost track momentum distribution shown as triangles. Raw track momentum distributions shown as squares. Embedded particle momentum distribution shown as circles. An exponential shape is seen for the raw and ghost tracks, while the embedded tracks has a box like distribution.

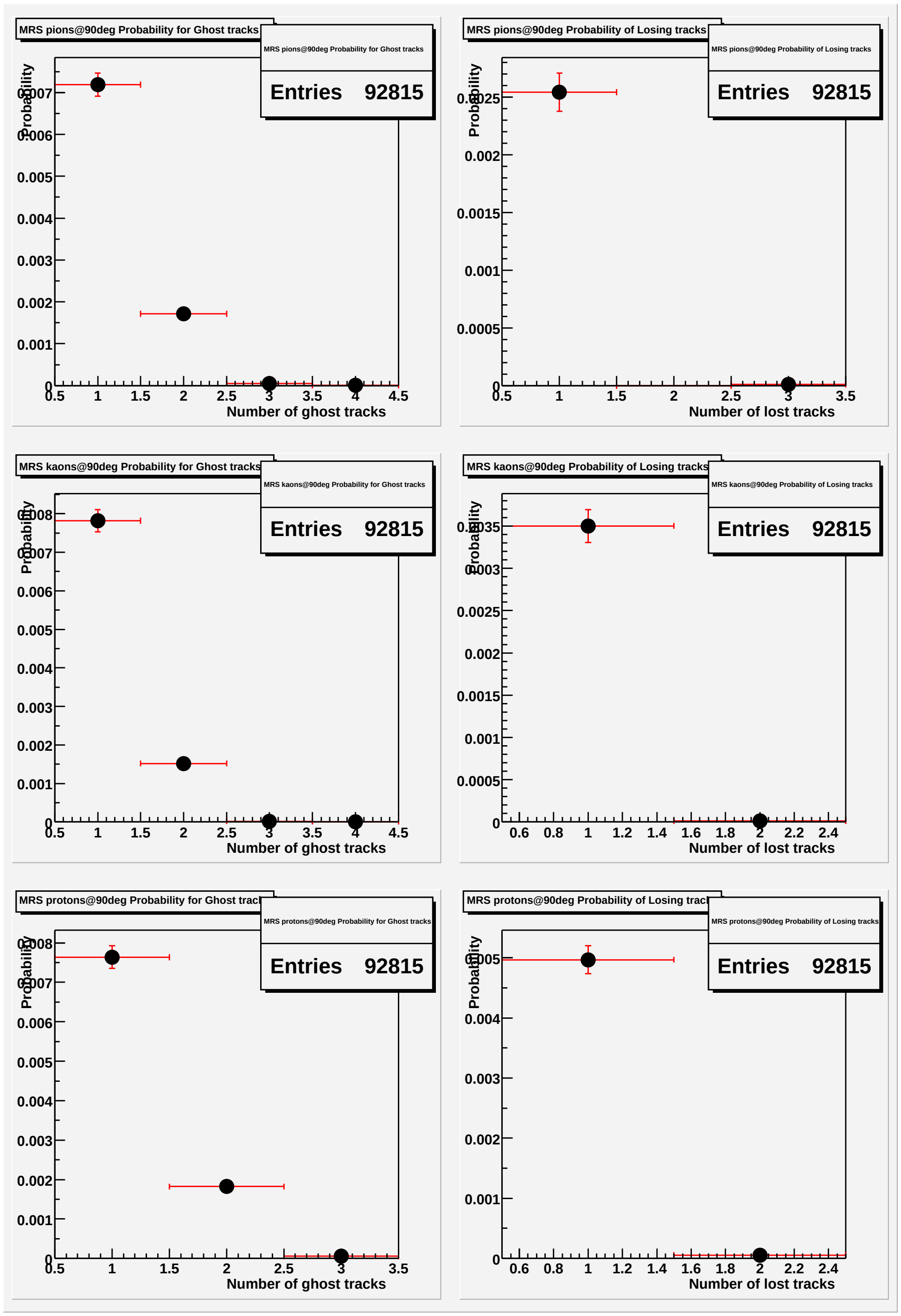

Figure 9.30: The probability for ghost tracks and for losing tracks for the MRS at 90°.

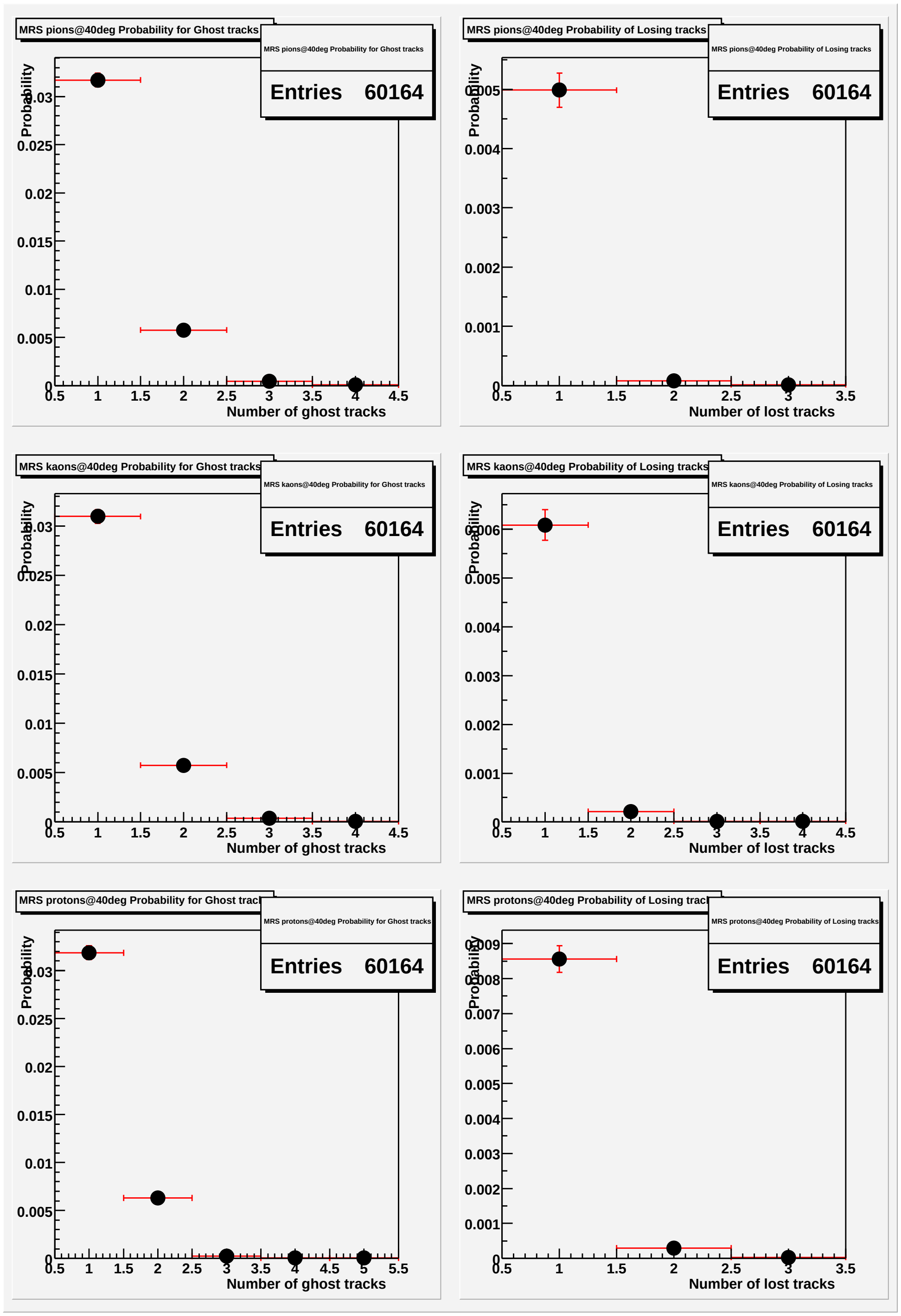

Figure 9.31: The probability for ghost tracks and for losing tracks for the MRS at 40°.

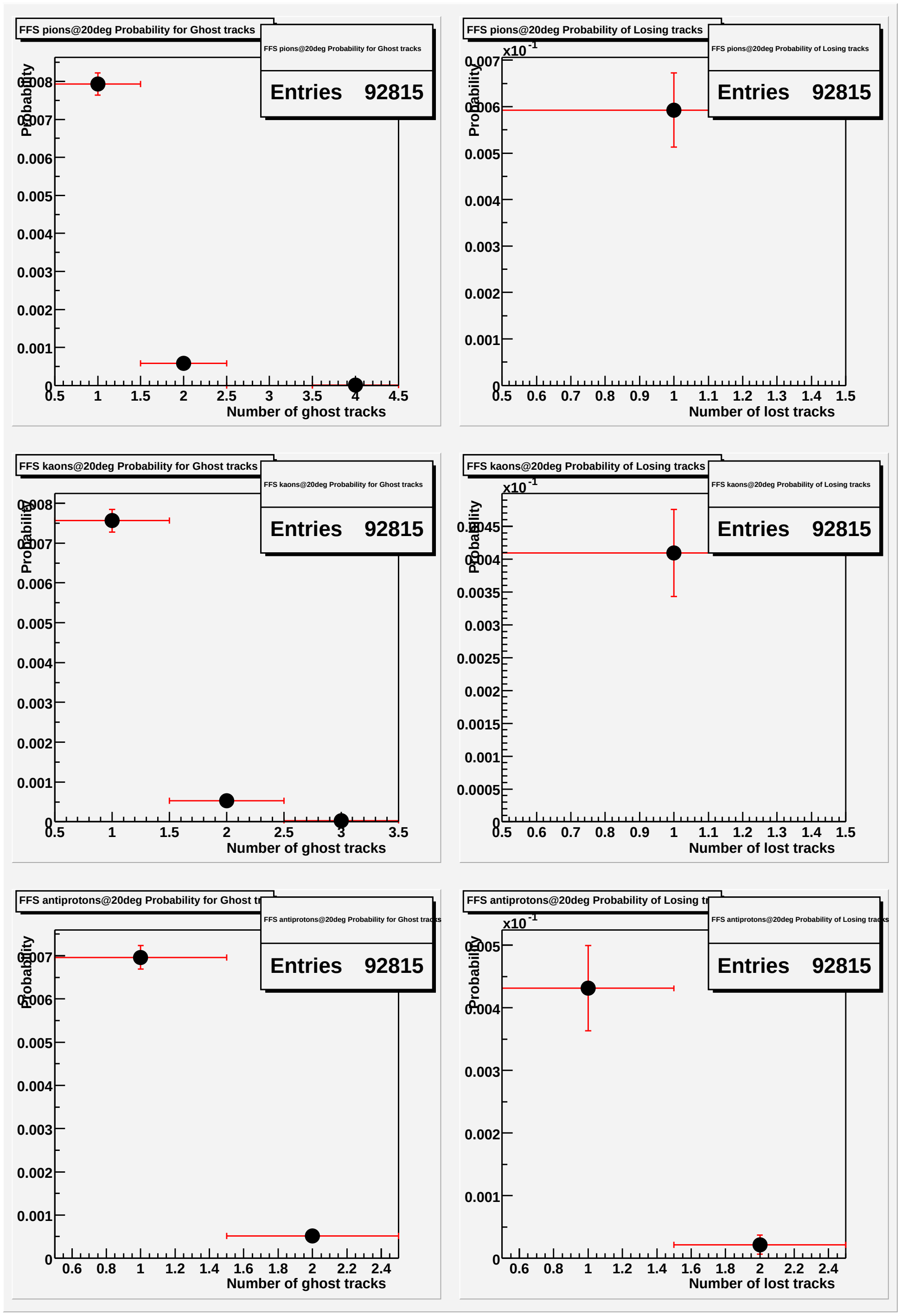

Figure 9.32: The probability for ghost tracks and for losing tracks for the FFS at 20°. Notice the 10^{-1} on the probability axis for losing tracks.

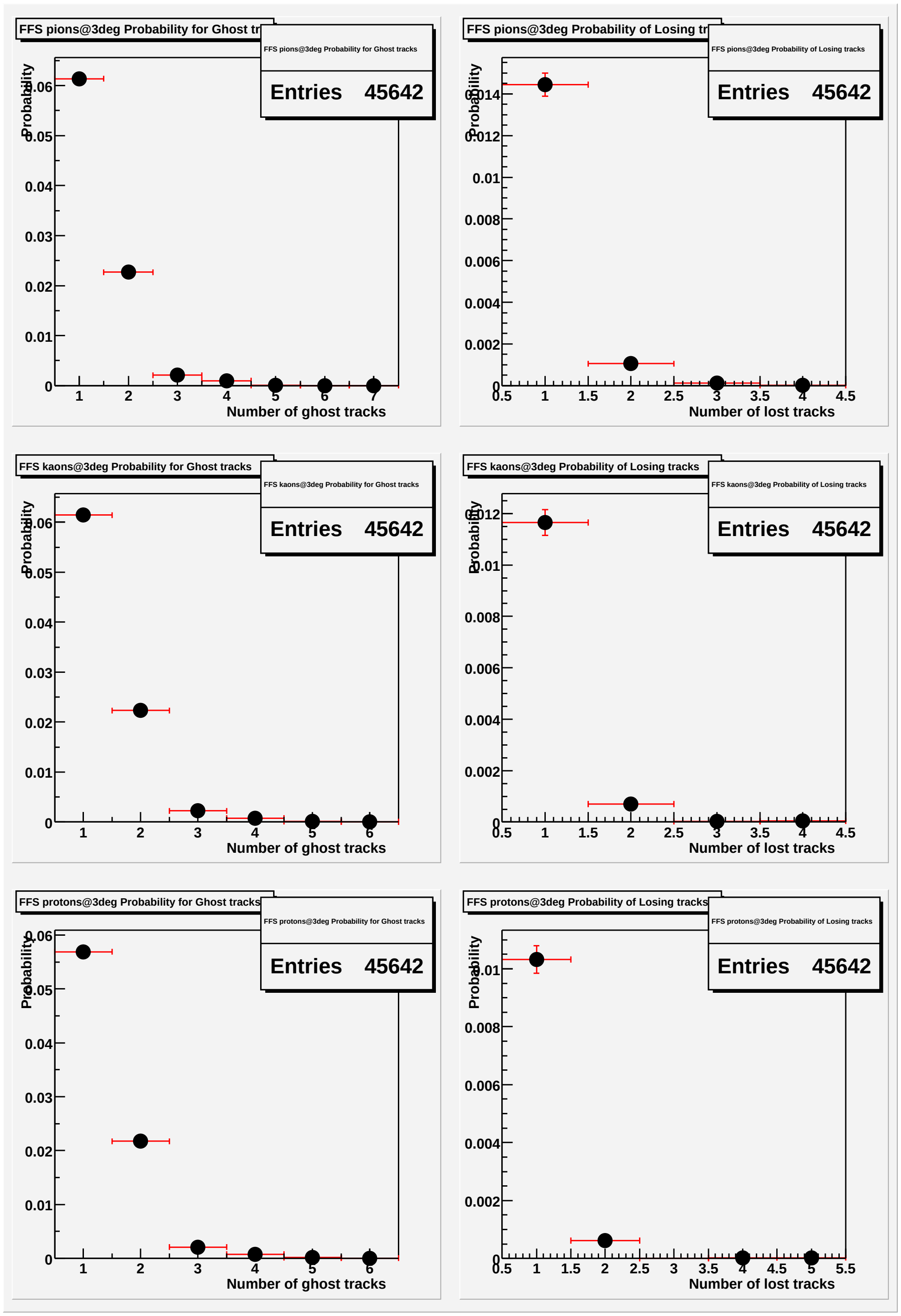

Figure 9.33: The probability for ghost tracks and for losing tracks for the FFS at 3°.

	θ	**1**	**2**	**3**	**4**	**5**	**6**	**7**
FFS	3.0°	6.13(±11)	2.268(±70)	0.208(±21)	0.099(±15)	0.009(±4)	0.002(±2)	0.002(±2)
- T1	3.0°	2.687(±76)	0.227(±22)	0.013(±5)	0.004(±3)	*NS*	*NS*	*NS*
- T2	3.0°	4.225(±94)	0.817(±42)	0.167(±19)	0.046(±10)	0.009(±4)	0.002(±2)	0.002(±2)
FFS	4.0°	3.048(±70)	1.145(±43)	0.060(±10)	0.032(±7)	0.002(±2)	0.003(±2)	*NS*
- T1	4.0°	1.078(±42)	0.060(±10)	0.002(±2)	*NS*	0.002(±2)	*NS*	*NS*
- T2	4.0°	2.439(±63)	0.283(±22)	0.037(±8)	0.008(±4)	*NS*	*NS*	*NS*
FFS	8.0°	1.886(±92)	0.279(±36)	0.014(±8)	0.005(±5)	*NS*	*NS*	*NS*
- T1	8.0°	0.333(±39)	0.009(±6)	*NS*	*NS*	*NS*	*NS*	*NS*
- T2	8.0°	1.430(±80)	0.132(±25)	0.018(±9)	*NS*	*NS*	*NS*	*NS*
FFS	12.0°	0.995(±34)	0.193(±15)	0.008(±3)	0.002(±2)	*NS*	*NS*	*NS*
- T1	12.0°	0.107(±11)	0.008(±3)	0.001(±1)	*NS*	*NS*	*NS*	*NS*
- T2	12.0°	0.920(±33)	0.037(±7)	0.002(±2)	*NS*	*NS*	*NS*	*NS*
FFS	20.0°	0.793(±29)	0.058(±8)	*NS*	0.001(±1)	*NS*	*NS*	*NS*
- T1	20.0°	0.051(±7)	0.002(±2)	*NS*	*NS*	*NS*	*NS*	*NS*
- T2	20.0°	0.660(±27)	0.019(±5)	*NS*	*NS*	*NS*	*NS*	*NS*
MRS	40.0°	3.171(±71)	0.577(±31)	0.043(±8)	0.007(±3)	*NS*	*NS*	*NS*
- TPM1	40.0°	0.641(±33)	0.039(±8)	*NS*	*NS*	*NS*	*NS*	*NS*
- TPM2	40.0°	0.213(±19)	0.008(±4)	*NS*	*NS*	*NS*	*NS*	*NS*
MRS	52.5°	1.254(±67)	0.080(±17)	*NS*	*NS*	*NS*	*NS*	*NS*
- TPM1	52.5°	0.470(±41)	0.018(±8)	*NS*	*NS*	*NS*	*NS*	*NS*
- TPM2	52.5°	0.095(±19)	*NS*	*NS*	*NS*	*NS*	*NS*	*NS*
MRS	60.0°	1.248(±38)	0.267(±18)	0.007(±3)	*NS*	*NS*	*NS*	*NS*
- TPM1	60.0°	0.344(±20)	0.013(±4)	*NS*	*NS*	*NS*	*NS*	*NS*
- TPM2	60.0°	0.091(±10)	*NS*	*NS*	*NS*	*NS*	*NS*	*NS*
MRS	90.0°	0.719(±28)	0.171(±14)	0.005(±2)	0.001(±1)	*NS*	*NS*	*NS*
- TPM1	90.0°	0.269(±17)	0.005(±2)	*NS*	*NS*	*NS*	*NS*	*NS*
- TPM2	90.0°	0.086(±10)	0.001(±1)	*NS*	*NS*	*NS*	*NS*	*NS*

Table 9.11: Probability for reconstructing ghost tracks when embedding **pions**. Numbers given in %. *NS* means "Not Seen". The numbers in the top row specifies the number of ghost tracks found. Errors given for the last digits. Not shown in the table is the probability for an 8. ghost track in the FFS at 4°: 0.002(±2)%.

	θ	**1**	**2**	**3**	**4**	**5**	**6**
FFS	3.0°	6.14(±11)	2.230(±69)	0.223(±22)	0.074(±13)	0.011(±5)	0.004(±3)
- T1	3.0°	2.685(±76)	0.271(±24)	0.033(±9)	0.009(±4)	*NS*	*NS*
- T2	3.0°	4.244(±94)	0.870(±43)	0.151(±18)	0.031(±8)	0.015(±6)	*NS*
FFS	4.0°	2.982(±69)	1.100(±43)	0.055(±10)	0.030(±7)	0.002(±2)	*NS*
- T1	4.0°	1.154(±44)	0.078(±11)	0.003(±2)	*NS*	*NS*	*NS*
- T2	4.0°	2.407(±62)	0.322(±23)	0.045(±9)	0.010(±4)	0.003(±2)	*NS*
FFS	8.0°	1.909(±92)	0.201(±30)	0.023(±10)	0.009(±6)	*NS*	*NS*
- T1	8.0°	0.338(±39)	0.009(±6)	*NS*	*NS*	*NS*	*NS*
- T2	8.0°	1.617(±85)	0.105(±22)	0.014(±8)	0.014(±8)	*NS*	*NS*
FFS	12.0°	0.927(±33)	0.186(±15)	0.008(±3)	*NS*	*NS*	*NS*
- T1	12.0°	0.105(±11)	0.004(±2)	*NS*	*NS*	*NS*	*NS*
- T2	12.0°	0.835(±31)	0.026(±6)	0.005(±2)	*NS*	*NS*	*NS*
FFS	20.0°	0.756(±28)	0.053(±8)	0.003(±2)	*NS*	*NS*	*NS*
- T1	20.0°	0.079(±9)	0.008(±3)	*NS*	*NS*	*NS*	*NS*
- T2	20.0°	0.659(±27)	0.017(±4)	0.002(±2)	0.001(±1)	*NS*	*NS*
MRS	40.0°	3.097(±71)	0.575(±31)	0.038(±8)	0.005(±3)	*NS*	*NS*
- TPM1	40.0°	0.710(±34)	0.050(±9)	*NS*	*NS*	*NS*	*NS*
- TPM2	40.0°	0.218(±19)	0.005(±3)	*NS*	*NS*	*NS*	*NS*
MRS	52.5°	1.324(±69)	0.069(±16)	0.007(±5)	*NS*	*NS*	*NS*
- TPM1	52.5°	0.470(±41)	0.015(±7)	*NS*	*NS*	*NS*	*NS*
- TPM2	52.5°	0.128(±22)	*NS*	*NS*	*NS*	*NS*	*NS*
MRS	60.0°	1.182(±37)	0.254(±17)	0.004(±2)	0.001(±1)	*NS*	*NS*
- TPM1	60.0°	0.325(±20)	0.013(±4)	*NS*	*NS*	*NS*	*NS*
- TPM2	60.0°	0.068(±9)	*NS*	*NS*	*NS*	*NS*	*NS*
MRS	90.0°	0.782(±29)	0.152(±13)	0.002(±2)	0.001(±1)	*NS*	*NS*
- TPM1	90.0°	0.281(±17)	0.011(±3)	*NS*	*NS*	*NS*	*NS*
- TPM2	90.0°	0.081(±9)	0.001(±1)	*NS*	*NS*	*NS*	*NS*

Table 9.12: Probability for reconstructing ghost tracks when embedding **kaons**. Numbers given in %. *NS* means “Not Seen”. The numbers in the top row specifies the number of ghost tracks found. Errors given for the last digits.

	θ	**1**	**2**	**3**	**4**	**5**	**6**	**7**
FFS	3.0°	5.69(±11)	2.173(±68)	0.210(±21)	0.077(±13)	0.015(±6)	0.004(±3)	*NS*
- T1	3.0°	2.531(±74)	0.213(±22)	0.018(±6)	0.002(±2)	*NS*	*NS*	*NS*
- T2	3.0°	4.266(±95)	0.848(±43)	0.145(±18)	0.031(±8)	0.015(±6)	0.004(±3)	0.002(±2)
FFS	4.0°	2.703(±66)	1.084(±42)	0.070(±11)	0.022(±6)	0.008(±4)	0.002(±2)	*NS*
- T1	4.0°	1.121(±43)	0.065(±10)	0.003(±2)	*NS*	*NS*	*NS*	*NS*
- T2	4.0°	2.311(±61)	0.337(±24)	0.037(±8)	0.015(±5)	*NS*	*NS*	*NS*
FFS	8.0°	1.827(±91)	0.237(±33)	0.009(±6)	*NS*	0.005(±5)	*NS*	*NS*
- T1	8.0°	0.333(±39)	0.018(±9)	*NS*	*NS*	*NS*	*NS*	*NS*
- T2	8.0°	1.265(±76)	0.123(±24)	0.023(±10)	0.005(±5)	*NS*	*NS*	*NS*
FFS	12.0°	0.785(±30)	0.178(±15)	0.005(±2)	0.001(±1)	*NS*	*NS*	*NS*
- T1	12.0°	0.102(±11)	0.002(±2)	*NS*	*NS*	*NS*	*NS*	*NS*
- T2	12.0°	0.738(±30)	0.031(±6)	0.004(±2)	*NS*	0.001(±1)	*NS*	*NS*
FFS	20.0°	0.696(±27)	0.052(±7)	*NS*	*NS*	*NS*	*NS*	*NS*
- T1	20.0°	0.050(±7)	0.001(±1)	*NS*	*NS*	*NS*	*NS*	*NS*
- T2	20.0°	0.637(±26)	0.015(±4)	0.004(±2)	*NS*	*NS*	*NS*	*NS*
MRS	40.0°	3.186(±72)	0.630(±32)	0.023(±6)	0.003(±2)	0.003(±2)	*NS*	*NS*
- TPM1	40.0°	0.695(±34)	0.042(±8)	*NS*	*NS*	*NS*	*NS*	*NS*
- TPM2	40.0°	0.213(±19)	0.008(±4)	*NS*	*NS*	*NS*	*NS*	*NS*
MRS	52.5°	1.221(±66)	0.062(±15)	0.004(±4)	*NS*	*NS*	*NS*	*NS*
- TPM1	52.5°	0.452(±41)	0.022(±9)	*NS*	*NS*	*NS*	*NS*	*NS*
- TPM2	52.5°	0.084(±17)	0.004(±4)	*NS*	*NS*	*NS*	*NS*	*NS*
MRS	60.0°	1.270(±39)	0.285(±18)	0.008(±3)	*NS*	*NS*	*NS*	*NS*
- TPM1	60.0°	0.344(±20)	0.013(±4)	*NS*	*NS*	*NS*	*NS*	*NS*
- TPM2	60.0°	0.079(±10)	0.007(±3)	*NS*	*NS*	*NS*	*NS*	*NS*
MRS	90.0°	0.764(±29)	0.182(±14)	0.005(±2)	*NS*	*NS*	*NS*	*NS*
- TPM1	90.0°	0.245(±16)	0.012(±4)	*NS*	*NS*	*NS*	*NS*	*NS*
- TPM2	90.0°	0.073(±9)	0.001(±1)	*NS*	*NS*	*NS*	*NS*	*NS*

Table 9.13: Probability for reconstructing ghost tracks when embedding **protons**. Numbers given in %. *NS* means “Not Seen”. The numbers in the top row specifies the number of ghost tracks found. Errors given for the last digits. Not shown in the table is the probability for an 8. ghost track in T2 at 3°: 0.002(±2)%.

Detector	θ	**1 lost**	**2 lost**	**3 lost**	**4 lost**	**5 lost**
FFS	3.0°	1.44(±11)	0.105(±70)	0.013(±21)	0.002(±15)	*NS*
- T1	3.0°	5.067(±76)	0.220(±22)	0.007(±5)	0.004(±3)	*NS*
- T2	3.0°	0.673(±94)	0.031(±42)	0.007(±19)	*NS*	*NS*
FFS	4.0°	0.482(±70)	0.012(±43)	*NS*	*NS*	*NS*
- T1	4.0°	2.260(±42)	0.038(±10)	*NS*	*NS*	*NS*
- T2	4.0°	0.329(±63)	0.003(±22)	*NS*	*NS*	*NS*
FFS	8.0°	0.370(±92)	0.018(±36)	*NS*	*NS*	*NS*
- T1	8.0°	0.941(±39)	0.014(±6)	0.005(±0)	*NS*	*NS*
- T2	8.0°	0.219(±80)	*NS*	*NS*	*NS*	*NS*
FFS	12.0°	0.077(±34)	*NS*	*NS*	*NS*	*NS*
- T1	12.0°	0.262(±11)	0.002(±3)	*NS*	*NS*	*NS*
- T2	12.0°	0.051(±33)	0.001(±7)	*NS*	*NS*	*NS*
FFS	20.0°	0.059(±29)	*NS*	*NS*	*NS*	*NS*
- T1	20.0°	0.175(±7)	0.001(±2)	*NS*	*NS*	*NS*
- T2	20.0°	0.022(±27)	*NS*	*NS*	*NS*	*NS*
MRS	40.0°	0.499(±71)	0.008(±31)	0.002(±8)	*NS*	*NS*
- TPM1	40.0°	2.909(±33)	0.033(±8)	*NS*	*NS*	*NS*
- TPM2	40.0°	0.130(±19)	0.002(±4)	*NS*	*NS*	*NS*
MRS	52.5°	0.368(±67)	0.007(±17)	*NS*	*NS*	*NS*
- TPM1	52.5°	2.169(±41)	0.026(±8)	*NS*	*NS*	*NS*
- TPM2	52.5°	0.106(±19)	*NS*	*NS*	*NS*	*NS*
MRS	60.0°	0.346(±38)	0.002(±18)	*NS*	*NS*	*NS*
- TPM1	60.0°	1.704(±20)	0.010(±4)	0.001(±0)	*NS*	*NS*
- TPM2	60.0°	0.056(±10)	*NS*	*NS*	*NS*	*NS*
MRS	90.0°	0.254(±28)	0.000(±14)	0.001(±2)	*NS*	*NS*
- TPM1	90.0°	1.377(±17)	0.013(±2)	*NS*	*NS*	*NS*
- TPM2	90.0°	0.046(±10)	*NS*	*NS*	*NS*	*NS*

Table 9.14: Lost tracks after the embedding of **pions**. Number given in %. *NS* means "Not Seen". The numbers in the top row specifies the number of ghost tracks found. Errors given for the last digits.

Detector	θ	**1 lost**	**2 lost**	**3 lost**	**4 lost**	**5 lost**
FFS	3.0°	1.17(±11)	0.070(±69)	0.002(±22)	0.004(±13)	*NS*
- T1	3.0°	4.480(±76)	0.161(±24)	0.011(±9)	0.002(±4)	*NS*
- T2	3.0°	0.594(±94)	0.020(±43)	*NS*	*NS*	*NS*
FFS	4.0°	0.406(±69)	0.012(±43)	*NS*	*NS*	*NS*
- T1	4.0°	1.867(±44)	0.037(±11)	*NS*	*NS*	*NS*
- T2	4.0°	0.266(±62)	0.003(±23)	*NS*	*NS*	*NS*
FFS	8.0°	0.324(±92)	*NS*	*NS*	*NS*	*NS*
- T1	8.0°	0.850(±39)	0.018(±6)	*NS*	*NS*	*NS*
- T2	8.0°	0.201(±85)	*NS*	*NS*	*NS*	*NS*
FFS	12.0°	0.063(±33)	*NS*	*NS*	*NS*	*NS*
- T1	12.0°	0.266(±11)	0.004(±2)	*NS*	*NS*	*NS*
- T2	12.0°	0.048(±31)	*NS*	*NS*	*NS*	*NS*
FFS	20.0°	0.041(±28)	*NS*	*NS*	*NS*	*NS*
- T1	20.0°	0.149(±9)	0.001(±3)	*NS*	*NS*	*NS*
- T2	20.0°	0.013(±27)	*NS*	*NS*	*NS*	*NS*
MRS	40.0°	0.608(±71)	0.022(±31)	0.002(±8)	0.002(±3)	*NS*
- TPM1	40.0°	3.368(±34)	0.065(±9)	0.002(±0)	*NS*	*NS*
- TPM2	40.0°	0.151(±19)	*NS*	*NS*	*NS*	*NS*
MRS	52.5°	0.474(±69)	*NS*	*NS*	*NS*	*NS*
- TPM1	52.5°	2.348(±41)	0.040(±7)	*NS*	*NS*	*NS*
- TPM2	52.5°	0.077(±22)	*NS*	*NS*	*NS*	*NS*
MRS	60.0°	0.421(±37)	0.005(±17)	*NS*	*NS*	*NS*
- TPM1	60.0°	2.020(±20)	0.014(±4)	*NS*	*NS*	*NS*
- TPM2	60.0°	0.069(±9)	*NS*	*NS*	*NS*	*NS*
MRS	90.0°	0.350(±29)	0.001(±13)	*NS*	*NS*	*NS*
- TPM1	90.0°	1.681(±17)	0.018(±3)	*NS*	*NS*	*NS*
- TPM2	90.0°	0.086(±9)	*NS*	*NS*	*NS*	*NS*

Table 9.15: Lost tracks after the embedding of **kaons**. Number given in %. *NS* means "Not Seen". The numbers in the top row specifies the number of ghost tracks found. Errors given for the last digits.

Detector	θ	**1 lost**	**2 lost**	**3 lost**	**4 lost**	**5 lost**
FFS	3.0°	1.03(±11)	0.061(±68)	0.000(±21)	0.002(±13)	0.002(±6)
- T1	3.0°	4.377(±74)	0.143(±22)	0.007(±6)	0.002(±2)	*NS*
- T2	3.0°	0.684(±95)	0.020(±43)	0.002(±18)	*NS*	*NS*
FFS	4.0°	0.404(±66)	0.010(±42)	0.000(±11)	0.002(±6)	*NS*
- T1	4.0°	1.640(±43)	0.023(±10)	*NS*	*NS*	*NS*
- T2	4.0°	0.251(±61)	0.007(±24)	0.000(±8)	0.002(±5)	*NS*
FFS	8.0°	0.329(±91)	*NS*	*NS*	*NS*	*NS*
- T1	8.0°	0.722(±39)	0.005(±9)	*NS*	*NS*	*NS*
- T2	8.0°	0.183(±76)	0.005(±24)	*NS*	*NS*	*NS*
FFS	12.0°	0.057(±30)	*NS*	*NS*	*NS*	*NS*
- T1	12.0°	0.218(±11)	*NS*	*NS*	*NS*	*NS*
- T2	12.0°	0.033(±30)	*NS*	*NS*	*NS*	*NS*
FFS	20.0°	0.043(±27)	0.002(±7)	*NS*	*NS*	*NS*
- T1	20.0°	0.198(±7)	*NS*	*NS*	*NS*	*NS*
- T2	20.0°	0.023(±26)	*NS*	*NS*	*NS*	*NS*
MRS	40.0°	0.856(±72)	0.030(±32)	0.003(±6)	*NS*	*NS*
- TPM1	40.0°	3.937(±34)	0.082(±8)	*NS*	*NS*	*NS*
- TPM2	40.0°	0.208(±19)	*NS*	*NS*	*NS*	*NS*
MRS	52.5°	0.623(±66)	0.004(±15)	*NS*	*NS*	*NS*
- TPM1	52.5°	2.862(±41)	0.033(±9)	*NS*	*NS*	*NS*
- TPM2	52.5°	0.124(±17)	*NS*	*NS*	*NS*	*NS*
MRS	60.0°	0.616(±39)	0.014(±18)	*NS*	*NS*	*NS*
- TPM1	60.0°	2.518(±20)	0.032(±4)	*NS*	*NS*	*NS*
- TPM2	60.0°	0.113(±10)	*NS*	*NS*	*NS*	*NS*
MRS	90.0°	0.497(±29)	0.005(±14)	*NS*	*NS*	*NS*
- TPM1	90.0°	2.114(±16)	0.026(±4)	*NS*	*NS*	*NS*
- TPM2	90.0°	0.109(±9)	*NS*	*NS*	*NS*	*NS*

Table 9.16: Lost tracks after the embedding of **protons**. Number given in %. *NS* means "Not Seen". The numbers in the top row specifies the number of ghost tracks found. Errors given for the last digits.

9.8 Systematic uncertainties

The systematic uncertainties in the efficiency calculations have been obtained by varying the digitization constants within reasonable limits. Three parameters were varied, see section 6.3 on page 33 for an explanation of the parameters. The $ADCgain$ and the transverse and longitudinal diffusion velocity, D_T and D_L, were multiplied by 0.75 and 1.25. The result is shown in figure 9.34 and 9.35. The analysis was only done using digitized pions.

Changing the $ADCgain$ increases/decreases the height of the peak of the cluster, while changing D_T and D_L results in wider or narrower clusters.

Finally the longitudinal residuals, δ_L, were multiplied by 2. This is shown in figure 9.36 on page 127. This did not produce any big change in the efficiency.

In the MRS there are known distortions that are not well described by the digitization. Figure 6.7 on page 40 shows that the δ_L are a bit too small for the MRS. The efficiency may not show a linear dependence on the residuals in the MRS either. There is probably a sharp transition, where the efficiency will fall rapidly when the residuals gets bigger than the tracking search parameters. More analysis is needed to check this.

A test was done, where both the longitudinal and the transverse residuals, δ_L and δ_T, were both multiplied with 2. The results can be viewed in figure 9.37 on page 128. There is a clear indication that the matching start to fail more often, at least for the MRS. When matching is demanded for the singly digitized track, the change is not very big, the bottom part of figure 9.37. The efficiency loss rises an order of magnitude when matching is not demanded. This did not happen for the FFS. The matching parameters are discussed in section 7.5 on page 49, and are shown in table 9.8 for the two analyzed runs. The spreads in the slope matching parameters are much bigger in the MRS than in the FFS. Multiplying δ_L and δ_T with 2, seems to have a bigger impact on the distribution of the matching parameters in the MRS. The distribution gets too broad to be within the σ limits in table 7.5 on page 49.

Run	**M**	$d\alpha_{y,offset}$	$d\alpha_{y,\sigma}$	dY_{offset}	dY_{σ}	$dAng_{offset}$	$dAng_{\sigma}$
5713	D5	-0.0038128	0.0041058	-0.1615248	0.3956338	-0.0030748	0.0065568
5548	D2	-0.0005168	0.0025198	0.1205688	0.4119108	0.0012918	0.0033338

Table 9.17: Matching parameters for the MRS at 90° in run 5713 and the FFS at 3° in run 5548. The parameters are described in section 7.5 on page 49. **M** specifies the magnet.

In figure 9.35 on page 126, changing the ADCgain clearly has the biggest impact on the efficiency in the FFS, while only changing the transversal and longitudinal diffusion velocity has the smallest. The MRS shows similar changes in efficiency when the ADCgain and the longitudinal residuals are varied in

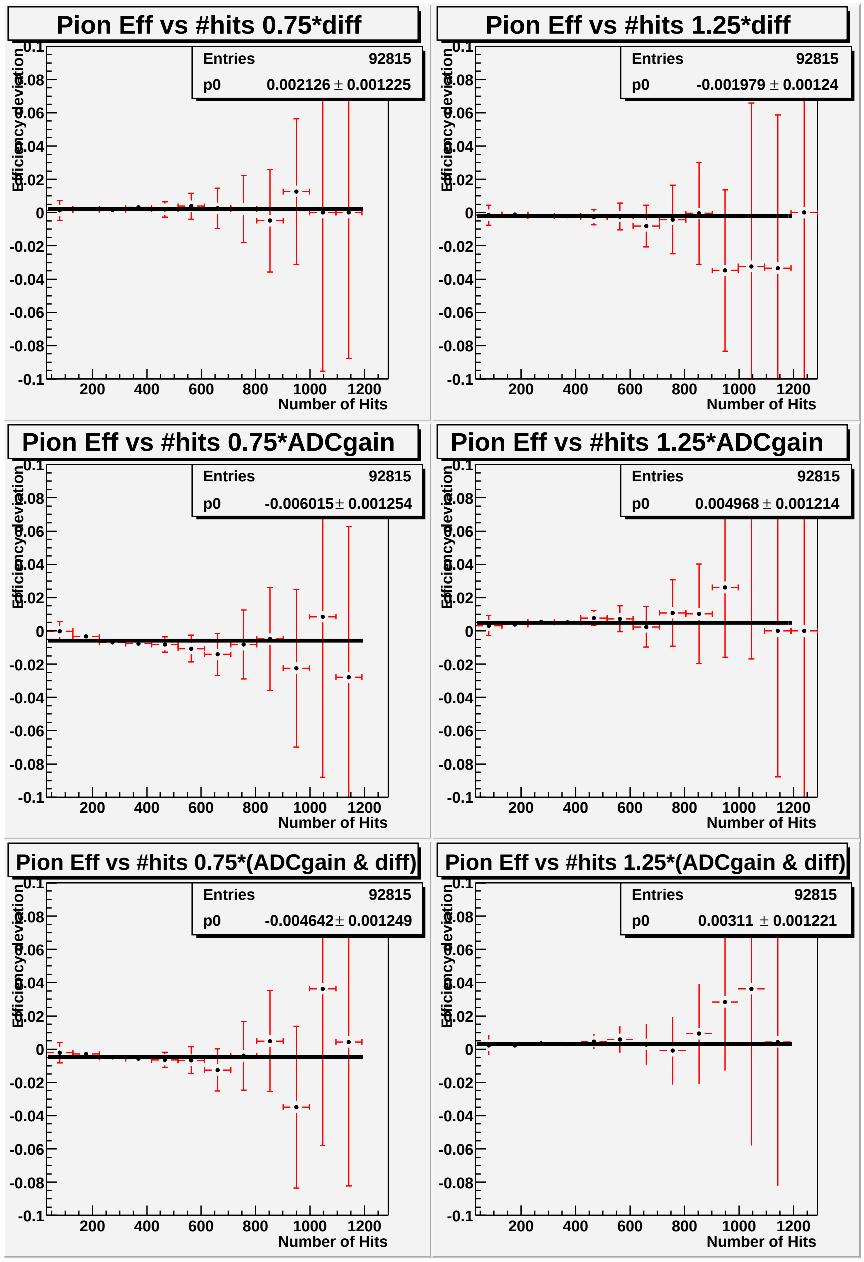

Figure 9.34: The histograms shows the difference in efficiency, for the MRS at 90°, between the results obtained using the parameters in appendix A on page 150 and the results obtained by changing the parameters. D_T and D_L are multiplied with 0.75 and 1.25 in the top row. The ADCgain is multiplied with 0.75 and 1.25 in the middle row. In the bottom row both the ADCgain, D_T and D_L are multiplied with 0.75 and 1.25.

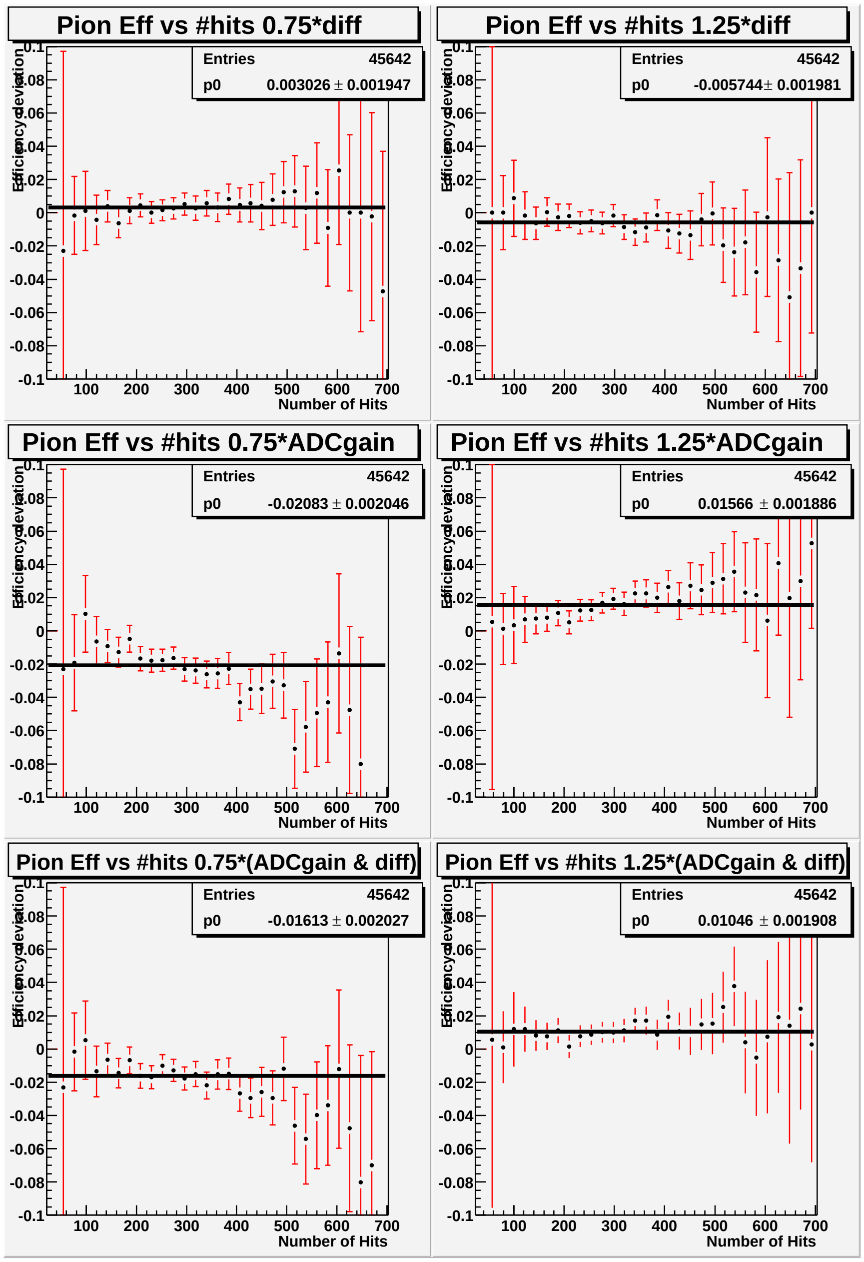

Figure 9.35: The histograms shows the difference in efficiency, for the FFS at 3°, between the results obtained using the parameters in appendix A on page 150 and the results obtained by changing parameters. D_T and D_L are multiplied with 0.75 and 1.25, respectively in the top row. The ADCgain is multiplied with 0.75 and 1.25 in the middle row. In the bottom row both the ADCgain, D_T and D_L are both multiplied with 0.75 and 1.25.

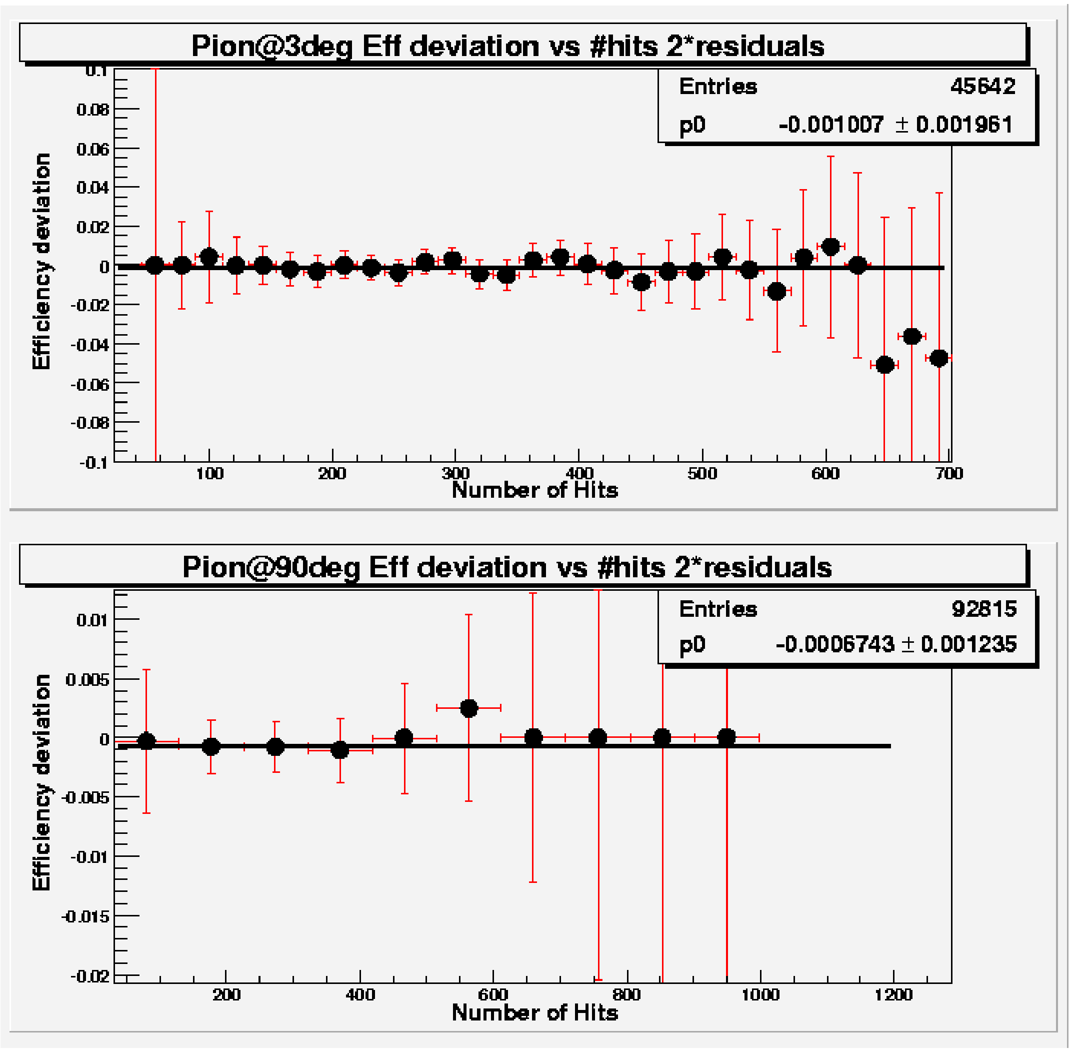

Figure 9.36: The histograms shows the difference in efficiency, for the FFS and MRS, between the results obtained with results obtained by multiplied the parameters in appendix A on page 150 and the results obtained by multiplying the longitudinal residuals, δ_L, with 2. The effect on the efficiency is very small.

figure 9.34 on page 125.

Comparing figure 9.36 with 9.37 indicates that multiplying the δ_T with 2 was an overkill for the MRS. The digitization seems to reproduce the δ_T reasonably well in figure 6.8 on page 41. δ_L is not that well reproduced, figure 6.7 on page 40.

To make an estimate on the efficiency loss, when the residuals are varied, an estimation of a linear dependence of the efficiency as a function of the residuals was made. This will be an over-estimate, since it is not believed to be linear

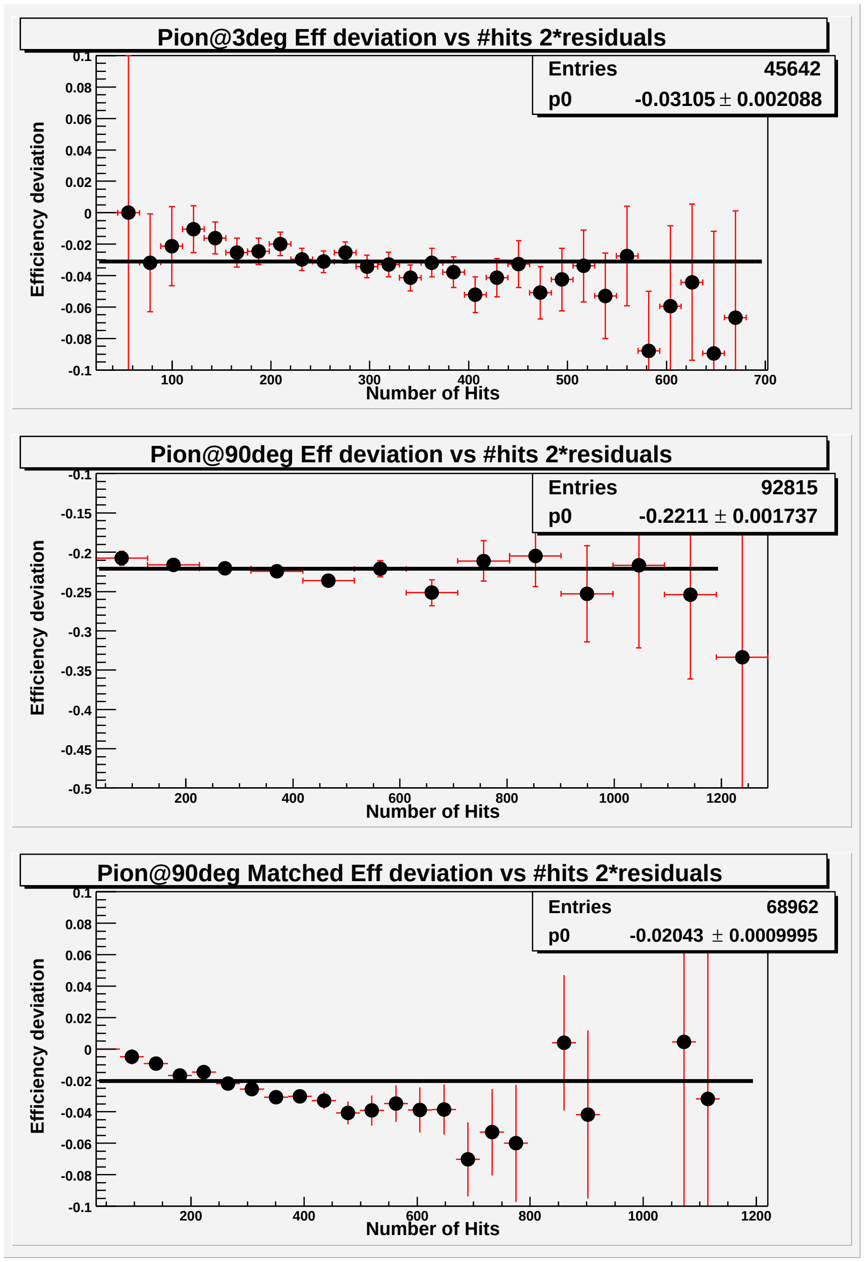

Figure 9.37: The histograms shows the difference in efficiency, for the FFS and MRS, between the results obtained with the parameters in appendix A on page 150 and results obtained by multiplying transverse and longitudinal residuals, δ_T and δ_L, with 2.

as discussed above. From figure 6.8 on page 41 it seems that δ_T should not be changed by more than $5-10\%$, while δ_L could be multiplied by a factor of 2. If the multiplied factor of both residuals in figure 9.37 is changed from 2 to 1.25, assuming a linear dependence, the efficiency loss is:

- **MRS** residual efficiency loss: $0.25 \cdot 22.1\% = 5.5\%$
- **FFS** residual efficiency loss: $0.25 \cdot 3.1\% = 0.8\%$

Since all these parameters independently influences the efficiency, and are the parameters that the digitization depends most on, an estimation of the total systematic uncertainty can be made by taking the square root of the sum of squares of these quantities. The quantities used are: *ADCgain*, diffusion velocity and residuals:

$$\Delta\varepsilon_{low} = -\sqrt{\varepsilon(ADCgain \cdot 0.75)^2 + \varepsilon((D_L \& D_T) \cdot 1.25)^2 + \varepsilon((\delta_L \& \delta_T) \cdot 1.25)^2} \quad (9.2)$$

$$\Delta\varepsilon_{high} = \sqrt{\varepsilon(ADCgain \cdot 1.25)^2 + \varepsilon((D_L \& D_T) \cdot 0.75)^2} \quad (9.3)$$

This results in an estimated systematic uncertainty of:

- **MRS** systematic uncertainty: -5.5% $+0.5\%$.
- **FFS** systematic uncertainty: -2.3% $+1.6\%$

All the numbers presented here are results obtained by averaging over all centralities and vertices. All the figures may also be fitted with a first degree polynomial, which will give a more accurate systematic uncertainty estimate as a function of the number of hits in the TPC. This has not been done in this thesis, but would be a natural extension of this work, since occupancy dependent efficiency corrections are clearly called for.

Chapter 10

Two track resolution

There are many things to consider when the efficiency of a TPC is to be determined. As mentioned in chapter 8 on page 58 there are limits both physically in the detector and in the reconstruction software. This chapter will try to establish how close two tracks can be and still be reconstructible. If they are close enough the hardware/software will only recognize one track. This can contribute to the probability of losing tracks, i.e. efficiency loss, if the possibility of two tracks being close to each other is large. The probability will depend on the occupancy. This feature is already incorporated in the efficiency analysis. If two tracks are close to each other and only one is reconstructed one track is necessarily lost.

The two track resolution is particularly important for HBT[1] studies.

Once again BRAG has been used to throw particles through the TPCs. The analysis is done in the following way:

1. **Produce particles** in brag with almost the same angle in θ and ϕ. 2° was chosen for θ and ϕ in the MRS, and 0.5° in the FFS.
2. **Digitize** the particles using the code in *BRAT* and the parameters in appendix A on page 150.
3. **Add** the digitized events together using *BrTpcAddSeqModule* (see section 4.3 on page 22).
4. **Try to reconstruct** the two tracks using the packages in *BRAT*. Also reconstruct the two events before they are embedded into each other.

If two lines are reconstructed in the "embedded" event, these lines must be compared to the original tracks. If a overlap bigger than 0.6 is found for both of the compared tracks, the two tracks are reconstructed. If these two embedded

---

[1] Hanburry-Brown-Twiss' method for finding the radius of the fireball created in a nucleus-nucleus collision.

tracks are reconstructed, there is a possibility that the tracking algorithm has made them cross each other. This is illustrated in figure 10.1. The tracks can cross each other if one or both of them are subject to multiple scattering. This must be determined before it is possible to say that the tracks are reconstructed.

Two separately digitized tracks already crossing each other, before they are embedded, are not considered in the calculations presented here. This must therefore be checked before the embedding.

The determine whether the tracks cross each other, the entrance and exit points, in the TPC, of the two tracks are compared. Let track 1 enter the TPC volume at $(x_{E,1}, y_{E,1})$ and exit at $(x_{X,1}, y_{X,1})$. And correspondingly for track 2, entry at $(x_{E,2}, y_{E,2})$ and exit at $(x_{X,2}, y_{X,2})$. Any of the following criteria determines that the two tracks are crossing each other:

- $(x_{E,1} < x_{E,2})$ && $(x_{X,1} > x_{X,2})$
- $(x_{E,1} > x_{E,2})$ && $(x_{X,1} < x_{X,2})$
- $(y_{E,1} < y_{E,2})$ && $(y_{X,1} > y_{X,2})$
- $(y_{E,1} > y_{E,2})$ && $(y_{X,1} < y_{X,2})$

where **&&** means **logical and**.

All the simulated particles had a momentum of $1.0\,GeV$.

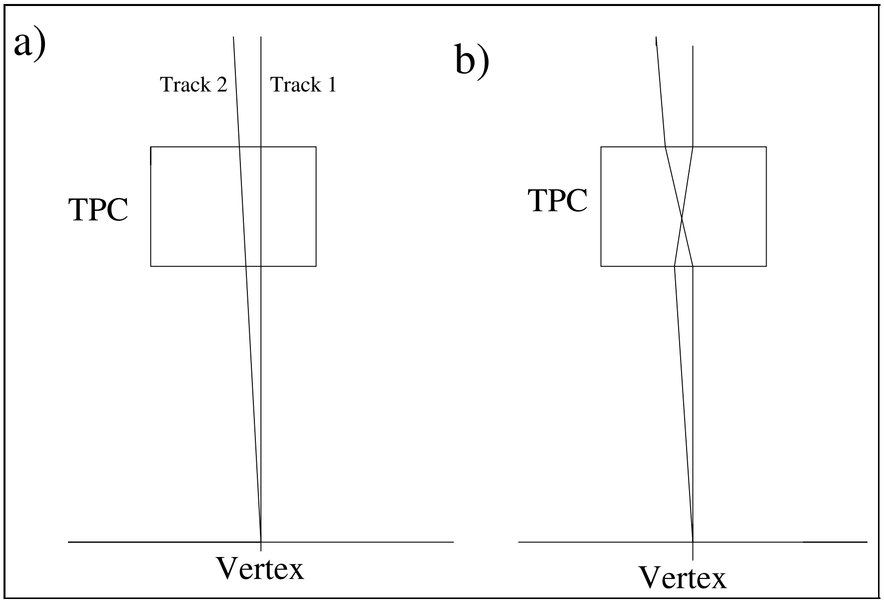

Figure 10.1: In a) the lines are reconstructed correctly inside the TPC volume. But in b) the algorithm has not reconstructed them in a correct way.

There are two things that might contribute to the two track resolution. Cluster deconvolution is the first one. Since the tracks lie close, their clusters will often end up partially on top of each other. They then have to be deconvoluted to two clusters after the first part of the clustering has been done. This might not always be possible. The second contribution is the multiple scattering of the two particles. Since they are very close to each other, zig-zag patterns in the hits may cause the the tracking algorithm to give some hits belonging to one track to the other, and vice versa. They may end up crossing each other. The reconstructed tracks might therefore not have enough overlap with their original tracks.

10.1 The resolution of the TPCs

This analysis has been done for all the TPCs. The resolution is plotted as a function of the average distance between the tracks inside the TPC volume. The reason for not using the absolute angle between the tracks (since they originate from the same vertex) is that the TPCs are quite a long distance from the vertex. Just a slight distortion in the tracks can therefore make the tracks become parallel. In these cases the angle will not give us much sensible information. The average distance is found between the two separately digitized tracks, both in this section and the next.

The resolution limit is defined as the shortest distance between the tracks where the reconstruction probability reaches maximum. This maximum is essentially at 100%, since there are only two digitized tracks in the event.

The average distance between the tracks is found by making a track that is exactly in the middle of the two tracks, i.e. the perpendicular distance from this constructed line to one of the original tracks is the same as the distance to the other track. This is the minimum distance. The average distance between the two tracks is therefore two times the perpendicular distance from the constructed line to one of the other tracks at $Z = 0$[2]. This calculation is only true if the tracks do not cross each other.

If the two tracks are parametrized like this:

$$X = A_n \cdot Z + a_n \tag{10.1}$$

$$Y = B_n \cdot Z + b_n \tag{10.2}$$

where the subscript n denotes the track number (1 or 2), the line between these two will look like this:

---

[2] In local coordinates, $Z = 0$ is the center plane of the TPC. See 8.1 on page 59.

$$
\begin{aligned}
A_m &= \frac{A_1 + A_2}{2} && (10.3)\\
B_m &= \frac{B_1 + B_2}{2} && (10.4)\\
a_m &= \frac{a_1 + a_2}{2} && (10.5)\\
b_m &= \frac{b_1 + b_2}{2} && (10.6)\\
X &= A_m \cdot Z + a_m && (10.7)\\
Y &= B_m \cdot Z + b_m && (10.8)
\end{aligned}
$$

The perpendicular plane to this line at $Z = 0$ ($Y_0 = b_m$ and $X_0 = a_m$) looks like this:

$$
\begin{aligned}
D = A_m \cdot a_m + B_m \cdot b_m && (10.9)\\
A_m \cdot X + B_m \cdot Y + Z - D = 0 && (10.10)
\end{aligned}
$$

The intersection point Z value, Z_1, between track 1 and this plane is:

$$Z_1 = \frac{D - a_1 \cdot A_m - b_1 \cdot B_m}{A_1 \cdot A_m + B_1 \cdot B_m + 1} \tag{10.11}$$

The distance between the two points, $(X_0, Y_0, 0)$ and $(A_1 \cdot Z_1 + a_1, B_1 \cdot Z_1 + b_1, Z_1)$, can then easily be calculated. The average distance, d, between the to tracks is then:

$$d = 2 \cdot \sqrt{(A_1 \cdot Z_1 + a_1 - a_m)^2 + (B_1 \cdot Z_1 + b_1 - b_m)^2 + Z_1^2} \tag{10.12}$$

Since different particles deposit different amounts of energy pr cluster or hit, two particle species can also be mixed together, which may change the resolution. Therefore pions have been mixed with itself, protons and kaons, kaons has been mixed with itself and protons and protons has been mixed with protons. Since the TPCs have many more pads pr row then rows pr TPC, the angle of the track relative to the TPC opening plane may also change the two track resolution. Therefore the particles have entered the TPC approximately perpendicular to the TPC opening plane, and at an angle $\sim 75°$ for TPM1 and TPM2. In the FFS the distance to the TPCs from the nominal vertex are large ($478\,cm$ for T1 and $780\,cm$ for T2). This physical dimension of D1 makes it nearly impossible to get an entry angle which deviates much from $\sim 90°$ for

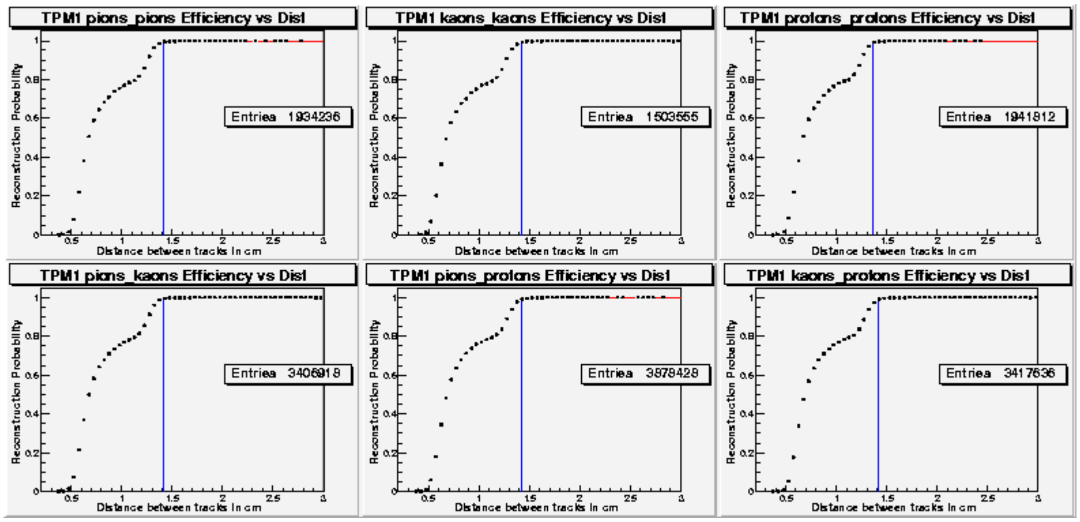

Figure 10.2: The probability of finding the two spaced tracks for TPM1 at $\sim 90°$. The graph seems to flatten out at about $1.4\,cm$.

identifiable tracks[3]. The results from the analysis is presented in the following figures. Figure 10.2 shows the results for particles going at $\sim 90°$ into TPM1.

From the figure it is seen that the resolution is $1.4\,cm$ for all type of particle mixing. The resolution is lowered if the particles go through the TPC at a lower angle as is seen in figure 10.3 on the following page. Between $\sim 0.9\,cm$ and $1.2\,cm$ there is a small shoulder for all the particles. This will be discussed in section 10.3 on page 141.

The $\sim 76°$ particles in figure 10.3 on the following page does not show such a sharp transition as for the $\sim 90°$ angle, but it flattens out at between $1.5\,cm$ (protons with protons) and $1.6\,cm$. The shoulder is still there, starting at $1.0\,cm$ and ending at $1.2\,cm$, but is not as dominant as in figure 10.2.

The resolution for TPM2 (figure 10.4) is slightly poorer than TPM1, about $1.7\,cm$. In addition there seems to be two very small shoulders as the probability rises, the first one at about $0.9\,cm$ and the next one at about $1.4\,cm$. The first is the most prominent, but they are very small compared to figure 10.2.

There is a big difference betweem TPM2 at 90° and 75°, figure 10.5. The resolution drops with about $0.7\,cm$, and shows the poorest resolution of about $2.4\,cm$. One of the shoulders seem to have shown up more clearly just before the probability reaches 1. This might be somewhere in the area $1.7 - 2.2\,cm$. There might be a suggestion to a shoulder in some of the figures at around $0.7\,cm$, but this is not much of a shoulder compared to the higher one.

T1 (figure 10.6) has the second best resolution of about $1.4\,cm$. This TPC only shows one weak shoulder located at $\sim 1\,cm$

---

[3] T2 is rotated 1.9° relative to T1

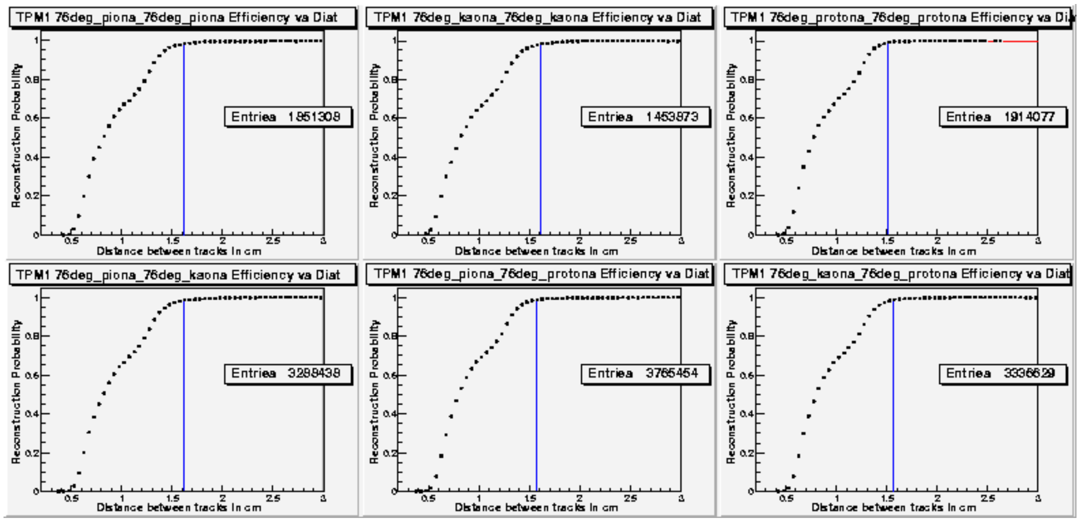

Figure 10.3: The probability of finding the two closely spaced tracks for TPM1 at ~ 76°. The graph seems to flatten out at about 1.6 *cm*.

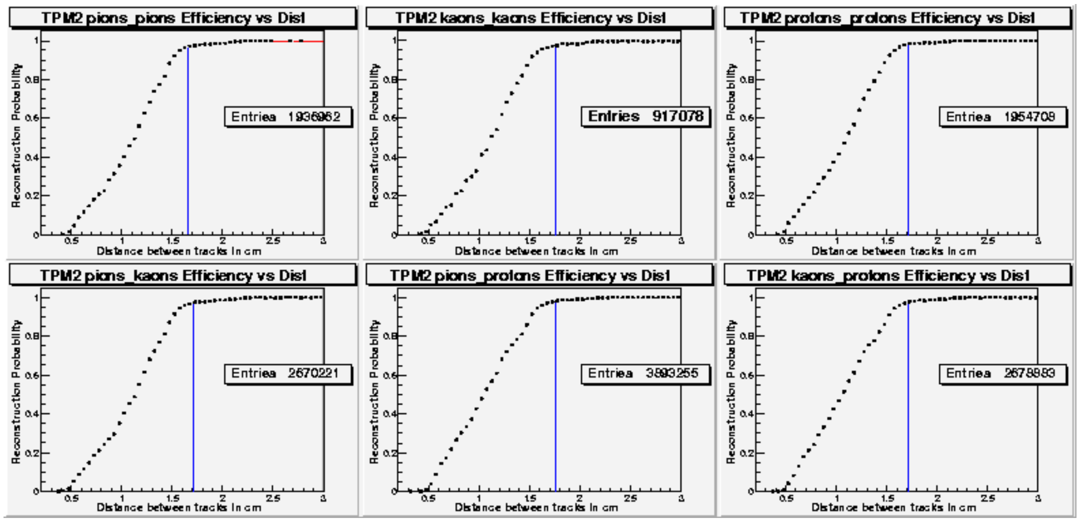

Figure 10.4: The probability of finding two closely spaced tracks in TPM2. The figure seems to flatten out at around and average distance between the tracks of 1.7 *cm*.

T2 (figure 10.7) has the second poorest two track resolution. The resolution seems to lie around 2.0 *cm*. There are two very prominent shoulders. The first one starts at 0.6 *cm* and ends at 0.8 *cm*. The other starts at 1.3 *cm* and ends at 1.6 *cm*.

The two tracks resolution does not show any dependence on the different

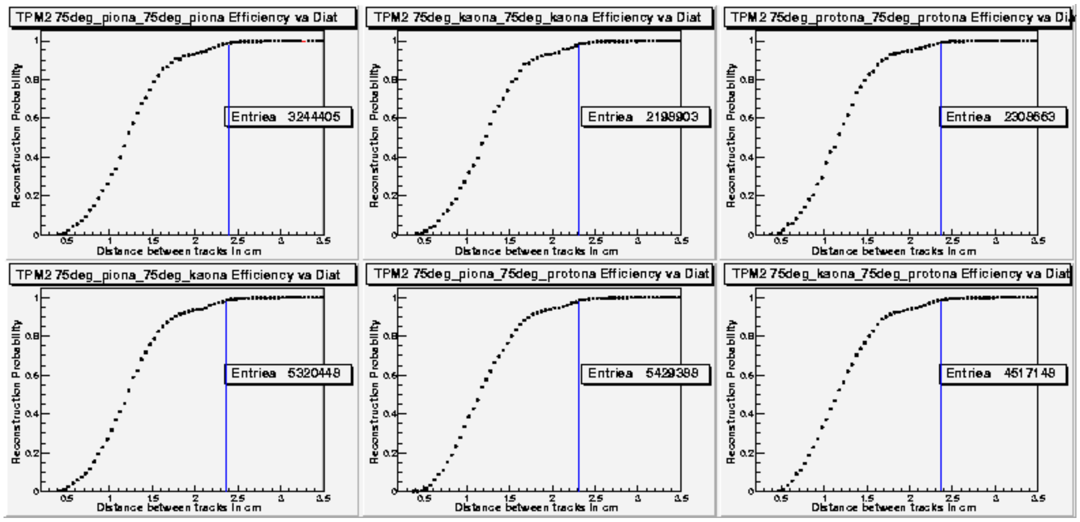

Figure 10.5: The probability of finding two closely spaced tracks in TPM2 at 75°. The figure seems to flatten out at around and average distance between the tracks of 2.4 cm.

mixing of particles. All the particles had a momentum of 1.0 GeV/c, so different particles produces different kinds of clusters. All the plateaus has a pretty sharp transition, which enables a good determination of the two track resolution. Table 10.1 summarizes the results.

Above these distances, the tracks may safely be used for HBT analysis.

Detector	**Resolution**	**Angle**	**Entry**	**Exit**
TPM1	1.4 cm	0.85°	1.1 cm	1.7 cm
TPM1 76°	1.6 cm	0.94°	1.3 cm	1.9 cm
TPM2	1.7 cm	0.33°	1.6 cm	1.9 cm
TPM2 75°	2.4 cm	0.45°	2.2 cm	2.6 cm
T1	1.4 cm	0.16°	1.3 cm	1.5 cm
T2	2.0 cm	0.14°	1.9 cm	2.1 cm

Table 10.1: Summary of the Two track resolution. The Angle column is a calculated angle assuming the particles come from the same vertex. The Entry and Exit columns are the distance between the tracks as the enter and exit the TPC, using the calculated angle.

10.2 Two track crossing probability

Figure 10.8 on page 138 shows another interesting feature of the tracking algorithm, the probability for the tracking algorithm to make the two tracks cross

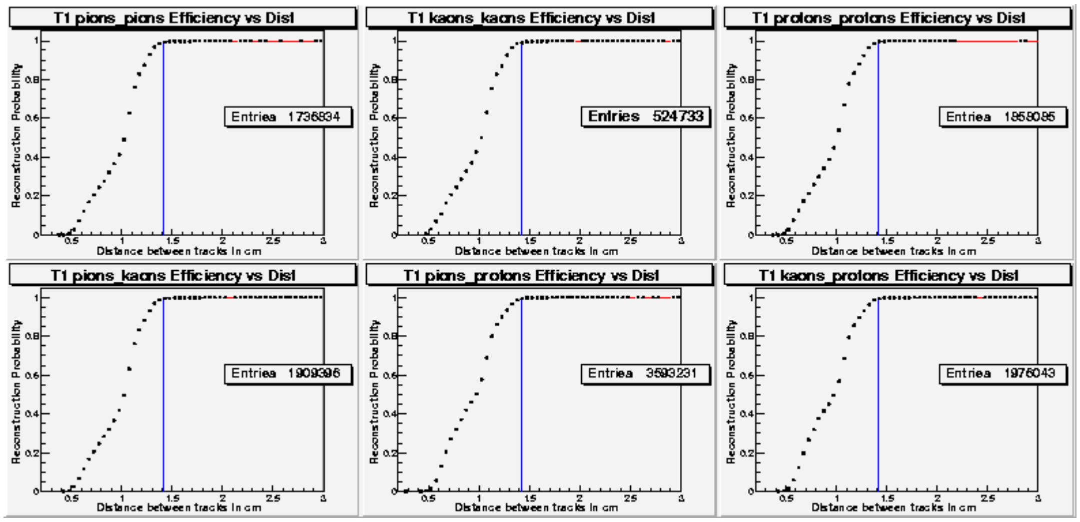

Figure 10.6: The probability of finding two closely spaced tracks in T1. The resolution is about 1.4 cm for all the particles.

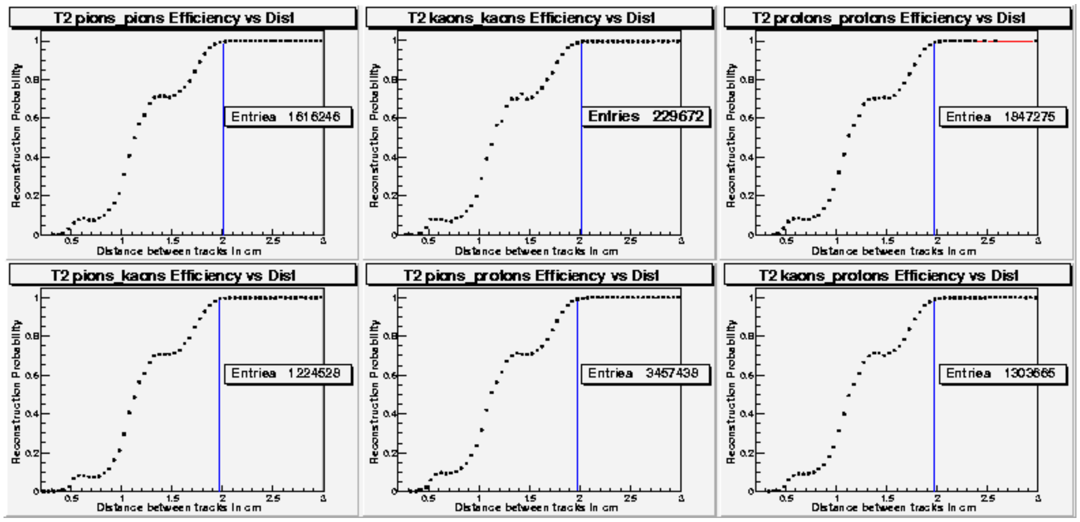

Figure 10.7: The probability of finding two closely spaced tracks in T2. The resolution is about 2.0 cm.

each other.

The distance calculation is still vaild, since it is calculated between the two singly digitized none-crossing tracks. The analysis is only done when the two singly digitized tracks do not cross.

In figure 10.8 on the next page the crossing probability is shown for TPM1, with the particles entring the TPC at ~ 90°. The highest peak is found around

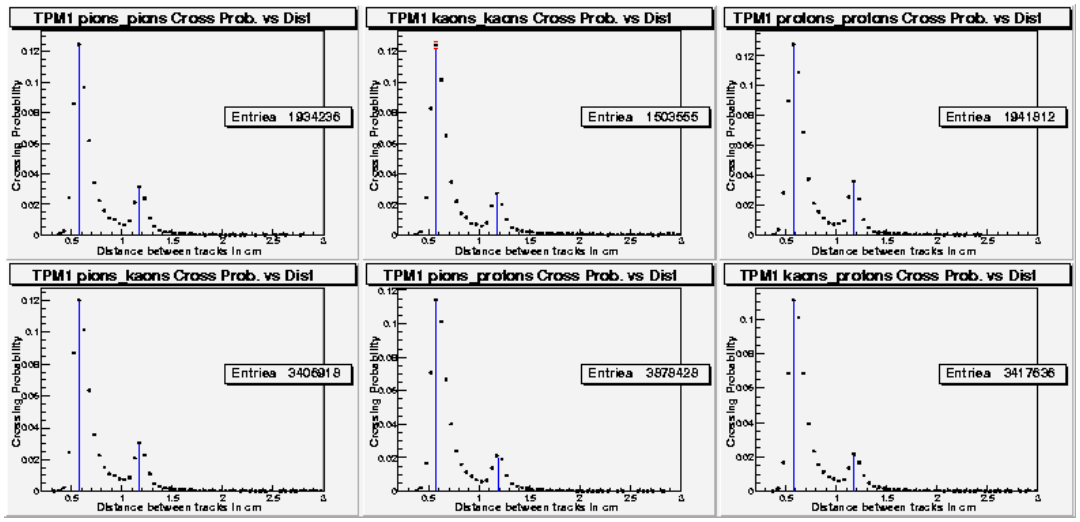

Figure 10.8: The probability for the tracking algorithm to make the two tracks cross in TPM1 for different mixing of particles. The peaks are all located at the same places: at 0.6 *cm* and 1.2 *cm*.

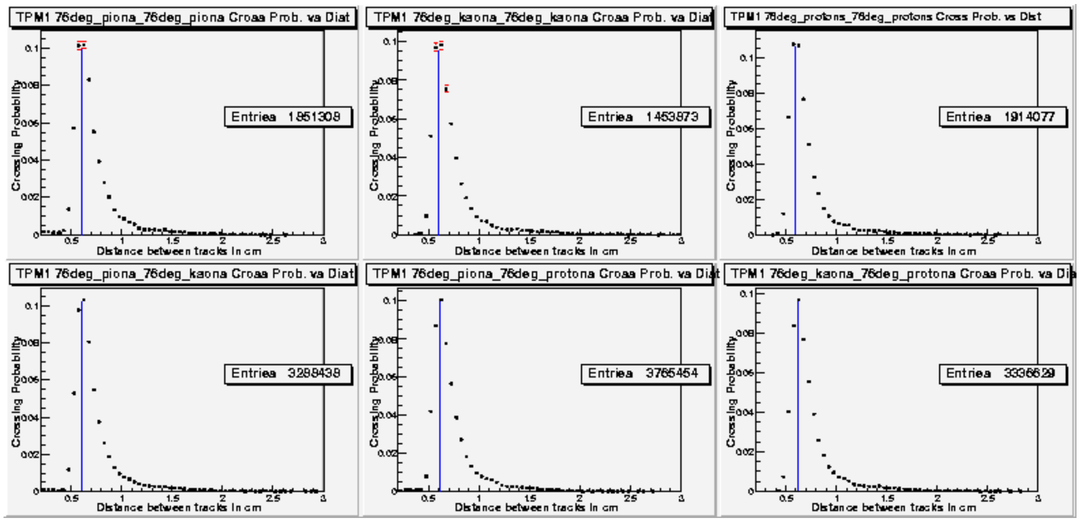

Figure 10.9: The probability for the tracking algorithm to make the two tracks cross in TPM1 at 76° for different mixing of particles. There is only one peak and it is located at 0.6 *cm*.

0.6 *cm*, with another small peak at double this value, 1.2 *cm*. This second peak is not present in figure 10.9, where the particles entring the TPC at $\sim 76°$, but the first peak is there at the same spot. Kaons with kaons and kaons with protons shows a hint that there may be another rise in the probability at around

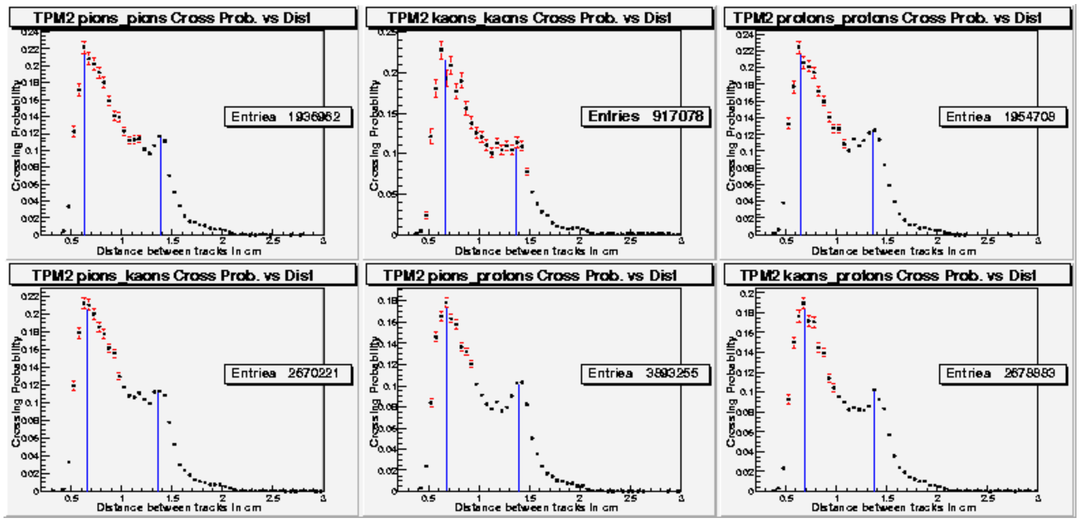

Figure 10.10: The probability for the tracking algorithm to make the two tracks cross in TPM2 for different mixing of particles. The peaks are located at 0.7 *cm* and 1.4 *cm*.

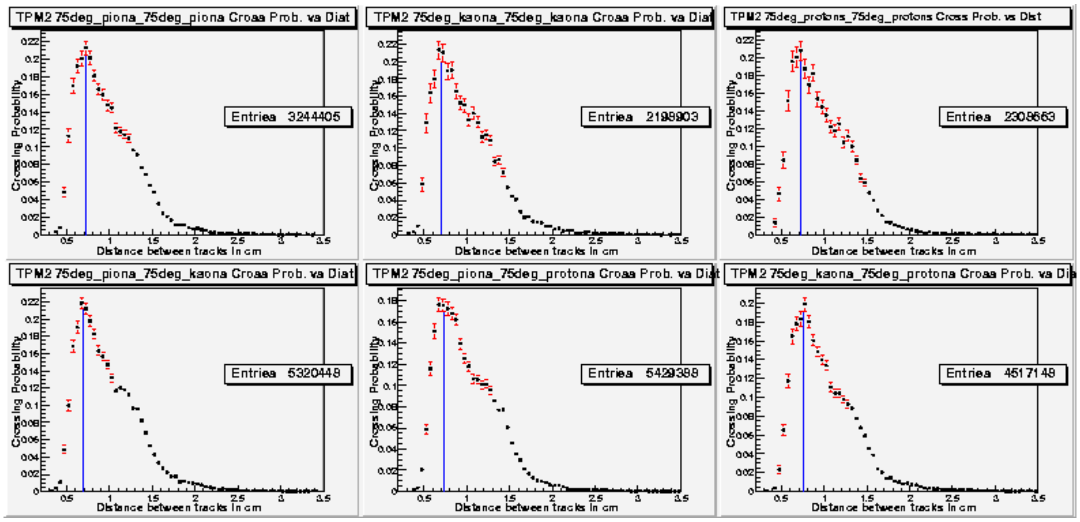

Figure 10.11: The probability for the tracking algorithm to make the two tracks cross in TPM2 for different mixing of particles entering the TPC at ∼ 75°. There is only one clear peak at 0.7 *cm*. There is another peak partially buried under the largest one, located at ∼ 1.2 *cm*.

1.4 *cm*, but it is not evident.

Figure 10.10, TPM2, is also plotted as a function of the average distance between the two tracks, as the two next figures. Again this double peak shows

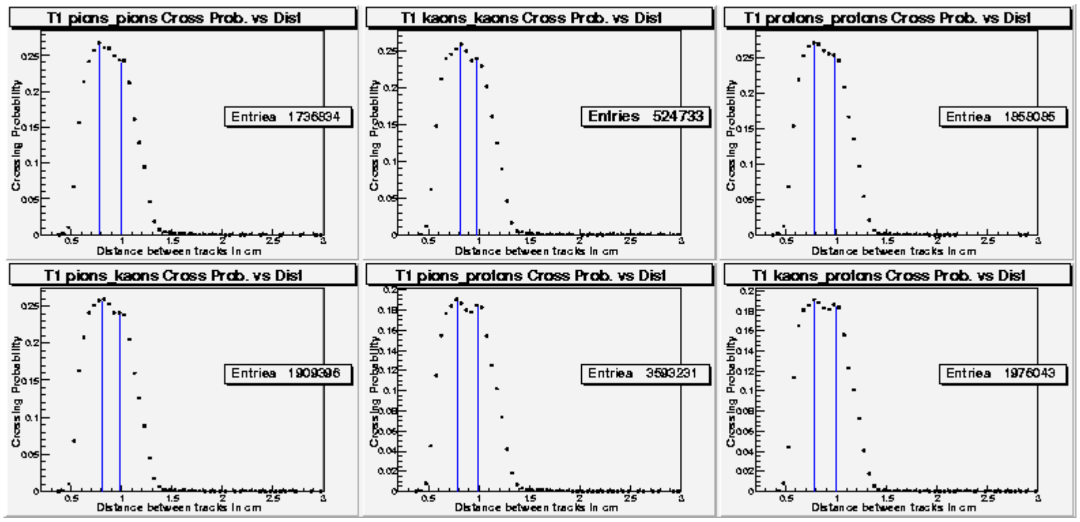

Figure 10.12: The probability for the tracking algorithm to make the two tracks cross in T1 for different mixing of particles. There are to close lying peaks located at 0.8 *cm* and 1.0 *cm*.

up. The first one at about 0.7 *cm* and the next at double this value, 1.4 *cm*. When the particles enter the TPC at ∼ 75° the second peaks has moved much closer to the first one, figure 10.11 on the preceding page. The first one is easily seen at 0.7 *cm*, while the second is probably at ∼ 1.2 *cm*.

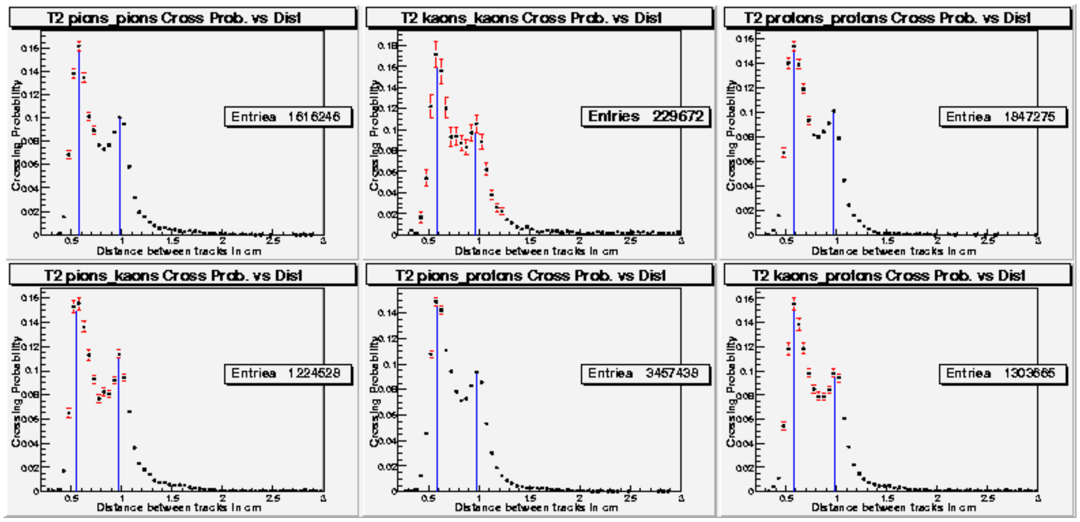

Figure 10.13: The probability for the tracking algorithm to make the two tracks cross in T2 for different mixing of particles. There are two well separated peaks located at 0.6 *cm* and 1.0 *cm*.

Figure 10.12 on the page before shows the results for T1. It has one broad peak, that seems to be composed of two close lying peaks, located at $0.8\,cm$ and $1.0\,cm$.

The crossing probability in T2 shows two peaks in figure 10.13. The peaks are located at $0.6\,cm$ and $1.0\,cm$.

There does not seem to be any dependence on the mixing of particles.

10.3 The shoulders and double peaks

These shoulder and (double) peaks might be a "quantization" feature from the physical design of the TPCs or from the software. When two tracks are very close, many of the clusters might be shared by more than one track. The tracking algorithm does not allow more than 3 (default value) hits to be shared by two tracks. In addition many of the clusters will be multihit clusters[4]. These clusters will only be divided into two (or more) hits if the σ of the cluster is above $1.6\,cm$ (default value), which is approximately the resolution of the TPC as seen in table 10.1 on page 136. The physical constraint still lies in the width of the pads. Figure 10.2 — 10.6 clearly drop to zero at around $0.4\,cm$, which is approximately the effective width of the pads in the TPCs, see table 10.2 on the following page. It is worth noting that T2 is divided into to pieces. The first and second half of it is separated by $12.5\,cm$. T2 has two very dominant shoulders.

The first thing to compare is the the position of the shoulders relative to the position of the peaks in the "crossing" histograms, see table 10.2 on the next page. Some of the particle mixings show a loose correlation in the position of the shoulders and crossing peaks, but this seems to be a coincidence, since most do not. The first crossing peak is located at nearly the same position in all the TPCs, $\sim 0.6 - 0.7\,cm$.

There must be some deeper underlying reason for these behaviours. In figure 10.14 on page 143, the number of track pairs who shares hits and who have at least one deconvoluted multihit[5] are plotted as a function of their distance, for pions mixed with pions in TPM1. All occurances were two tracks where reconstructed regardless of they were crossing each other or if they had enough overlap with their original track are included in the figure. Figure 10.15 shows the same for T2.

There is a close relation with sharing hits and the second peak in the crossing probability. The first peak is maybe shown as a shoulder as the probablity for sharing hits increases as the tracks gets very closely spaced. The tracking algorithm seems to make the tracks cross each other when there are many

---

[4] See section 7.4 on page 47 for clusters and tracking. In this section the multihits are hits that originate from a cluster that has been divided into two or more clusters.

[5] See section 7.4 on page 47 for an explanation on cluster status.

(maximum of 3 in this analysis) shared hits, which is seen to happen more frequently at certain distances. There seems to be no correlation between the shoulder or the crossing probability and if the tracks have any deconvoluted hits. All the other TPCs show the same behaviour, and is not shown.

Tracks passing "between" 2 pads have a less pronounced cluster than tracks passing over the middle of the pad. If this phenomna is to be studied any further it should probably be done on the cluster level. There is no obvious correlation with the figures in section 6.3.2 on page 36 either.

An interresting feature seen in table 10.2, is that the crossing peaks seem to coincide approximately with 1.5 and 3 effective pad widths.

It is still unknown why the shoulders appear.

Detector	TPM1	TPM1 76°	TPM2	TPM2 75°	T1	T2
Pad Length	3.05	3.14	2.50	2.58	4.00	4.00
Pad Width	0.39	0.40	0.47	0.49	0.35	0.35
Shoulder 1	0.9-1.2	1.0-1.2	0.9	0.7	1.0	0.6-0.8
Shoulder 2	—	—	1.4	1.7-2.2	—	1.3-1.6
Crossing 1	0.6	0.6	0.7	0.7	0.8	0.6
# Pads	1.5	1.5	1.5	1.3	2.3	1.7
Crossing 2	1.2	—	1.4	1.2	1.0	1.0
# Pads	3.0	—	3.0	2.6	2.9	2.9

Table 10.2: All number are given in *cm*. Size of the pads in the TPCs. Shoulder 1 and 2 are the shoulders seen in figure 10.2 — 10.7. Crossing 1 and 2 are the peaks seen in figure 10.8 — 10.13. The pad distance and row distance is not the actual width and length of the pad, it includes the empty space between the pads and rows. The # **Pads** rows denote how many pad widths the crossing peak corresponds to, i.e. $\frac{Crossing}{Pad\ dist}$.

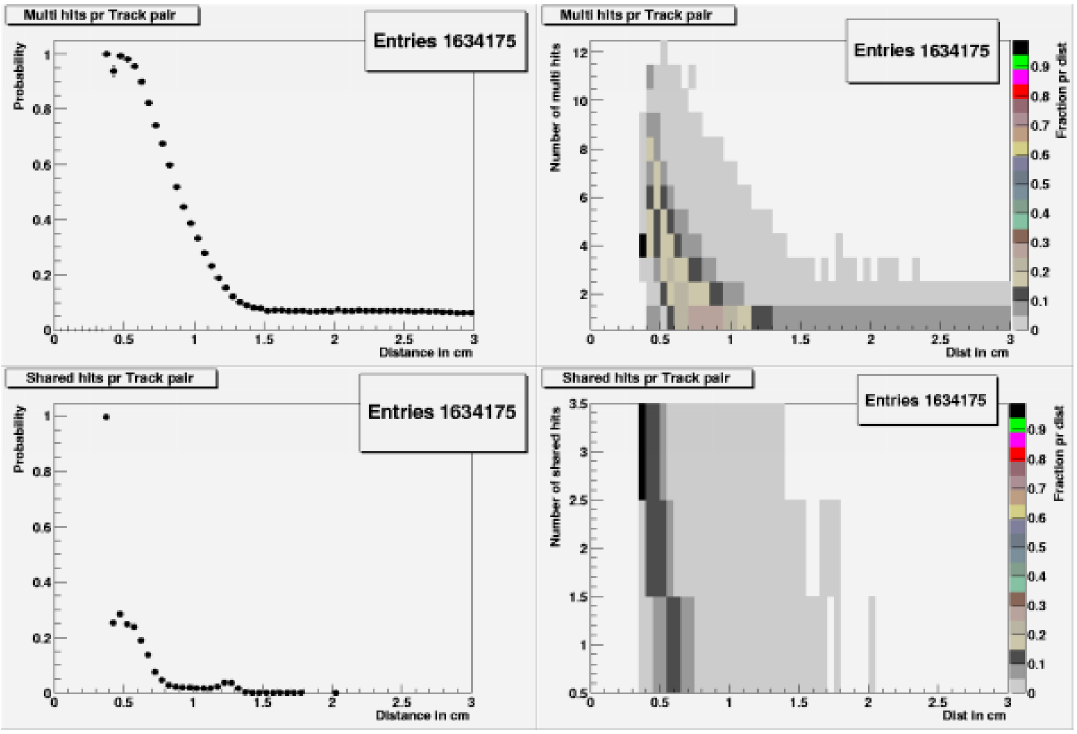

Figure 10.14: The bottom figures show all reconstructed track pairs that share hits in TPM1, regardsless if they are crossing each other or have enough overlap with their origninal track to be considered properly reconstructed. The small peak in the bottom row is located at the same position as the second peak in figure 10.8 on page 138, 1.2 cm. There seem to be no correlation between the crossing probability or the shoulders and if the tracks have deconvoluted hits in the top figures.

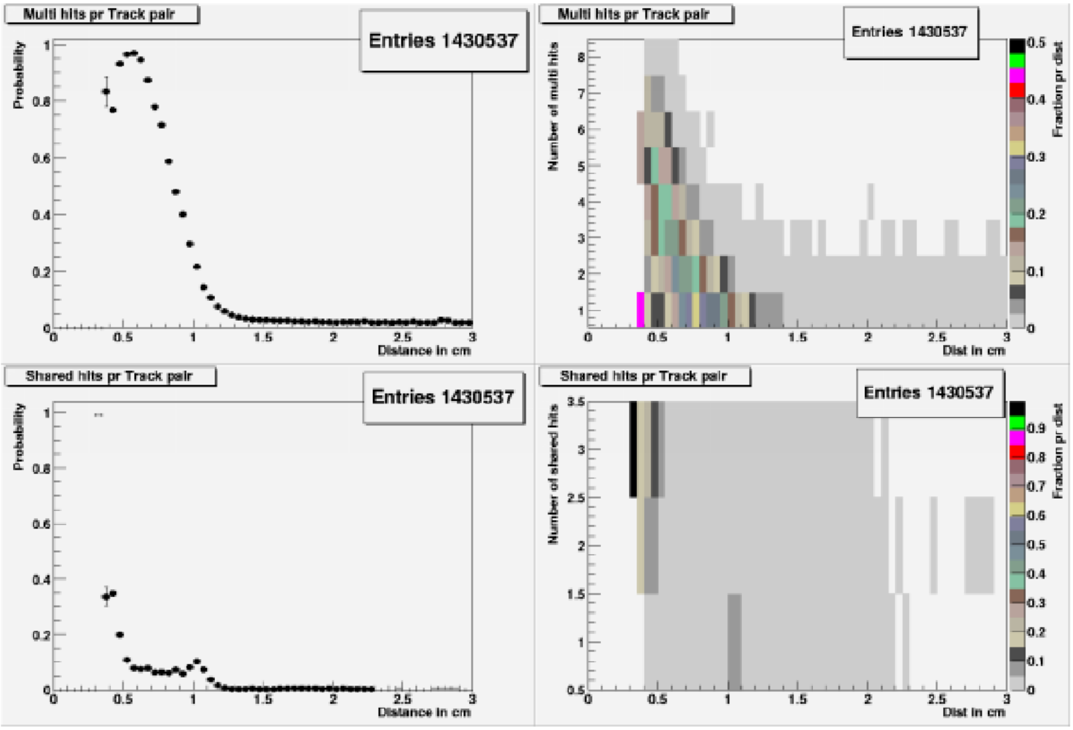

Figure 10.15: The bottom figures show all reconstructed track pairs that share hits in TPM1, regardsless if they are crossing each other or have enough overlap with their origninal track to be considered properly reconstructed. The small peak in the bottom row is located at the same position as the second peak in figure 10.8 on page 138, 1.2 cm. There seem to be no correlation between the crossing probability or the shoulders and if the tracks have deconvoluted hits in the top figures.

Chapter 11

Conclusion

The results presented in chapter 9 are heavily dependent on the digitization. It is very important that the hits are digitized in a way that resembles a real cluster of ADC values. Only slight differences may result in a large difference in the efficiency. If the clusters are too high and narrow it will result in a too large efficiency, while very wide, low clusters will result in a too poor efficiency. There is also the issue of choosing the residuals, which residuals are the distance from the centroid of the cluster to the trajectory. The efficiency dependence may be non-linear, showing a sudden drop when th residuala are of the same size when the as the hit search window used in the tracking. Too large residuals give lower efficiency, while too small results in a too large value. Distortions, not implemented in the digitization, are known to bepresent, in particular in TPM1 and TPM2. This may reduce the efficiency even further. Mimicking distortions is done in section 9.8, where the systematic uncertainties are discussed, by varying the residuals.

In chapter 9 the efficiency is presented as a function of total number of hits in the TPCs, centrality, number of spectrometer tracks, vertex position, momentum and as $\varepsilon(p_T, y)$ diagrams.

The efficiency falls linearly, as expected, with the occupancy. The FFS did not have the same linearity with the number if hits in different spectrometer settings, as the MRS did. Further investigations are needed to establish why this happens. There seemed to be a hint of non-linearity between the number of tracks and number of hits, but it was impossible to draw any decisive conclusion, without more detailed studies.

The vertex position does not seem to play any important role in the efficiency. As shown in the figures in section 9.3, the efficiency had a small dependence on the vertex position, but it seemed arbitrary if it increased or decreased with the vertex position. The changes in efficiency with vertex position were also small compared to the systematic uncertainties seen in section 9.8.

The efficiency did not depend much on the momentum of the particles either, as long as they were well within the acceptance of the magnetic field. When the momentum got to the low end of the momentum range, the efficiency suddenly fell off. This can be explained by more multiple scattering experienced by these low momentum particles' increasin residuals, making them more difficult to reconstruct. The average multiple scattering angle is proportional to $1/\beta^2$. The residuals, as a function of momentum, influenced in particular the matching efficiency as seen in section 9.8. A weak, but significant deoendence, was also seen at the higher momentam and seemed to follow the $\frac{dE}{dx}(p)$ variation.

The momentum resolution was examined in section 9.5. It was shown to be reasonable good, but had slight dependence on the momentum. The momentum smearing is strongest for particles in the high end of the momentum range. This can influence yields and particle spectra plotted against the momentum. Quantitative effects in spectra and yields has not been investigated, and should definitely be looked at in the future. The overall momentum resolution, averaged over momenta, was $\sim 2-3\%$.

Investigations were also conducted on edge effects in section 9.6. None were discovered using the embedding method. The only conclusion is that it will probably never have any effect on spectrometer tracks, since they are too far from the side walls of the TPCs.

The results in section 9.1 and 9.2 showed that there is a strong dependence on the occupancy. Measured particles should therefore be efficiency corrected using the occupancy. This may be done by using the total number of hits in the TPCs or using the centrality.

If the centrality is to be used, the corrections can be done in the same manner as the acceptance corrections, briefly discussed in section 8.5. Using $\varepsilon(p_T, y)$ corrections can be done after all the data is analyzed. This would require $\varepsilon(p_T, y)$ diagrams, with not too coarse centrality bins, in the desired centrality range, for all the spectrometer settings in the analyzed data. This also requires the raw data to binned with respect to the occupancy, i.e. the centrality. This is not done in the current analysis chain used on the raw data, and would require it to be modified.

If the corrections are made from the number of hits in the TPC using the present standard analysis pipeline, it has to be done event by event before the (p_T, y) histogramming and the acceptance corrections. Each spectrometer setting would not necessarily have to be analyzed for efficiency analyzed in the MRS, since the efficiency showed the same parametrization on the occupancy dor all settings, see section 9.1. The FFS, on the other hand, would need an analysis in each setting, see section 9.2, because it has a setting dependent parametrization.

These two methods impose two completely different strategies, which will probably be discussed by the collaboration before a decision, on which method to use, is made. Correcting for efficiency event by event, using a parametrization, seems a good, and perhaps the best, solution. There is no strong dependence on the momentum, and correcting with $\varepsilon(p_T, y)$ might be an overkill, but would fall nicely in line with the acceptance corrections.

Finally, the probabilities for ghost tracks and lost tracks were discussed in section 9.7. They showed up numerously. Why as many as 8% of the events, in some spectrometer settings, produced at least one ghost track, after embedding, was not discovered. The spectrometer ghost tracks was nearly always composed of at least one local ghost track. There seemed to be a occupancy dependence in the ghost track probability, which would suggest that they originate from a combinatorial source. This must be much more closely examined. A solution to to this problem could perhaps be solved by improvements in the tracking software. Another possibility is to correct for the ghost track contribution, perhaps as a fucntion of momentum and occupancy.

The digitization parameters have been chosen with care by Trine S. Tveter. Never the less it is the digitization that determines the systematic uncertainty for a set of fixed cut parameters in the clustering and tracking. The default values in BRAT was used for all the analyzed data presented here. This might not necessarily be the best choice. The statistical uncertainty can be made arbitrarily small and easily negligible by doing the analysis over a huge number of events. As distortions are not propperly implemented into the digitization, further investigations on the efficiency remains important work for the future. As shown in section 9.8 on page 124 the systematic uncertainty is of the order 2-5%. This seems a reasonable number. Another good test would have been to compare the results presented here with results obtained from the method proposed in [27]. This would have given a better estimate of the systematic uncertainty. Unfortunately direct comparison with these results was not feasible, but showed similar results for the efficiency.

In the future the time-of-flight should also be implemented in the efficiency analysis. Embedding of tracks could be also implemented in the other tracking and PID detectors. Efficiency as a function of the occupancy can then be obtained for all these detectors.

In chapter 10 the twotrack resolution of the TPCs was presented. The number obtained from this simulation analysis, is a guideline for how closely spaced two track can be to be cleanly recontructible. This type of information can be important in HBT analysis. The crossing probability shown in section 10.2, could be a hint to the source of the ghost tracks at high track densities in the TPCs.

Just before this thesis was ready to be delivered, a small bug was discovered in the class "BrEffGeantModule", which resulted in a small contamination of the embedded particles duw to decay in flight. Not all the reconstructed particles were of the specified type. A short check of the analyzed files gave the results shown in table 11.1. The total contamination is at the most 2,5%, usually $< 1\%$, so this should not have any effect on the conclusions drawn in this thesis. All the embedded particles of wrong type were among the decay products of the specified particle.

The efficiency results must be applied to the raw data. This will affect the spectra and yield. The collaboration must decide on a framework for the efficiency corrections that fits into the current analysis chain. To what extent the physics results will be affected remains to be seen. The biggest impact will probably be on high p_T physics, since the momentum reconstruction is not too good in this momentum range.

Run	θ	**P**	**T**	e^+	e^-	μ^+	μ^-	π^+	π^-	K^+	K^-	p^+
5713	90.0°	π^+	**0.299**	*NS*	*NS*	0.298	*NS*	*NS*	*NS*	*NS*	*NS*	0.001
5713	90.0°	K^+	**0.092**	0.005	*NS*	0.053	*NS*	0.026	0.008	*NS*	*NS*	*NS*
5713	90.0°	p^+	—	—	—	—	—	—	—	—	—	—
5642	60.0°	π^+	**0.280**	*NS*	*NS*	0.280	*NS*	*NS*	*NS*	*NS*	*NS*	*NS*
5642	60.0°	K^+	**0.036**	0.005	*NS*	0.021	*NS*	0.008	0.002	*NS*	*NS*	*NS*
5642	60.0°	p^+	—	—	—	—	—	—	—	—	—	—
5677	52.5°	π^+	**0.277**	*NS*	*NS*	0.277	*NS*	*NS*	*NS*	*NS*	*NS*	*NS*
5677	52.5°	K^+	**0.055**	0.004	*NS*	0.047	*NS*	0.004	*NS*	*NS*	*NS*	*NS*
5677	52.5°	p^+	—	—	—	—	—	—	—	—	—	—
5508	40.0°	π^+	**0.291**	*NS*	*NS*	0.289	*NS*	*NS*	*NS*	*NS*	*NS*	0.002
5508	40.0°	K^+	**0.087**	0.003	*NS*	0.063	*NS*	0.017	0.002	*NS*	*NS*	0.002
5508	40.0°	p^+	—	—	—	—	—	—	—	—	—	—
5713	20.0°	π^-	**2.954**	*NS*	*NS*	*NS*	2.941	*NS*	*NS*	*NS*	*NS*	0.013
5713	20.0°	K^-	**0.937**	*NS*	0.008	*NS*	0.678	0.038	0.201	*NS*	*NS*	0.012
5713	20.0°	p^-	**0.096**	*NS*	0.003	*NS*	*NS*	0.054	0.030	*NS*	*NS*	0.009
5677	12.0°	π^+	**2.549**	*NS*	*NS*	2.527	*NS*	*NS*	0.004	*NS*	*NS*	0.018
5677	12.0°	K^+	**1.250**	0.007	*NS*	0.981	*NS*	0.237	0.018	*NS*	*NS*	0.007
5677	12.0°	p^+	**0.008**	*NS*	*NS*	*NS*	*NS*	0.004	0.004	*NS*	*NS*	*NS*
5642	12.0°	π^+	**1.581**	*NS*	*NS*	1.563	*NS*	*NS*	0.006	*NS*	*NS*	0.012
5642	12.0°	K^+	**1.236**	0.019	*NS*	1.041	*NS*	0.170	0.001	*NS*	*NS*	0.005
5642	12.0°	p^+	**0.011**	*NS*	0.001	*NS*	0.001	0.004	0.005	*NS*	*NS*	*NS*
5573	8.0°	π^+	**1.882**	*NS*	*NS*	1.873	*NS*	*NS*	*NS*	*NS*	*NS*	0.009
5573	8.0°	K^+	**0.963**	0.023	*NS*	0.744	*NS*	0.178	0.009	*NS*	*NS*	0.009
5573	8.0°	p^+	—	—	—	—	—	—	—	—	—	—
5508	4.0°	π^-	**0.839**	*NS*	*NS*	*NS*	0.829	0.008	*NS*	*NS*	*NS*	0.002
5508	4.0°	K^-	**1.408**	*NS*	0.012	*NS*	1.218	0.013	0.143	*NS*	*NS*	0.022
5508	4.0°	p^-	**0.086**	*NS*	*NS*	*NS*	*NS*	0.057	0.027	0.002	*NS*	*NS*
5548	3.0°	π^+	**1.299**	*NS*	*NS*	1.277	*NS*	*NS*	0.013	*NS*	*NS*	0.009
5548	3.0°	K^+	**1.569**	0.011	*NS*	1.284	*NS*	0.252	0.015	*NS*	*NS*	0.007
5548	3.0°	p^+	**0.035**	*NS*	*NS*	*NS*	*NS*	0.015	0.013	0.007	*NS*	*NS*

Table 11.1: Contamination of the simulation files for their respective runs. "—" means uncontaminated simulations files. *NS* means not seen. **P** specifies the intended simulation particle. **T** is the total contamination. Numbers given in %.

Appendix A

Digitization parameters

The digitization constants discussed in section 6.3 on page 33 are related to the following function calls:

Constant	Function
σ_{PRF}	*SetAnodeGap()*
D_T	*SetDtrans()*
D_L	*SetDlong()*
τ	*SetTauScale()*
k	*SetAbsorp()*
$N_{tot}/N_{eff,pad}$	*SetN0_pad_to_tot()*
$ADCgain$	*SetADCGain()*

For TPM1 the following parameters have been used:

```
BrDigitizeTpc::SetUseGongTimeResp(kTRUE);
BrDigitizeTpc::SetTauScale(0.40);
BrDigitizeTpc::SetNoise(2);
BrDigitizeTpc::SetAbsorp(0.015);
BrDigitizeTpc::SetN0_pad_to_tot(4.0);
float adcgain=BrDetectorParamsTPC::GetADCGain();
BrDigitizeTpc::GetDetectorParamsTPC()->SetADCGain(adcgain*3.6);
BrDigitizeTpc::GetDetectorParamsTPC()->SetDlong(0.024);
BrDigitizeTpc::GetDetectorParamsTPC()->SetDtrans(0.017);
BrDigitizeTpc::GetDetectorParamsTPC()->SetAnodeGap(0.25);
```

For TPM2:

```
BrDigitizeTpc::SetUseGongTimeResp(kTRUE);
BrDigitizeTpc::SetTauScale(0.40);
BrDigitizeTpc::SetNoise(2);
BrDigitizeTpc::SetN0_pad_to_tot(8.0);
```

```
BrDigitizeTpc::SetAbsorp(0.015);
float adcgain=BrDetectorParamsTPC::GetADCGain();
BrDigitizeTpc::GetDetectorParamsTPC()->SetADCGain(adcgain*4.7);
BrDigitizeTpc::GetDetectorParamsTPC()->SetDtrans(0.023);
BrDigitizeTpc::GetDetectorParamsTPC()->SetDlong(0.028);
BrDigitizeTpc::GetDetectorParamsTPC()->SetAnodeGap(0.32);
```

For T1:

```
BrDigitizeTpc::SetUseGongTimeResp(kTRUE);
BrDigitizeTpc::SetTauScale(0.40);
BrDigitizeTpc::SetNoise(2);
BrDigitizeTpc::SetN0_pad_to_tot(5.0);
BrDigitizeTpc::SetAbsorp(0.03);
float adcgain=BrDetectorParamsTPC::GetADCGain();
BrDigitizeTpc::GetDetectorParamsTPC()->SetADCGain(adcgain*2.2);
BrDigitizeTpc::GetDetectorParamsTPC()->SetDtrans(0.020);
BrDigitizeTpc::GetDetectorParamsTPC()->SetDlong(0.027);
BrDigitizeTpc::GetDetectorParamsTPC()->SetAnodeGap(0.30);
```

For T2:

```
BrDigitizeTpc::SetUseGongTimeResp(kTRUE);
BrDigitizeTpc::SetTauScale(0.40);
BrDigitizeTpc::SetNoise(2);

BrDigitizeTpc::SetN0_pad_to_tot(5.0);
BrDigitizeTpc::SetAbsorp(0.03);
float adcgain=BrDetectorParamsTPC::GetADCGain();
BrDigitizeTpc::GetDetectorParamsTPC()->SetADCGain(adcgain*2.0);
BrDigitizeTpc::GetDetectorParamsTPC()->SetDlong(0.028);
BrDigitizeTpc::GetDetectorParamsTPC()->SetDtrans(0.030);
BrDigitizeTpc::GetDetectorParamsTPC()->SetAnodeGap(0.30);
```

Appendix B

BEAT

The BEAT GUI is shown in figures B.1 — B.5. BEAT can interperate the parameters shown in table B.1 on page 157.

Below is an example of how you might start beat without the GUI. Create a file that may look something like this:

```
#!/bin/bash
bratmain beat.C \
        -i /direct/brahms+data04/data/raw \
        -s ~/scratch/cdat/run5713 \
        -o test.root \
        -Q parameters/Matchoffsets5300-6000.ffs \
        -r 5713 \
        -q 0 \
        -b 10 \
        -n 20 \
        -L -20 \
        -R 20 \
        -t 6 \
        -M kTRUE \
        -e 500 \
        -Z kTRUE \
        -B kTRUE
```

Then allow it to be executed by typing at the command prompt:
prompt> chmod u+x <filename>
prompt> <filename>
BEAT should start executing the efficiency analysis.

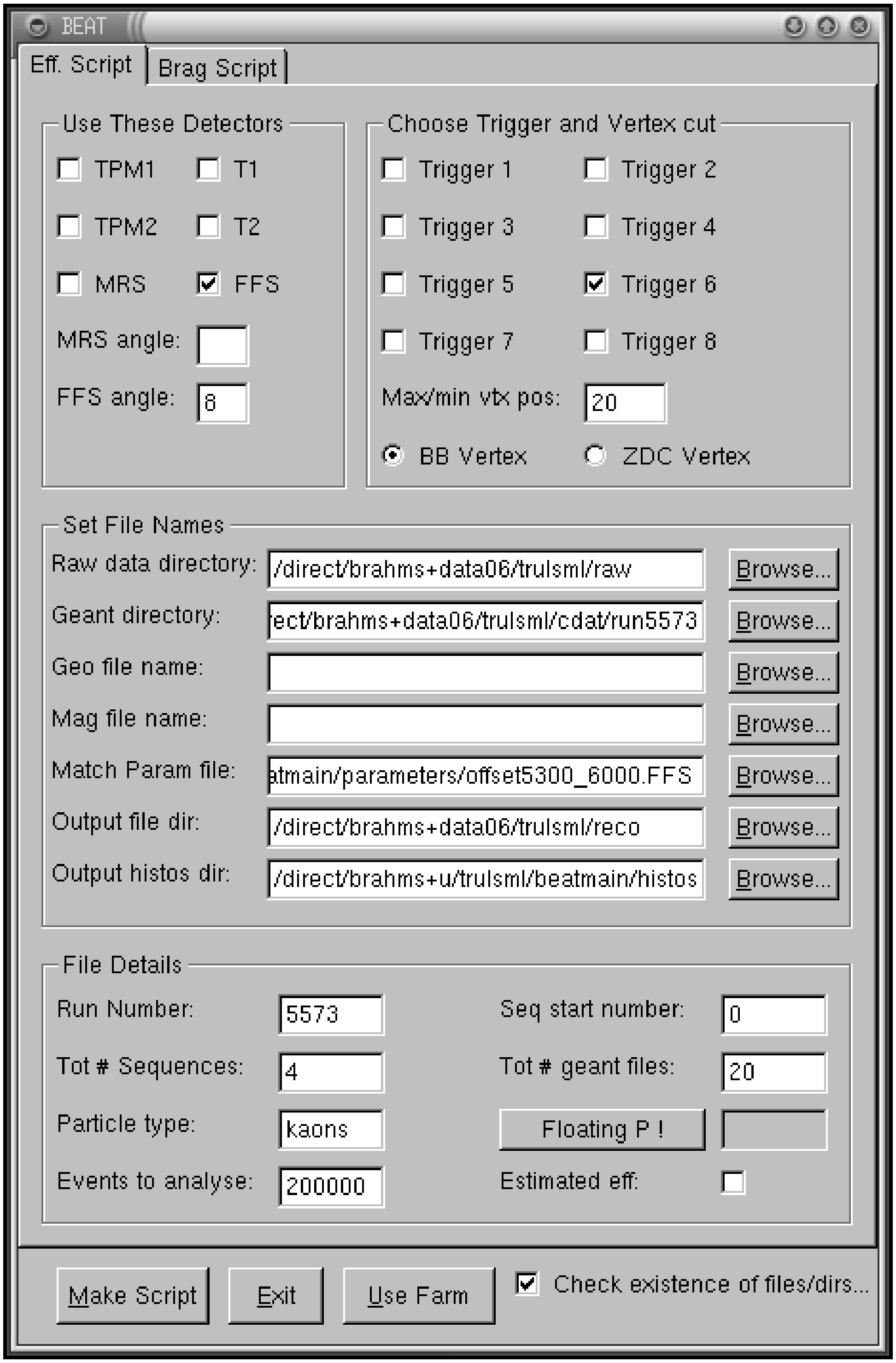

Use These Detectors

☐ TPM1 ☐ T1
☐ TPM2 ☐ T2
☐ MRS ☑ FFS

MRS angle:
FFS angle: 8

Choose Trigger and Vertex cut

☐ Trigger 1 ☐ Trigger 2
☐ Trigger 3 ☐ Trigger 4
☐ Trigger 5 ☑ Trigger 6
☐ Trigger 7 ☐ Trigger 8

Max/min vtx pos: 20

● BB Vertex ○ ZDC Vertex

Set File Names

Raw data directory: /direct/brahms+data06/trulsml/raw
Geant directory: ect/brahms+data06/trulsml/cdat/run5573
Geo file name:
Mag file name:
Match Param file: atmain/parameters/offset5300_6000.FFS
Output file dir: /direct/brahms+data06/trulsml/reco
Output histos dir: /direct/brahms+u/trulsml/beatmain/histos

File Details

Run Number: 5573
Tot # Sequences: 4
Particle type: kaons
Events to analyse: 200000
Seq start number: 0
Tot # geant files: 20
Estimated eff: ☐

☑ Check existence of files/dirs...

Figure B.1: The efficiency BEAT GUI. This generates scripts to run the Efficiency analysis.

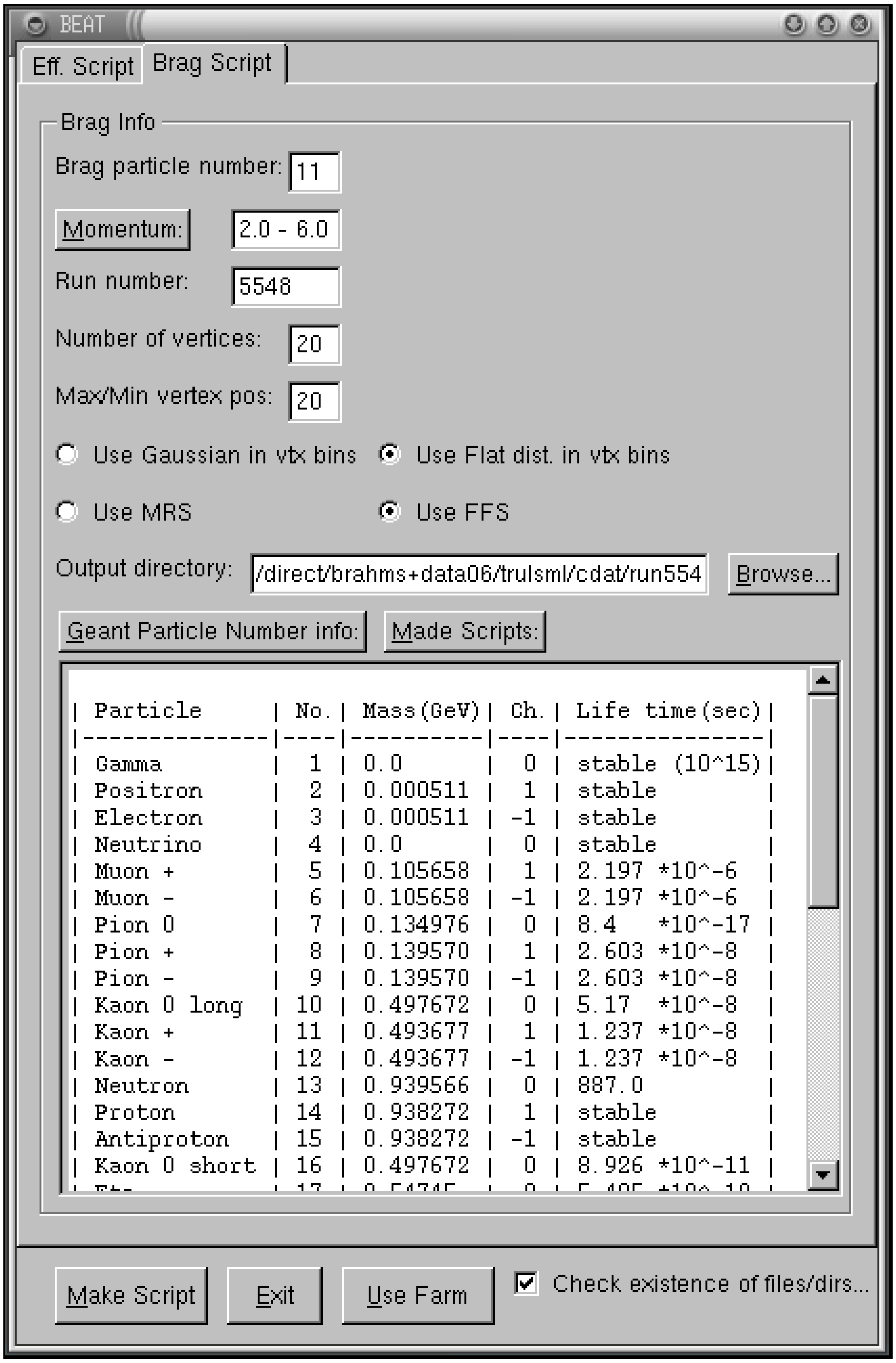

Brag particle number: 11

Momentum: 2.0 - 6.0

Run number: 5548

Number of vertices: 20

Max/Min vertex pos: 20

○ Use Gaussian in vtx bins ● Use Flat dist. in vtx bins

○ Use MRS ● Use FFS

Output directory: /direct/brahms+data06/trulsml/cdat/run554

```
| Particle      | No. | Mass(GeV) | Ch. | Life time(sec) |
|--------------|----|----------|----|----------------|
| Gamma         |  1 | 0.0       |  0 | stable  (10^15)|
| Positron      |  2 | 0.000511  |  1 | stable         |
| Electron      |  3 | 0.000511  | -1 | stable         |
| Neutrino      |  4 | 0.0       |  0 | stable         |
| Muon +        |  5 | 0.105658  |  1 | 2.197 *10^-6   |
| Muon -        |  6 | 0.105658  | -1 | 2.197 *10^-6   |
| Pion 0        |  7 | 0.134976  |  0 | 8.4   *10^-17  |
| Pion +        |  8 | 0.139570  |  1 | 2.603 *10^-8   |
| Pion -        |  9 | 0.139570  | -1 | 2.603 *10^-8   |
| Kaon 0 long   | 10 | 0.497672  |  0 | 5.17  *10^-8   |
| Kaon +        | 11 | 0.493677  |  1 | 1.237 *10^-8   |
| Kaon -        | 12 | 0.493677  | -1 | 1.237 *10^-8   |
| Neutron       | 13 | 0.939566  |  0 | 887.0          |
| Proton        | 14 | 0.938272  |  1 | stable         |
| Antiproton    | 15 | 0.938272  | -1 | stable         |
| Kaon 0 short  | 16 | 0.497672  |  0 | 8.926 *10^-11  |
```

☑ Check existence of files/dirs...

Figure B.2: The brag BEAT GUI. This generates brag scripts to make the simulation files. The big text field shows either which numbers belong to which particle in brag or the scripts that have been made. This is selected by pressing one of the buttons above it.

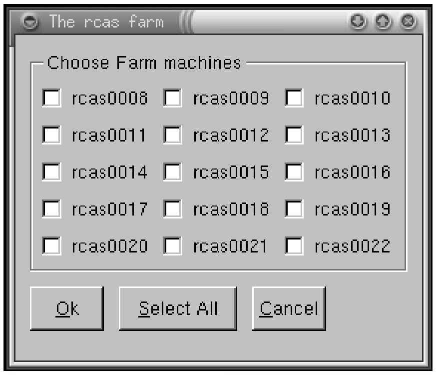

Figure B.3: The farm widget. It pops up when the "Use Farm" button is pressed. Selects nodes for running the analysis on the rcas farm.

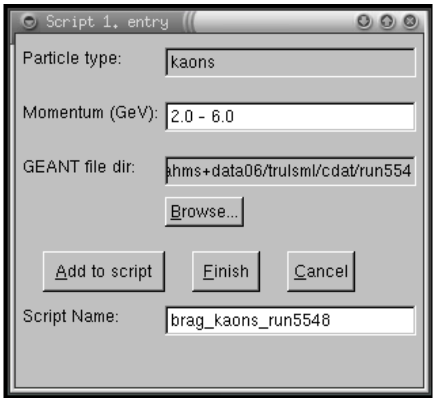

Particle type: kaons

Momentum (GeV): 2.0 - 6.0

GEANT file dir: hms+data06/trulsml/cdat/run554

Script Name: brag_kaons_run5548

Figure B.4: The script widget. It pops up when the "Make Script" button is pressed. The name of the script is specified together with the first entry.

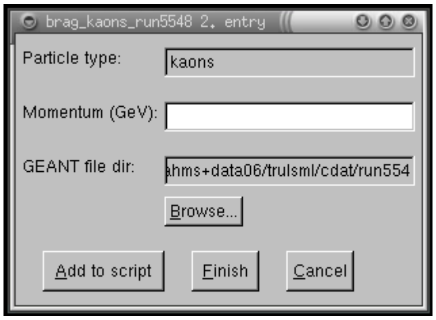

Particle type: kaons

Momentum (GeV):

GEANT file dir: hms+data06/trulsml/cdat/run554

Figure B.5: More particle species and energies are specified here.

Long Option	**Short**	**Description**
–bb	-B	Vertex cut with BB, default is false
–cluster	-C	Vertex cut with cluster, default is false
–debug	-d	Debug level, default is 0
–energy	-E	Energy of geant particle, default is 0
–events	-e	Number of events to analyze, default is 500
–ffs	-F	Analyze the FFS (T1, T2 & combined), default is false
–ffsangle	-a	Angle of the FFS, default is 0
–geofile	-g	Geometry file name, default is
–ginput	-s	Geant Input Directory, default is cdat/
–help	-h	Show this help, default is true
–histogram	-H	Histogram file name, default is
–input	-i	Raw Data Input Directory, default is
–magfile	-m	Magnet file name, default is
–matching	-Q	Matching parameter file name, default is
–maxvtx	-z	Abs vertex max value, default is 0
–mrs	-M	Analyze the MRS (TPM1, TPM2 & combined), default is false
–mrsangle	-A	Angle of the MRS, default is 0
–numgeant	-n	Number of geant files, default is 1
–numofseq	-b	Number of sequence to analyze, default is 999
–output	-o	Output file name, default is
–parameter	-p	Detector Parameter File, default is DetectorParameters.txt
–particle	-P	Particle to analyze, default is
–runno	-r	Run Number, default is 0
–seqno	-q	Sequence Number, default is 0
–skip-events	-c	Number of events to skip, default is 5
–speak	-S	Print ẽff, 0=off, 1=terminal, 2=widget, default is 0
–t1	-3	Analyze T1, default is false
–t2	-4	Analyze T2, default is false
–tpm1	-1	Analyze TPM1, default is false
–tpm2	-2	Analyze TPM2, default is false
–track	-T	Vertex cut with track, default is false
–treeoutput	-O	Tree output file name, default is
–trigger	-t	Analyze only triggers, default is 0

... continued on the next page ...

... continued from previous page ...

Long	**Short**	**Description**
–usegeomagDB	-D	Use geo/mag database parameters, default is false
–verbose	-v	Verbose output, default is 0
–version	-V	Version number, default is false
–zdc	-Z	Vertex cut with ZDC, default is false

Table B.1: The options in BEAT.

Appendix C

Analyzed runs

The efficiency analysis was done on the following runs:

Run	**5508**	**5548**	**5573**	**5642**	**5677**	**5713**
Events	234818	241958	149365	339276	109749	362116
Trig1	222569	233939	134210	325065	106590	347901
Trig4	224219	235667	135938	328440	107668	354067
Trig6	69668	75208	42033	100568	33477	192377
FFS	4.0°	3.0°	8.0°	12.0°	12.0°	20.0°
MRS	40.0°	*40.0°*	*40.0°*	60.0°	52.5°	90.0°
D2	1402/A	923/B	552/B	690/B	348/B	281/A
D5	500/B	*1000/A*	*1000/B*	500/A	500/A	350/B

Table C.1: The runs used in the efficiency analysis, except for the MRS at 40° in run 5548 and 5573, emphasized in the table. The last two rows, the magnetic field in the magnets, are in units of *Gauss*. The As and Bs are the polarity of the magnetic field.

The analysis was done on all the trigger 6 events in each of these runs, except run 5713 where only half of them were analyzed.

Appendix D

The BRAHMS collaboration

At the time of writing, the BRAHMS collaboration consists of these members from the following institutions:

I. G. Bearden[7], D. Beavis[1], Y. Blyakhman[6], J. Brzychczyk[4], B. Budick[6], H. Bøggild[7], C. Chasman[1], P. Christiansen[7], J. Cibor[4], R. Debbe[1], E. Enger[2], J. J. Gaardhøje[7], M. Germinario[7], K. Grotowski[4], J. I. Jordre[9], F. Jundt[3], K. Hagel[8], O. Hansen[7], A. Holm[7], C. Holm[7], A. K. Holme[2], H. Ito[11], E. Jacobsen[7], A. Jipa[10], C. E. Jørgensen[7], E. J. Kim[5], T. Kosic[4], T. Kreutgel[4], T. M. Larsen[2], J. H. Lee[1], Y. K. Lee[5], S. Lindal[2], G. Løvhøiden[2], Z. Majka[4], A. Makeev[8], B. McBreen[1], M. Mikelsen[2], M. Murray[8], J. Natowitz[8], B. S. Nielsen[7], K. Olchanski[1], D. Ouerdane[7], J. Olness[1], R. Planeta, F. Rami[3], D. Roehrich[9], B. H. Samset[2], S. Sanders[11], I. S. Zgura[10], R. A. Sheetz[1], Z. Sosin[10], P. Staczel[7],T. F. Thorsteinsen[10] +, T. S. Tveter[2], F. Videbæk[1], R. Wada[8], A. Wieloch[4], Z. Yin[9], S. Zgura[10].

[1] Brookhaven National Laboratory, Upton, NY 11973-5000, USA.
[2] Fysisk Institutt, University of Oslo, Blindern, Norway.
[3] IReS, University Louis Pasteur, Strasbourg, France.
[4] Jagiellonian University, Krakow, Poland.
[5] Johns Hopkins University, Baltimore, USA.
[6] New York University, USA.
[7] Niels Bohr Institute, University of Copenhagen, Denmark.
[8] Texas A&M University, College Station. USA.
[9] University of Bergen, Norway.
[10] University of Bucharest, Romania.
[11] University of Kansas, USA.
+ Deceased.

Bibliography

[1] J. D. Bjorken. Highly relativistic nucleus-nucleus collisions: The central rapidity region. *Phys. Rev.*, D27:140–151, 1983.

[2] L. D. Landau. *Izv.Akad.Nauk.Ser.Fiz*, 17(88):51, 1953.

[3] Djamel Ouerdane for the BRAHMS collaboration. Rapidity Dependence of Charged Particle Yields for Au+Au $\sqrt(s_{NN}) = 200GeV$. *To appear in the QM proceedings*, 2002.

[4] Peter Christiansen. Proton and antiproton analysis. BRAHMS analysis note 42, Niels Bohr Institute, Copenhagen, Denmark, December 2002.

[5] RHIC design manual. Technical report, BNL. http://www.rhichome.bnl.gov/NT-share/rhicdm/.

[6] K. Adcox et al. Centrality dependence of $\pi^{\pm}$, $k^{\pm}$, p and $\overline{p}$ production from $\sqrt{s_{NN}} = 130\,GeV$ Au + Au collisions at RHIC. *Phys.Rev.Lett.*, 88:242301, 2002.

[7] K. Adcox et al. Centrality dependence of charged particle multiplisity in Au-Au collisions at $\sqrt{s_{NN}} = 130\,GeV$. *Phys. Rev. Lett.*, 86:3500–3505, 2001.

[8] I. G. Bearden et al. The BRAHMS experiment at RHIC. Technical report, 2001. To appear in Nucl. Inst. Meth. A.

[9] B.R Martin & G. Shaw. *Particle Physics*. John Wiley & Sons, 1997.

[10] Peter Christiansen for the BRAHMS collaboration. Rapidity Dependence of Net-protons at $\sqrt(s_{NN}) = 200GeV$. *To appear in the QM proceedings*, 2002.

[11] I. G. Bearden et al. Rapidity dependence of Charged anti-particle-to-particle ratios in Au+Au collisions at $\sqrt(s_{NN}) = 200$ GeV. *Phys. Rev. Lett.*, submitted, 2002.

[12] The GEANT software. http://geant4.cern.ch/asd/geant/index.html.

[13] W. G. Gong. The STAR-TPC Slow Simulator. Technical report, STAR collaboration, 1995.

[14] Flemming Videbaek. BRAHMS conseptual design report. Technical report, BRAHMS collaboration. http://www4.rcf.bnl.gov/brahms/WWW/cdr/cdr.html.

[15] The ROOT software. http://root.cern.ch/.

[16] The MySql (open source database) software. http://www.mysql.com/.

[17] How to install and use BRAT. http://pii3.brahms.bnl.gov/ brahmlib/.

[18] Brahms shift instructions. http://pii3.brahms.bnl.gov/ operator/BrahmsUser/BRAHMSUser.htm.

[19] How to use TThread in ROOT. http://www-linux.gsi.de/ go4/HOWTOthreads/.

[20] Jens Ivar Jørdre. Performance of the Time Projection Chamber of the BRAHMS experiment at RHIC. Master's thesis, University of Bergen, 2001.

[21] Bjørn H. Samset. Vertex determination in the BRAHMS experimentet and measurements of centrality dependent charged particle production in au-au collisions at $\sqrt{s_{NN}} = 130\ AGeV$. Master's thesis, University of Oslo, 2001.

[22] Christian Holm Chistensen and Claus E. Jørgensen. Centrality estimates using the scintilator tiles in the multiplicity array. BRAHMS analysis note 22, Niels Bohr Institute, Copenhagen, Denmark, February 2001.

[23] Christian Holm Chistensen. Comparing centrality methods to impact parameter. BRAHMS analysis note 37, Niels Bohr Institute, Copenhagen, Denmark, September 2001.

[24] I. G. Bearden et al. Charged particle densities from Au+Au collisions at $\sqrt{(s_{NN})} = 130$ GeV. *Phys. Lett. B*, 523:227, 2001.

[25] Ramiro Debbe. Stop the press! Rings out of RICH. BRAHMS analysis note 15, BNL, Brookhaven, Long Island, USA, November 2000.

[26] Peter Christiansen. Particle ratios from BRAHMS at $\sqrt{s_{NN}} = 200\,GeV$. In *Presented at the 18th Winter Workshop on Nuclear Dynamics.*, January 2002. http://www4.rcf.bnl.gov/brahms/WWW/publications.html.

[27] Pawel Staszel. Track Reconstruction Efficiency in FS Tracking Detectors. BRAHMS analysis note 38, Niels Bohr Institute, Copenhagen, Denmark, November 2001.